School of Engineering
Cardiff University
United Kingdom

Fatigue of Reinforced Concrete Beams Retrofitted with Ultra-High Performance Fibre- Reinforced Concrete

THIS THESIS IS SUBMITTED IN PARTIAL FULFILMENT OF THE REQUIREMENTS FOR THE DEGREE OF DOCTOR OF PHILOSOPHY (PhD)

By

Bakr Salahuddin Al-Azzawi
B.Sc., M.Sc.

January 2018

DECLARATION AND STATEMENTS

DECLARATION

This work has not been submitted in substance for any other degree or award at this or any other university or place of learning, nor is being submitted concurrently in candidature for any degree or other award.

Signed ……..…... (**Bakr Al-Azzawi**) Date……..….

STATEMENT 1

This thesis is being submitted in partial fulfilment of the requirements for the degree of Doctor of Philosophy (PhD).

Signed ……..…. (**Bakr Al-Azzawi**) Date……..….

STATEMENT 2

This thesis is the result of my own independent work/investigation, except where otherwise stated, and the thesis has not been edited by a third party beyond what is permitted by Cardiff University's Policy on the Use of Third Party Editors by Research Degree Students. Other sources are acknowledged by explicit references. The views expressed are my own.

Signed ……..… (**Bakr Al-Azzawi**) Date……..….

STATEMENT 3

I hereby give consent for my thesis, if accepted, to be available online in the University's Open Access repository and for inter-library loan, and for the title and summary to be made available to outside organisations.

Signed ……..…. (**Bakr Al-Azzawi**) Date……..….

Synopsis

Concrete structures deteriorate over time due to different reasons and thus may not perform their function satisfactorily. Repair and rehabilitation of deteriorated concrete structures is often preferred over demolition and rebuilding for economic reasons. Various metallic and non-metallic materials have been used in the past for repair and rehabilitation. These materials have advantages and disadvantages. The latter are connected with the mismatch in the properties of these materials with the material of the structure being repaired which often resulted in unwanted failure modes, e.g. delamination. For this reason, new cement-based ultra-high performance reinforced with steel fibres repair materials have been developed in the last two decades, which restore (and even enhance) the structural response and improve the durability of repaired concrete structures. One such ultra-high-performance fibre-reinforced concrete material is CARDIFRC. It is characterized by very high compressive strength, high tensile /flexural strength, and high energy-absorption capacity. However, it is very expensive and thus industrially uncompetitive due to the very high cost of thin brass-coated steel fibres used in it.

It is therefore important to develop a version of CARDIFRC that is industrially competitive. This is one of the objectives of this research. An ultra-high-performance fibre-reinforced concrete (UHPFRC) has been developed that is far less expensive than CARDIFRC and at the same time self-compacting. The steps necessary to achieve this have been described in this work. In addition, a full mechanical and fracture characterisation (i.e. size-independent fracture energy and the corresponding bi-linear stress-crack opening relationship) of this UHPFRC is presented. A nonlinear cracked hinge model has been used to back calculate the stress-crack opening relation of this material in an inverse manner from the test data.

The second objective of this research concerns the flexural fatigue behaviour of this new UHPFRC. Tests have been conducted under several stress amplitude ranges. It has been found that the distribution of fibres plays a vital role in its fatigue resistance. Regions with few or no fibres can drastically reduce its fatigue life. As expected, non-zero mean stress leads to a significant reduction in the fatigue life of a material compared to cyclic loading with zero mean. The variation in compliance during cyclic loading has been used to estimate the expected fatigue life under a given cyclic load range, since the tests were terminated at one million cycles.

The third objective of this research concerns the flexural fatigue behaviour of RC beams retrofitted with precast strips of this self-compacting UHPFRC on the tension face. Fatigue tests under several stress amplitude ranges have shown that this UHPFRC is an excellent retrofit material under fatigue loading. Again, the variation in compliance during the fatigue loading has been used to estimate the expected fatigue life for retrofitted RC beams.

DEDICATION

To my loved country Iraq and my family who has been a constant source of support and encouragement during the preparation of this research.

ACKNOWLEDGEMENTS

First of all, I would like to present my sincere thanks is to my supervisor, Professor Bhushan Karihaloo for his priceless guidance and support. I appreciate his valuable discussions and continuous advice that help me much in completion this study. This work would not have been completed without his support.

I would like also to express my thanks to my co-supervisor Dr. Kulasegaram for his support and encouragement.

Many thanks to the staff of research office and the technical staff of concrete laboratory at Cardiff University / School of Engineering, for their encouragement and help during my PhD journey.

Further thanks and appreciation is expressed to my loved country, Iraq represented by Ministry of Higher Education and Scientific Research/ Al Nahrain University for funding my study and giving me this opportunity.

Finally, warm and special thanks are expressed to my parents, wife, all my family and friends for their prayers and support during the period of this research.

Bakr Al-Azzawi

TABLE OF CONTENTS

LIST OF FIGURES

LIST OF TABLES

NOTATIONS

SCC	Self-compacting concrete
NC	Normal concrete
a	Notch depth, mm
a_l	Transition ligament length, mm
E	Modulus of elasticity, GPa
FPZ	Fracture process zone
FCM	Factious crack model
MOR	Modulus of rupture
f_c	Cube compressive strength, MPa
f_t	Splitting (indirect) tensile strength, MPa
G_f	Size-dependent fracture energy, N/m
G_F	Size-independent fracture energy, N/m
GGBS	Ground granulated blast furnace slag
l_{ch}	Characteristic length, mm
LEFM	Linear fracture mechanics
NLFM	Nonlinear elastic fracture mechanics
SP	Super-plasticizer
T_{500}	Time taken for SCC to spread 500mm in the flow test, s
T_{500j}	Time taken for SCC to spread 500mm in the J-ring test, s
TPB	Three-point bending test
TSD	Tension softening diagram
W	Beam depth, mm
B	Beam width, mm
δ	The non-dimensional mid-span deflection
w_c	the critical crack opening displacement, mm
a/W	Notch to depth ratio
$\sigma(w)$	The cohesive stress-crack
HPRCCs	High Performance Fibre Reinforced Cement Composites
UHPFRC	Ultra-High-Performance Fibre Reinforced Concrete
FRC	Fibre Reinforced Concrete
FRP	Fibre Reinforced Plastics

Ci	The initial compliance
N	Number of cycles sustained by each test specimen
N_f	Number of cycles to failure
N_{pf}	Predicted number of cycles until failure
R	Stress ratio
σ_m	Mean stress
$\Delta\sigma$	The stress range
$\Delta\sigma_0$	The cyclic stress range with zero mean stress
$\Delta\sigma_{\sigma m}$	The cyclic stress range with non-zero mean stress
σ_F	The static flexural strength
σ_y	The yield stress

Chapter One

Introduction

1.1 Introduction

Concrete is probably the most widely used contemporary construction material thanks to its significant resistance in compression. It is utilized, for instance, in building, bridges, roads and marine structures. Evaluation of both the mechanical and fracture properties including strength, stiffness and fracture energy has been widely conducted at room temperature. Several textbooks cover the applications and the details of the concrete properties (e.g. Neville, 1995 and Karihaloo, 1995).

However, low tensile strength, low ductility, and low energy absorption are main weaknesses of concrete. A major reason of the poor tensile behaviour of concrete is the presence of defects.

Many flaws are found in plain and reinforced concrete structures, even before they are mechanically loaded. A stable growth of these flaws, and especially the small cracks (micro-cracks) can be expected under external loading, followed by their merger with existing or newly-formed micro-cracks until large fractures are formed which cause the failure of the structure.

The design of concrete structures is performed without regard to either the propagation of large cracking zones through them or an energy failure criterion. Fracture mechanics provides an energy-based failure theory that could be used in designing cement-based structures, since it studies the response and failure of structures as a result of crack initiation and propagation (Karihaloo, 1995).

Since cracking in concrete is inevitable, enhancing concrete toughness and reducing the size and amount of flaws in concrete would improve concrete performance. This can be achieved by adding a small fraction (usually 0.5–2% by volume) of short fibres to the concrete mix during mixing (Wang et al., 2000). The fibres bridge across the cracks in

the matrix during the fracture process thus increasing resistance to crack propagation and crack opening before being pulled out or stressed to rupture.

Traditional fibre-reinforced concrete (FRC) demonstrates an increase in ductility over that of plain concrete, while High Performance Fibre Reinforced Cementitious Composites (HPFRCCs) present significant strain-hardening response. Hence, a large amelioration in both strength and toughness compared with the plain concrete is acquired (Shah et al., 1999).

HPFRCCs have been made possible by the recent advances in manufacturing processing that permit the inclusion of a large amount of fibres in the cement based matrix without affecting the workability of the mix. Silica fume and surfactants which reduce water demand give these improvements to the HPFRCCs where the matrix become denser and thereby increases the fibre-matrix interfacial bond (Morin et al., 2001).

Concrete structures can deteriorate and hence need repair after long periods in service. Therefore, one of the major challenges facing structural engineers is repairing and strengthening of reinforced concrete structures.

The term retrofitting of reinforced concrete members has a broad meaning. It includes increasing the load carrying capacity of structural members and enhance their performance in such a way that least maintenance is necessary during the service life.

Diverse methods of strengthening reinforced concrete (RC) structures using various materials have been studied and applied in the retrofitting field. Among the most commonly used option is by bonding a steel plate to the tension side of the beam. The speed of implementation of this technique is its major advantage. However, several problems have been noticed and recorded with this technique, such as potential steel corrosion that adversely leads to deterioration of the bond at a glued steel–concrete interface. In addition, the need of using joint systems due to the limited workable

lengths and handling heavy steel plates is another drawback of using steel plates (Jones et al., 1988).

In recent years, fibre reinforced plastic plates (FRP) have gained prominence in concrete structural retrofitting field. The high stiffness-to-weight ratio and improved durability over steel plates are the main features of using FRP as a retrofitting material (Ekenel et al., 2006; Meier, 1997). However, many problems have been noticed, such as the possibility of brittle debonding failures (Buyukozturk et al., 2004) which may considerably decrease the efficiency of the strengthening. The large mismatch in the tensile strength and stiffness with that of concrete is the cause of this unfavourable brittle failure. Moreover, an impairment of the interface between FRP composites and concrete is expected due to the long exposure to temperature variation (Sen et al., 2000; Mei and Chung, 2000).

A novel material suitable for strengthening structural members subjected to severe mechanical and environmental actions is the ultra-high performance fibre-reinforced concrete (UHPFRC). It possesses outstanding properties: relatively high compressive strength, high tensile strength, strain-hardening behaviour under tensile stress (given a certain volume of fibres) and very low permeability since an optimised dense matrix is used (Makita and Brühwiler, 2014a; Martín-Sanz et al., 2016).

Contemporary line of research for repairing or strengthening concrete members is in the use of cement-based materials. Within this class, a new retrofitting material has been developed at Cardiff University called the CARDIFRC (Benson and Karihaloo, 2005a, b; Benson et al., 2005). It overcomes some of the problems (Karihaloo et al., 2002) identified above for steel plates and FRP composites which are primarily due to the mismatch of their tensile strength, stiffness and coefficient of linear thermal expansion with the parent concrete being retrofitted. The findings showed that the retrofitting of

RC members using CARDIFRC plates on the tension face improves the flexural load carrying capacity and decreases the crack width and the deflection.

Many concrete structures are usually subject to repetitive cyclic loads in addition to the static loads, which cause a permanent increase in strain and a steady decrease in the stiffness of the structure that leads to structural failure at a load level inferior to its static capacity.

Fatigue may be recognized as a process of progressive, permanent internal structural changes in a material exposed to repeated loading (ACI 215R-74). In concrete, fatigue is a process of progressive, permanent evolution of small flaws existing in the material by repetitive loads, which lead to a considerable increase of irrecoverable strain. These imperfections may be present in concrete due to concrete shrinkage, or may be caused by application of external loads.

Fatigue loading is usually divided into two categories (RILEM Committee 36-RDL, 1984) i.e. low-cycle and high-cycle loading. Low-cycle loading includes the application of a few load cycles at high stress levels. On the other hand, high cyclic loading is characterised by a large number of cycles at lower stress levels.

Abundant research on the development of Fibre Reinforced Concretes (FRCs) and particularly of High Performance Fibre Reinforced Cementitious Composites (HPFRCCs) is focused on minimising the detrimental effect of cracking in concrete. It has been found that the addition of fibre reinforcement to concrete has a twin effect on its fatigue performance. On the one hand, by bridging micro-cracks, fibres are able to hinder the crack propagation process, thus improve the composite performance under fatigue loading. On the other hand, flaws and initial micro-crack density may be increased by adding fibres (Nicolaides et al., 2010).

1.2 Aim of the Thesis

The primary aim of this thesis is to explore the potential of a self-compacting UHPFRC developed based on CARDIFRC Mix II as a suitable material for retrofitting RC flexural members subjected to cyclic loading. To achieve this aim, the following investigations were undertaken.

- Firstly, a self-compacting and industrially competitive ultra-high performance fibre-reinforced concrete (UHPFRC) based on CARDIFRC Mix II was developed and fully characterized with respect to its mechanical and fracture properties;
- Secondly, the fatigue response of this UHPFRC version of CARDIFRC under cyclic flexure loading was investigated;
- Finally, the performance of RC beams retrofitted with the UHPFRC version of CARDIFRC and subjected to static and cyclic loading in three-point bending was thoroughly examined.

1.3 Outline of the Thesis

The contents of the thesis are organised in chapters as follows:

Chapter-1 presents a general introduction to the study, as well as the objectives and an outline of the thesis.

In **chapter 2**, the behaviour of normal strength concrete (NSC), fibre reinforced concrete (FRC) and high performance fibre reinforced cementitious composites (HPFRCCs) is briefly reviewed. In addition, a brief description of self-compacting concrete and the requirements for self-compaction are discussed.

The advantages of this class of material (HPFRCCs) and the effect of silica fume, super-plasticiser and fibres on the mechanical behaviour are explained. Finally, the main types of HPFRCCs are identified, giving prominence to CARDIFRC and the commercial version of CARDIFRC.

Chapter-3 provides background information on the basic concepts of the fracture mechanics approach (FM), and a brief discussion of the non-applicability of linear elastic FM to concrete. Then the concepts of non-linear fracture theories for concrete are explained. A brief description of those aspects of fracture mechanics that will be useful for subsequent chapters are included here.

Chapter-4 reviews the retrofitting of concrete structures with different methods such as steel plates, fibre reinforced plastics FRP and High Performance Fibre Reinforced Cementitious Composites (HPFRCs) such as CARDIFRC. A description of each system is given. In addition, this chapter presents an overview on fatigue cyclic loading, and highlights the behaviour of concrete, fibre reinforced concrete and RC beams under cyclic loading showing how usually the experimental data are represented by using the S-N curves.

Chapter-5 presents the experimental work carried out to produce a self-compacting version and industrially competitive ultra-high performance fibre-reinforced concrete (UHPFRC) based on CARDIFRC Mix II. A full mechanical and fracture characterization (i.e. size-independent fracture energy and the corresponding bi-linear stress-crack opening relationship) of this UHPFRC is provided. The resulting UHPFRC has inferior mechanical properties than the original CARDIFRC Mix II due to the absence of thin small brass-coated steel fibres (4.5% by volume; 6 mm long).

Nevertheless, it is much tougher than the original CARDIFRC Mix II thanks to the use of a larger volume fraction (2.5% against 1.5%) of longer steel fibres (30 mm against 13 mm).

The size-independent fracture energy G_F is determined using the concept of boundary effect model proposed by Duan et al. (2003). Three-point bend (TPB) tests have been conducted on the self-compacting version of CARDIFRC Mix II and G_F is assessed using a simple method proposed by Abdalla and Karihaloo (2003) and Karihaloo et al. (2003a).

The parameters of the bi-linear stress-crack opening relation of the UHPFRC self-compacted version of CARDIFRC Mix II are identified using an inverse approach, based on the non-linear hinge model proposed by Olesen (2001), for crack growth from a pre-existing notch. This model was used to simulate the static response of the UHPFRC self-compacted version of CARDIFRC Mix II prisms under three-point bending test.

Chapter-6, presents the flexural fatigue behaviour of the self-compacted UHPFRC version of CARDIFRC Mix II in terms of its S–N curve. The change in compliance under cycling and the effect of cyclic loading with non-zero mean stress are also discussed. Basquin's Law is used to relate cyclic fatigue life with the applied cyclic stress range, and Goodman rule is used to evaluate the influence of the non-zero mean stress on the fatigue life. In addition, fibre distribution and its effect on the fatigue life is studied. It is found that poor distribution of fibres plays a significant role in reducing the fatigue life. Furthermore, an estimation of the fatigue life of the UHPFRC material is acquired from the recorded variation in the compliance.

In **Chapter-7,** the performance of reinforced concrete (RC) beams and RC beams retrofitted with a self-compacting ultra-high performance fibre-reinforced concrete (UHPFRC) material is investigated under three-point bend cyclic loading. No delamination of the retrofit strip is observed in any of the fatigue tests and the retrofitted beams act as a composite structure. The endurance limit of the retrofitted RC beams with a 35 mm thick UHPFRC strip is improved from approximately 40% to approximately 60% of the static three-point flexural strength. The fatigue life of the retrofitted RC beams with the UHPFRC strips is estimated from the recorded variation in the compliance.

In **Chapter 8,** a summary of major conclusions and recommendations for future work in this field of study is reported**.**

Parts of the work reported in this thesis have been published in journal papers or have been presented at two Conferences. For easy reference, the publications are listed below:

- Al-Azzawi, B.S. and Karihaloo, B.L., 2016. Fracture and fatigue of a self-compacting version of CARDIFRC mix II. In: *24th Proceedings Conference of the Association for Computational Mechanics in Engineering (ACME),* Cardiff, UK.
- Al-Azzawi, B.S. and Karihaloo, B.L., 2016. Mechanical and fracture properties of a self - compacting UHPC, In: *21st European Conference on Fracture (ECF21),* Catania, Italy.

- Al-Azzawi, B.S. and Karihaloo, B.L., 2017a. Mechanical and fracture properties of a self-compacting version of CARDIFRC Mix II. *Sādhanā*, doi: 10.1007/s12046-017-0641-9, *42*(5), pp.795-803.
- Al-Azzawi, B.S. and Karihaloo B.L. 2017b. Flexural fatigue behaviour of a self-compacting ultra-high performance fiber-reinforced concrete. *ASCE Journal of Materials in Civil Engineering.*, doi: 10.1061/ (ASCE) MT. 1943-5533.0002051, 29(11), 04017210.
- Al-Azzawi, B.S. and Karihaloo, B.L. Application of a self-compacting ultra-high performance fibre-reinforced concrete to retrofit RC beams subjected to repeated loading. *Sādhanā*, (paper in press).

Chapter Two

High Performance Fibre-Reinforced Cementitious Composites (HPFRCCs)

2.1 Introduction

Concrete can be considered as the most important building material and its consumption is increasing in all countries in the world. It is well known that concrete is a relatively brittle material, i.e. it has relatively low tensile strength and poor resistance to crack opening and propagation. Plain concrete includes numerous micro-cracks and hence the rapid propagation of these micro-cracks under applied stress is responsible for the low tensile strength of the material (Ramakrishnan, 1995).

The mismatch of the elastic moduli of cement paste and the aggregate leads to stress concentration, which is partially responsible for the bond failure at the aggregate-paste interface causing the propagation of cracks in NC (Newman, 1965). Usually cracks take a path around the aggregates through the cement aggregate interfaces (Bentur and Mindess, 1986); hence, the essential factor limiting the strength development is the aggregate-matrix interface (Struble et al., 1980).

The drawbacks of concrete can be overcome by reinforcing with short discontinuous fibres, which in turn can restrain the propagation of cracks and restrict the crack width (Qian et al., 2000). The role of steel fibres can be perceived mainly after matrix cracking in concrete, which help in bridging the propagating cracks (Stroeven and Babut, 1986). However, the addition of steel fibres at high dosages was found to affect the workability of the fresh concrete significantly and to increase the cost (Grünewald, 2004, Sivakumar and Santhanam, 2007). Moreover, during vibration, fibres might move and segregate to the bottom of the framework leading to an uneven dispersal of fibres that will further affect the homogeneity of the mix (Gettu et al., 2005). In addition, the lack of skilled workers to perform a fully compacted concrete where there is limited or no access for

vibrators have led researchers to explore self-compacted concrete SCC to solve these problems.

Initial ideas of SCC were generated in Japan; Okamura proposed such type of concrete in 1986 (Okamura and Ouchi, 2003). Since then, the use of SCC has rapidly increased because of the needs to produce durable concrete structures, the potential economic opportunities and improvement of the working circumstances (Bonen and Shah, 2005). The inclusion of fibres in SCC will extend their benefits in the fresh state with an enhanced post-cracking performance, bridge cracks and retard their propagation and thus improve the tensile and flexural strength and fracture toughness in the hardened state thanks to the fibres (El-Dieb and Taha, 2012**).**

Mainly an increase in the ductility is exhibited in the conventional FRC compared to the plain matrix, whereas HPFRCC display a fundamental strain-hardening type of response and a large improvement is acquired in both its strength and toughness compared with the plain matrix (Shah et al., 1999). High Performance Fibre Reinforced Cement Composites (HPRCCs) represent a class of cement composites whose stress-strain response in tension undergoes strain-hardening behaviour accompanied by multiple cracking, leading to a high failure strain capacity. The behaviour of this class of material, as well as other HPFRCCs that have been presented to the industry so far will be discussed next.

2.2 Fibre Reinforced Concrete

A fibre is a small piece of reinforcing material possessing certain characteristic properties. They can be circular or flat. Fibres suitable for reinforcing concrete have been produced from steel, glass, synthetics like acrylic, aramid, carbon, nylon,

polyester, polyethylene, and polypropylene. Natural fibres like; sisal, coconut, bamboo, and jute have also been used in concrete (ACI, 1996).

The fibre is often described by a convenient parameter called 'aspect ratio' (Shetty, 2005).The purposes of reinforcing the cement-based matrix with fibres are to increase the tensile strength by delaying the growth of cracks, and to increase the toughness by transmitting stress across a cracked section so that much larger deformation is possible beyond the peak stress than without fibre reinforcement (Neville, 2010, Caverzan et al., 2012).The essential role of the fibres in hardened concrete at low volume fractions is to modify the cracking mechanism. Ramakrishnan (1995) mentioned that, by modifying the cracking mechanism the macro-cracking becomes micro-cracking and therefore the permeability is reduced by smaller cracks and the ultimate strain is enhanced. Brandt (2008) stated that it is might be convenient from both safety and

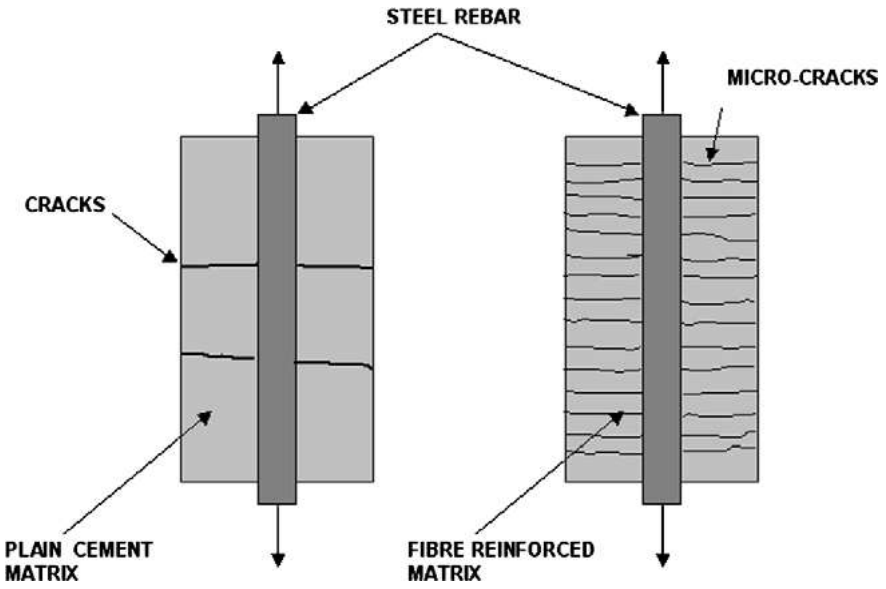

Figure 2.1 Crack pattern in reinforced concrete (RC) and fibre reinforced concrete (FRC) elements subjected to tension (After Brandt, 2008)

durability viewpoints to replace the large single cracks with dense systems of micro-cracks by using fibres (Fig. 2.1). The failure in a cementitious composite begins with the formation of micro-cracks that propagate and eventually coalesce to generate macrocracks, which cause fracture if not controlled. The existence of fibres in a cementitious matrix mitigates and stops the propagation of micro-cracks and macro-cracks (Banthia and Gupta, 2004).

The pre-peak as well as post-peak region of the load–deflection curve were enhanced due to the addition of fibres resulting in increasing the flexural strength and toughness, respectively. The performance of the fibre reinforced concrete is controlled mainly by the volume of the fibres, the physical properties of the fibres and the matrix, and the bond between the two.

The most popular fibres used in concrete is steel fibres that are in general carbon steels or alloy (stainless) steels. In refractory applications and marine structures, the latter are used mostly for corrosion resistance. The use of straight, smooth fibres such as those used originally became outdated since sufficient bond with the matrix was not developed, whereas roughness of surface, hooked or enlarged ends, or are crimped or deformed along their lengths are the most important features of modern fibres, which are intended to improve the bond (Bentur and Mindess, 2007).

Generally, addition of steel fibres participate in the energy absorbing mechanism (by bridging action) whereas, the retardation of the formation of micro-cracks is due to the contribution of the non-metallic fibres. Addition of steel fibres does not significantly increase the compressive strength, unless high fibre volumes are used. Sivakumar and Santhanam (2007) investigated the performance of the combination of hooked steel and a non-metallic fibre up to a volume fraction of 0.5%. They documented fibre concrete

composites produced using polypropylene, glass and polyester fibres in combination with steel fibres. They stated that the beneficial ramifications of adding non-metallic fibres (like glass, polyester, polypropylene etc.) are for controlling the propagation of micro cracks in the plastic stage of concrete. This is attributed to their high aspect ratios and increased fibre availability (because of lower density as compared to steel) at a given volume fraction. Nevertheless, their contribution to post-cracking behaviour is insignificant compared to steel fibres. Therefore, using hybrid fibres can generate synergetic interaction between fibres that may boost the advantages that can be achieved by mono-fibre, consequently, a cementitious composite with both improved strength and ductility can be obtained (Pakravan et al., 2017, Mindess, 2014).

2.3 Self-Compacting Concrete

Generally, vibration is used to achieve the required compaction, reduce the porosity and the air entrapped in the concrete. However, even for skilled workers, a lot of effort is required to vibrate densely reinforced concretes. The mechanical features of the concrete in its hardened state are influenced straightaway when there is a lack of good vibratory compaction. Consequently, voids are formed which results in reducing the compressive strength, also the natural physical and chemical protection proffered by concrete is greatly affected (Gaimster and Dixon, 2003).

Self-compacting concrete is characterized by its ability to fill formwork, encapsulate reinforcement bars, and flow under its own weight. At the same time, it is cohesive enough to maintain its homogeneity without segregation or bleeding. This drastically promotes (Mindess 2014):

- The working environment (reducing the noise level and reduce health effects on operators using hand-held vibrators) during construction,
- The productivity by reducing the construction time (the anchorages of the Akashi-Kaikyo Suspension Bridge, Japan, from 2.5 years to 2 years). By using SCC effectively, productivity in the building industry might be improved by 5-10%.
- Potentially enhances the homogeneity and quality of the concrete. In addition, larger architectural freedom can be achieved in structural design by using SCC.

In summary, ample opportunities can be provided by SCC for concrete construction with improved performance of concrete structures as well as providing noise and vibration-free environment.

2.3.1 Definitions of Self-Compacting Concrete

The British Standard (BS EN 206-9, 2010) defines "SCC is the concrete that is able to flow and compact under its own weight, fill the formwork with its reinforcement, ducts, boxouts etc, whilst maintaining homogeneity".

SCC has been defined in several ways by researchers, but in almost the same terms as a highly flow-able concrete that should meet the following requirements: (Ozawa et al., 1989; Khayat and De Schutter, 2014; Skarendahl 2000;);

- **Flow-ability**: concrete should be able to flow into and fill all spaces within the formwork under its own weight without any external aid or vibration.
- **Passing ability**: SCC should pass through all openings such as the spaces between reinforcing bars and within the formwork without blocking.

- **Segregation resistance**: SCC should be able to fulfil the above two requirements without any migration or separation of its material constituents and maintain its homogeneity during flow.

Different test apparatus and methods have been proposed to assess that the requirements of SCC are fulfilled. The workability tests which are recommended by the EN standard (BS EN 206-9:2010) are discussed, namely the slump flow test for flowing ability, L-box and J-Ring tests for passing ability, and visual examination and sieve stability tests for segregation resistance.

2.3.2 Flow-Ability Test

2.3.2.1 Slump Flow Test

The slump flow test evaluates the deformation capacity of SCC under its own weight without external forces against the friction of the base plate. The slump flow test is one of the most popular test to appraise the deformation capacity of SCC because the procedure and tools are relatively simple (Takada and Tangtermsirikul, 2000).

In the slump flow an ordinary slump cone is placed on a non-absorbing levelled flat steel surface with a plane area of at least 900 mm x 900 mm and filled with SCC, then cone is the lifted and the mean diameter is measured after the concrete has ceased flowing. Two horizontal perpendicular diameters d1 and d2 as illustrated in Figure 2.2 are recorded and the average flow spread diameter is calculated.

The rate of deformability can be estimated by determining the T_{500} time (T_{500}, the time from lifting of the cone to the concrete spreading to a 500mm diameter), while the segregation resistance can to a certain degree be visually inspected. Segregation can be visibly assessed by observing the flowing process and the edge of the spread after the

concrete stops; also, it should be ensured that no coarse aggregates and fibres have lifted in the centre of flow. According to the latest mix design guidelines for self-compacting concretes (BS EN 206-9, 2010) two viscosity classes are introduced: viscosity class 1 (VS1) and viscosity class 2 (VS2) depending on whether $T_{500} < 2$ sec or ≥ 2 sec.

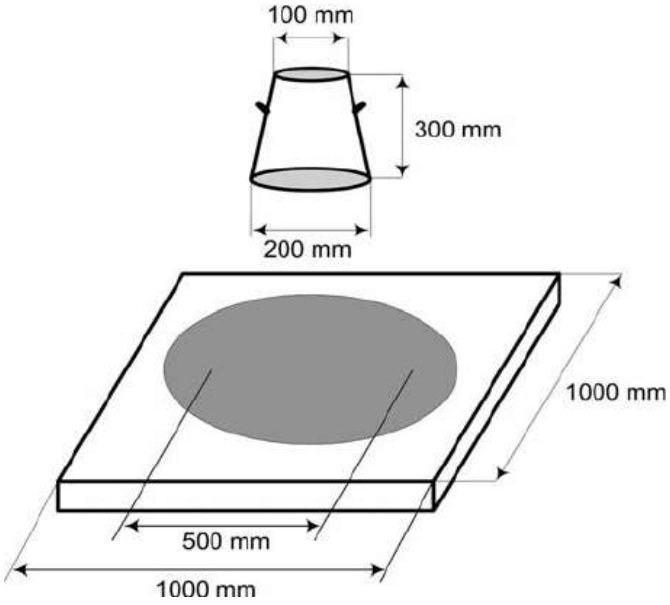

Figure 2.2 Slump test apparatus with upright cone

2.3.3 Passing Ability Tests

2.3.3.1 J-Ring Test

The J-Ring test is used in conjunction with a slump test to determine the passing ability of a SCC mixture. The equipment consists of an open steel circular ring with diameter 300 mm, and 16 steel rods (ϕ16 mm) and 100 mm height, as shown in the Figure 2. 3. The slump cone is placed centrally in the J-Ring and filled with concrete, while pressing the slump cone to the base plate. The cone is lifted perpendicular to the steel base plate allowing the concrete to flow freely, and the final diameter of the concrete spread is measured (the average of two diameters measured in two perpendicular directions). The

time needed for the flow to reach 500 mm diameter is recorded as T_{500J}, and the flow allowed stopping before recording the remaining measurements.

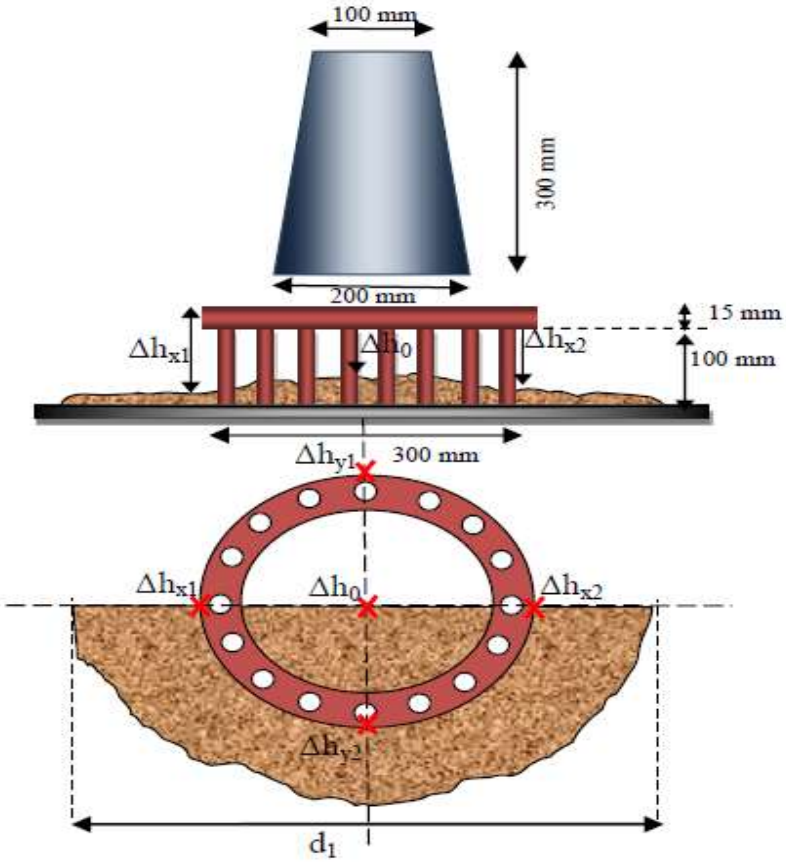

Figure 2.3 J-ring test apparatus

2.3.3.2 L-Box Test

This test evaluates the filling ability of SCC and the capacity to pass through narrow openings including spaces between reinforcement and other obstacles without blocking. The apparatus has a rectangular section box in the shape of an 'L', with a horizontal and vertical section separated by a sliding gate as shown in Figure 2.4. The L-Box is equipped with reinforcement bars separated by narrow openings that are designed to evaluate the passing ability of a SCC mixture.

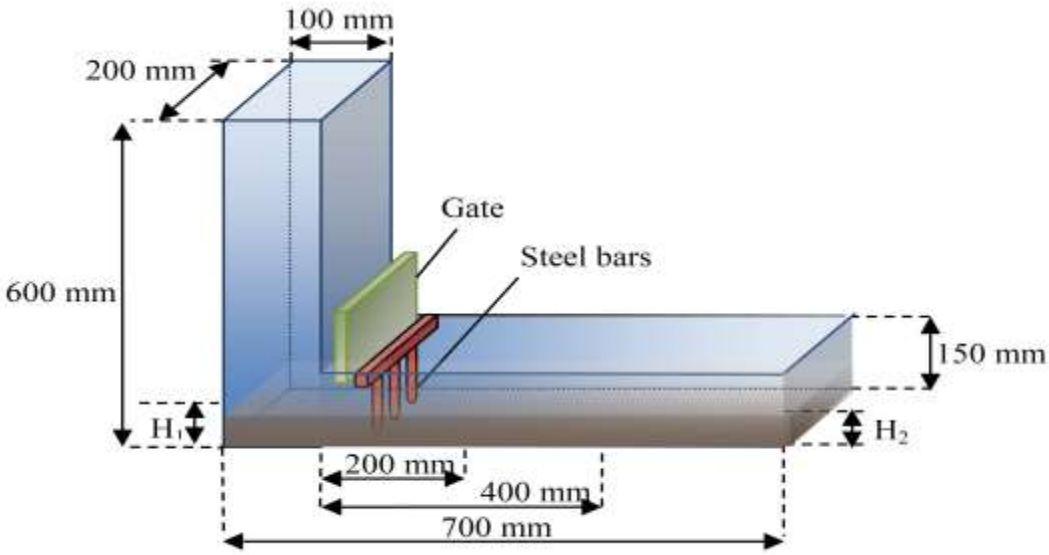

Figure 2.4: L-box test apparatus

2.4 High Performance FRC (HPFRC)

Although cementitious materials have proven their versatility in many construction applications worldwide, their inherited low strain capacity in tension and consequently low fracture energy has led researchers to find solutions to improve these features. The very high cement content, the very low water content, and the high dosage of superplasticizer affect the properties of the fresh concrete in some ways in a manner different from the ordinary mixes (Neville, 1995). High Performance Fibre Reinforced Cement Composites (HPRCCs) have a mixture of cementitious materials, sand, fibre reinforcement, and admixtures. Low water-to-cementitious materials ratio, high mechanical strengths and ductility and extended service life due to their refined microstructures can represent the main features of HPRCCs (Meng et al., 2017).

In contrast to normal concrete (NC) and/or Fibre Reinforced Concrete (FRC), HPFRCC materials show enhanced properties in terms of higher ductility, durability and energy dissipation capacity. These advances are based on the use of silica fume and surfactants,

which reduce water demand and densify the matrix, thereby improving the fibre-matrix interfacial bond (Morin et al., 2001).

When concrete, mortar or FRC are subjected to tension, initial linear increase of stress is noticed, and later brittle degrading behavior at first cracking due to inability to transfer tensile stresses across the crack surface is recognized, this stage is called strain softening. In contrast, multiple cracking is distinguished after first cracking in HPFRCC materials, exhibiting a hardening behavior, and considerable amount of energy is absorbed that is proportional to the area under the curve. The softening branch follows that stage. The main difference between conventional FRC and high performance fibre reinforced cement composites (HPFRCC) is illustrated in Fig 2.5 (Naaman, 2007, Brandt, 2008).

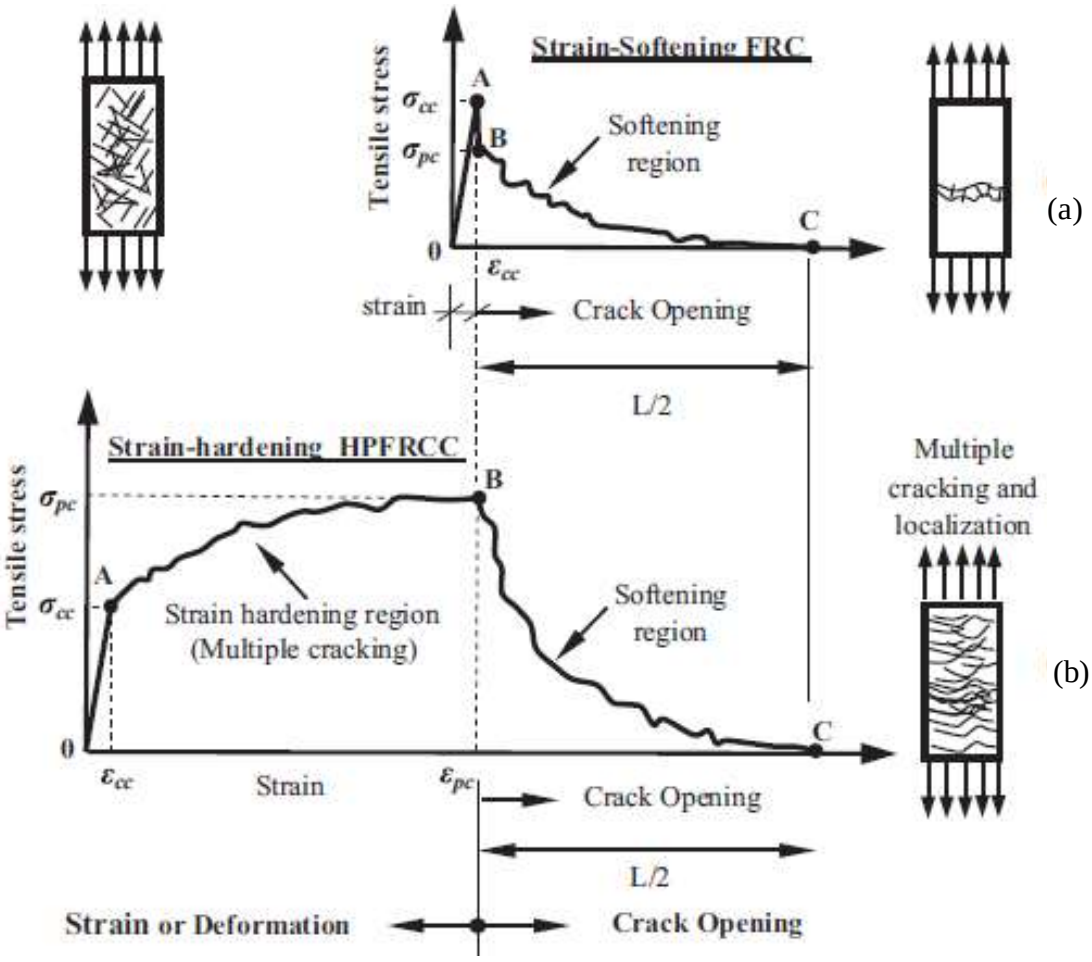

Figure 2.5 Comparison of typical stress–strain response in tension of HPFRCC with conventional FRCC, (a) conventional FRC, (b) HPFRCC (After Naaman, 2007).

FRC has been classified by fibre content, and by mechanical behaviour, likely because the former influences the latter: FRC with low fibre volume fractions (< 1%) is utilized for reducing shrinkage cracking (Balaguru and Shah, 1992). This low fibre volume fraction is used in structures like slabs and pavements that have large exposed surface leading to high shrinkage cracking. FRC with moderate fibre volume fractions (between 1% and 2%), display enhanced mechanical properties including modulus of rupture (MOR), fracture toughness, and impact resistance. High volume fraction (greater than 2%), which generally labelled as high performance FRC, (HPFRCC).

HPFRCC exhibits apparent strain-hardening behaviour. A new class of HPFRCC materials has been recently developed at Cardiff University, designated CARDIFRC. It is characterized by high tensile/flexural strength and high-energy absorption capacity (Karihaloo et al., 2002).

2.5 Types of HPFRCC

HPFRCCs include materials such as SIFCON (Slurry Infiltrated Fibre Concrete), MDF (Macro Defect Free), ECC (Engineered Cementitious Composites), Fibre Reinforced DSP (Densified Small Particle Systems), CRC (Compact Reinforced Composite), RPC (Reactive Powder Concrete) and CARDIFRC. These materials have showed noticeable combinations of strength and ductility as well as long-term durability (Karihaloo et al., 2002). We shall give brief description of RPC, DSP and CARDIFRC next.

2.5.1 Reactive Powder Concrete (RPC)

Reactive Powder Concrete RPC has been developed by the Scientific Division of Bouygues, at St Quentin en Yvelines in France.

High silica fume content and very low water to cement ratio are the characteristics of this material. It offers very high mechanical and durability properties (Richard and Cheyrezy, 1994). The ductility estimated in terms of fracture energy is increased by one to two orders of magnitude in comparison with the conventional concrete. RPC possesses very high strength: it is usually divided into two grades: RPC 200 and RPC 800MPa. The outstanding mechanical properties achieved are Young's modulus and fracture energy in the range of 50–75 GPa and 12–40 kJ/m^2, respectively.

As reported by Richard and Cheyrezy (1995) and Li and Fischer (2006) in RILEM Workshop the development of RPC was based on the following principles:

- Increased matrix homogeneity which is achieved by lack of coarse aggregates and the replacement of natural sand with very fine quartz sand;
- Enhancement of compacted density through optimization of the grading, microsilica improves the compacted density of the mix thereby reducing voids and defects.
- Improvement of ductility by incorporating small-sized steel fibres.
- Enhancement of microstructure (by the use of a high dosage of silica fume and post-set heat-treatment),
- Reduction of the water to cement ratio and inclusion of superplasticiser ensures a workable mix.

A great attention is given to the properties of the matrix, to maintain its homogeneity by limiting the size of the quartz sand to 0.6 mm and improving the microstructure by thermal curing. The combination of these two characteristics was proposed to be the key element for the superior behaviour, as seen by the high compressive and flexural strengths (likely to be between 30 and 60 MPa).

2.5.2 DSP Cementitious Materials

Densified cement ultra-fine particle based materials DSP was developed by the Danish cement producer, Aalborg Portland-Cement. Production of this material is made possible by superplasticizers and silica fume to systems that can be densely packed in a low stress field and with very low water content (Bache, 1981).

DSP belongs to a class of materials formed from densely packed particles of a size ranging from 0.5 to 100μm, and homogeneously arranged ultra-fine particles ranging in size from about 50A˚ to 0.5 μm and arranged in the spaces between the larger particles.

To achieve the desired mechanical properties, the dense packing of the particles (sand, cement and ultra-fine silica) together with fibres is fundamental. It is also the prime feature of HPFRCC materials. Materials such as DSP combine very densely packed cement particles (5-10μm) and ultra-fine silica fume (0.1-0.2μm) filling the spaces between the cement particles and, normally densely arranged fibres (Bache, 1981; Bache, 1987). The new binder is very strong with a compressive strength of 150 MPa - 270 MPa, but also very brittle, like glass, thus in itself unsuitable as a structural material. Therefore, to improve the tensile properties of DSP based matrix, fine, strong and stiff fibres is used in the mix. The fibres improve the tensile properties of DSP based matrix, such as Densit®.

2.5.3 CARDIFRC

Many attempts were carried out at CARDIFF University (Karihaloo and De Vriese, 1999; Sullivan, 1999; Karihaloo et al., 2002) to reproduce RPC and Densit® with materials widely used by the UK concrete industry. The mechanical properties were found to be inferior to those announced in the literature (Richard and Cheyrezy, 1995; Bache, 1981), and the workability of some mixes was poor.

Thus a new composite was created based on maximizing the density of the matrix by a continuous grading of its particles in the range of 0.5–2 mm, and reinforcing it by 0.15 mm diameter steel fibres with length of 6 and 13 mm. The constitutive equations used to describe and optimize the composite address the different stages of the loading of the

composite. Benson (1999) also investigated another type of HPFRCC with 6 mm coarse aggregate. A satisfactory workability was produced but with inferior mechanical properties comparing with those achieved with mixes containing no coarse aggregate (i.e. Densit® and RPC) (Benson, 2003).

To achieve good workable mixes with a very low water/binder ratio and a high volume fraction of steel fibre, further studies were continued at Cardiff to gain concrete with high ductility with a relatively high tensile strength. Large amounts (up to 8 % by volume) of short steel fibres (6-13 mm long, 0.15 mm diameter) were added in a cementitious matrix densified by the use of silica fume to achieve the required result. Instead of ordinary river sand and coarse aggregates, the matrix contains only very fine quartz sands (up to 2mm). By optimizing the grading of fine sands, the water demand was considerably reduced without affecting the workability of the mix. As a result of many trial mixes and testing, the mixes shown in Table 2.1 are the optimized ones. Two different mix classes (designated CARDIFRC, Mix I and Mix II) of high-performance concrete differing mainly by the maximum size of quartz sand used in the mix have been developed using novel mixing procedures.

There are significant differences between CARDIFRC mixes and RPC and DSP mixes. The innovative technique of using the two different types of fibre in combination to the high volume fraction was found to be quite beneficial to the load deflection response of the matrix in terms of both strength and ductility. In addition, the use of two grades of fine quartz sand (Table 2.1) shows considerable enhancement in the performance of Mix I. Similarly, in Mix II in order to maximize the dry density of the mix, three grades of fine quartz were used. In its hardened state CARDIFRC is characterized by very high compressive strength (in excess of 200 MPa), tensile /flexural strength (up to 30 MPa),

high energy-absorption capacity (up to 20,000 J/m^2). Table 2.2 shows the properties of CARDIFRC.

Table 2.1 Mix proportions for optimised CARDIFRC® Mix I and Mix II (per m3)

Constituents	Mix I (kg/m^3)	Mix II (kg/m^3)
Cement	855	744
Microsilica	214	178
Quartz sand:		
9-300 µm	470	166
250-600 µm	470	-
212-1000 µm	-	335
1-2 µm	-	672
Water	188	149
Superplasticiesr	28	55
Fibres: - 6 mm	390	351
- 13mm	78	117
Water / cement	0.22	0.20
Water/ binder	0.18	0.16

2.5.3.1 Commercial Version of CARDIFRC

In view of the high cost of fibres, a commercial variant of the material has been developed in collaboration with a leading concrete construction company. It differs from the original CARDIFRC mixes through;

a) A reduction in the cost by replacing expensive brass-coated small steel fibres with less expensive longer steel fibres.

b) The avoidance of the need for vibratory compaction by creating a self-compacting mix.

c) The creation of a sustainable and environmentally friendly material with a low carbon footprint.

The eventual commercial version of CARDIFRC contained only 2.5% by volume of 30 mm long Dramix fibres with crimped ends. It had no short steel fibres, but contained 0.02% by volume of sacrificial polymeric fibres to give it the required 120 min fire rating.

Table 2.2 Typical material properties of CARDIFRC® Mix I and Mix II.

Material Properties	Mix I	Mix II
Indirect tensile strength (MPa)	28.6	21.4
Size- Independent Specific Fracture Energy (N/m)	22909	17875
Compressive (MPa)	194.0	207.0

This version was self-compacting with a horizontal spread of 750 mm in the slump cone test; the spread of 500 mm was reached in 3 sec. (Karihaloo, 2012).

This version was obtained by replacing 36.4% of cement in the original CARDIFRC Mix I with ground granulated blast furnace slag (GGBS) to increase the powder volume, and by using the more effective Glenium Ace 333 superplasticiser instead of the naphthalene-based superplasticiser in the original CARDIFR mix I. The mix proportions of this commercial version are given in Table 2.3.

This industrially competitive self-compacting variant of CARDIFRC is ideal for manufacturing pre-cast pre-stressed concrete elements without shear reinforcement for use in structural applications where steel has often been used.

Extensive testing on full size pre-cast pre-stressed girders made from this material was conducted. Their load bearing capacities at both the serviceability and the ultimate limit states far exceeded the expected values (Karihaloo, 2012).

Table 2.3 Mix proportions of the commercial version CARDIFRC Mix I

Constituents	Amount (kg/m^3)
Cement	543.5
Micro-silica	214
GGBS	311.5
Quartz sand:	
9-300 µm	470
250-600 µm	470
Water	188
Superplasticiesr	20.68
Fibres: - 30 mm Dramix	195
- Polymeric	0.156
Water / cement	0.22
Water/ binder	0.18

2.5.3.2 The Effect of Steel Fibre

The tensile load carrying capacity increased due to the incorporation of fibres in the CARDIFRC and turns the material from brittle one into a very ductile one. Furthermore, to prevent corrosion, brass-coated steel fibres (diameter 0.15 mm, 6 mm or 13 mm long) are used in CARDIFRC mix.

The use of long and short fibres was found necessary to improve the material properties, whilst minimizing loss of workability. The short fibres prevent micro-crack

growth and coalescence (Tjiptobroto and Hansen, 1993) and provide a high tensile strength. Long fibres provide increased ductility, greater pull-out strength and will bridge wider cracks (Sullivan, 1999).

The high toughness of the material is due to the mechanism of fibre pull-out which is the preferred failure mode, rather than the fracture failure mechanism, because of its ability to redistribute stresses (Caverzan et al., 2012).

The disadvantage of long fibres is that they have an adverse effect on workability and an optimum content of steel fibres should be adopted to balance the workability, and mechanical performance (Sivakumar and Santhanam, 2007, Wille et al., 2011).

The effect of fibres on the compressive strength of ultra-high strength concretes, such as RPC, is less clear. The fibres are added foremost to provide considerable ductility to these materials (Bentur and Mindess, 2007). However, they can also provide some significant strengthening at high enough fibre volumes. For instance, Karihaloo and De Vriese (1999) found an increase in compressive strength from about 120 MPa to about 145 MPa (21%) when fibres increased from nothing to 4% by volume.

2.5.3.3 Volume Fraction of Fibre

Generally, as the volume fraction of fibre increases and as the fibres are more uniformly dispersed, the growth of micro-cracks is hindered, and the localisation of deformation is delayed with a consequent substantial increase in the tensile strength and strain capacities of the composite (Balaguru and Shah, 1992). An experimental programme was conducted on the effect of fibre content on the fracture properties of concrete by Mobasher et al. (1990). They concluded that as the volume fraction of fibres increases

the growth of micro-cracks was hindered through an arrest mechanism, the matrix fracture toughness was increased and higher peak load could be sustained.

Karihaloo and De Vriese (1999) studied the influence of the volume fraction of steel fibre upon the mechanical properties of reactive powder concrete. The mixes contained four different volume fractions of steel fibre V_f =1- 4%. The fibres were straight steel wires, 6 mm long and 0.16 mm in diameter. It was detected that an increase in the specific fracture energy and the indirect tensile strength (splitting strength) of the composite is due to the increase in the volume fraction of steel fibre.

Hoy and Bartos (1999) reported that a significant loss of workability when higher volumes of steel fibre are added to concrete and greater chance that fibres will interlock. For these reasons, there is an optimum fibre content for any given fibre matrix combination. Undoubtedly, lack of homogeneity and poorer workability will be produced when higher fibre contents is added to the mix, while lower fibre contents will result in less efficient reinforcement. The influence of increasing fibre volume and its efficiency on the behaviour of a SFRC element modifies entirely its behaviour under load. While the conventional SFRC element is characterized by initial linear increase of stress and after the 1st crack opening there is a softening branch, in contrary, where the reinforcement is sufficient, after the 1st crack there is a strain hardening stage which accompanies multiple cracking and considerable amount of energy is absorbed (Brandt, 2008).

2.5.3.4 Aspect Ratio of Fibre (*L/d*)

Physically, aspect ratio is a relative term describing the fibre length divided by the diameter. Generally, higher aspect ratio fibres perform better than lower aspect ones. It was found that when the aspect ratio increased from 47 to 100, there is a monotonic

increase in compressive strength and ductility (Gopalaratnam and Shah, 1986). Sullivan (1999) also found that long fibres increased both the tensile strength and ductility of concrete. Karihaloo and De Vriese (1999) mentioned that an increase in fibre length and thus of aspect ratio seems to be more effective than an increment only in volume fraction of fibres. The incorporation of long fibre (13 mm) in CARDIFRC mixes is a primary reason for enhancing its ductility. Singh (2016) reported that the post-peak characteristics of the SFRC under compression shows an improvement and the extent of this improvement depends upon the fibre parameters (the fibre aspect ratio and the volume fraction), where the higher the value of the fibre parameters (aspect ratio and the volume fraction) nominated in the design more is the improvement in the post-peak characteristics of the SFRC (Figure 2.6).

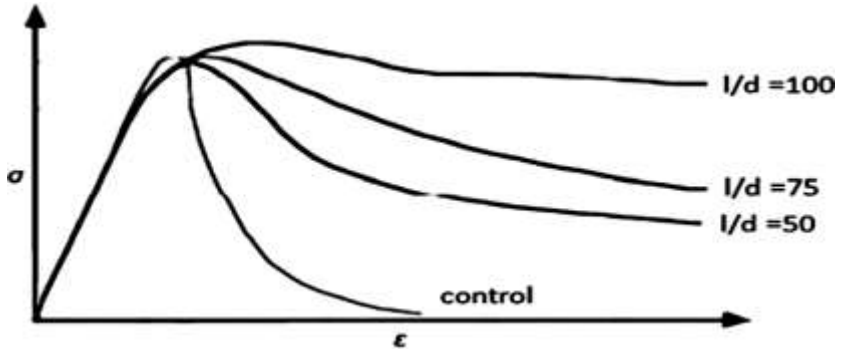

Figure 2.6 A typical stress–strain response of SFRC under compressive with different values of aspect ratio. (After Singh, 2016)

2.5.3.5 Fibre Distribution

The performance of concrete can be ameliorated by including fibres to the matrix which in turn retard the crack propagation during loading. Fibre efficiency depends on how they are distributed and oriented in a cementitious matrix (Grunewald et al., 2013).

It was found that the mechanical performance of any HPFRCC depends to a high degree on even distribution of fibres in the matrix (Farhat et al., 2007). Vodicka et al. (2004)

stated that there is a minimum fibre content required if a homogeneous distribution is to be obtained, and they estimated to be in the range of 30–40 kg/m^3. They stated that, the hazard of a non- homogenous fibre distribution becomes increasingly likely for very low fibre contents (less than about 25 kg/m^3 of fibres). Singh (2016) reported that special procedures are needed to verify the uniform fibre distribution in the concrete mix when the aspect ratio of steel fibres is more than 50. Of these using bundled fibres, which are glued together with a water-soluble gum, is recommended

Computerized Topography (CT) imaging and sectioning of specimens have confirmed that the novel mixing procedures used for the production CARDIFRC ensures remarkably homogeneous mixes with a uniform distribution of up to 8 % of vol. for long and short fibres (Karihaloo and Jefferson, 2001).

Destructive and non-destructive testing techniques were used by Benson (2003) to verify that the mixing procedures used to produce CARDIFRC do indeed result in a uniform distribution of the steel fibres. CT results showed that the fibres are nearly uniformly distributed with random orientation in the mixes. Destructive testing (image analysis) also confirmed these findings and showed that the fibre distribution was generally uniform.

Farhat et al. (2007) reported that a uniform distribution of fibres throughout the bulk of the material is important to ensure its excellent fatigue performance. They tested large beams of CARDIFRC (100/100/500 mm), and it was found that the scatter in these beams was very high and a rather poor fatigue performance. An additional testing series was performed on thin slabs (360/90/35 mm), rather than beams, the fatigue performance was much better for upper load levels below 80% of the average static strength no failure occurred. They attributed the difference in fatigue behaviour between

the beams and slabs mainly to the fibre orientation and distribution, which was evaluated with CT imaging, where a much better fibre distribution could be obtained in the thin slabs.

2.5.3.6 The Effect of Silica Fume

Silica fume is a by-product from electric furnaces used in the manufacture of silicon metal, ferrosilicon and other silicon alloys (Aïtcin, 2004), which improves concrete properties in fresh and hardened states.

The individual particles are extremely fine, approximately 1/100th the size of an average cement particle, most of them having a diameter ranging between 0.03 and 0.3 μ m; the median diameter is typically below 0.1 μ m (Neville, 1995).

Because of its fine particles, large surface area, and the high SiO_2 content, silica fume is a very reactive pozzolan when used in concrete. It is frequently used in amounts between 5% and 10% by mass of the total cementitious material (Brandt, 2008; Caldarone, 2008). It is used either as a cement replacement material to reduce the cement content or as an additive material to enhance the performance of concrete.

Fresh concrete containing silica fume is more cohesive and less prone to segregation and bleeding than concrete without silica fume. These effects are caused primarily by the high surface area of the silica fume to be wetted; there is very little free water left in the mixture for bleeding (King et al., 2012).

The extremely fine particles of silica fume have the ability of to be located in very close vicinity to the aggregate particles, that is, at the aggregate-cement paste interface, which is known to be a source of weakness in concrete. Therefore, the so-called interface zone

has improved properties with respect to micro-cracking and permeability (Neville, 1995).

The substantial functions of silica fume in concrete are (Siddique and Khan, 2011):

- Pore-size refinement and matrix densification: Essentially, silica fume acts as filler due to its fineness and hence it fits into the spaces between grains. It causes a significant reduction in the volume of large pores at all ages.
- Pozzolanic reaction: The formation of Calcium Hydroxide crystals (CH) during the chemical reaction of Portland cement represent a source of weakness because cracks can readily diffuse through or within these crystals without any considerable resistance affecting the strength, durability and other properties of concrete. Additional binder material called Calcium Silicate Hydrate (C-S-H) formed from the reaction of silica fume with CH, which is comparable to the Calcium Hydroxide formed from Portland cement and water and therefore reduces the CH content.

One of the main advantages of using silica fume particles with cement is to fill the spaces between the cement particles and thus achieving very dense packing system. Bache (1981) attributed these to the following:

- The silica particles are smaller than even the finest cement wich can produce by grinding and are therefore more conductive to dense packing into the spaces between the cement particles.
- The silica particles, being formed by condensation from gas phase, are spherical in shape (unlike crushed cement particles, which are angular) and this makes the silica particles even more suitable for dense packing than very fine cement.
- The particles are chemically less reactive than cement, which eliminates the problem of too rapid hardening encountered with very fine cement; in addition, the silica is

likely to ensure the formation of a coherent structural skeleton between the cement particles, resulting in a fine dense micro structure.

Recently, many studies have been conducted to evaluate the effect of micro-silica on the mechanical properties of concrete mixture (Biswal and Sadangi, 2011; Karatas et al., 2010; Memon, 2013; Wongkeo et al., 2014). The performance of HSC under impact and fatigue can be improved by using silica fume, since it can improve the interface structure, eliminate weaknesses of the interface, enhance the interfacial bond strength, and reduce the number and size of original cracks (Yan et al., 1999).

2.5.3.7 The effect of Dispersing Agent (Superplasticizer)

The new cement-based materials have a very low porosity, which is achieved by the addition of very small reactive particles whose role is to fill the interstitial space between larger particles. This addition can lead to very dense, high-strength, hardened materials, but with more demand of water and this leads to a reduction in workability. Thus, a high range water-reducing admixture is often introduced to promote the workability.

The main functions of superplasticizer in concrete as reported by Neville and Brooks (2010) are:

- Higher strength can be achieved by decreasing the water/ cement ratio with the same workability by adding superplasticizer.
- The same workability can be achieved by reducing the cement content and hence the heat of hydration in mass concrete.
- Ease placing in inaccessible areas as the workability increased, without subjecting to excessive bleeding or segregation.

The addition of a superplasticizer deflocculates the cement particles and frees the trapped water by their dispersing action and hence enhances the flow-ability of concrete. Mixes of dry particles with small amount of water tend to restrain a good distribution of the water between solid particles, thus preventing ultimately an optimal repartition of the hydrates formed between the particles. Therefore, the paste has a very low initial fluidity.

Adding superplasticizer minimizes the surface tension of water and allows the permeation of the fluid in between the solid particles and hence an adequate permeability to water is acquired. Small amounts of superplasticizer can provide a high level of fluidity despite using low water content (Morin et al., 2001).

Superplasticizer is added to the CARDIFRC matrix in order to achieve a very workable mix at low water/cement ratio, thus obtaining dense packing which lead to high strength and durability. Dugat et al. (1996) reported that by using superplasticizer with silica fume it is possible to reduce the water/cement ratio to less than 0.15. This helps reduce the total pore volume of the cement paste and the average diameter of the pores, hence improving durability.

2.4 Bridging Action of the Fibres

The studies showed that the most substantial property of a fibre reinforced cementitious composite is the fibre bridging across the matrix crack (Li at el., 1991, Lim and Li, 1997).

The addition of fibres to concrete mixes considerably enhance many of the engineering properties of HPFRCCs, particularly toughness. As fibres are randomly distributed in

the concrete matrix, cracks can reach a fibre which can stop crack growth, when propagating through concrete (Barluenga, 2010).

The inclusion of fibres acts as crack arrester; they restrict the development of crack and thus transforms an inherently brittle matrix into a strong composite with better crack resistance and ductility. Moreover, the fibres help to transfer loads at the internal micro-cracks (Ramesh et al., 2003).

An important factor to be considered when the properties of steel fibre concrete are quoted, is the fibre orientation relative to the direction of applied stress. Clearly, the orientation of the fibre relative to the plane of a crack in concrete influences the reinforcing capacity of the fibre. The maximum benefit occurs when the fibre is unidirectional and parallel to the applied tensile stress, and the fibres are of less benefit when randomly oriented in three dimensions (Neville and Brooks, 2010).

Balaguru and Shah (1992) reported that when the matrix cracks, the load is transmitted across the crack by the fibre. Since fibres are randomly dispersed throughout the matrix, their orientations relative to the direction of the applied load are an important factor. In a matrix containing randomly distributed fibres, few fibres align in the direction of applied load; instead almost all fibres are oriented at different angles to the load direction (Figure 2.7). Moreover, the observations confirmed that after matrix cracking, the load and energy required to pull-out a steel fibre from the matrix can be higher for fibres inclined to the load direction, this is known as dowel action. When a fibre is pulled out from the cementitious matrix, the snubbing friction at the fibre exit point can increase the pull-out resistance, and contribute to the overall composite action. Naaman and Shah (1976) mentioned that inclined fibres can take a greater load as they bend.

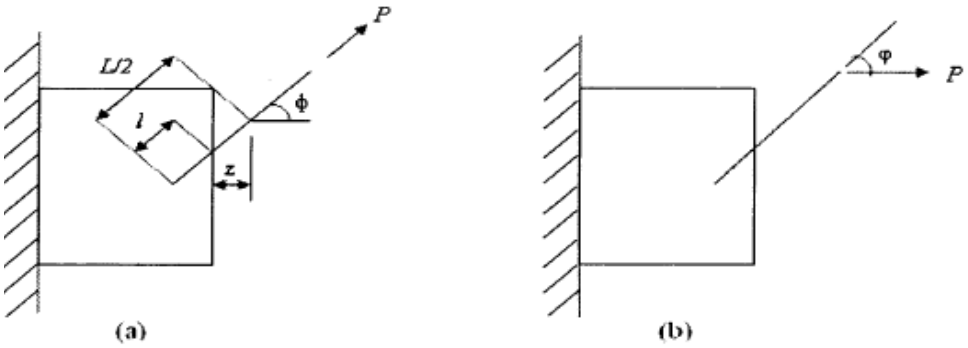

Figure 2.7 (a) A single fibre pull-out without snubbing ($\phi = 0$) and (b) with snubbing ($\phi \neq 0$, $\phi = \varphi$) (After Karihaloo and Wang, 2000)

2.5 Concluding Remarks

As has been argued, the failure in concrete initiates with the formation of micro-cracks that propagate and eventually coalesce to generate macro-cracks, which cause fracture if not controlled. However, the inclusion of fibres in concrete stops the propagation of micro-cracks and macro-cracks thus increasing the ductility of concrete. High and ultra-high performance fibre-reinforced concrete (HPFRC and UHPFRC) have been developed to achieve strength and toughness requirements that conventional FRC cannot achieve. A HPFRC is a mixture of cementitious materials, sand, fibre reinforcement, and admixtures; it is characterized by low water-to-cementitious materials ratio, high mechanical strengths and ductility, and prolonged service life due to its refined microstructure. An UHPFRC has even more refined microstructure and superior mechanical, fracture and durability properties than HPFRC. CARDIFRC is a class of UHPFRC; it is characterized by very high compressive strength, high tensile /flexural strength, and high energy-absorption capacity. However, CARDIFRC was initially developed only for small-scale niche applications due to the very high cost of thin brass-coated steel fibres. The need of producing cheaper versions of CARDIFRC and employing it in large volume applications, minimizing the health and environmental hazards by creating self-compacting mixes not requiring noisy

vibration and replacing some cement with an industrial waste material GGBS. In addition, by using longer steel fibres (30mm instead of 13 mm) it is possible to enhance its toughness further at the expense of a tolerable reduction in the strengths. This has been tried for CARDIFRC Mix I. In this work this approach will be extended to CARDIFRC Mix II, because the latter offers room for further reduction in cost because it uses coarser sand (2 mm) than the finer and more expensive sand (0.6 mm) used in Mix I. The development and characterisation (from both mechanical and fracture points of view) of this UHPFRC version of CARDIFRC will be reported in Chapter 5.

Chapter Three

Fracture Behaviour of Concrete

3.1 Introduction

Based on their tensile stress-deformation response, most engineering materials can be categorized into three main classes:

- Brittle: stress suddenly drops to zero when a brittle material fractures.
- Ductile: stress remains more or less constant when a ductile material yields.
- Quasi-brittle: stress decreases gradually after the peak stress with increasing deformation.

Due to the fact that concrete is not a homogeneous material, many inherent flaws are present in a concrete structure such as air voids, water filled pores and shrinkage cracks. Under external loading the existing flaws, e.g. micro-cracks grow stably and coalesce with existing or newly-formed micro-cracks until large macro-cracks are formed that lead to the failure of the structure. Fracture mechanics provides an energy based failure theory that can be used in designing concrete structures. It explains the response and failure of structures as a consequence of crack initiation and propagation (Karihaloo, 1995).

3.2 Linear Elastic Fracture Mechanics (LEFM)

3.2.1 Griffith's Theory of Brittle Fracture

The mechanism of fracture of brittle materials was first explained by Griffith (1920). He argued that the presence of small cracks and other impurities in brittle materials introduce high stress concentrations near their tips and therefore, the tensile strength of material is exceeded earlier than when the stress is uniformly distributed in the material. This explains the large contradiction between the theoretically predicted and real tensile

strengths of these materials. Fracture initiates at these cracks as a result of very high tensile stress concentrations.

Griffith considered a large thin plate of unit thickness containing a crack of length 2a subjected to a uniform tensile stress σ (Figure 3.1a).

From Inglis' (1913) solution for a slit-like cut of length 2a, the vertical displacement of the upper face of the cut is given by:

$$v(x) = \frac{2\sigma}{E}\sqrt{a^2 - x^2} \qquad 0 \leq \boxed{x} \leq a \tag{3.1}$$

where E is Young's modulus.

It is seen from Figure 3.1 that the elastic plate with the slit-like cut of length 2a can be considered as the superposition of an elastic plate without a crack under external load σ and the same plate without external load σ but with equal and opposite stresses (i.e. -σ) applied gradually to the faces of the crack. In this procedure, on each of the two faces, the stress σ is displaced by the amount *v(x)* of Equation (3.1), so that the amount of the work extracted is:

$$W = 2\left(-\frac{\sigma}{2}\int_{-a}^{a} v(x)dx\right) = -\frac{\pi a^2 \sigma^2}{E} \tag{3.2}$$

The factor 2 in Equation (3.2) indicates the two faces of the crack, whereas the factor ½ appears because the stress gradually increases from 0 to σ. Equation (3.2) represents the work extracted *W* which is equal to the elastic strain energy released *U* during the crack growth, if the loaded panel boundaries are fixed and cannot displace (Karihaloo, 1995).

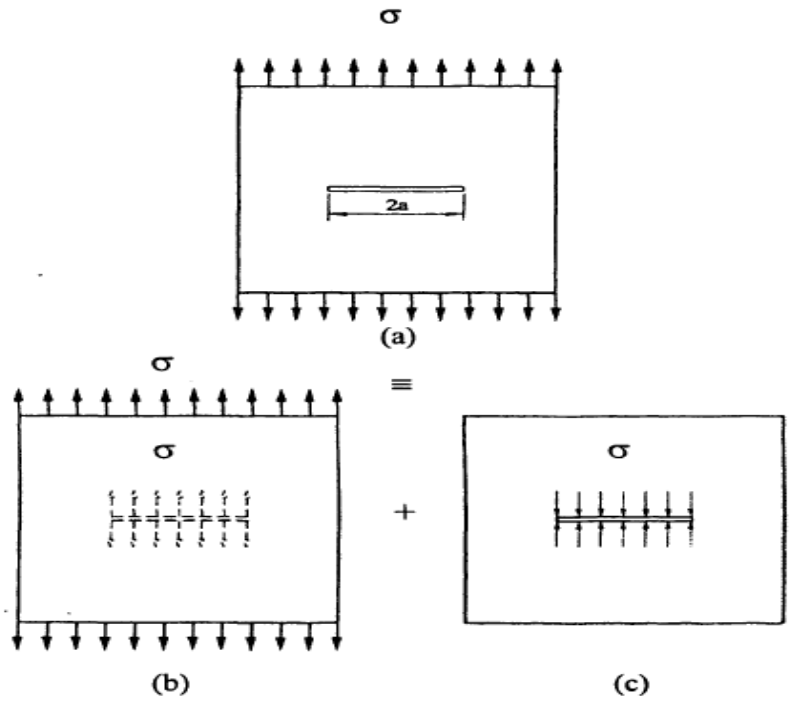

Figure 3.1 The principle of superposition (a) the plate is under external tension (b) uncracked plate under σ (c) plate without external σ but with equal and opposite stress applied to the crack to create a stress-free crack (After Karihaloo, 1995).

If however the panel boundaries are free to move, the elastic strain energy U of the panel will increase during the crack formation, and W is equal to the change of the potential energy Π of the system. If the growth of a crack is stable, then for an incremental crack growth,

$$dW = -d\Gamma \tag{3.3}$$

where

$$\Gamma = 4a\gamma \tag{3.4}$$

γ is the surface energy density, i.e. the energy required to create a unit crack surface.

The energy equilibrium condition for stable crack growth may be obtained by minimizing the energy change in Equation (3.3) with respect to the change in crack length da:

$$\frac{\partial}{\partial a}(W + \Gamma) = 0 \tag{3.5}$$

Substituting Equations (3.2) and (3.4) into Equation (3.5) and performing the differentiation gives:

$$\sigma^2 = \frac{2E\gamma}{\pi a} \tag{3.6}$$

Equation (3.6) is referred to as the Griffith fracture criterion. It states that for a given material (i.e. given E and γ)

$$\sigma\sqrt{\pi a} = \sqrt{2E\gamma} = const. \tag{3.7}$$

In other words, according to the Griffith fracture criterion or the global energy criterion a brittle material will fracture when the stress σ reaches a critical value σ_c that satisfies Equation (3.7).

If $\sigma < \sigma_c$ no crack growth will occur since the energy stored in the system is lower than the critical amount. However, if $\sigma \geq \sigma_c$ the crack will advance catastrophically since any extension of the crack length, a, will lower the critical stress, σ_c.

Equation (3.7) shows that the strength of a brittle material σ_c is dependent on physical parameters such as the Young modulus, the surface energy density, and the length of the crack.

3.2.2 Irwin's Theory of Brittle Fracture

Although ductile materials were not included in Griffith's considerations, Irwin (1957) suggested that Griffith's theory could be applied to materials that exhibit plastic deformation (ductile materials). He determined that there was also a certain energy from plastic deformation that had to be added to the surface energy of Griffith theory to work

for ductile materials as well. If this energy used in the plastic deformation is included in Equation (3.7) then it becomes:

$$\sigma = \sqrt{\frac{2\,E(\gamma+\gamma_P)}{\pi\,a}} \tag{3.8}$$

where, γ_p is the energy used in the plastic deformation associated with crack extension.

Irwin noted that in the neighbourhood of the sharp crack tips, the stress components are the same regardless of the shape of the body and the manner of loading.

Generally, there are three possible modes of deformation at a crack tip (Figure 3.2):

- Mode I - opening or tensile mode, where the crack surfaces move directly apart (Figure 3.2a).
- Mode II - sliding or in-plane shear mode, where the crack surfaces slide over one another in direction perpendicular to the leading edge of the crack (Figure 3.2b).
- Mode III - tearing or anti-plane shear mode, where the crack surfaces move relative to one another and parallel to the leading edge of the crack (Figure 3.2c).

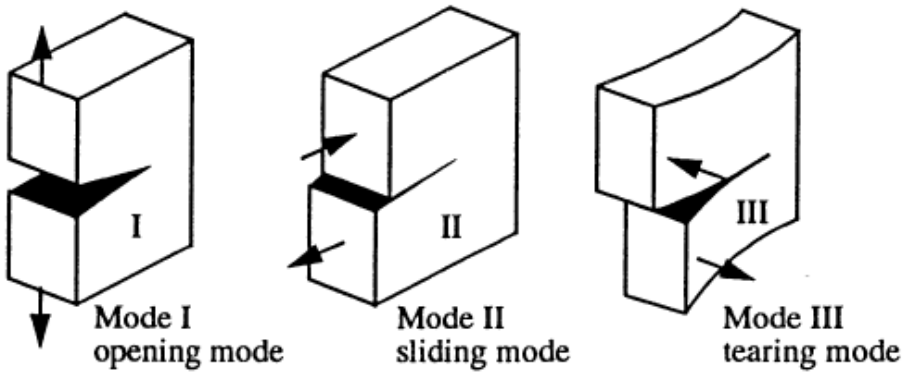

Figure 3.2 Modes of crack propagation, (a): Mode I, (b): Mode II, (c): Mode III (After Karihaloo, 1995)

The most severe of the loading states is Mode I, as the propagation of a crack in real material under pure Mode II or III conditions requires a great amount of energy, due to high friction between crack faces. The stress intensity factor K_i depends on the geometry of the body and the manner in which the loading is applied, for Mode I, K_i can be represented as K_I . For the geometry shown in Figure 3.3, K_I is given by:

$$K_I = \sigma \sqrt{\pi\, a} \qquad (3.9)$$

In general, K_I is finite and positive. It can never be negative, but there can be situations when K_I vanishes. The shapes of the crack tip zones and the stress distributions ahead of the tips are shown in Figure 3.4 for $K_I > 0$, $K_I < 0$ and $K_I = 0$. When $K_I = 0$ (Figure 3.4c), the crack faces close smoothly and the stresses ahead of the crack tip are finite.

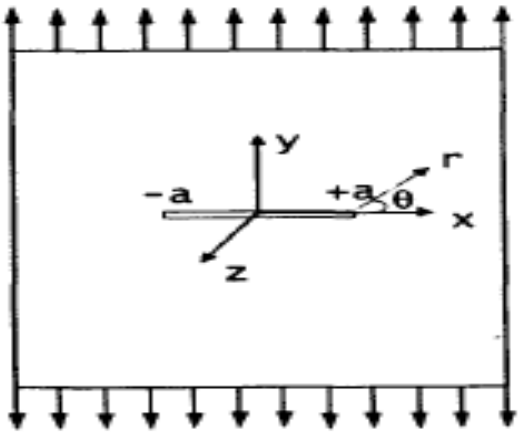

Figure 3.3 An infinite elastic body with a sharp crack of length 2a under Mode I. (After Karihaloo, 1995)

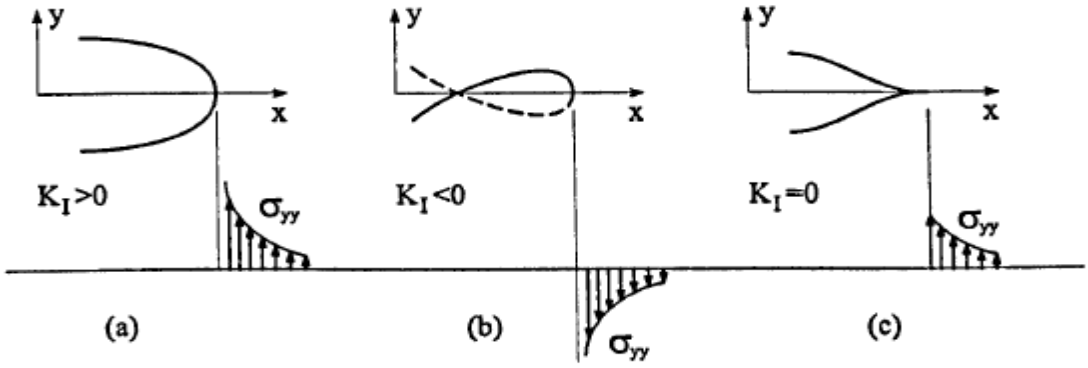

Figure 3.4 Shapes of traction-free crack tip zones and distribution of normal stress, in front of the crack tip for $K_I>0$, $K_I<0$ and $K_I = 0$ (After Karihaloo, 1995).

Irwin stated that, when the stress intensity factor K_I reaches a critical value, denoted as K_{Ic} crack propagation will occur. This critical value is a material constant and is called the fracture toughness of the material. However, if the external loading results in a K_I lower than the critical value, K_{Ic}, no crack propagation will occur. The distinction between K_{Ic} and K_I is important, and it is similar to the distinction between strength and stress. In other words, the connection between K_{Ic} and the stress intensity factor K_I for the opening mode crack is similar to that of a material's tensile strength and the stress in a tensile specimen (Brown and Srawley, 1966). For the geometry and Mode I of Figure 3.3, Irwin's criterion gives:

$$\sigma_c\sqrt{\pi\, a} = K_{Ic} \qquad (3.10)$$

According to this relation, when the external stress reaches the value σ_c the crack will propagate. Comparing Equations (3.7) and (3.10) shows clearly that the Irwin local stress criterion at the crack tip where the fracture process is taking place coincides with the Griffith global energy criterion. The constant in the right-hand side of equation (3.7) can be identified with K_{Ic}, i.e.

$$\sqrt{2E\gamma} = K_{Ic} \quad (3.11)$$

or

$$K_{Ic}^2 = EG_c \quad (3.12)$$

where G_c is the critical Griffith surface energy density or the critical energy release rate, $G_c = 2\gamma$.

Today, since it is much easier to determine directly the critical fracture toughness K_{Ic} than it is to determine the surface energy density, Irwin's fracture theory is more widely used than Griffith's (Karihaloo, 1995).

The fracture toughness of a material can be determined from a pre-cracked specimen.

The most commonly used specimen shape for the determination of K_{Ic} is a notched beam loaded in three-point bending. The specimen is loaded gradually until the sharp-notch begins to propagate. The corresponding maximum load is used for the calculation of the bending moment at mid-span (M_{max}) and the critical stress intensity factor K_{Ic} is then calculated using the formula (Karihaloo, 1995):

$$K_{Ic} = \frac{6YM_{max}\sqrt{a}}{BW^2} \quad (3.13)$$

where Y is a function of $a = a/W$ (i.e. the ratio of the depth of notch to the height of the specimen), B and W are the width and height of the beam, respectively.

3.2.3 Barenblatt's Cohesive Crack Model

The main features of LEFM described above are (Karihaloo, 1995):

- Besides the usual two elastic constants E and ν, one additional material parameter is involved in describing the brittle fracture. This parameter may be associated

with the energy of the body (G_c) or to the stress field near the tip of a sharp crack present in the body (KIc).

- The stresses and strains in the vicinity of a sharp crack tip are very large (at the tip itself they tend to infinity).
- The entire body remains elastic during the fracture process, and energy is only dissipated at a point (crack tip).

The contradiction between the linear elastic fracture model and the real physical situation at the crack tip had been recognised by Griffith (1920). He therefore, proposed that the crack faces should be permitted to close smoothly (Figure 3.4c) under the effect of large cohesive forces.

The fracture mechanics analysis based on the concept of a crack-tip cohesive zone, was given firstly by Barenblatt (1959) in which he assumed that there were large cohesive forces *q(x)* acting over a small zone of length *c* (*c*<<*a*; Figure 3.5) near the crack tip and that the crack faces close smoothly.

Because the distribution of these cohesive forces is generally unknown and due to the existence of other impurities near the crack tip it is difficult to ascertain the distribution. Irwin (1957) had also recognized that the fracture process cannot be focused at a point but should occur over a finite, though small, zone, the so-called Fracture Process Zone (FPZ). He provided a crude assessment of its size (r_p) by restricting the transverse normal stress in the fracture criterion equation (3.10) to the tensile strength f_t of the brittle material

$$r_P = \frac{1}{\pi}\frac{K_{Ic}^2}{f_t^2} = \frac{1}{\pi}\frac{EG_c}{f_t^2} \qquad (3.14)$$

Another cohesive crack model, similar to the Barenblatt cohesive crack model, was proposed by Dugdale (1960) and Bilby et al. (1963) to describe the behaviour of the elastic-plastic materials. In this model, they allowed the plastic zone to form at each crack tip and extend as far as is necessary to satisfy the yield condition. Therefore, the closing stress over the plastic zone will be constant and equal to the yield stress of the material (σ_y).

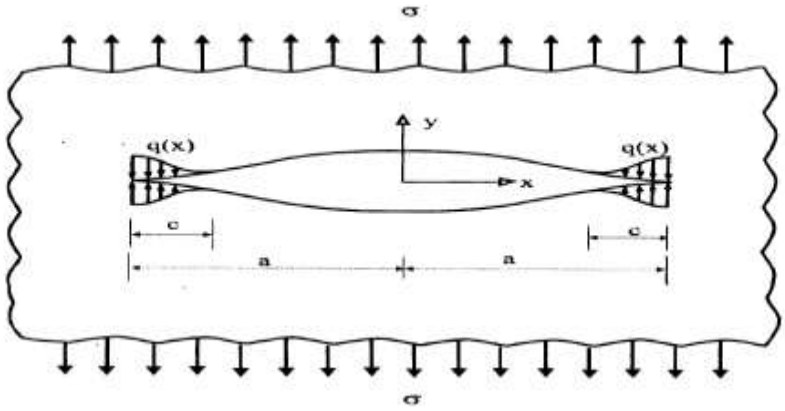

Figure 3.5 Barenblatt cohesive crack model in Mode I. Note c<< a (After Karihaloo, 1995).

3.2.4 Is LEFM Applicable to Concrete?

Attempts were made to apply LEFM to concrete, which was considered a brittle material, but these proved ineffective, since cement-based materials exhibit a totally different response.

Figure 3.6a illustrates the typical load-deformation response of these materials in tension/flexure. It can be seen that these materials exhibit strain hardening prior to the attainment of their tensile capacity (region AB). In addition, there is a region of tension softening (i.e. an increase in deformation with decreasing tension carrying capacity) after the attainment of the maximum load (BC). This is mostly a result of arbitrarily formed micro-cracks. The aggregate interlock and other frictional effects give rise to the tail region of tension softening (CD). These types of material are called quasi-brittle.

The pre-peak non-linearity has only a secondary impact on the fracture behaviour of concrete. The primary impact is due to the tension softening response because it reduces the energy available for release into the crack tip region and thus leads to an increase in the fracture surface area.

In other words, the primary reason for the deviation of the fracture behaviour of concrete from the LEFM prediction is the formation of an extensive fracture process zone ahead of the pre-existing notch/crack, as illustrated in Figure 3.6b.

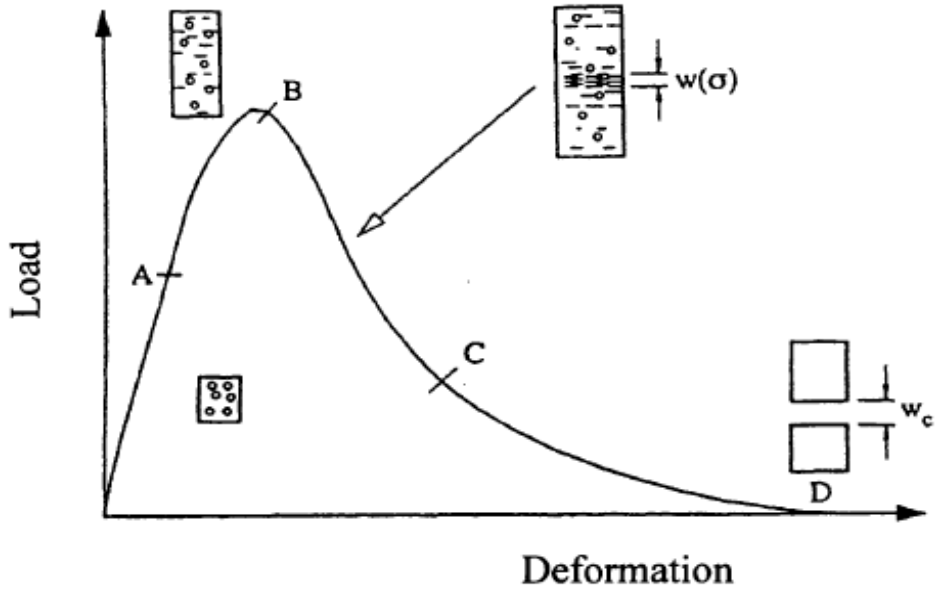

Figure 3.6a Typical load-deformation response o f a quasi-brittle material in tension / flexure.

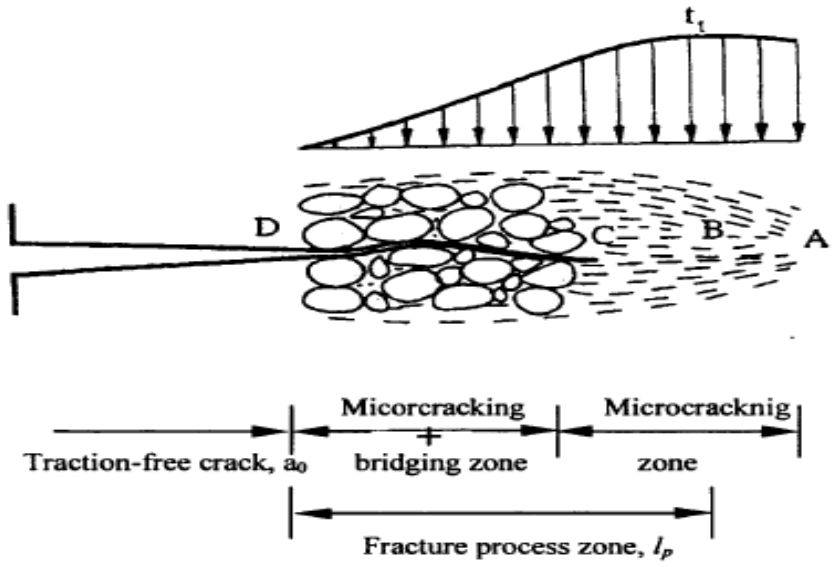

Figure 3.6b The fracture process zone ahead of the real traction-free crack (After Karihaloo,1995)

3.2.5 Fracture Process Zone (FPZ)

The Fracture Process Zone (FPZ) is defined as the inelastic zone around the crack tip and corresponds to the region of tension softening of the load-deformation curve (Figure 3.6). The microstructure of the material and the stress field existing ahead of an introduced macro-crack are the factors that affect the size of the fracture process zone (Karihaloo, 1995). In the FPZ, energy is dissipated on micro-cracking at aggregates due to the presence of a macro-crack, debonding of aggregates, coalescence of debond crack with a macro-crack and the crack bridging (Figure 3.7).

In the FPZ, some parts of crack surfaces may still be in contact after cracking, i.e. the advancing crack is not continuous. As a result, the stress gradually decreases after the peak load, sudden failure is prevented, and a softening type of response is observed. The heterogeneity of concrete leads it to have a sizeable fracture process zone, which is in violation with the basic assumption of the linear elastic fracture mechanics.

Therefore, to predict the fracture behaviour of concrete, the size of the fracture process zone must be included in the models (Bazant and Planas, 1997).

Moreover, it has been noticed that the load carrying capacity of concrete structures decreases with increasing structural size. This is also a consequence of the existence of FPZ. When a concrete structure is loaded, the strain energy produced by the applied load is transformed to the energy consumed to create new fracture surfaces and the energy absorbed in the FPZ. Therefore, the larger the structure's size, the lower the nominal strength. However, when the size of concrete structure becomes massive the strength approaches a constant value (Shah et al., 1995).

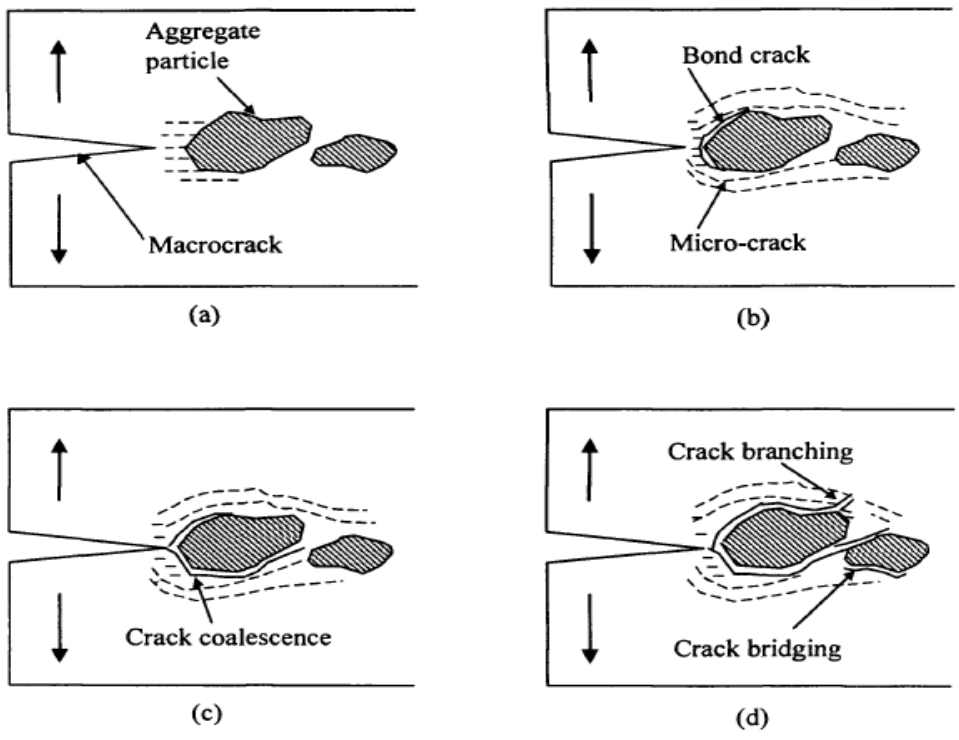

Figure 3.7 Schematic representation of the fracture process zone (a) micro-cracking at aggregate, (b) deboning and micro cracking, (c) coalescence of debond crack with macro crack, and micro cracking, (d) crack bridging, debonding, crack branching and micro cracking (After Karihaloo, 1995).

3.3 Nonlinear Fracture Mechanics (NLFM)

The reason behind the inapplicability of linear elastic fracture mechanics is the fact that concrete has a large fracture process zone. The non-linear fracture theory applicable to ductile materials, such as metals is different from that applicable to quasi-brittle materials like concrete or rock. The reason behind that is because the fracture process zone, though small, in ductile materials is surrounded by a large nonlinear plastic zone, whilst in quasi-brittle materials the fracture process zone covers nearly the whole zone of nonlinear deformation. The nonlinear zone is nearly absent in brittle materials. This is illustrated in Figure 3.8.

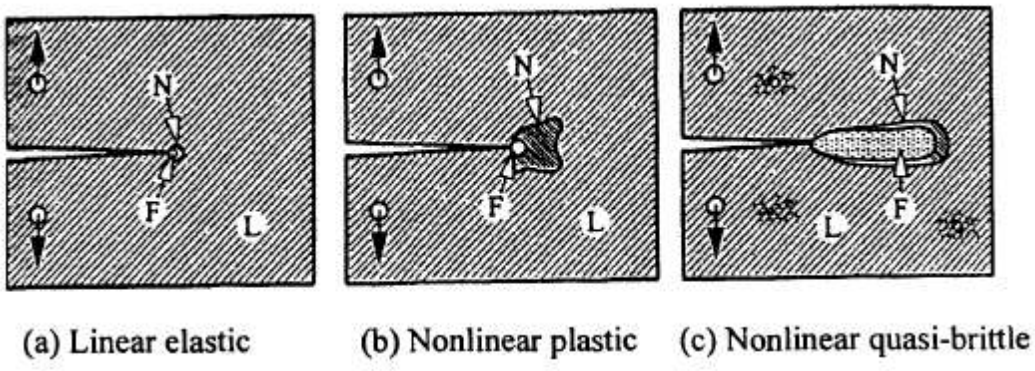

Figure 3.8 Distinguishing features of fracture in (a) a linear material, (b) a ductile material, (c) a quasi-brittle material. L refers to linear elastic region, N to nonlinear zone, and F to fracture process zone (After ACI Report 446.1 R-91).

3.3.1 Fictitious Crack Model (FCM)

Hillerborg et al. (1976) proposed the first non-linear theory of fracture mechanics for concrete. It includes the tension softening fracture process zone through a fictitious crack ahead of the pre-existing crack whose faces are acted upon by a certain closing stress (Figure 3.9). In this model, the real traction-free crack of length a_0 (the true or

physical crack through which no stresses can be transmitted) terminates in a fictitious crack representing the discontinuous fracture process zone. The faces of the fictitious crack close smoothly, so that $K_I = 0$ at its tip and the stress is finite equal to the tensile strength of concrete. This model is known as the Fictitious Crack Model (FCM).

In this model, the constitutive relation is split into a linear stress-strain relation up to the peak load and a stress-crack opening relation for the softening behaviour in the cracked section, Figure 3.9.

There are some points of similarity between this model and the Dugdale and Barenblatt models mentioned above. Like these models, a negligible thickness is assumed for the FPZ and the crack tip faces close smoothly ($K_I = 0$). On the other hand, there are some major differences. The closing stresses in the FCM are not constant, as they are in the Dugdale model. They increase from zero at the tip of the pre-existing stress-free crack to the tensile strength of the material, f_t at the tip of the fictitious crack. The distribution of the closing stress, $\sigma(w)$, along the fracture process zone (FPZ) depends on the opening of the fictitious crack faces, w. The size of the fracture process zone (l_p in Figure 3.9) in the FCM may not be small in comparison with the length of the pre-existing macro crack unlike in the Barenblatt model.

It was observed earlier that a single parameter is needed to depict a brittle material in linear elastic fracture mechanics (e.g. K_{Ic} in Irwin's theory). However, in the fictitious crack model, it is necessary to have two material parameters. These are:

- The shape of the stress-displacement relation $\sigma(w)$ in the softening zone.
- The area under the tension-softening curve, which is the specific fracture energy G_F of concrete

$$G_F = \int_0^{w_c} \sigma(w)dw \tag{3.15}$$

where, w_c is the critical crack opening displacement when the closing stress is equal to zero.

There is also another material parameter which can be obtained from the above information, namely the characteristic length of the material

$$l_{ch} = \frac{EG_F}{f_t^2} \tag{3.16}$$

The characteristic length, l_{ch} is related to the heterogeneity of the material microstructure, giving an indication of its brittleness. The longer the characteristic length, l_{ch}, the more ductile (i.e. less brittle) the material. It should however be stressed that l_{ch} is a derived material property with the dimension of length, not to be confused with the fundamental property l_p.

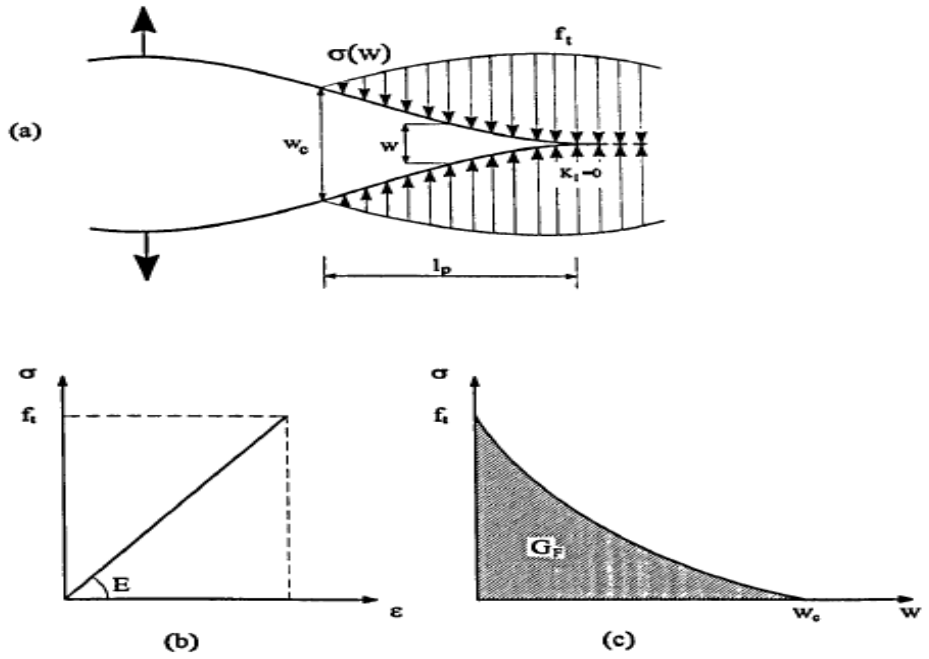

Figure 3.9 (a) A real traction-free crack of length a_0 terminating in a fictitious crack of length l_p whose faces close smoothly near its ($K_I = 0$). (b) The material ahead of the fictitious crack tip is assumed to be linear, (c) But the material within the fracture process zone is softening; the area under softening curve equals fracture energy G_F (after Karihaloo, 1995).

The fictitious crack model was originally developed for the description of the softening behaviour of plain concrete (Hillerborg et al., 1976). Later it was shown that this approach also can be applied to FRC (Hillerborg, 1980).

A modification of the fictitious crack model by Hillerborg et al. (1976) was developed by Bazant & Oh (1983), where the fracture process zone was modelled by a band of uniformly and continuously distributed (smeared) micro-cracks of width h_b (Figure 3.10a). Constant crack propagation is supposed by progressive micro-cracking within this band, which is characterized by a stress-strain relationship (Figure 3.10b). The crack opening displacement w is equal to the product of the strain and the width of the crack band, h_b. This is the so-called Crack Band Model (CBM).

The energy consumed by the crack growth per unit area of the crack band, G_F, is the product of the area under the stress- strain curve in Figure 3.10b, and the width of the crack band, h_b

$$G_F = h_b \left[1 + \frac{E}{E_t}\right].\frac{f_t^2}{2E} \tag{3.17}$$

where E is the modulus of elasticity, E_t is the strain- softening modulus, and f_t is the tensile strength of the material.

It may be observed that three additional material parameters, namely h_b, f_t and E_t, are required, in addition to E, in the crack band model.

An approximate function $h_b = n_a d_a$ has been proposed to calculate the h_b value, where d_a is the maximum aggregate size in concrete and n_a is a constant, which is proposed by Bazant and Oh (1983) to be equal to 3 for concrete, without any physical basis. It should be noticed that as the band width h_b in the CBM tends to zero, then the FCM and CBM

models will merge. Thus, the major difference between the two models is the thickness of the fracture process zone.

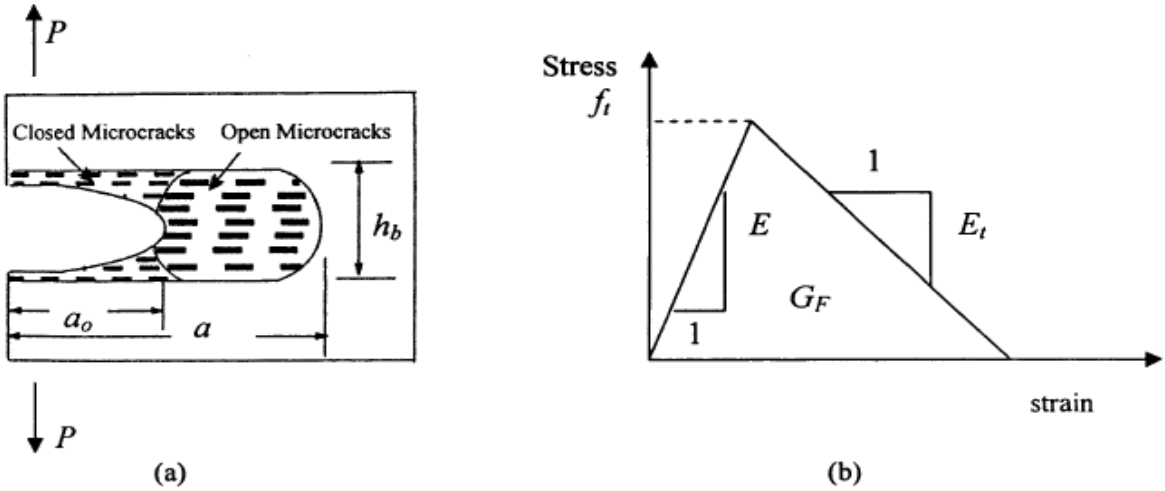

Figure 3.10: Crack band model for fracture of concrete (a) a micro crack band fracture and (b) stress strain curve for the micro crack band (After Shah et al., 1995).

3.4 Stress-Crack Opening Relationship of Concrete

The fictitious crack model originated by Hillerborg et al. (1976) for the description of the softening behaviour of plain concrete has been widely accepted and used in the research community in the last two decades. This is due to the fact that this model is able to closely describe the fracture behaviour of concrete and because it gives a good explanation of many previously unexplained phenomena like e.g. the size effect.

However, the knowledge of the new material property named the stress-crack opening relationship $\sigma(w)$ is considered the major restriction in the use of the model. The direct determination of this property has proved to be a major problem. Thus, many researchers (e.g. Roelfstra and Wittmann, 1986) focussed on indirect determination of the stress-crack opening relation based on the determination of the load-displacement curve of a three-point bend specimen and a subsequent inverse analysis in which a finite

element model forms the basis of the modelling. In the inverse analysis, the parameters of the assumed approximate stress-crack opening relation are identified by matching the resulting load-deflection or load-crack mouth opening diagram with experimentally recorded diagram. Optimization algorithms are used for this identification which minimise the error between the simulated and recorded diagrams (Kitsutaka, 1997; Ostergaard, 2003; Sousa and Gettu, 2006).

Many different approximations of the stress-crack opening relation have been reported in the literature, including linear, bilinear, exponential and polynomial functions (see e.g. Karihaloo, 1995).

A linear stress-crack opening relation was used by Ulfkjaer et al. (1995) for modelling flexural failure of concrete beams. Olesen (2001) modelled the bending failure of FRC beams in the same way, using however a bilinear stress-crack opening relation. This is the most popular relation. The popularity of the bilinear approximation of the stress-crack opening relation stems from the fact that it captures the two major mechanisms responsible for the observed tension softening in concrete, namely microcracking and aggregate interlock. The initial, steep branch of the bilinear relation is a result of microcracking, whereas the second, tail branch is a result of aggregate interlock which is primarily governed by the maximum size and texture of the coarse aggregate used in the concrete mix (Abdalla and Karihaloo, 2004).

Uchida et al. (1995) used a poly-linear stress-crack opening relation in combination with FE-analysis to various kinds of concrete including porous concrete and fibre reinforced high strength concrete to determine indirectly the tension softening diagrams. They found that the tensile strength is not very sensitive to the shape of the softening diagram.

3.4.1 Cracked Hinge Model

The basic idea of the non-linear cracked hinge model, first introduced by Ulfkjaer et al. (1995) and subsequently developed by Stang and Olesen (1998), Olesen (2001), and Ostergaard (2003), is to isolate the part of the beam close to the propagating crack and model it as a short beam segment subjected to a bending moment and a normal force.

The concept of the hinge views the crack as a local change in the overall stress and strain field. Therefore, the disturbance of the strain field, caused by the presence of the crack, is confined to take place between rigid boundaries and is assumed to vanish outside a certain bandwidth. Each rigid boundary may translate and rotate such that it may be joined with an un-cracked beam. Thus, outside of this band the structural element is modelled using the elastic beam theory. Details of the approach based on the hinge model will be given in Chapter Five.

3.5 Concluding Remarks

It has been demonstrated that the formation of an extensive fracture process zone ahead of the pre-existing notch/crack, is the primary reason for the breakdown of linear elastic fracture mechanics. The primary impact on the fracture behaviour of concrete is due to the tension softening response because it reduces the energy available for release into the crack tip region and thus leads to an increase in the fracture surface area, while the pre-peak non-linearity has only a secondary effect.

Thus, it is essential to include the fracture process zone in the modelling of fracture behaviour of concrete. This can be done by using the Fictitious Crack Model (FCM), where the constitutive relation is split into a linear stress-strain relation up to the peak

load and a stress-crack opening relation for the softening behaviour in the cracked section. It was assumed that the distribution the closing stress, $\sigma(w)$, along the fracture process zone (FPZ) depends on the opening of the fictitious crack faces, w. However, two material parameters are necessary for the fictitious crack model, the shape of the stress-displacement relation $\sigma(w)$ in the softening zone and the specific fracture energy G_F of concrete. Diverse stress-crack opening relationships have been used in literature, linear, bilinear, exponential and polynomial. The bilinear approximation of the stress-crack opening relation has become popular since it captures the two major mechanisms responsible for the observed tension softening in concrete, namely micro-cracking and aggregate interlock. This approximation will be discussed and be used in Chapter 5 to characterise the self-compacting UHPFRC.

Chapter Four

Retrofitting of Concrete Structures and Fatigue Behaviour of Concrete

4.1 Retrofitting by FRC (Conventional and HPFRC)

4.1.1 Introduction

In recent years, repair and strengthening of existing structures have been among the most important challenges in civil engineering. Therefore, many strengthening techniques have been applied to retrofit RC structures.

The primary reasons for strengthening and repair of structures include:

- Improving the resistance or stiffness to withstand increased loads;
- Increasing the load-carrying capacity for higher allowable loads;
- Removing premature failure due to insufficient detailing;
- Restoring lost load carrying capacity due to overloading, earthquake and other types of degradation caused by aging such as: corrosion, erosion, etc. (Malek et al., 1998).

Some of the concrete structures or parts of it are not satisfying their structural functions due to different reasons, such as faults on the concrete caused by inadequate construction, fire damage and deterioration caused by environmental action. Therefore repairing of deteriorated concrete structures becomes important and has attained popularity rather than rebuilding or demolishing.

Over the past couple of decades several systems have been developed for retrofitting concrete structures. Among these are bonding by steel or fibre reinforced plastic FRP plates to the tension side of beams. However, some problems have been recorded with these techniques, e.g. corrosion of steel, which can damage the bond at the steel concrete interface, and premature debonding of FRP.

Some new repair materials were developed in the last decade, such as High-Performance Fibre Reinforced Cementitious Composites (HPFRCCs), which enhance the structural response and extend the durability of concrete structures. They are more reliable and effective materials for retrofitting because they are compatible with concrete (Lim and Li, 1997; Karihaloo et al., 2000; Karihaloo et al., 2002; Habel et al., 2006). Among these is CARDIFRC, where some of the problems related to the current techniques based on externally bonded steel plates and FRP have been overcome.

4.1.2 Externally Bonded Steel Plates

The technique of bonding steel plates to the external surfaces of reinforced concrete structures by a structural adhesive become worldwide since the late 1960s (Barnes and Mays, 1999). The advantages of this method can be summarised as follows (An et al., 1991; Barnes et al., 2001): Possible increase in the beam ductility; can be rapidly used to strengthen the structure whilst it is still in use; both the serviceability and the ultimate load capacity of the section can be increased; accessibility for inspection and maintenance; the configuration of the structure is not modified.

The main drawback of steel bonded plate systems is corrosion of plate during natural exposure (Grace et al., 1999), where bond strength gradually decreases at the steel epoxy interface, and eventually results in a brittle failure of the structure.

Many experimental works have been performed to investigate the behaviour of reinforced concrete beams strengthened in flexure and shear by Adhikary and Mutsuyoshi (2006), Altin et al. (2005), Arslan et al. (2008), Aykac et al., (2012), Barnes and Mays (2006). These investigations indicate that bonding of steel plates to the

surface of concrete beam can produce a substantial enhancement in structural performance under both service and ultimate load conditions.

4.1.3 Fibre Reinforced Plastics (FRP)

Although strengthening of RC beams using steel plates became popular worldwide, corrosion is one of the major shortcomings of this technique. This led researchers to investigate corrosion-free composite materials. Fibre reinforced polymer (FRP) is one of these materials, which offers many advantages. Depending on the member type, the objective of strengthening may be one or a combination of several of the following (Buyukozturk et al., 2004): To increase axial, flexural or shear load capacities; to increase stiffness to reduce deflections under service and design loads; to increase the remaining fatigue life.

The major fibres in FRP materials used in the construction industry are carbon (CFRP), glass (GFRP) and aramid (AFRP) fibres (Jumaat et al., 2011).

Through experimental and theoretical studies, the externally bonded FRP composites can be used to enhance the desired performance of a structural member such as its load carrying capacity and stiffness, ductility, performance under cyclic and fatigue loading (Buyukozturk et al., 2004). Thin FRP laminates are durable, have high strength and stiffness to weight ratio, are chemically inert, cost effective, and offer significant potential because of their lightweight (Buyukozturk and Hearing, 1998).

Existing studies showed that there are several types of failure of FRP plate bonded flexurally strengthened beams. These typical failure modes are (Gao et al., 2007; Teng et al., 2008) (Figure. 4.1)

- Flexural failure by FRP rupture
- Flexural failure by concrete crushing
- Shear failure
- Concrete cover separation
- Plate end interfacial debonding (delamination of FRP plate).

FRP tensile rupture failure mode is possible when the amount of reinforcement in concrete section is small. While concrete crushing mode in the compression zone can occur when the amount of reinforcement is large (Bakis et al., 2002). FRP rupture generally occurs following the yielding of the steel tension bars (Teng et al., 2008). The flexural behaviour of reinforced concrete members strengthened with FRP materials has been investigated by a wide range of researchers (Dong et al., 2013; Esfahani et al., 2007; Grace et al., 1999; Smith et al., 2011). The findings demonstrated that strengthening increased the flexural strength and stiffness of the strengthened beams and cracks become smaller and more evenly distributed.

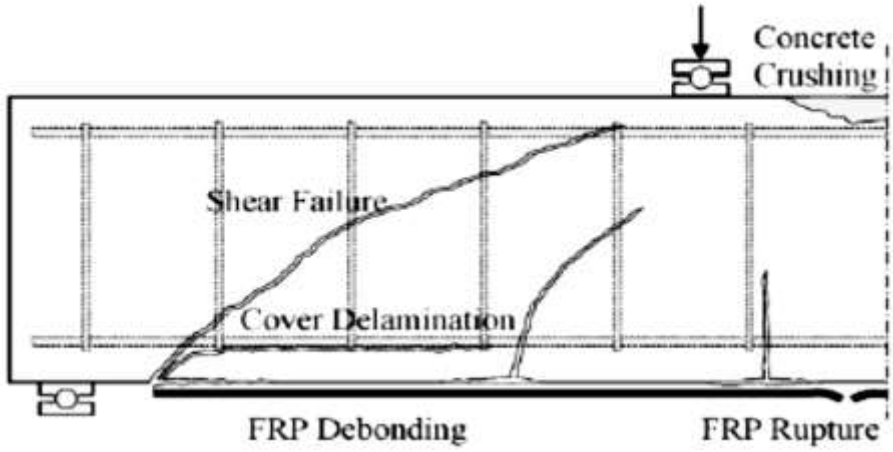

Figure 4.1 Failure modes for FRP strengthened beams (After Buyukozturk et al., 2004)

A wide range of published research displayed the influence of FRP materials on RC beam behaviour under shear (Islam et al., 2005; Jain and Sikka, 2015; Önal, 2014; Obaidat et al., 2011). Shear failure mode is catastrophic and usually occurs without previous warning and in a brittle manner. Several reasons can produce shear failure such as insufficient shear reinforcement or reduction in steel area due to corrosion, increased service load, construction defects (Farhat, 2004). Different retrofitting methods and materials have been employed for shear strengthening since externally bonded FRP reinforcement can increase the shear capacity, including a fibre wrap, strips and grids, all made up of carbon fibre (Figure 4.2) (Islam et al., 2005). Other methods employed for shear strengthening of RC beam sections are bonding U jackets, vertical strips and wing plates (Al-Sulaimani et al., 1994).

The most widespread failure modes among the five modes are those related with concrete peel-off and delamination of FRP strip from the concrete surface (Buyukozturk and Hearing, 1998).

In both concrete cover separation and delamination of FRP plate modes, failure starts from a plate end and occurs in concrete either adjacent to the adhesive layer (delamination of FRP) or at the level of the steel tension reinforcement (cover separation) (Gao et al., 2007; Jumaat et al., 2011). These failure modes are undesirable because the FRP plate would not be completely employed.

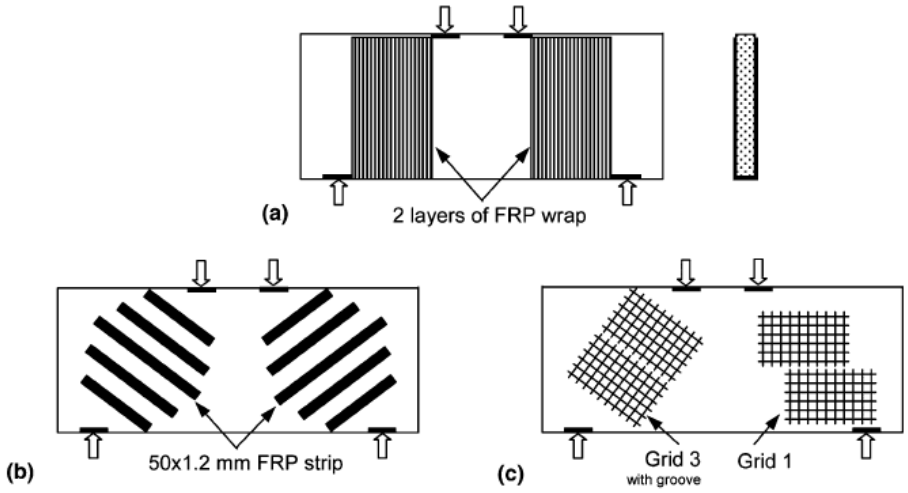

Figure 4.2 Different CFRP arrangement: (a) FRP wraps (b) FRP strips (c) Grids (After Islam et al., 2005)

4.1.4 High Performance Fibre Reinforced Cementitious Composites

4.1.4.1 Retrofitting with CARDIFRC

CARDIFRC is a new material that has been developed in Cardiff University; it belongs to the class of high performance fibre reinforced cementitious composites (HPFRCC). The special characteristics (high tensile/flexural strength and high energy absorption capacity) of CARDIFRC make it particularly suitable for retrofitting of existing concrete structures. The main feature of CARDIFRC mixes for retrofitting is that unlike steel and FRP, their tensile strength, stiffness and coefficient of linear thermal expansion are comparable to that of the material of the parent member (Karihaloo et al., 2002). Farhat, (2004) demonstrated the main advantages of using CARDIFRC as a retrofitting material as follows:

- Enhancing the serviceability of RC concrete structure.
- Gradual failure without delamination can be guaranteed.
- Ensuring compatibility with the material of the structure being retrofitted.

Two techniques - direct casting or adhesive bonding of pre-cast strips to RC beams can be used for retrofitting RC beams with CARDIFRC.

Although the primary results of Alaee (2002) showed that the direct casting can be successfully used for improving the flexural capacity of damaged beams, great care is required to ensure that the retrofit material adheres securely to concrete. Furthermore, the need of special formwork requirement might limit this application in practice.

4.1.4.1.1 Flexural Strengthening

Flexural strengthening of the damaged RC beams can be attained by bonding CARDIFRC strips on the prepared surface of tensile face of beams in different configurations. Karihaloo et al. (2003b) used damaged RC beams retrofitted with CARDIFRC strips to investigate the flexural behaviour. The experiments were conducted on two types of beams: beams without shear reinforcement, which were designed to fail either in flexure or in shear, and beams with sufficient shear reinforcement. The retrofitted beams were loaded to failure and compared with the control beams; all beams failed at loads at least equal to the average failure load of the control beams with flexural, shear or a combination of flexural and shear failures modes.

4.1.4.1.2 Flexural and Shear Strengthening

Flexural and shear strengthening of the damaged RC beams can be achieved by bonding CARDIFRC strips on the prepared surface of tensile face and each side of beams in different configurations (Figure 4.3). In comparison with beams retrofitted in tension only, substantial enhancements in load carrying capacity and serviceability in terms of reduction in the number and the width of the cracks have been achieved by using the

different types of flexural and shear strengthening configurations (Karihaloo et al. (2003). Alaee (2002) investigated retrofitting RC beams with one strip on the tension face and short strips on both sides to avoid shear cracks with sufficient shear reinforcement (Figure 4.3f). It was found that this technique is very effective in improving flexural and shear behaviour but does not improve the load carrying capacity of the RC beams. To attain very high load carrying capacity and stiffness without any shear reinforcement, the beams were retrofitted with one retrofit strip on the tension face; the sides of the beams may be fully covered by retrofit strips. Alaee and Karihaloo (2003a-b) developed two analytical models. The first model established on the classical theory, where the moment resistance and load- deflection behaviour was predicted, while the second used a purely fracture mechanics approach and followed the initiation and propagation of flexural cracks. These models were found to give predictions in good agreement with the test findings.

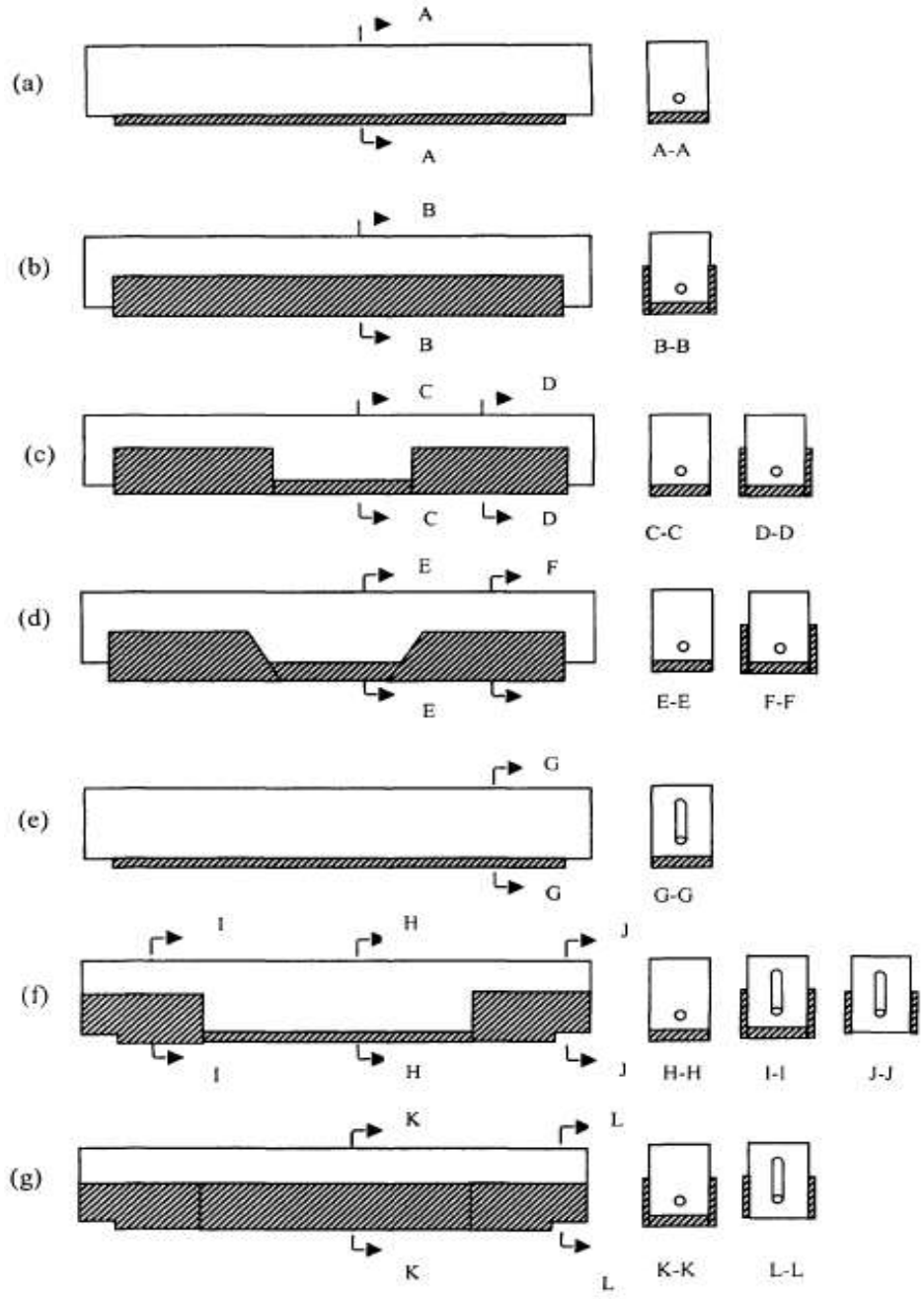

Figure 4.3 Configurations of retrofitting RC beams with CARDIFRC®. Beams retrofitted with: (a) one strip on the tension face, (b) one strip on the tension and two strips on sides, (C) one strip on the tension face and four rectangular strips on sides, (d) one strip on the tension and four trapezoidal strips on sides, (e) one strip on the tension, (f) one strip on the tension and four short strips on sides covering supports and ends of tension strip, and (g) one strip on the tension and four short and two continuous strips on sides, fully covering supports and tension strip sides (After Karihaloo et al., 2003).

4.2 Fatigue Response of Concrete

4.2.1 Introduction

A plain concrete member, when subjected to repeated loads, may exhibit excessive cracking and may eventually fail after a sufficient number of load repetitions, even if the maximum load is less than the static strength of a similar specimen.

The fatigue strength of concrete is defined as a fraction of the static strength that it can support repeatedly for a given number of cycles. (ACI Committee 215, 1986).

Concrete fatigue is a process of progressive, permanent development of small imperfections existing in the material by repetitive loads. These imperfections may be present in concrete due to concrete shrinkage, or may be caused by application of external loads. Also, this is attributed to the propagation of internal micro-cracks, which results in a significant increase of irrecoverable strain.

Fatigue loading is usually divided into two categories (RILEM Committee 36-RDL, 1984) i.e. low-cycle and high-cycle loading. Low-cycle loading involves the application of a few load cycles at high stress levels. On the other hand, high cyclic loading is characterised by a large number of cycles at lower stress levels.

The progressive bond deterioration between coarse aggregates and the cement paste or by development of cracks existing in the cement paste are the main reasons of the occurrence of fatigue. The mechanism of fatigue failure in concrete or mortar can be divided into three distinct stages. The first stage involves the weak regions within the concrete or mortar and is termed flaw initiation. The second stage is characterised by slow and progressive growth of the inherent flaws to a critical size. In the final stage,

when a sufficient number of unstable cracks have formed, a continuous or macro-crack will develop, eventually leading to failure (Gao and Hsu, 1998).

Several parameters were observed to affect the dynamic response of concrete, which were analysed and their influence explained. The most important of these parameters are the following: steel fibres, concrete confinement, curing conditions, humidity, temperature, number of load cycles and strain or stress rate (Nicolaides, 2004). A double effect of including fibres to concrete can be expected on the fatigue performance of concrete. By bridging cracks, the fibres can retard the crack growth process, providing an additional fatigue life to concrete. On the contrary, fibres added to concrete might themselves be the source of further flaws and reduce the fatigue life of concrete.

4.2.2 S-N Curves

When materials are subjected to a great number of cyclic loadings two featured types of behaviour are found: some materials, such as steel, will never fail under these cyclic loadings as long as the maximum stress in the cycle is lower than a specific stress called the fatigue limit. Other materials like concrete, eventually fail in spite of the peak load in the cycle being well within the elastic range (Actin, 2004).

Most studies on the fatigue of concrete have so far been directed to relate the applied cyclic stress to the fatigue life of concrete (Oh, 1986). The experimental data are usually represented in terms of Wöhler diagrams, also known as S-N curves. These are semi-logarithmic representations, where the maximum stress $S = \sigma_{max}$ is indicated along the vertical axis and the logarithm of the number of cycles to failure or fatigue life N_f along the horizontal axis. Usually σ_{max} is represented as a fraction of the static strength at which ultimate failure occurs. These curves are mostly recorded for zero average cyclic stress.

For stress controlled loading, the stress range $\Delta\sigma$ is the difference between the maximum and the minimum stress during the cycle. The stress amplitude σ_a is half the stress variation. Mean stress σ_m and stress ratio R are used to specify the loading (Figure 4.4);

$$\Delta\sigma = \sigma_{max} - \sigma_{min} \quad ; \qquad \sigma_a = \frac{1}{2}\Delta\sigma \; ;$$

$$\sigma_m = \frac{1}{2}(\sigma_{max} + \sigma_{min}); \qquad R = \frac{\sigma_{min}}{\sigma_{max}}$$

For high cycle fatigue the (S-N)-curve, it is found that the experimental data can be fitted to an equation called Basquin's Law;

$$\Delta\sigma N_f^a = c_1 \tag{4.1}$$

where $\Delta\sigma$ is the stress range (with zero mean stress), N_f is the number of cycles to failure and a (between $\frac{1}{8}$ and $\frac{1}{15}$ for most materials) (Ashby and Jones, 1996) and c_1 are constants to be determined from tests.

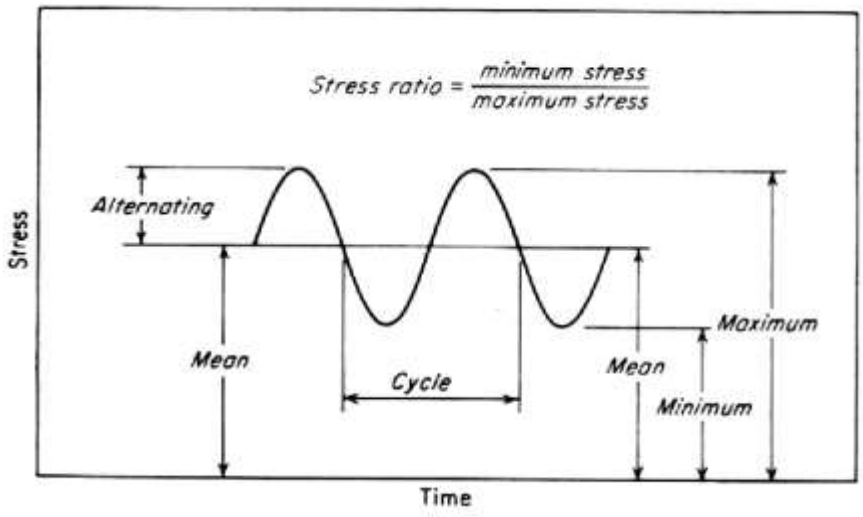

Figure 4.4 Fatigue terms used in the analysis

For low-cycle fatigue of un-cracked components where σ_{max} or σ_{min} are above the yield stress, Basquin's Law no longer works, as show in Figure 4.5. But another empirical approach known as the Coffin-Manson Law can be used:

$$\Delta\varepsilon^{Pl} N_f^b = C_2 \tag{4.2}$$

where b (0.5 to 0.6) and C_2 are constants.

To calculate the lifetime, the preceding approach assumes fully reversed fatigue loads, so that the mean stress σ_m is zero.

As the material is subjected to a mean tensile stress (i.e. σ_m is no longer zero), the stress range must be decreased to maintain the same N_f as an increase in mean stress will always cause a reduction in the fatigue life (Hertzberg,1995; Campbell, 2008). A number of mathematical models have been developed to study the influence of the mean stress. Among these are;

1. The Goodman theory,

2. The Gerber theory, and

3. The Soderberg theory.

The mathematical expression for each is as follows:

$$\Delta\sigma_{\sigma m} = \Delta\sigma_0 \left(1 - \frac{|\sigma_m|}{\sigma_F}\right) \quad \text{Goodman's theory} \tag{4.3}$$

$$\Delta\sigma_{\sigma m} = \Delta\sigma_0 \left(1 - \left(\frac{\sigma_m}{\sigma_F}\right)^2\right) \quad \text{Gerber theory} \tag{4.4}$$

$$\Delta\sigma_{\sigma m} = \Delta\sigma_0 \left(1 - \frac{|\sigma_m|}{\sigma_y}\right) \quad \text{Soderberg theory} \tag{4.5}$$

where $\Delta\sigma_0$ is the cyclic stress range with zero mean stress, $\Delta\sigma_{\sigma m}$ is the cyclic stress range with non-zero mean stress, $|\sigma_m|$ is the absolute value of the mean stress, σ_F is the static flexural strength and σ_y is the yield stress. A graphical comparison of these equations is shown in Figure 4.6.

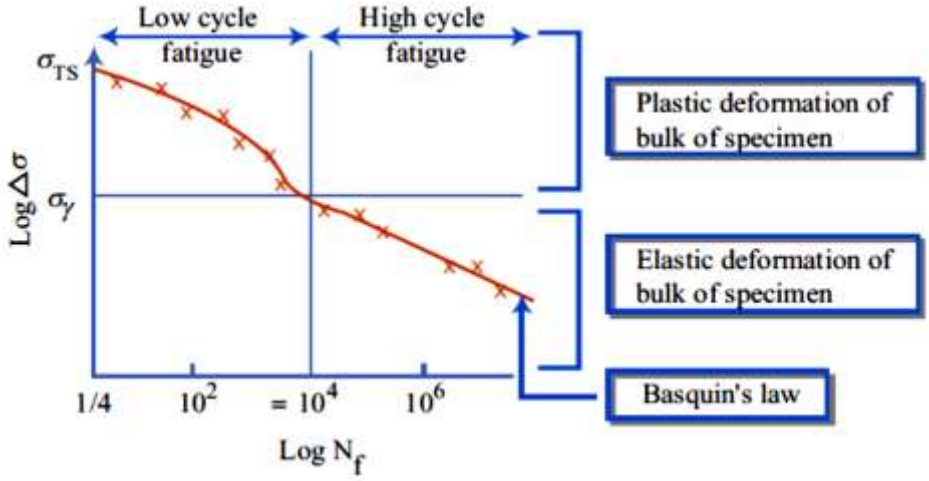

Figure 4.5 Initiation-controlled high-cycle fatigue - Basquin's law (After Ashby and Jones, 1996).

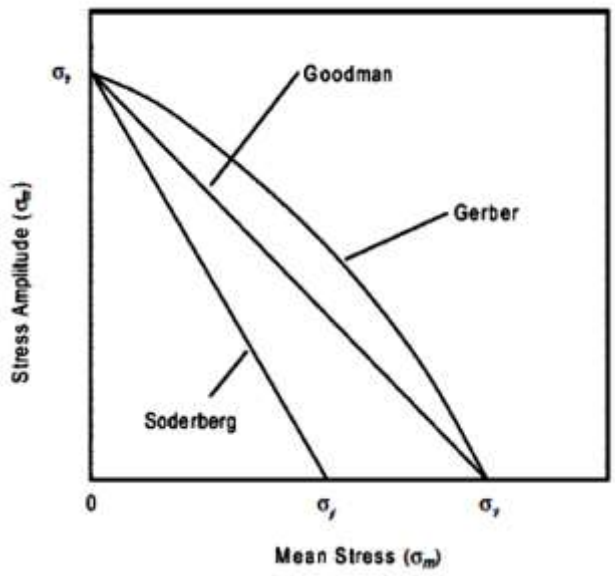

Figure 4.6 Graphical representation of Gerber, Goodman and Soderberg theories (After Campbell, 2008)

A significant influence on the fatigue life (Maddox, 1975; Campbell, 2008) can be expected for non-zero mean stress. Figure 4.7 gives an example of the effect of mean stress on the fatigue life of steel. As the mean stress increases, the fatigue life decreases (Tilly, 1979). A similar effect can be expected in concrete. The effect of mean stress on the fatigue life will be discussed in Chapter Six.

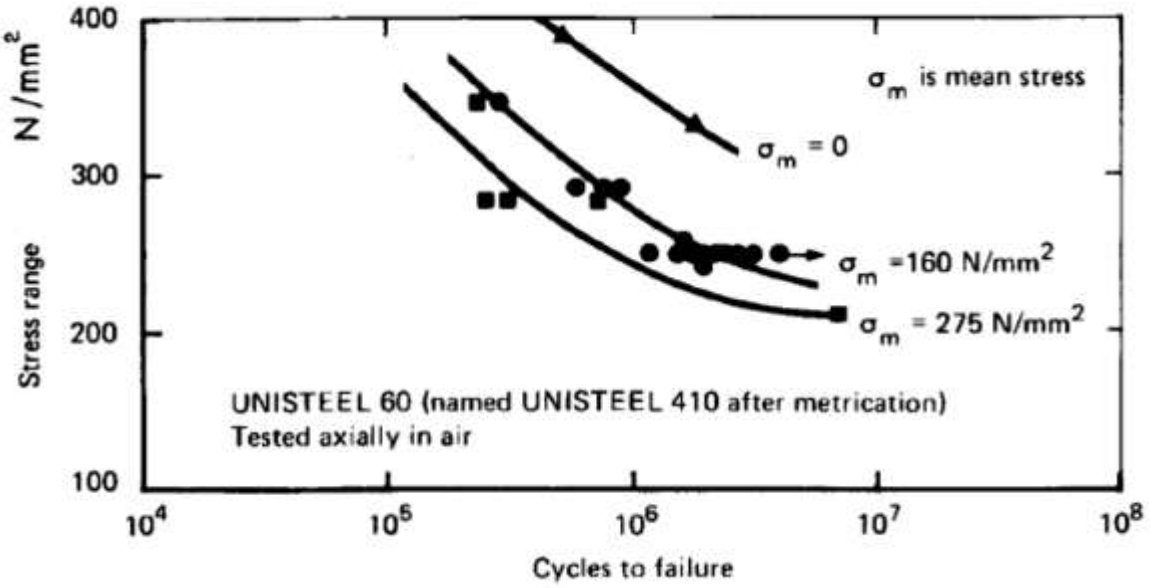

Figure 4.7 Effect of mean stress on the fatigue life of the steel (After Tilly, 1979)

4.2.3 Fatigue Crack Growth Behaviour: Paris Law

The relation between the crack propagation rate and the stress intensity factor range (ΔK) in metallic materials exhibits three regions: threshold region, steady growth, and unstable growth/fracture as shown in Figure 4.8. In the threshold stage, crack growth is initially quite rapid, with the curve generally having a steep slope (Dowling, 2012). The next stage is the stable crack growth region; this part is obviously linear with the crack growth rate and stress intensity factor range increasing at the same rate. Finally, the growth rate again accelerates in unsteady way as the stress intensity factor range

becomes large, typically as the crack reaches its critical length and fracture takes place. A fundamental fracture mechanics approach relates the crack length increment per load cycle ($\Delta a/\Delta N$) to the applied stress intensity factor range (Paris Law);

$$\frac{da}{dN} = A\Delta K^m \tag{4.6}$$

where a = crack length; N = number of load cycles; A = Paris constant; m = Paris exponent; and ΔK = crack stress intensity factor range in a load cycle.

The cyclic stress intensity ΔK increases with time (at constant load) because the crack grows in tension (Ashby and Jones, 1996). It is found that the crack growth per cycle, $\Delta a/\Delta N$, increases with ΔK in the way shown in Fig. 4.8. In addition, the crack growth rate depending not only on the stress intensity factor range (ΔK), the growth rate also depends on the stress ratio, R ($\sigma_{min}/\sigma_{max}$).

The growth rate will increase and be influenced by an increase in the stress ratio R. However, if testing conditions, such as the R value and testing frequency, are kept constant the growth rate will only depend on the stress intensity factor range (Dowling, 2012). Hence the fatigue life N_f can be computed if ΔK is known:

$$N_f = \int_{a_i}^{a_f} \frac{1}{A(\Delta K)m} da \tag{4.7}$$

where a_i is initial crack length and a_f is final crack length.

Several researchers have attempted to apply the Paris law to describe the crack growth during the acceleration stage of fatigue crack growth in concrete (Baluch et al., 1987; Bazant and Schell, 1993). It has been found that the Paris law coefficients are dependent on the material composition (Bazant and Schell, 1993) which probably demonstrate the large differences in the values of the Paris law coefficients reported by different authors.

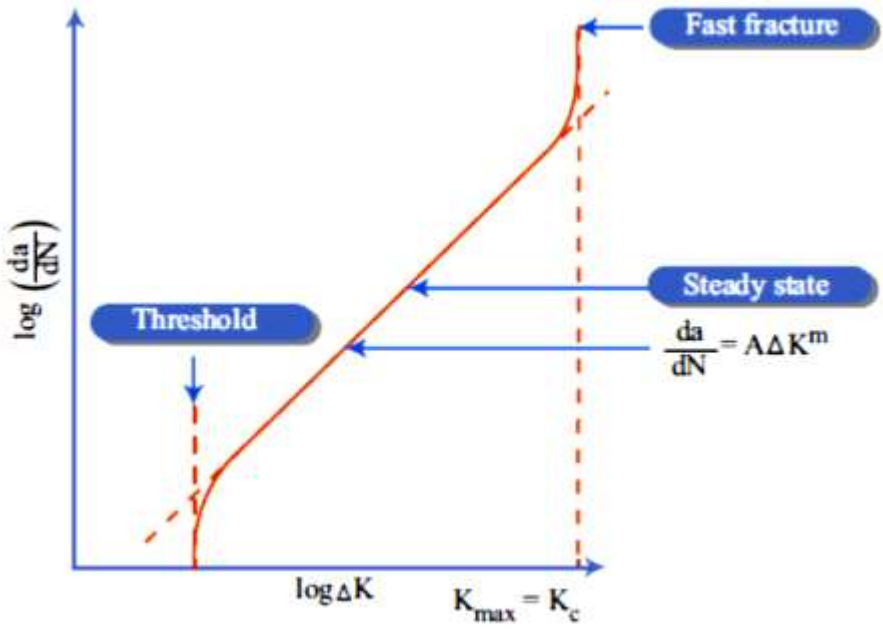

Figure 4.8 Fatigue crack-growth rates for pre-cracked material (After Ashby and Jones, 2002).

4.2.4 Fatigue Response of Concrete

When plain concrete is subjected to repeated loading, it might fail at stress levels less than its static ultimate strength. The fatigue mechanism of concrete can be traced to the progressive deterioration of the bond between the coarse aggregate and the cement paste and due to the growth of the existing micro-cracks and emergence of new ones in the cement paste (RILEM, 1984).

Under repeated cyclic loading, concrete mechanical properties change; a permanent increase of strain in concrete occurs, whereas the modulus of elasticity shows a decrease in its magnitude (Holmen, 1982).

Fatigue damage in concrete can be classified into three phases in terms of increasing maximum strain.

In the first stage, which is called the initiation phase, a fast increase of strain increases is observed, but at a progressively decreasing rate, with increasing number of cycles. The second phase (the stability state phase) occurs where strain growths linearly with

increasing number of cycles. Finally, the last phase represents instability; where a rapid increase in strain with increasing rate leads to failure. Figure 4.9 shows an example of a plot of the relationship between the maximum strain versus the relative number of cycles representing the three stages of the fatigue damage in concrete (Neville, 1995).

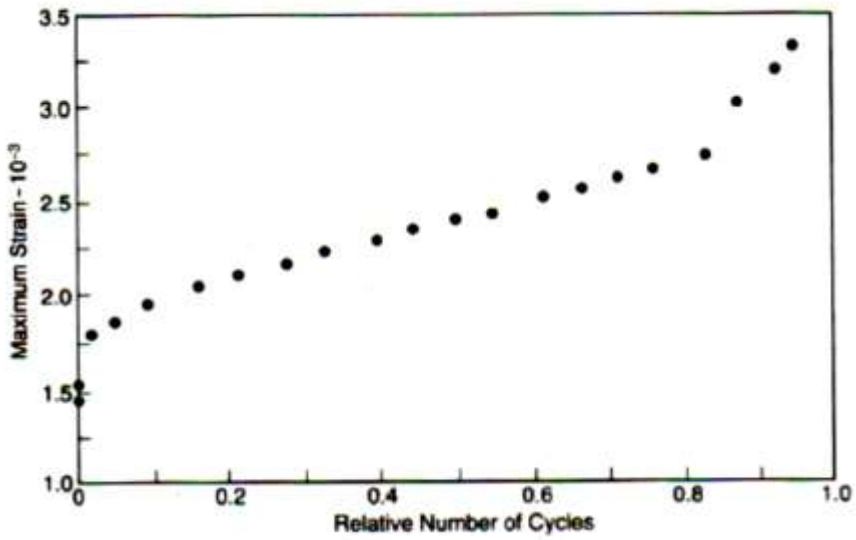

Figure 4.9 Relationship between the maximum strain and relative number of cycles of concrete under compressive cyclic loading (After Neville, 1995)

4.2.5 Fatigue Response of FRC

As stated beforehand, the development of fatigue failure in concrete can be divided into three phases. Therefore, it is feasible to hinder and control the growth of the flaws in the second stage by including closely spaced and randomly dispersed fibres as reinforcements (Lee and Barr, 2004).

Poor resistance against fatigue crack initiation and growth under tensile loading can be attributed to the low tensile strength of plain concrete. Thus, by means of reinforcing a concrete with short fibres (i.e. steel, polymeric or natural fibres), fatigue life would be improved (Matsumoto and Li, 1999; Wang et al., 2000; Bentur and Mindess, 2007). In

addition, a significant improvement in the load-bearing capacity due to the inclusion of steel fibres is acquired (Morris and Garrett, 1981). Moreover, because of the ability of fibres to restrict crack growth and transfer tensile stresses, the flexural fatigue strength is considerably enhanced in SFRC (Singh et al., 2008). Lee and Barr (2004) observed from collecting data of several researchers, that the presence of fibres does not appear to enhance the fatigue life of concrete under compressive fatigue loading. However, inclusion of fibres improves the fatigue performance under flexural fatigue loading. A probable explanation of their observations was fibres could bridge cracks and expand fatigue life. While, fibres cannot show their true efficiency under compressive loading, as the mode of failure is different.

The enhancement of the fatigue life of concrete with the addition of fibres is related to the distribution of fibres in concrete. Actually, a poor dispersion of fibres in concrete leads to a detrimental effect on the fatigue life of concrete (Cachim et al., 2002). On the other hand, the presence of fibres increases pore and initial micro-crack density, resulting in strength decrease. The overall outcome of these two competing effects depends significantly on the fibre volume (Grzybowski and Meyer, 1993).

The weakness of the interfacial zone is efficiently strengthened by adding silica fume, where the number and size of cracks are reduced and enhances the ability of steel fibres to resist cracking and inhibit damage. As a result, the performance of HPFRC subjected to dynamic loading due to the participation of steel fibres and silica fume can increase greatly (Karihaloo, 1995).

All studies confirm that steel fibres do increase the fatigue properties of the concrete, in terms of higher endurance limits, finer cracks and much more energy absorption to failure. In addition, higher fibre volumes, and deformed fibres (instead of using straight

and smooth ones), lead to greater improvements, as do higher aspect ratios (Benture and Mindess, 2007).

4.2.6 Fatigue Behaviour of RC Beams

Fatigue performance of RC beams involves composite action between steel and concrete. Concrete mechanical properties change under repeated cyclic loading where the strains in concrete increase permanently, while the modulus of elasticity decreases (Holmen, 1982). In the case of a reinforcing bar, cyclic load causes micro-cracking that produce a stress concentration at the bar surface. As the cyclic stress continues, the crack propagates, causing a sudden fracture.

Generally, fatigue failure in RC beams is attributed to the fatigue fracture of steel reinforcing bars, where the steel rebar is considered the limiting fatigue component since concrete experiences fatigue cracking at far fewer cycles and has a lower fracture toughness (Dowling, 2012).

Fatigue failure of steel rebar is often accompanied by a fracture surface that shows two kinds of surface: one smooth and the other rough as shown in Figure 4.10. The smoother zone, with the dull, rubbed appearance, is caused by rubbing of the crack faces during crack propagation, while the remaining zone of more jagged surface texture is produced due to final fracture in tension when the cross section of the member is no longer able to carry the applied load (ACI 215R-74). The progress of crack propagation can also be indicated by beach marks spreading away from where the crack initiated. These beach marks are semi-elliptical rings left in the material due to the progressing crack tip.

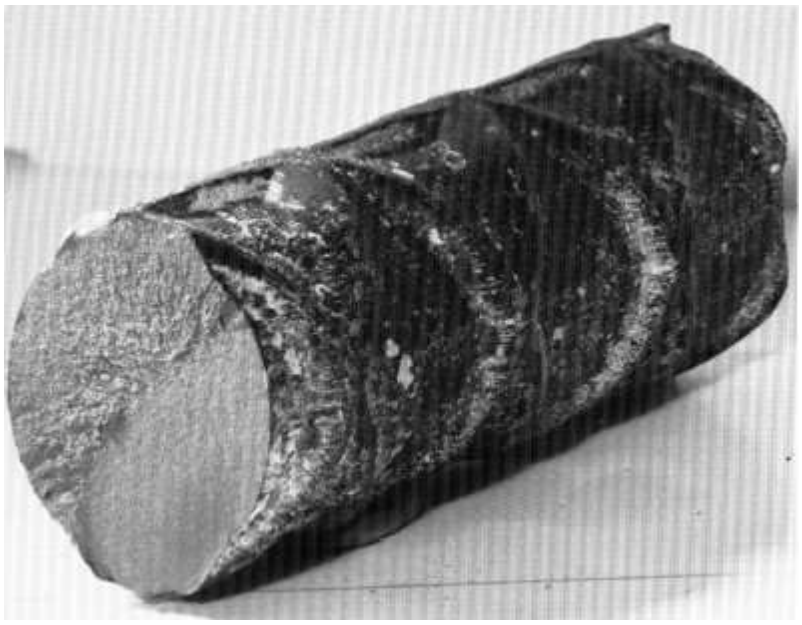

Figure 4.10 Fatigue fracture of a reinforcing bar (ACI 215R-74)

It was found that, although the fatigue of concrete could be expected under high compressive stresses, reinforced members fail because of brittle fracture of the steel reinforcing bar (Johansson, 2004; Loo et al., 2012). This phenomenon can be elucidated with the concrete ability for redistribution of stresses. The extreme compressive fibres of the concrete section degrade due to high stress fatigue loading. Then less-fatigued fibres resist stresses inside the compression zone. Because of this redistribution of compressive stress, the lever arm is minimized and to maintain equilibrium, the reinforcing bar is required to support a greater tensile load that finally leads to bar fracture (Zanuy et al., 2007; Barnes and Mays, 1999). Therefore, the fatigue performance, due to this stress redistribution behaviour, can be enhanced by increasing the amount of steel in the reinforced concrete beams. Nevertheless, over-reinforced beams are exposed to fatigue failure of the compressed concrete, especially under high-load levels (Zanuy et al., 2009).

4.2.7 Review of Fatigue Experimental Work

Jun and Stang (1998) studied the behaviour of fibre reinforced concrete under cyclic flexural loading. The response of one type of polypropylene and two types of steel fibres in two volume concentrations were examined and the load deflection responses were acquired for firm amplitude fatigue loading, as well as for static loading.

They deduced that all the tested steel fibre types improved the fatigue strength, and also that the fatigue strength improved with increasing fibre volume concentration, if the change in static performance was not taken into account. However, the fatigue performance of specimens with high fibre volume concentrations (2%) measured relative to the static strength was found to decrease compared to the lower fibre volume concentration (1%). Therefore, it was suggested that an optimum fibre volume concentration around 1% (vol.) should be used (less than 2 vol. percent).

Two types of hooked-end steel fibres were used in fibre reinforced concrete by Cachim et al. (2002), and their fatigue behaviour was investigated and compared under compression. The fatigue life of specimens with short fibres (30 mm length) was observed to be slightly longer than that of plain concrete, whereas the fatigue life of specimens with longer fibres (60 mm length) was smaller than that of plain concrete. The main reason is related to the fact that the fatigue phenomenon is related to initial imperfections, such as micro-cracks or voids, existing in concrete. Thus, the presence of fibres, especially long ones, may be an additional cause of imperfections.

It was deduced that the addition of fibres may have a detrimental effect on the fatigue life of concrete, if the fibres are not well dispersed in concrete. In point of fact, the distribution of the fibres in concrete is the key to improve the fatigue life of concrete.

Through the study of the fatigue behaviour of high strength concrete (HSC) in compression, Kim and Kim (1996) observed that the total strain at the fatigue failure point approximately coincided with the strain of descending part in monotonic stress-strain curve. They found that the fatigue life decreased with increasing concrete strength. While fatigue strain of HSC was smaller than that of LSC, the rate of fatigue strain increment of HSC was greater than that of NSC. Therefore, HSC was more brittle than NSC under fatigue loading. Also, it was noticed that the fatigue crack growth rate increased with the strength of concrete. This trend was attributed to the rapid fatigue failure of higher strength concrete.

Cylindrical specimens made of NSC as well as HSC with and without steel (SFR) and carbon fibres (CFR) were tested and the fatigue crack growth in concrete with cyclic direct tension tests was examined by Cangiano et al. (1998).They detected that the effect of steel fibres was more obvious in HSC than in NSC and carbon fibres had less influence on N_{max} than steel fibres. It was concluded that the higher the percentage of fibre the higher the maximum number of cycles. This was attributed to the different levels of micro-cracking and fracture process zone formation.

The maximum number of load cycles measured on un-notched specimens was significantly larger than those for the notched normal strength concrete specimens. A possible reason for this discrepancy might be the notches causing stress concentrations and supporting the development of the FPZ.

The mechanical properties of concrete and their variations subjected to low cyclic loads were studied by Ballatore and Bocca (1997). It was deduced that as concrete subjected to uniaxial compressing loading, the concrete was seen to undergo strain hardening and an increase in stiffness due to effects of dynamic loading, as revealed by an increase in

the material's failure load and modulus of elasticity. It was thought that the dynamic loading reduced the pore space in the concrete, so that in the subsequent static compressive tests deformability was hindered by improved material compaction.

The experimental work of Naaman and Hammoud (1998) brought to light that the two mixes reinforced with 2% (vol.) hooked-end steel fibres, with aspect ratios of either 60 or 100, showed essentially similar behaviour under fatigue loading. This may imply that the influence of aspect ratio on fatigue life was not as significant as the volume fraction of fibres. However, a more realistic explanation is that, with hooked-end fibres, the fibre pull-out resistance after debonding is primarily controlled by the end hook and not by the fibre length.

Nicolaides (2004) found that achieving an even distribution of fibres in CARDIFRC is more difficult in specimens of (100*100*500mm) than in specimens of (360*90*35mm). This distribution of fibres within the matrix of the beam is a critical parameter affecting the fatigue performance of steel fibre reinforced concrete. Moreover, it was concluded that the endurance limit of CARDIFRC specimens of dimensions 360x90x35 mm is approximately at 85% of its flexural strength which is an excellent and absolutely consistent fatigue response.

These specimens were tested after the fatigue test in static three-point bending. The specimens tested at 80%, 85% and 90% Pu in fatigue, showed a small increase in their flexural strength. This result confirms previously noted results in the literature, that prior cycling may lead to an improvement in strength (Naaman and Hammoud, 1998). It was proposed that this increase is attributed to the densification of the material, caused by stress cycling.

It was found that CARDIFRC specimens that sustained low number of cycles had high value of initial compliance which indicates the existence of initial internal damage or a very weak plane (devoid of fibres) in the area of the maximum applied moment, leading to a large initial deformation.

On the other hand, at each load amplitude, the specimen that sustained high number of cycles had a low value of initial compliance, which indicates that for particular specimen which had a substantial number of fibres in the area of the maximum applied moment, leading to a small initial deformation. Therefore, a rough estimate of the total fatigue life of the particular specimen can be used to obtain from the compliance method, only after a relatively small number of cycles.

Parvez and Foster (2014) reported the results of an experimental study on the performance of SFRC beams tested in fatigue using four-point bend test. Two series of reinforced concrete beams, 1200 and 3000 mm for span, with variable fibre contents (0.4%, 0.8%) were tested under constant amplitude cyclic loading. The load ranges were 20–74% and 20–70% of static failure load for series 1 and series 2, respectively. It was deduced that the SFRC beams had lower deflections and smaller crack widths over the full period of cyclic loading compared to that of the control specimens. SFRC beams with span (3000mm) containing 0.4 and 0.8% of fibre by volume at a stress level of 0.7 showed an increased fatigue life of 47 and 182%, respectively, compared to that of non-fibre reinforced beams. They stated that the improved fatigue life results due to using steel fibres is because of their ability to reduce the stress range in the reinforcing bar.

Since the tensile behaviour of UHPFRC depends on fibre orientation and distribution, Makita and Brühwiler (2013b) proposed that steel rebars could be arranged in UHPFRC, subsequently called R-UHPFRC, to provide a significant increase in

resistance and improvement of structural behaviour for UHPFRC. Also, due to fibre orientation and distribution, the alteration in tensile behaviour of UHPFRC is reduced when steel rebars are added.

It was deduced that the maximum fatigue force level and the stage of the fatigue test influence the fatigue resistance of R-UHPFRC. Furthermore, the fatigue capacity of both material components could be enhanced by the stress distribution and transfer between UHPFRC and steel rebars. Fatigue deformation behaviour of R-UHPFRC depends on the stage of the fatigue test. In the early stage of the fatigue test, UHPFRC mainly determines the fatigue behaviour of R-UHPFRC. Whereas, in the middle and final stages of the fatigue test, steel rebars mostly determine the fatigue behaviour of R-UHPFRC.

Ruiz et al. (2012) investigated the loading frequency effect on the fatigue compressive behaviour of a plain concrete and two types of FRCs. Four different loading frequencies were set as 4 Hz, 1 Hz, 0.25 Hz and 0.0625 Hz, respectively, and 85% of the compressive strength the maximum stress was applied on the specimen and the stress ratio was set constant as 0.3. The results illustrated that the number of cycles to failure decreases as the loading frequency decreasing. Furthermore, this decrease is more pronounced for plain concrete. However, the fibres can improve the fatigue behaviour significantly under low loading frequencies. Such trend can be attributed to the effectiveness of the fibres in bridging the cracks, and thus inhibiting crack extension during the load cycles.

4.3. Concluding Remarks

It is usually desirable to strengthen structures instead of rebuilding them. Over the years diverse structural strengthening/retrofitting techniques have been devised such as external bonding of steel plates, fibre reinforced plastic and the recently developed retrofitting with HPFRCCs.

As has been mentioned at the beginning of this chapter, although the technique of bonding steel plates to the external surfaces of reinforced concrete structures has become widely used in the world with its many advantages, corrosion is considered as one of the major deficiencies of this technique.

Thus, several techniques have been developed to alleviate the corrosion issue. FRP composites were proposed among other materials as an alternative to steel plates thanks to their non-corrosive nature. In addition, their high mechanical strength and low weight, ease of handling, good fatigue resistance, and flexibility of size, shape or quality make FRP one of the promising materials to strengthen and retrofit concrete structures. However, concrete peel-off and delamination of FRP strip from the concrete surface are the most widespread and undesirable failure modes since FRP plate would not be fully utilized.

UHPFRC is particularly suitable for retrofitting structural elements by waterproofing them, thereby extending lifespan and enhancing durability. Furthermore, the brittleness of concrete has been overcome via addition of fibres into the cementitious matrix, thus leading to exceptional mechanical and durability features. A gradual failure without delamination can be ensured when UHPFRC (such as CRDIFRC) is retrofitted to concrete since compatibility with the material of the parent member can be achieved.

Therefore, bonding RC beams with CARDIFRC strips can increase the flexural and shear capacity by bonding the strips on the appropriate surface.

The outstanding features of UHPFRC, lower self-weight than steel plate, non-corrodible behaviour, smaller carbon footprint have the potential to make UHPFRC a desirable material for retrofitting. However, they are very expensive and therefore not industrially competitive. There is thus a need to create industrially competitive version of CARDIFRC. This will be attempted in present thesis.

Chapter Five

Mechanical and Fracture Properties of a Self-Compacting Version of CARDIFRC Mix II

5.1 Introduction

Conventional concrete irrespective of its compressive strength has poor tensile and flexural properties and cracks easily (has low toughness), impairing its long-term durability. Attempts have been made in the past, based on ad hoc trial and error tests, to improve the tensile/flexural strengths but this has been accompanied by a reduction in the toughness. The root cause of the intrinsic competition between the strength and toughness is explained by the non-linear theory of fracture of Hillerborg et al. (1976). According to this theory the measure of the ductility of a plain or fibre-reinforced concrete mix is its characteristic length (Bache, 1981; Karihaloo, 1995) $l_{ch} = (EG_F)/(f_t)^2$, where f_t is the tensile strength, G_F the toughness and E the Young modulus of the mix. The maximization of l_{ch} of an FRC mix by trial and error enabled researchers to develop a class of ultra-high performance fibre-reinforced cement-based composites (UHPFRC), such as DENSIT (Bache, 1981), RPC and DUCTAL (Bonneau et al., 1996; Bonneau, 1997; Morin et al., 2001) characterised by high compressive strength, high tensile/flexural strength, and high toughness.

In the development of CARDIFRC, which also belongs to the class of UHPFRC, the optimization problem of maximizing l_{ch} was solved mathematically. This required a knowledge of the constitutive equations relating the mechanical response parameters (E, f_t, G_F, and compressive strength f_c) to the mix and fibre parameters (water to binder ratio, maximum size of fine aggregate, volume fraction of aggregate, surfactant to water ratio, fibre length, fibre diameter, and fibre volume fraction), collectively called the micro-structural parameters. These were developed by Karihaloo et al. (1996) using micro-mechanical principles. The constitutive relations formed the constraints in the

optimization problem (Lang-Kornbak and Karihaloo, 1996). The method of its production and its mechanical and fracture properties were reported in a series of papers (Benson and Karihaloo, 2005 a,b; Benson et al., 2005). Extensive tests have shown that it has remarkable durability and resistance to thermal cycling and cyclic loading (Farhat et al., 2007; Nicolaides et al., 2010). Computerized tomography imaging and sectioning of specimens have confirmed that the production procedures ensure a remarkably homogeneous mix with a uniform distribution of fibres (Benson et al., 2005).

Moreover, it improves with age and has self-healing properties because of un-hydrated cement and silica fume. Tests have shown that its toughness increased in 2 years from 20,000 J/m^2 to more than 32,000 J/m^2 (Nicolaides, 2004). Recent studies (Petrov et al., 2012; Bragov et al., 2013) have proved that CARDIFRC is very resistant to dynamic loading making it suitable for building critical civil (e.g. nuclear containment vessels) and military infrastructure in order to render it less susceptible to failure under loading by blasts and explosions.

There has been enormous interest in the development of different UHPFRC variants in recent years. The developments until 2007 have been included in the monograph of Bentur and Mindess (2007). More recent developments have been reported at the quadrennial RILEM workshops organised by Naaman and Reinhardt, the most recent one being held in Stuttgart in 2015 (Reinhardt et al., 2015). In fact, the understanding of the manufacture and testing of UHPFRC has progressed to a state that it can be distilled and simplified for the purposes of engineering design practice. This has resulted in the FIB Model Code 2010. In the terminology of FIB Model Code 2010, CARDIFRC, together with DENSIT, RPC, and DUCTAL, belongs to the class of UHPFRC that exhibits strain hardening under axial tension. However, the rapid

development of UHPFRC has not been matched by its industrial uptake. This is not only because of the traditional conservativeness of the construction industry, but also because of the high cost of UHPFRC. Therefore, there is enormous scope for improving the cost-competitiveness of existing UHPFRC.

This Chapter describes an attempt at improving the cost-competitiveness of CARDIFRC. It summarises the steps taken to produce an industrially competitive version of CARDIFRC. The full mechanical characterisation of the resulting UHPFRC has been provided using standard testing procedures. The fracture properties however were obtained using non-standard procedures which made it necessary to provide a brief theoretical background of these procedures.

5.2 Development of Self-Compacting UHPFRC from CARDIFRC Mix II

CARDIFRC refers to two main groups of mixes – Mixes I and II – differing primarily in the maximum size of quartz sand used. Both mixes use a large amount of 6 and 13 mm long (0.15 mm diameter) brass-coated steel fibres (total volume fraction 6%). Mix I contains quartz sand up to only 0.6 mm in size, whereas in Mix II the maximum quartz sand size is 2mm. They were initially developed only for small scale niche applications, e.g. retrofitting of existing concrete structures (Farhat et al., 2007; Karihaloo et al., 2002; Alaee and Karihaloo, 2003a) or jointing of pre-cast concrete elements because of the very high cost of thin brass-coated steel fibres. However, detailed cost analysis in collaboration with a large construction company showed that CARDIFRC can be modified and adapted to make it highly competitive even in a variety of hitherto-unforeseen very large volume applications, e.g. manufacturing pre-cast pre-stressed concrete elements without shear reinforcement for use in structural applications. The

advantage of this variant over the competing steel is lower self-weight (which forms a large part of design load), corrosion resistance, and smaller carbon footprint. The development of industrially competitive versions of CARDIFRC in the category of ultra-high performance concrete (UHPFRC) required innovative solutions to many problems. Among these were: (i) reduction of costs by replacing the thin expensive brass-coated steel fibres with only 2.5% by volume of thicker and cheaper steel fibres, 30mm long and 0.55 mm diameter, with an acceptable reduction in the compressive and flexural strengths (about 30%) but an actual increase (by about 100%) in the toughness; (ii) avoidance of health and environmental hazards by creating self-compacting mixes not requiring noisy vibration and replacing some cement with an industrial waste material, GGBS; (iii) improvement in the fire resistance to 120 min by using sacrificial polymeric fibres that melt creating channels for the expansion of steam during a fire (Karihaloo, 2012a). The enhanced durability of UHPFRC leads to a longer life and sustainability thereby avoiding structural repair and maintenance costs, and yielding economic, environmental and social benefits. These solutions were first tried on CARDIFRC Mix I (Karihaloo, 2012a). Additional information on the role of fibre content and water to binder ratio on the performance of CARDIFRC Mix I can be found in (Karihaloo, 2012b). Apart from its compressive strength (160MPa), no other mechanical and fracture properties of this UHPFRC were measured. In this Chapter, these solutions will be tried on CARDIFRC Mix II. Full mechanical and fracture characterisation of the resulting UHPFRC will be provided. The bulk of the work reported in this Chapter has been published (Al-Azzawi and Karihaloo, 2017a).

5.3 Materials

All constituents used in UHPFRC based on CARDIFRC Mix II were locally available. These included Portland cement Class I 42.5 N, ground-granulated blast furnace slag (GGBS), various grades of quartz sand, Glenium Ace 499 superplasticizer, Elkem Microsilica powder, and 55/30 BG Dramix steel fibres with crimped ends (30 mm long and 0.55 mm diameter, aspect ratio 55). No sacrificial polymeric fibres for enhanced fire resistance were used in this mix. In common with the development of self-compacting mixes from parent vibrated mixes, the powder volume was substantially increased while simultaneously the amount of coarser ingredients was slightly decreased. Thus, 36.4% of cement in the original CARDIFRC Mix II was replaced with GGBS to increase the powder volume and reduce the carbon footprint, while the total amount of quartz sands was reduced by 4.8%. The larger powder content in the self-compacting version required a higher dosage of superplasticizer for attaining the necessary flow-ability (SP/water 0.41 as opposed of 0.37 in the original vibrated CARDIFRC Mix II). The mix proportions are given in table 5.1. For comparison, the mix proportions of the original vibrated CARDIFRC Mix II are shown in parenthesis in the table.

5.3.1 Self-Compacting Mix Preparation

The mix was prepared in a pan mixer. The volume of a batch was calculated based on the required cube, cylinder and beam test specimens with an allowance for at least four slump flow tests and for some wastage. The mixing procedure recommended by Benson and Karihaloo (Benson and Karihaloo, 2005a) was followed by adding the finest constituent micro-silica to the coarsest (1-2 mm quartz sand) and mixing them for two minutes. This was followed by the addition of the next coarsest constituent

(0.212 - 1 mm quartz sand) and the next finest constituent (GGBS) and mixing for a further two minutes. Finally, the next coarsest constituent (9-300 μm quartz sand) and the next finest (cement) were added and mixed for a further two minutes. The dry mix was fluidised by a mixture of water and two-thirds of the total superplasticizer (the same amount as in the original CARDIFRC Mix II) in several steps as follows: One-half of the water-superplasticizer mixture was added to the dry mix and mixed for two minutes, followed by one-half of the remaining mixture and mixing. This process of progressive halving of the fluid mixture and mixing was continued until the entire fluid mixture was added. Then the 30 mm long fibres were added. These fibres are supplied by the manufacturer in small packages of about 50 fibres lightly glued together by water-soluble glue. They were scattered slowly and evenly into the rotating pan mixer by hand to avoid their clumping in the mix. Lastly, the remaining one-third of the superplasticizer was added and mixed for two minutes.

Table 5.1 Mix constituents of the self-compacting UHPFRC version of CARDIFRC Mix II (kg/m^3)

Constituent	Dosage (kg/m^3)
Cement	450.3 (744)
Silica fume	169.5 (178)
GGBS	258.0 (0)
Quartz sand:	
9-300μm	158.0 (166)
0.212-1 mm	318.9 (335)
1-2 mm	639.7 (672)
Water	141.8 (149)
Superplasticizer (SP)	58.5 (55)
Fibres: 30 mm Dramix (Vol. 2.5%)	195.0
Water/(Cement+GGBS)	0.20 (0.20)
Water/binder	0.16 (0.16)
SP/water	0.41 (0.37)
Slump flow spread (mm)	705
t_{500} (s)	2.73

5.3.2 Slump Flow Test

Before transferring the wet fibre-reinforced mix into the slump cone, the mix was visually inspected to estimate its flow-ability. If it appeared to be stiff, additional superplasticiser was added and mixed again for 2 minutes. It was then transferred into the slump cone and the test was performed according to BS EN 12350-8, 2010. If it did not meet the flow-ability criterion, namely that the time to reach the flow diameter of 500 mm (t_{500}) is less than 3 s, additional superplasticizer was added to the remaining mix in the pan mixer, and the test repeated. This time was chosen somewhat arbitrarily to be near the boundary, $t_{500} \leq 2$ s, between the two viscosity classes (VS1 and VS2) according to BS EN 206-9 2010. Two to three trials were needed to meet the flow-ability criterion. The slump flow spread of the self-compacting mix that met the target t_{500} is shown in Figure 5.1. The mix proportions of the UHPFRC based on CARDIFRC Mix II are given in Table 5.1.

Figure 5.1 Slump flow spread of UHPFRC based on CARDIFRC Mix II

5.3.3 Specimen Curing

The mix was then cast into standard cube (100 mm), cylinder (100 × 200 mm) and beam (100 × 100 × 500 mm) moulds. The specimens were de-moulded after 24 hours and placed in a water tank. The water was heated slowly to 90^{o}C in 24 hours to avoid thermal shock, and the specimens were cured at this elevated temperature for 7 days. The temperature was then reduced gradually to ambient condition within 24 hours. The specimens were taken out of the water tank and air dried prior to testing. It should however be noted that tests have shown (Karihaloo et al., 2002) that mixes can also be cured in water at ambient temperature for 28 days with no noticeable difference in the mechanical properties.

5.3Mechanical properties

5..4.1 Compressive strength

For the determination of the compressive strength of CARDIFRC Mix II, cubes were tested according to BS EN 12390-3, 2009. The tests were performed in a FARNELL Compression Testing Machine, with a load capacity of 2500 kN. The compressive strength for the UHPFRC CARDIFRC Mix II is f_c = 148 MPa with standard deviation of 6.7 MPa and coefficient of variation of 4.54%. The results of the test are tabulated in Table 5.2.

Table 5.2 Compressive strength results for UHPFRC CARDIFRC Mix II

Cub No.	Compressive Strength (MPa)
1	136.7
2	142.1
3	155.2
4	147.5
5	154.9
6	150.8
7	148.5
Mean f_c	148.0

5.4.2 Tensile splitting strength

The indirect tensile strength f_t of the UHPFRC CARDIFRC Mix II was determined according to BS EN 12390-6, 2009. The tests were performed also using a FARNELL Compressive Test Machine. Four 100 x 200 mm cylinder specimens were tested and the splitting strength (in MPa) was calculated for each specimen according to

$$f_t = \frac{2F}{\pi DL} \tag{5.1}$$

where F is the maximum failure load in (N), L is the length of the cylinder in (mm) and D is the diameter of the cylinder in (mm).

The tensile splitting strength is 18.5 MPa with standard of deviation of 1.2 MPa and coefficient of variation of 6.5%. The results of the test are tabulated in Table 5.3.

Table 5.3 Indirect Tensile splitting Strength results for UHPFRC CARDIFRC Mix II

Cylinder No.	Applied Load (kN)	Indirect Tensile splitting Strength (MPa)
1	643	20.47
2	565	17.99
3	566	18.02
4	570	18.14
	Mean f_t	18.5

5.4.3 Modulus of Elasticity

The modulus of elasticity of the UHPFRC CARDIFRC Mix II was measured on a cylindrical specimen according to BS 1881-121, 1983 at room temperature. The specimen was chosen at random taken from the group of specimens intended for tensile splitting test. An AVERY DENISON Type 7152, Servo-Hydraulic Testing Machine was used for the test, with a load capacity of 600 kN. Two strain gauges, 30 mm long, were glued to carefully prepared surface of the cylinder preparation for the measurement of strain. The specimen was loaded up to one third of their compressive strength and then unloaded. The loading-unloading procedure was repeated twice. The modulus of elasticity was calculated from the slope of the recorded stress-strain curves. The value is 45.2 GPa.

5.4.4 Modulus of Rupture (MOR)

The measurement of the modulus of rupture of the mix of UHPFRC CARDIFRC Mix II was carried on two 100x100x500 mm beams according to BS 1881-118, 1983, in 4-point bending (Figure 5.2). The test was performed in an AVERY-DENISON Type 7152, Servo-Hydraulic Testing Machine, with a load capacity of 600 kN. The MOR (MPa) is calculated as follows:

$$MOR = F.L/(d_1.{d_2}^2) \quad (5.2)$$

where F is the maximum failure load in (N), $d_1$and d_2 are the lateral dimensions of the cross section in mm and L is the distance between supporting rollers in mm. The MOR is 20.04 MPa with standard of deviation of 0.15 MPa and coefficient of variation of 0.72%. The results of the test are tabulated in Table 5.4.

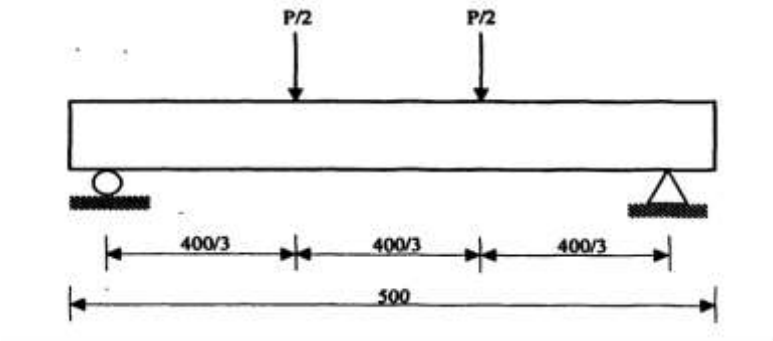

Figure 5.2 Schematic graph of the modulus of rupture (MOR) test.

Table 5.4 MOR results for UHPFRC CARDIFRC Mix II

Beam No.	Peak Load (kN)	MOR (MPa)
1	49.83	19.93
2	50.35	20.14
	Mean MOR	20.04

As expected, the compressive strength, the tensile splitting strength and the modulus of rupture of the UHPFRC are inferior to those of the CARDIFRC Mix II (Benson and Karihaloo, 2005b) because of the absence of thin short (6mm) brass-coated steel fibres (4.5% by volume). The modulus of elasticity, on the other hand, is only marginally reduced.

5.5 Fracture Properties

5.5.1 Specific Fracture Energy – Theoretical Background

Not only the superior mechanical properties of UHPFRC (Table 5.2 - 5.4) are of practical interest, but even more important is their superior fracture resistance. It is quantified by the energy consumed per unit area of crack surface, also called the specific fracture energy. No standard test exists for its measurement, but RILEM-50FMC 1985

has recommended a method based on the work-of-fracture, i.e. the area under the load-mid-span deflection curve of a notched beam loaded in three-point bending. According to the RILEM recommendation, the specific fracture energy G_f is the average energy given by dividing the total work-of-fracture by the projected fracture area (i.e. the area of initially un-cracked ligament) using a pre-cracked (notched) specimen.

This method is equally applicable to UHPFRC, despite the fact that the test may have to be terminated before the the tail part of the load-deflection plot has been registered, i.e. the specimen has completely fractured, because the fibre bridging provides substantial residual load bearing capacity up to very large crack openings. In this situation, the work-of-fracture is corrected using the procedure of Elices et al. (1992). Alternatively, the area under the load-deflection curve up to particular deflection levels may be expressed as a multiple of the area up to the limit of proportionality to determine the so-called toughness indices of UHPFRC, designated I_5, I_{10}, etc. where the subscript denotes the multiple of the area. A detailed review of the many variations of toughness index approach can be found in Bentur and Mindess (2007).

A commonly used specimen shape for the determination of G_f is a notched beam loaded in three-point bending (Figure 5.3). The specimen is loaded under displacement control and the variation of the load P is recorded against the mid-span deflection δ. The specific fracture energy G_f is then calculated using the formula:

$$G_f = \frac{1}{(W-a)\,B} \int P \, d\delta \tag{5.3}$$

Here, W, B and a the specimen depth, width and the notch depth, respectively.

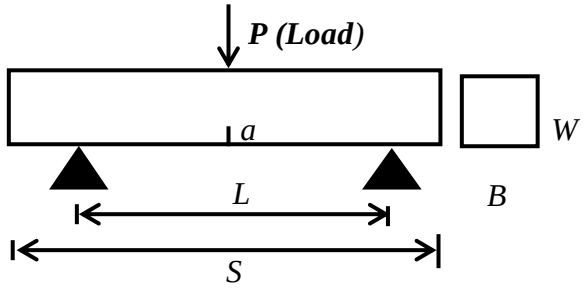

Figure 5.3 Notched Three-point bend testing configuration and geometry of specimen

In the case that the concrete fracture is modelled by a fictitious crack (Hillerborg, 1985), the energy dissipation for the crack propagation can be described by the cohesive stress-crack opening relation σ(w). More precisely, the specific fracture energy corresponds to the area under the σ(w) curve

$$G_F = \int_0^{w_c} \sigma(w)dw \tag{5.4}$$

where w_c is the critical crack opening.

Two regions, an inner softening zone, w_{sf}, and an outer micro-fracture zone w_f, form the fracture process zone (FPZ) around the propagating crack, (Hu and Wittmann, 1992) as illustrated in Figure 5.4.

The interconnected cracks are included in the inner softening zone w_{sf} along the aggregate and mortar interfaces. On the other hand, the outer micro-fracture zone contains isolated micro-cracks that are not interconnected. The main open crack plus a few large crack branches along the interfaces can be formed within the softening zone (Karihaloo B.L, 1995; Hu X. Z, 1995). The fracture energy consumed in the outer micro-fracture zone is small because the isolated micro-cracks do not participate in the concrete softening but to its non-linear response before the peak load.

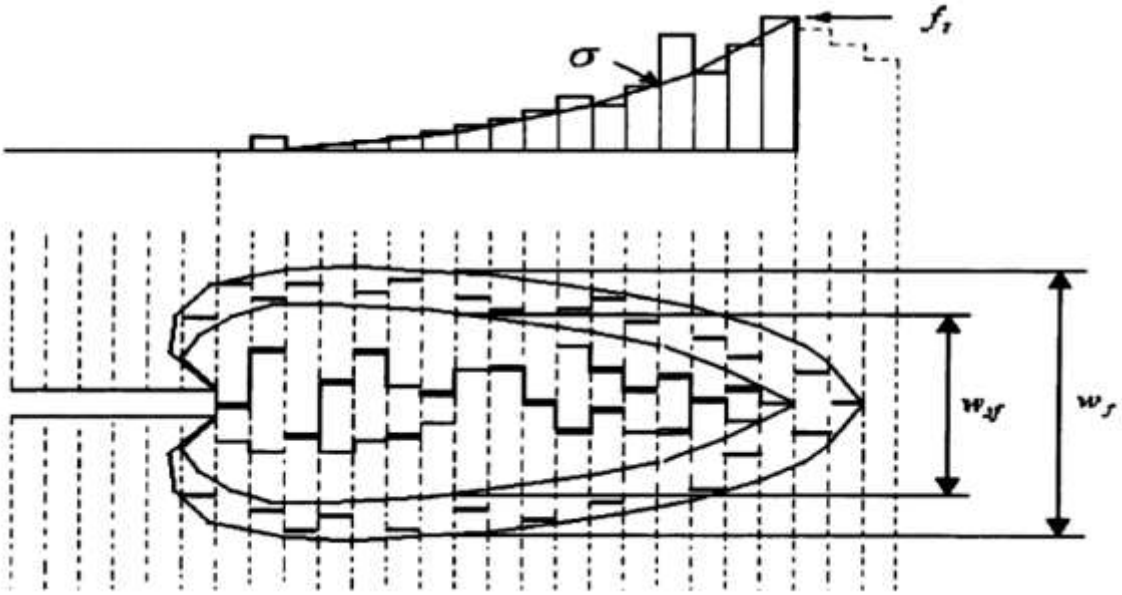

Figure 5.4 The fracture process zone and discreet bridging stresses. The FPZ is divided into the inner softening zone and the outer micro-fracture zone. wc is related to the width of the inner softening zone wsf (After Hu and Wittmann, 1992).

It was argued that the inner and outer zone width w_{sf} and w_f, may vary according to the crack tip stress field during crack propagation. Apparently the critical crack opening w_c is confined by the inner and the outer zone width. This confinement becomes more obvious when a FPZ approaches the free boundary of a specimen. Therefore, if equation (5.4) is used, a smaller w_c and a smaller fracture energy are found. This lead to the conclusion that the fracture energy G_F defined by equation (5.4) can be dependent on the location of FPZ in relation to the free boundary of the specimen.

The symbol g_f was used in equation (5.4) for the local fracture energy to differentiate the fracture energy G_F defined by equation (5.4) from that defined by equation (5.3).

Hu (1995), and Hu and Wittmann (2000) have made the following assumptions:

$$w_{sf}(x) \propto w_f(x)$$
$$w_c(x) \propto w_f(x) \qquad (5.5)$$
$$g_f(x) \propto w_c(x)$$

where *x* denotes a position along a fracture ligament in the FPZ and g_f (x) represents the local fracture energy.

The specific fracture energy, G_f, is known to vary with the size and shape of the test specimen. The cause of this variability is explained in Hu and Wittman (1992), namely that the local specific fracture energy is not constant along the crack path in a test specimen. It decreases as the crack grows along the un-notched ligament with the rate of decrease picking up speed as the crack approaches the back, stress-free boundary of the specimen. For this reason, the Hu-Wittmann model is also called the boundary effect model (Duan et al., 2003; Duan et al., 2007). They proposed a bi-linear approximation for the local fracture energy variation (g_f) along the crack path (Figure 5.5) with the intersection of the two asymptotes defining a transition ligament size (a_l) and used this approximation to derive relations between the measured size-dependent fracture energy (G_f), the transition length (a_l) and the size-independent fracture energy (G_F). The transition ligament size a_l is a parameter depending on both the material properties and specimen geometry.

$$G_f\left(\frac{a}{W}\right) = \begin{cases} G_F\left[1 - \frac{\frac{a_l}{W}}{2(1-\frac{a}{W})}\right] & 1 - \frac{a}{W} > \frac{a_l}{W} \\ G_F\left[\frac{(1-\frac{a}{W})}{2\frac{a_l}{W}}\right] & 1 - \frac{a}{W} \leq \frac{a_l}{W} \end{cases} \quad (5.6)$$

The values of G_F and a_l of a concrete mix are obtained from these relations once the size-dependent specific fracture energy (G_f) of the mix has been measured on specimens of different sizes and several notch to depth ratios using a least squares method on the over-determined system of equations. However, a simplification of this boundary effect

method was proposed in Abdalla and Karihaloo (2003), requiring only testing of notched beam specimens of identical size (beam height *W*, notch depth *a*) by the RILEM work-of-fracture method. One half of the specimens have a shallow starter notch (*a/W* = 0.1), while the other half have a deep starter notch (*a/W* = 0.6), straddling the expected transition length ratio a_l/W. This simplification reduces the number of test specimens and avoids the use of least squares minimisation. It was validated by Karihaloo et al. (2003a) on a series of available test results. It has been shown in Hu and Duan (2004) that although the measured values of G_f depend on *W* and *a/ W*, the above procedure indeed leads to a value of G_F that is essentially independent of the specimen size and relative notch depth.

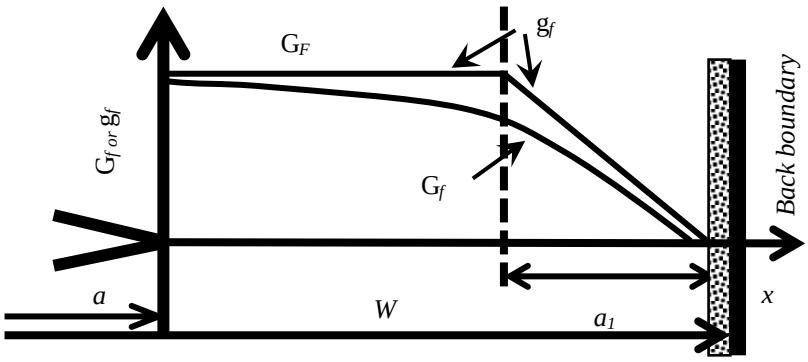

Figure 5.5 Bi-linear local fracture energy $G_f\left(\frac{a}{W}\right)$ variation along the un-notched ligament of a notched specimen (After Duan et al., 2003)

In recent works, a tri-linear approximation of the local fracture energy along the unbroken ligament was proposed by Muralidhara et al. (2010; 2011) and Karihaloo et al. (2013). As has been shown by acoustic emission data, the tri-linear approximation is closer to how the local fracture energy varies as the crack grows from a notched specimen (Muralidhara et al., 2010). The local fracture energy (G_f) first rises from the

fictitious boundary (notch tip), then remains nearly constant G_F, before reducing again as the crack approaches the stress-free back face boundary, Figure 5.6. Murthy et al. (2013) found that the bi-linear and tri-linear approximations result in nearly the same values of the size-independent specific fracture energy (G_F). For this reason, the simplified boundary effect method of Abdalla and Karihaloo (2003) based on the bi-linear approximation of Hu and Wittmann (1992) will be used below.

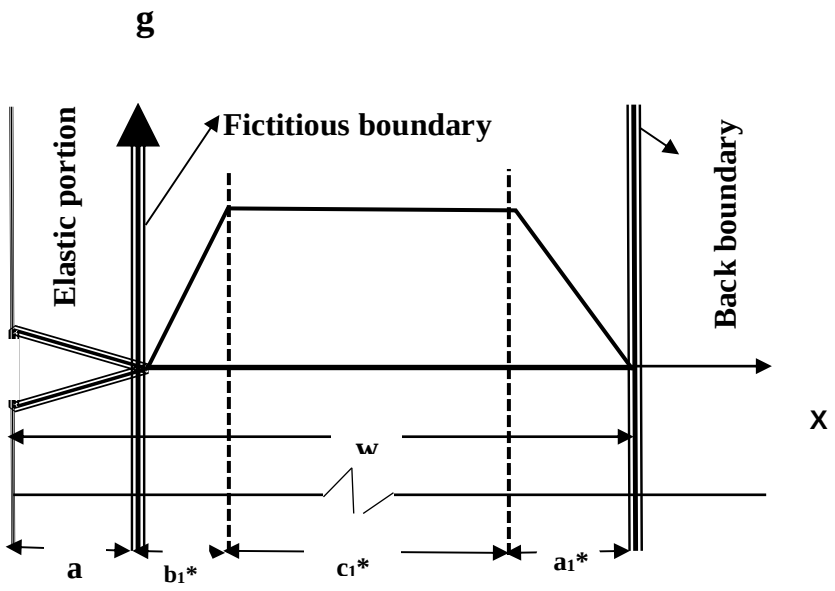

Figure 5.6 Tri-linear approximation of local fracture energy gf variation over the un-notched ligament length (After Muralidhara et al., 2010)

5.5.2 Test Results

Six prisms 100 x 100 x 500 mm were cast with the self-compacting UHPFRC. After curing, three prisms were notched to a depth of 10 mm and the remaining three to a depth of 60 mm using a diamond saw (width approximately 2 mm). They were tested in three-point bending over a loaded span of 400 mm.

The tests were performed in a stiff self-straining testing frame, fitted with a DARTEC 2500 kN dynamic-static actuator. The machine was powered by a 23 lit/min DARTEC hydraulic pump and was connected with a DARTEC 9600 Digital Feedback Controller.

Three types of measurement were recorded for each beam: (1) the load from the load cell of the testing machine; (2) the vertical deflection at one side of the specimen; and (3) the crack mouth opening displacement (CMOD), using a clip gauge (Figure 5.7).

The test was controlled first by a feedback signal from a crack mouth opening displacement (CMOD) gauge until the gauge reached its limit (around 3.5 mm), whereafter the control switched to mid-point displacement control. The load-CMOD was recorded until the gauge reached its limit, but the load-mid-point displacement continued to be recorded until the displacement reached 30 mm. The load had still not dropped to zero. The area under the load-deflection plot was therefore corrected to account for the unrecorded work-of-fracture using the procedure of Elices et al. (1992). For this the tail part of the recorded load-deflection curve was extended linearly until it met the horizontal axis (P = 0). The area of this triangle added to the area under the recorded curve. The total work-of-fracture was divided by the projected fracture area (i.e. area of initially un-cracked ligament) of the notched specimen to calculate the specific fracture energy $G_f\,(a/W)$ corresponding to a/W = 0.1 and 0.6. Finally, the size-independent specific fracture energy G_F and a_l were determined using the appropriate

relations of boundary effect model (Hu and Wittmann, 1992) (Equation 5.6). The values are reported in Table 5.5 and the load-deflection curves for both 10 and 60 mm notches are plotted in Figure 5.8. The size-independent specific fracture energy is 36300 N/m compared to about 20000 N/m for the original Mix II measured in axial tension. The increase in primarily due to the use of a larger volume (2.5%) of longer (30 mm) fibres in the UHPFRC compared with the CARDIFRC Mix II in which only 1.5% by volume of 13 mm long fibres was used.

Figure 5.7 Three-point testing configuration.

Table 5.5 Mean size-dependent fracture energies for a/W = 0.1 and 0.6 and size-independent specific fracture energy of UHPFRC version of CARDIFRC Mix II (bi-linear model)

Notch (mm)	G_f (N/m)	Mean G_f (N/m)	a_l (mm)	G_F (N/m)
10	29395.03 28903.98 32180.74	30192.00	30.3	36300
60	23009.37 23046.87 21596.64	22550.96		

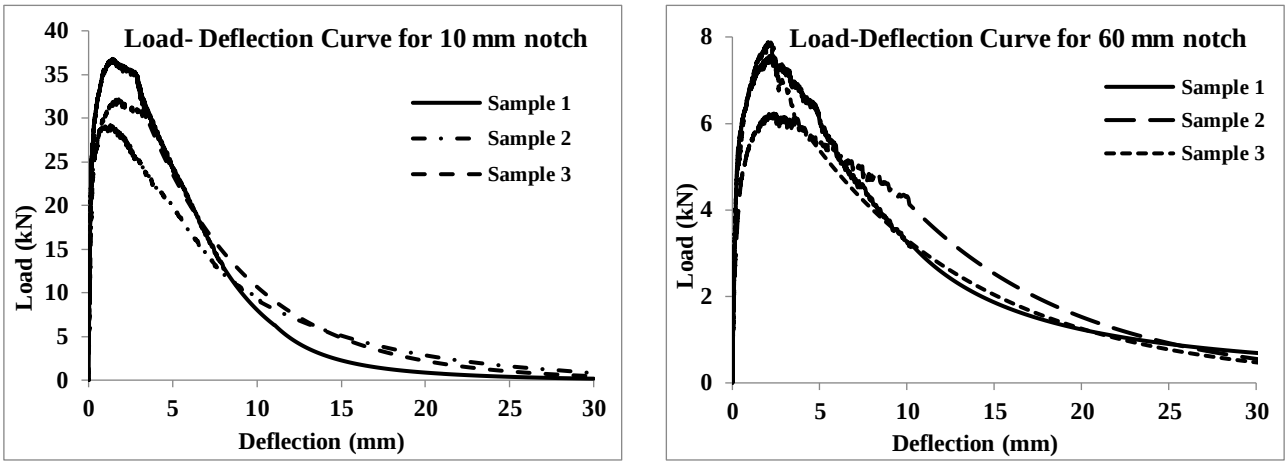

Figure 5.8 3-point bend test curves for UHPFRC CARDIFRC mixes II, notches 10 and 60 mm

5.5.3 Stress-Crack Opening Relation – Theoretical Background

The analysis of cracked concrete structures using the fictitious crack model (Hillerborg et al., 1976; Hillerborg, 1980) requires not just the size-independent fracture energy of the concrete G_F, but also its softening behaviour. In the fictitious crack model (FCM) it is assumed that after crack initiation, stresses may be transmitted across the fictitious crack faces. These crack bridging forces are assumed to be a function of the crack opening displacement given by the stress-crack opening relationship. The stress-crack opening relationship of the early FCM was modelled as a linear function which has been found not to capture the essence of the tension softening of concrete. After the initiation of a crack, concrete is known to soften rapidly because of micro-cracking, but the rate decreases thereafter because of aggregate interlock and other frictional processes, and especially fibre bridging forces. Therefore, to capture the observed tensile/flexural behaviour of fibre-reinforced concrete, the stress-crack opening relationship must be at least a bi-linear function (Olesen, 2001). The area under this bi-linear diagram is equal to G_F.

Ulfkjaer et al. (1995) proposed that the flexural failure of concrete beams may be modelled by the development of a fictitious crack in a central segment with a width proportional to the beam depth. They treated this segment as a cracked hinge (Figure 5.9) with a linear stress-crack opening relationship.

The bending failure was modelled (Olesen, 2001) in the same way, using a bi-linear stress-crack opening relationship instead. The isolation of the segment of a beam near the propagating crack and its modelling as a short beam segment subjected to a bending moment and a normal force is the basic concept of the non-linear cracked hinge model (Olesen, 2001), (Figure 5.9-a,b). This is a generic model applicable to both plain and fibre-reinforced concrete.

In the non-linear hinge model the crack is viewed as a local change in the overall stress and strain field. This change is assumed to vanish outside a certain band of width s (Figure. 5.9-a). Thus, outside of this band the structural element is modelled using the elastic beam theory.

The constitutive relationship for each segment inside the hinge is assumed to be linear elastic up to the peak load (phase 0), while the cracked state is approximated by a bi-linear softening curve as shown in Figure 5.10.

$$\sigma = \begin{cases} E\varepsilon & \text{Linear} - \text{elastic state} \\ \sigma(w) = g(w) f_t & \text{Post} - \text{peak cracked state} \end{cases} \tag{5.7}$$

Here, E is the elastic modulus, ε is the elastic strain, w is the crack opening, f_t is the uniaxial tensile strength; and $g(w)$ is the function representing the shape of the stress-crack opening relationship, normalized such that $g(0) = 1$

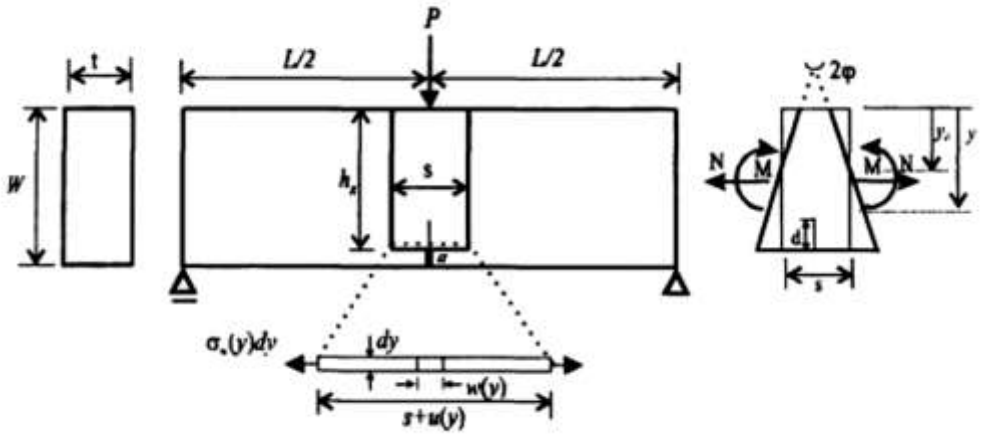

(a)

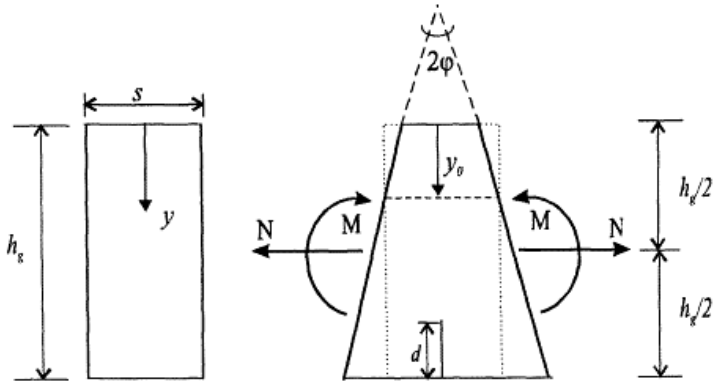

(b)

Figure 5.9 (a) Loading and geometry of cracked hinge model, (b) deformation of the cracked hinge

$$g(w) = b_i - a_i w = \begin{cases} b_1 - a_1 w & 0 \le w < w_1 \\ b_2 - a_2 w & w_1 \le w \le w_2 \end{cases} \quad (5.8)$$

where $b_1 = 1$, and the limits w_1 and w_2 are given by the intersection of the two line segments, and the intersection of the second line segment and the abscissa, respectively, $a_1$and a_2 represent the slopes of the first and the second line segments of the bilinear curve, respectively (Figure 5.10). For the assumed bilinear shape (Figure 5.10), we have:

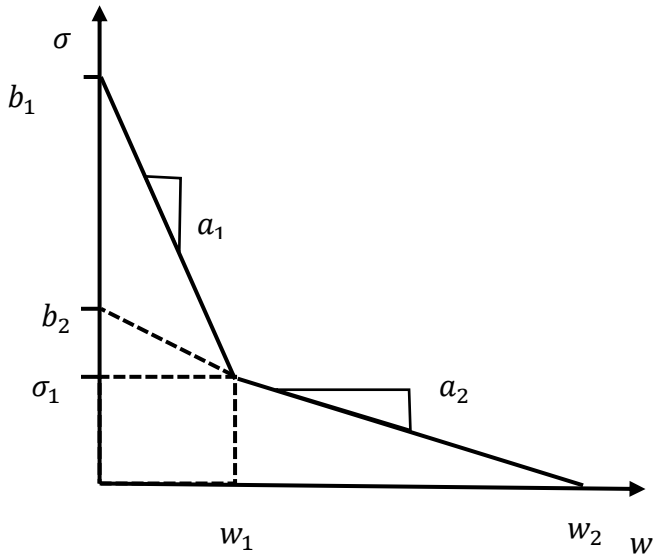

Figure 5.10 Bi-linear stress-crack opening diagram

$$w_1 = \frac{1-b_2}{a_1-a_2} \quad (5.9\text{ a})$$

$$w_2 = \frac{b_2}{a_2} \quad (5.9\text{ b})$$

The deformation of the hinge is described by half the angular deformation φ and the depth of the neutral incremental strip y_0 (Figures 5.9). The mean values of the curvature k^* and the distribution of longitudinal strains ε^* at a depth y are introduced as:

$$k^* = \frac{2\varphi}{s};\ \varepsilon^*(y) = 2(y - y_0)k^* \quad (5.10)$$

The deformation of an incremental strip is given by $u(y) = s\varepsilon^*(y)$, where s is the width of the hinge. In the case when the strip has cracked the deformation, $u(y)$ may also be obtained as the sum of the elastic deformation of the strip and the crack opening:

$$u(y) = s\varepsilon * (\ y) = s\frac{\sigma_w(w(y))}{E} + w(y) \tag{5.11}$$

The crack opening in the cracked incremental segment at the depth y,$w(y)$ has been introduced, and the associated crack bridging stress, $\sigma_w\big(w(y)\big) = f_t g\ \big(w(y)\big)$(Olesen, 2001) can be obtained by combining Equations (5.10) and (5.11):

$$\sigma_w\big(w(y)\big) = \frac{E}{s}\{2(y - y_0)\varphi - w(y)\} \tag{5.12}$$

By using Equation (5.8) it may also be written:

$$\sigma_w\big(w(y)\big) = f_t\{b_i - a_i w(y)\} \qquad i \in [1,2] \tag{5.13}$$

If Equations (5.12) and (5.13) are solved with respect to *w*(*y*) and $\sigma_w(w)$ for each value of *i*, the following solutions are obtained:

$$w(y) = \frac{2(y-y_0)\varphi-\varsigma_i}{1-\beta_i} \tag{5.14 a}$$

$$\sigma_w(\ w(y) = \frac{\varsigma_i- 2(y-y_0)\varphi\beta_i}{1-\beta_i}\frac{E}{S} \qquad i \in [1,2] \tag{5.14 b}$$

where the dimensionless parameters β_i and ς_i are defined by:

$$\beta_i = \frac{f_t s a_i}{E} \quad , \quad \varsigma_i = \frac{f_t s b_i}{E} \qquad i \in [1,2] \tag{5.15 a, b}$$

The solutions given in Equation (5.14) establish in an analytical form the crack opening profile *w*(*y*) and the stress distribution in the cracked part of the hinge $\sigma_w(w)$as functions of the hinge deformation φ and y_0. This fundamental result makes it possible to obtain closed-form solutions to the nonlinear constitutive behaviour of the cracked hinge as a whole. It is observed that the crack opening profile *w*(*y*) is linear

within each segment of the stress-crack opening relationship but the inclination with respect to the crack face is not the same in the two segments.

As a crack forms and then propagates from the bottom of the hinge, the stress distribution changes through three distinct phases (Figure 5.11). The crack-opening profile is divided into different intervals that are governed by the solutions in Equation (5.14) corresponding to different values of i. Besides y_0, these intervals are determined by the parameters y^*, y_1 and y_2 (Figure 5.11). An expression for y^* may be found from:

$$y^* = \frac{sf_t}{2\varphi E} \tag{5.16}$$

Expressions for y_1 and y_2 are obtained from Equation (5.14 a)

$$y_i = y_0 + \frac{1}{2\varphi}\left(\varsigma_i - (\beta_i - 1)\, w_i\right) \quad i \in [1,2] \tag{5.17}$$

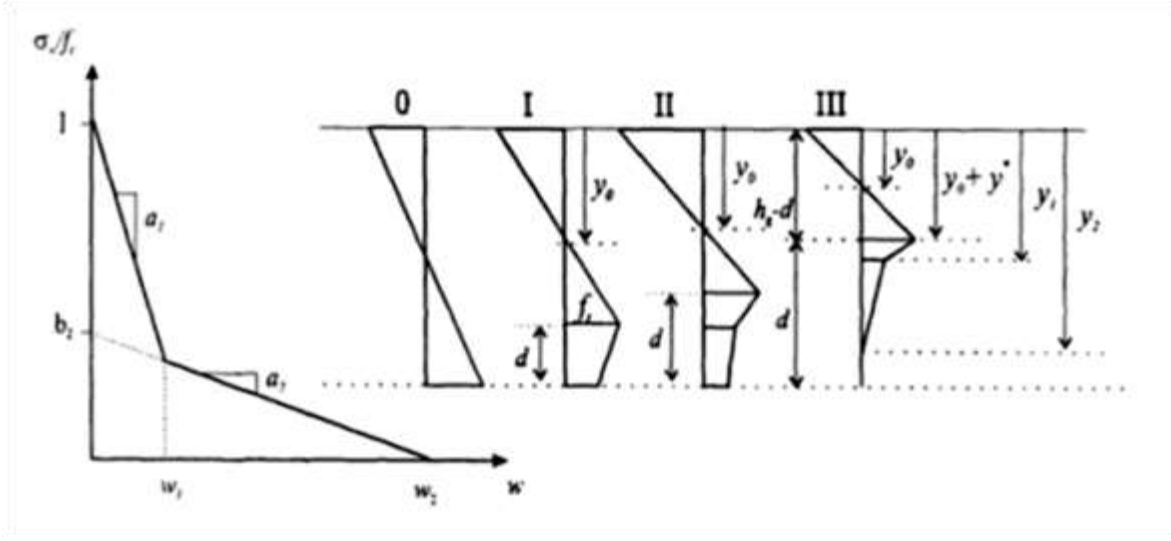

Figure 5.11 Definition of a bi-linear stress-crack opening relationship and the four different phases of crack propagation. Phase 0 = State of stress prior to cracking; Phases I-III = States of stress during crack propagation.

Analysis of the hinge element permits the determination of the external normal force *N* and bending moment *M* for any given value of the angular hinge deformation 2φ. The problem is solved in four phases, one for each state of crack propagation. Phase 0 represents the elastic state, where no crack has formed, while phases I, II and III represent different stages of propagation (linear, bilinear and bilinear with stress-free tail) (Figure 5.11). The solution is presented in terms of normalized properties, where the following normalizations are used (Olesen, 2001):

$$\mu = \frac{6}{f_t h^2 t} M; \quad \rho = \frac{1}{f_t h t} N; \quad \theta = \frac{hE}{s f_t} \varphi; \quad \alpha = \frac{d}{h} \qquad (5.18 \text{ a, b, c, d})$$

where t = width of the hinge in the direction normal to the paper; and d = depth of the fictitious crack, h and s are the height and width of the hinge, respectively (Figure 5.9a)

The hinge solution is expressed in terms of the normalized crack depth α and the normalized moment μ as functions of the normalized hinge deformation θ and the normalized normal force ρ.

The pre-peak elastic behaviour of the hinge is described by α_h =0 and μ = θ, where $0 \leq \theta \leq 1-\rho$, and where the onset of cracking is given by θ=1- ρ. The solutions covering each of the cracked Phases I, II, and III are given in Table 5.6

Table 5.6 The solution of cracked Phases I, II, and III.

Phase	α_h	μ	θ
I	$1-\beta_1-\sqrt{(1-\beta_1)\left(\frac{1}{\theta}-\beta_1\right)}$	$4\left(1-3\alpha_h+3{\alpha_h}^2-\frac{{\alpha_h}^3}{1-\beta_1}\right)\theta\ -3+6\alpha_h$	$\theta_{0-I}=1-\rho$
II	$1-\beta_2-\frac{1-b_2}{2\theta}-\sqrt{(1-\beta_2)\left(\frac{(1-b_2)^2}{4\theta^2(\beta_1-\beta_2)}-\beta_2+\frac{b_2}{\theta}\right)}$	$4\left(1-3\alpha_h+3{\alpha_h}^2-\frac{{\alpha_h}^3}{1-\beta_2}\right)\theta-3\ +6\alpha_h-\frac{(1-b_2)\left(3{\alpha_h}^2-\left(\frac{c}{2\theta}\right)^2\right)}{1-\beta_2}$	$\theta_{I-II}=\frac{1}{2}\left(1-\rho-c+\sqrt{(1-\rho-c)^2+\frac{c^2}{\beta_1-1}}\right)$
III	$1-\frac{1}{2\theta}\left(1+\sqrt{\frac{(1-b_2)^2}{\beta_1-\beta_2}+\frac{{b_2}^2}{\beta_2}}\right)$	$4\left(1-3\alpha_h+3{\alpha_h}^2-{\alpha_h}^3\right)\theta-3\ +6\alpha_h-3{\alpha_h}^2+\frac{1}{4\theta^2}\left(1-\frac{b_2}{\beta_2}\right)\left(1-\frac{b_2}{\beta_2}+c\right)\left(1+\frac{\beta_1 c}{1-\beta_1}\right)+\left(\frac{c}{2\theta}\right)^2$	$\theta_{II-III}=\frac{1}{2}\left(\rho(\beta_2-1)\ +\frac{b_2}{\beta_2}+\sqrt{\rho^2(\beta_2-1)^2+2\rho(\beta_2-1)\frac{b_2}{\beta_2}+\frac{(1-b_2)^2}{\beta_1-\beta_2}+\frac{b_2^2}{\beta_2}}\right)$

5.5.4 Three-Point Bend Beam Application

The three-point bend beam is a simply supported beam with a span length L, loaded at midspan by a transverse concentrated load of magnitude P. The nonlinear cracked hinge is incorporated into the notched beam at mid-span, and the load-deflection and load-CMOD relationships of the beam are established depending on the position of the fictitious crack along the depth of the beam.

The mid-span deflection, v, of the beam may be determined as the sum of the elastic beam deflection, v_e and the deflection due to the crack, v_c. The non-dimensional mid-span deflection, δ, is introduced by the normalisation

$$\delta = \frac{2v}{L}\,\frac{hE}{sf_t} = \frac{2v}{L}\,\frac{\theta}{\varphi} \tag{5.19}$$

where θ is the normalized angular hinge rotation φ (Figure 5.9b) (Equation 5.18c), L is the clear span, h and s are the height and width of the hinge, respectively as explained in the previous section. The normalised elastic deflection may be found from the normalised bending moment, which in turn is related to the normalised hinge rotation:

$$\delta_e = \frac{L}{3s}\,\mu(\theta) \tag{5.20}$$

where $\mu(\theta)$ is the normalized bending moment M at mid-span (Equation 5.18 a)

The deformation of the hinge is the sum of elastic deformation of the hinge and deformation due to the crack. The normalized deformation due to the crack only θ_c is found by subtracting the normalized elastic deformation θ_e from the total deformation of the hinge θ. The normalized elastic deformation of the hinge is given by $\theta_e = \mu(\theta)$. Now, since the normalized deflection due to hinge deformation is equal to the

normalized hinge deformation θ, the normalized deflection due to the crack δ_c is given by:

$$\delta_C = \theta_C = \theta - \mu(\theta) \tag{5.21}$$

The total normalized mid-span deflection may then be found from:

$$\delta = \delta_e + \delta_C = \theta + \left(\frac{L}{3s} - 1\right)\mu(\theta) \tag{5.22}$$

The central load on the beam is related to the normalized moment through:

$$P(\theta) = \frac{2}{3}\,\frac{f_t h^2 t}{L}\;\mu(\theta) \tag{5.23}$$

The prediction of the load-deflection curve requires knowledge of the bilinear softening diagram, as well as the position of the fictitious crack along the depth of the beam because the relevant expression for the normalized moment $\mu(\theta)$ depends on this position. The axial load and bending moment are related to the hinge rotation in three phases depending on the position of the fictitious crack (Figure 5.11) ahead of the real notch; (i) the fictitious crack is entirely on the first branch of the bilinear softening diagram; (ii) it is partly on the first and partly on the second branches, and (iii) it is entirely on the second branch. The full analytical expressions relating the hinge rotation to the bending moment in each of these three phases and in turn to the applied central load on the beam (Equation 5.23) are given in Appendix A.

5.5.5 Test Results

The unknown parameters of the bi-linear stress-crack opening diagram, e.g. w_1, w_2, f_t and σ_1/ f_t or a_1, a_2, f_t and σ_1/ f_t are identified in an inverse manner by minimizing the root mean square error between the recorded and predicted load-CMOD or the load-deflection diagram at many values of the applied central load. This is generally possible for all plain and conventional fibre-reinforced concrete mixes in which the load-CMOD and load-deflection diagrams can be recorded almost until the load has dropped to zero within the limits of measurement of the CMOD gauge (about 3.5 mm) or LVDT (can be up to 50 mm). For UHPFRC of the strain-hardening type though the inverse identification procedure can be applied only to the load-deflection plot which can be recorded to very large deflection values, but not to the load-CMOD record which is restricted by the range of CMOD gauge to almost only the pre-peak response. Accordingly, the parameters of the bi-linear tension softening diagrams for both notches have been identified using the inverse identification procedure on the load-deflection plots recorded up to a deflection of 30 mm.

It is assumed initially that $f_t = 0.65\ f_{st}$ (Neville, 1995), where f_{st} is the split cylinder strength.

Moreover, as is common in fibre-reinforced concrete the critical crack opening w_2 when the stress-transfer capacity is exhausted is assumed to be related to the length of the fibre. In other words, the stress-transfer capacity across a crack is assumed to be exhausted when the crack mouth has opened to such an extent that the fibres no longer bridge across it. Usually, this critical crack mouth opening to assumed to be less than one-half the fibre length, i.e. < 15 mm (Lange-Kombak and Karihaloo, 1997).

The parameters so identified are tabulated in Table 5.7 and shown in Figure 5.12. The recorded and predicted load-deflection curves for notch-to-depth ratios 0.1 and 0.6 are shown in Figure 5.13. The error shown in Table 5.7 is obtained by calculating the difference between the measured size-dependent fracture energy (G_f) and that given by the area under the stress-crack opening diagram for each notch depth (Figure 5.10)

$$G_f = \frac{1}{2} f_t \left(w_1 + \frac{\sigma_1}{f_t} w_2 \right) \tag{5.24}$$

An additional check on the accuracy of the parameters of the bi-linear stress-crack opening relation is provided by predicting the load-CMOD plot and comparing it with the restricted recorded plot. This is done in Figure 5.14 for one notch-to-depth ratio ($a/W = 0.1$), from which it can be concluded that the identified parameters for this notch-to-depth ratio are accurate.

The assumption that the response of the non-linear hinge is linear elastic up to the peak load implies that the pre-peak non-linear strain-hardening cannot be captured by the hinge model (Figures 5.13 and 5.14). This pre-peak non-linearity is known to be a result of diffuse micro-cracking whose density increases as the load is increased from the linear elastic proportional limit to the peak load. It can be captured by considering the effect of micro-cracks on the reduction in the stiffness using the micromechanical formulation of Budiansky and O'Connell (1976).

The parameters of the tension softening curves obtained using the non-linear hinge model correspond to the measured G_f (0.1) and G_f (0.6), but not to G_F.

Abdalla and Karihaloo (2004) proposed a simple method for the determination of the bi-linear softening diagram corresponding to the size-independent G_F of concrete mix by scaling the average parameters of the tension softening diagrams corresponding to

the size-dependent fracture energies G_f (0.1) and G_f (0.6) (Table 5.7). This scaling procedure was followed in this work, giving the parameters reported in the last row of Table 5.7. The corresponding tension-softening diagram is also shown in Figure 5.12.

Table 5.7 Bi-linear tension softening diagram parameters corresponding to a/W=0.1 and 0.6 and the size-independent G_F

Item	a_1 (mm^{-1})	a_2 (mm^{-1})	b_2	w_1 (mm)	w_2 (mm)	σ_1/f_t	f_t (MPa)	Percentage Difference (%)
a/W = 0.6	0.256	0.11	0.63	2.5	5.8	0.36	10.44	5.8
a/W = 0.1	0.16	0.07	0.59	4.55	8.43	0.27	9.54	7.4
G_F	0.18	0.09	0.66	3.76	7.38	0.324	12.02	

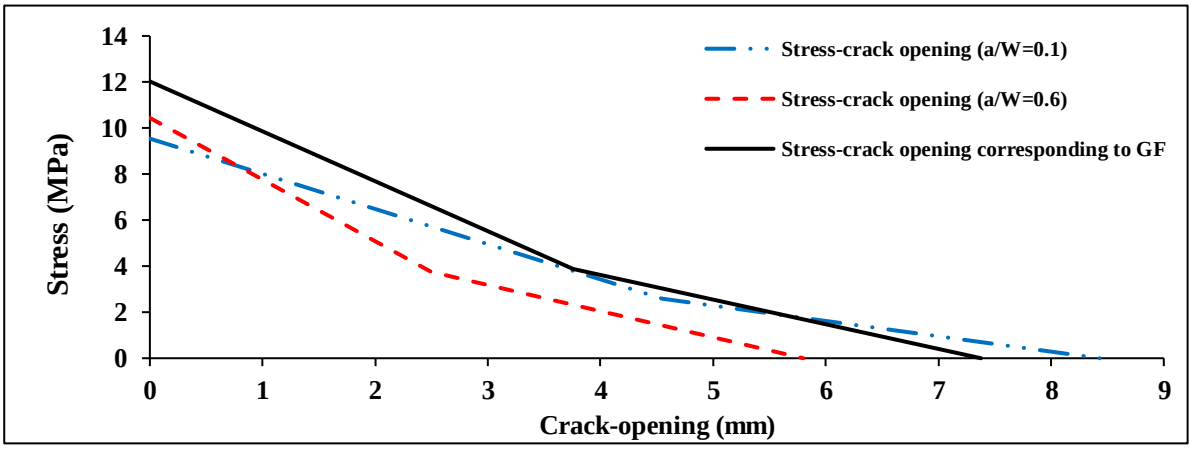

Figure 5.12 Bi-linear stress-crack opening relationships corresponding to a/W=0.6, 0.1 and G_F

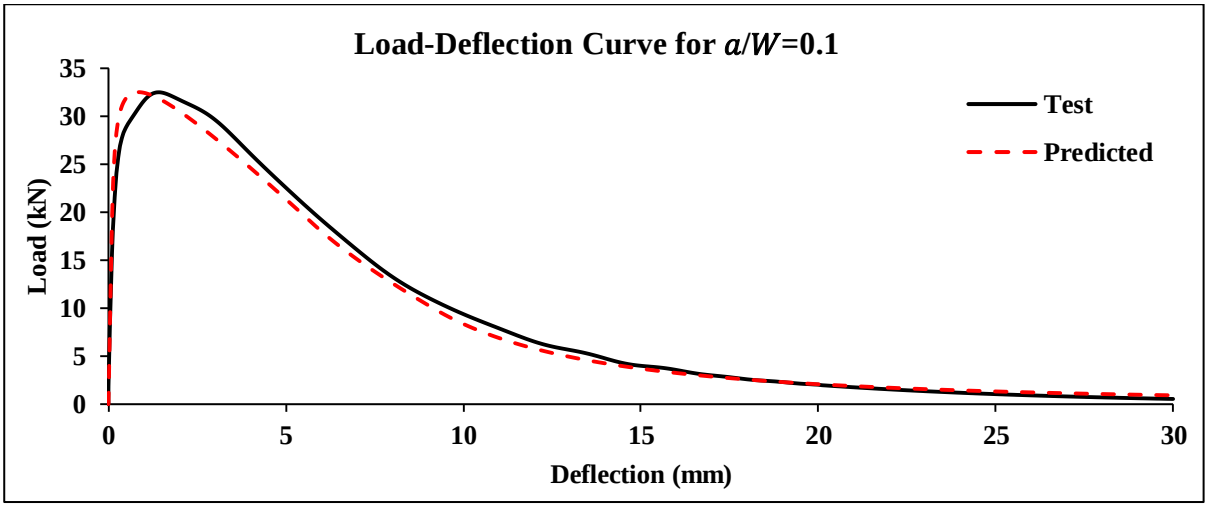

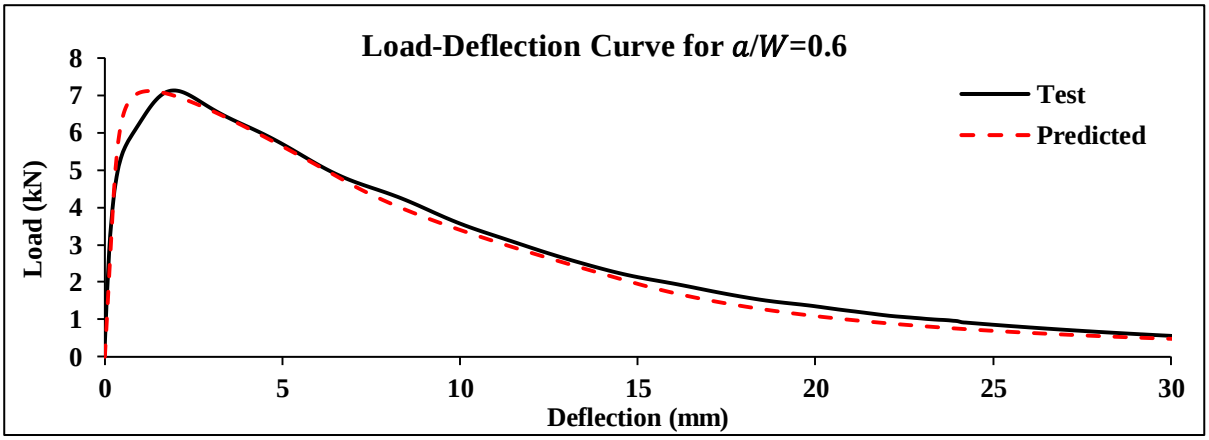

Figure 5.13 Predicted and recorded load-deflection curves for a/W=0.1 and 0.6

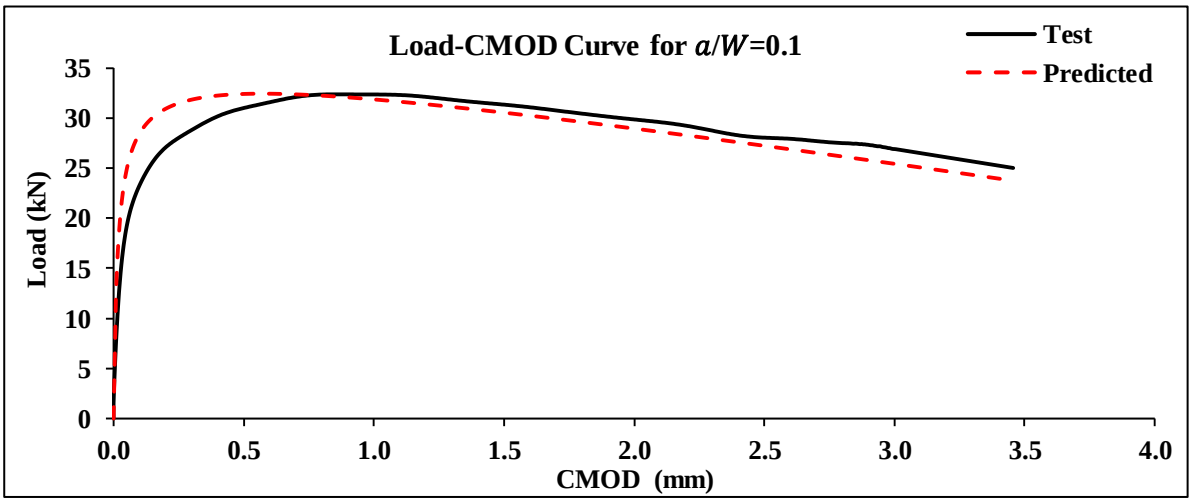

Figure 5.14 Predicted and recorded load-CMOD curves for a/W= 0.1

It should be mentioned that, as expected, the direct tensile strength of the UHPFRC is less than that of the original CARDIFRC Mix II (12.02 MPa in contrast to 15 MPa). This is because of the absence of short steel fibres (6 mm long, 4.5% by volume) in the UHPFRC.

5.6 Concluding Remarks

- A self-compacting UHPFRC based on CARDIFRC Mix II was developed and fully characterised from both the mechanical and fracture points of view. As expected, the resulting UHPFRC has inferior compressive, tensile and flexural strengths than the original CARDIFRC Mix II. This is due to the absence of thin small brass-coated steel fibres (4.5% by volume; 6 mm long) in the UHPFRC. The UHPFRC is however much tougher thanks to the use of a larger volume fraction (2.5% against 1.5%) of longer steel fibres (30 mm against 13 mm).
- An inverse approach based on the non-linear hinge model for crack growth from a pre-existing notch was used to identify the parameters of the bi-linear stress-crack opening relation of the UHPFRC.
- The load-deflection and load-CMOD curves of notched beams predicted using the bi-linear stress-crack opening relations were shown to be in very good agreement with the recorded experimental results, except in the pre-peak non-linear region.

Chapter Six

Flexural Fatigue Behaviour of A Self-Compacting Ultra-High Performance Fibre-Reinforced Concrete

6.1 Introduction

Fatigue is recognized to be responsible for the majority of failure of concrete structures subjected to repeated loading. The fatigue strength (i.e. endurance limit) of concrete is defined as the fraction of the static strength that it can support repeatedly for a given number of cycles (ACI 215R-74). The heterogeneity of concrete and the excessive micro-cracking within the material due to exposure to repeated loading leads to its degradation and results in a steady decrease in the stiffness of the material, which may eventually lead to fatigue failure under very low load amplitude (Hsu, 1981). In this Chapter, we will investigate the flexural fatigue behaviour of the self-compacting UHPFRC whose mechanical and fracture properties were described in Chapter 5.

The addition of fibres to the concrete increases the deformation at failure and to an improvement of fatigue life of concrete (Cachima et al., 2002). However, the addition of fibres to concrete has a dual effect on the fatigue performance of concrete. On the one hand, they increase the fatigue life of concrete by bridging the cracks and thus retarding their growth. However, on the other, they may become the source of additional defects if not properly and evenly distributed in the concrete matrix (Nicolaides, 2004; Farhat et al., 2007; Nicolaides et al., 2010).

Different methods have been employed in the fatigue life assessment of plain and fibre-reinforced concrete under tensile cyclic or compressive cyclic loading (Goel and Singh, 2014; Korte et al., 2014; Makita and Bruhwiler, 2014a; Medeiros et al., 2015; Parvez and Foster, 2014; Choi et al., 2016; Chen et al., 2017; Li et al., 2016; Muller and Mechtcherine, 2017). The most common approach to quantify the fatigue behaviour of concrete is the stress-life, S–N, method, and the mean fatigue life of concrete under given constant-amplitude cyclic stress can be predicted by the S-N curve (Oh, 1986; Xiao et al., 2013; Goel and Singh, 2014). For this method, samples are load cycled at a

variety of constant amplitude stress ranges until failure, resulting in the stress-life plots of stress range versus number of cycles to failure. There is however no information available on the flexural fatigue behaviour of ultra-high performance fibre-reinforced concrete (UHPFRC).

In this chapter, the flexural fatigue behaviour of this UHPFRC is reported in terms of its S-N curve, the change in compliance under cycling and the effect of cyclic loading with non-zero mean stress. It is found that the distribution of fibres plays a crucial role in the fatigue life of UHPFRC. Uniform distribution of fibres ensures that the material has very high fatigue endurance limit - more than 80% of its static flexural strength (24.36 MPa) - but this limit reduces significantly to approximately 64% of the corresponding lower static strength (22.02 MPa) if the distribution is non-uniform with regions of few or no fibres. The bulk of the work reported here has been published in Al-Azzawi and Karihaloo (2017b).

6-2 A Self-Compacting Ultra-High-Performance Fibre-Reinforced Concrete (UHPFRC): Materials and Mix Preparation

The details of the process of conversion of the original vibrated Mix II to a self-compacting UHPFRC may be found in Chapter Five. Here only a brief account is given of how the thin slab specimens for fatigue testing were cast and cured. The choice of the thin specimens was dictated by the intended structural application of this material for retrofitting of RC beams subjected to cyclic loading. The thickness of the specimens (35 mm) is therefore just over one fibre length (30 mm) ensuring that the fibres will be preferentially oriented along the length of the specimen. From the flexural application point of view this is the most desired orientation of fibres (Ferrara et al., 2011; Orbe et

al., 2012). It should be mentioned that in a self-compacting UHPFRC the randomly distributed fibres in the mix reorient themselves with the direction of flow (i.e. along the length of the specimen) (Deeb et al., 2014). Moreover, as the mix requires no external vibration for compaction the wall effect on the fibre distribution produced by the formwork is minimal, if not altogether absent.

The mix was prepared in a pan mixer using the mix proportions given in Chapter five (Table 5.1). The quantity of mix prepared was calculated based on the volume of required specimens. The mixing followed the procedure recommended in (Benson and Karihaloo 2005a) by adding the finest constituent to the coarsest one (details can be found in Chapter five, Section 5.3.1).

The mix was poured into a steel mould partitioned for two 1030x100x35mm slab specimens with a scoop (Figure 6.1). The self-compactibility of the mix ensures that the mix flows and fills the entire mould without external vibration. The surface of the mould was finished with a trowel. The slabs were demoulded 24 hours after casting and cured in a heated water tank for 9 days (for details, see Chapter five, Section 5.3.3).

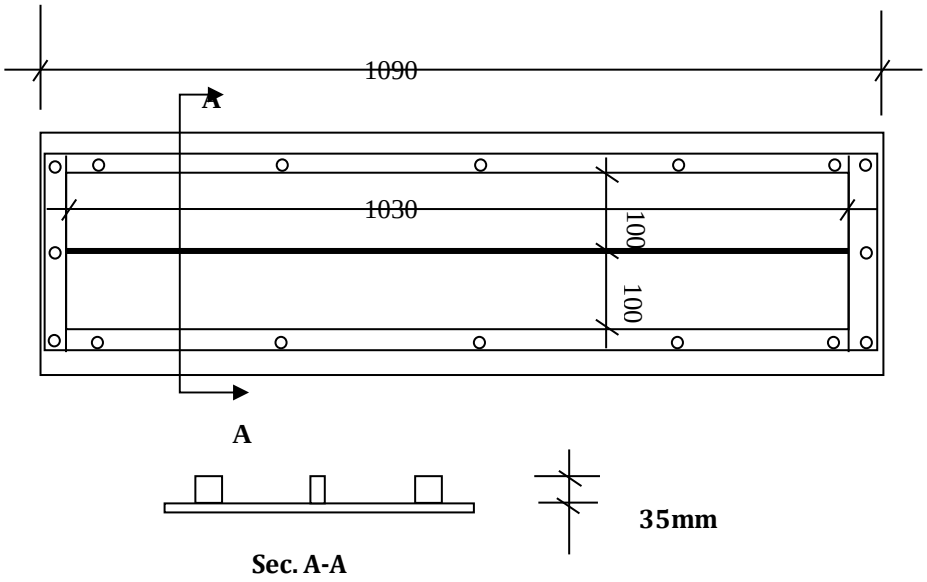

Figure 6.1 Steel mould for casting two slabs

The slabs were air dried prior to testing. Each slab was cut with a diamond saw to give three 340x100x35 mm specimens. As mentioned above, the self-compactibility of the mix ensures that the mix flows as a homogeneous mass without segregation of the heavier particles or fibres and fills the entire mould without external vibration, so that all three specimens are expected to be nearly identical as far as the fibre distribution is concerned.

6-3 Three-Point Flexural Test on 340x100x35mm Specimens

The determination of the fatigue life by three point bend tests on un-notched specimens requires the knowledge of the monotonic three-point flexural strength of the material. To determine this strength three-point bend test was carried out on four 340x100x35 mm specimens simply supported over a span of 300 mm. The static 3-point bend load central deflection plots are shown in Figure 6.2 and the resulting mean 3-point flexural strength is given in Table 6.1.

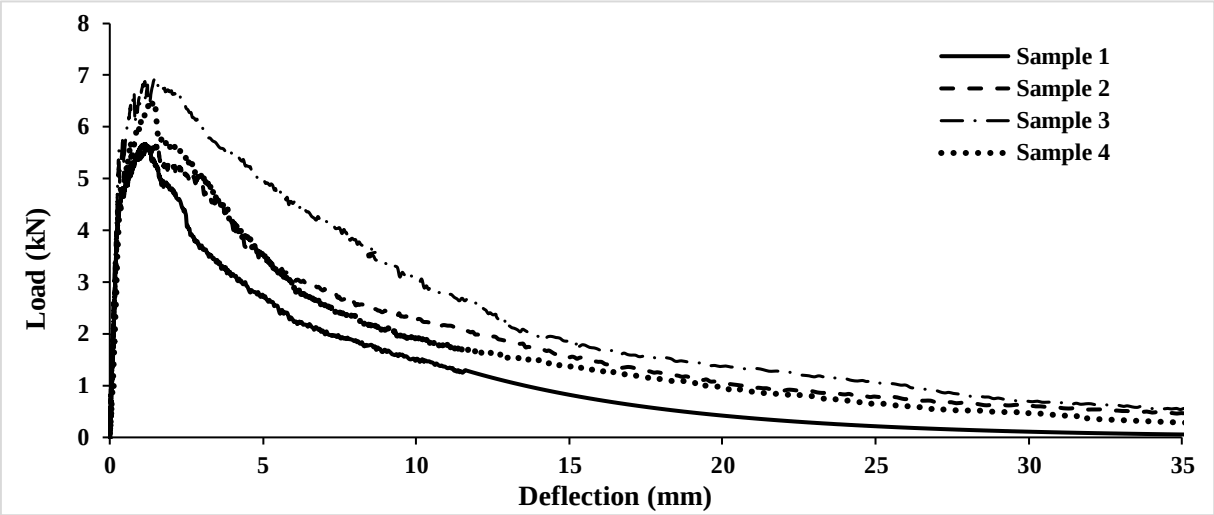

Figure 6.2 The static 3-point bend load-central deflection for four samples (340x100x35mm)

Table 6.1 Three-point flexural strength of UHPFRC based on vibrated Mix-II

Sample No.	Failure load(kN)	3-point flexural strength (MPa)
1	5.67	20.17
2	5.67	20.17
3	6.96	24.76
4	6.46	22.98
Mean	6.19	22.02

6.4 Flexural Fatigue Tests on 340x100x35mm Specimens

The fatigue test was carried out in three-point bending in a stiff testing frame, fitted with a 20 kN dynamic-static actuator. The central deflection was measured by a single linearly varying displacement transducer (LVDT) placed underneath the specimen at its mid-span.

The specimen was simply supported over a span of 300 mm. To prevent it from moving laterally during the cyclic load application special mechanical stops in the form of a rod with a wider circular head were positioned in line with the simple supports on either side of the specimen. The circular heads of the mechanical stops did not actually

touch the specimen (there is a gap of 2 mm) unless it moved laterally from its original position (see photo of test set up in Figure 6.3). The actuator was connected to a digital feedback controller. In addition, a bridge/transducer amplifier was used and connected to the controller to amplify and adjust the signal from the LVDT and to convert it to a mechanical reading in mm.

Four measurements were recorded on each specimen: (1) the cyclic load; (2) the central deflection; (3) the time; and (4) the number of cycles. The test was carried out with the sinusoidal load varying between two limits. The minimum load level corresponded to 9.69% of the monotonic static three-point bend strength (22.02MPa) and the maximum load level corresponded to 64.62%, 72.70% or 88.85% of the monotonic strength. Before the cyclic load was applied, the specimen was loaded and unloaded three times between 0.6 kN and 3 kN (corresponding to approximately 50% of the monotonic flexural failure load, Table 6.1) in order to eliminate any slack in the machine-specimen testing system. The frequency of cyclic loading used was 5 Hz. The test was stopped after the specimen failure or after one million cycles, whichever occurred first.

The choice of the frequency was made bearing in mind the time required for the test beam to reach one million cycles (it should not be excessively long) and the avoidance of side effects. Thus lower frequencies were not chosen in order to complete the test in a reasonable time (56 h for one million cycles at 5 Hz), whereas higher frequencies were not chosen to minimise inertial effects. The choice of the frequency meant that the last specimen was tested more than two weeks after the first specimen in the single testing machine. However, this difference in the age of the specimens is not expected to make a noticeable difference to their fatigue performance, just as it does not affect their flexural strength.

Figure 6.3 Photo of test set up, showing the specimen on simple supports and two mechanical stops. There are two more mechanical stops on the other side of the specimen

6.5 Flexural Fatigue Test Results

Tests have been performed in the sinusoidal load ranges between 0.6 – 4.0 kN, 0.6 – 4.5 kN, and 0.6 – 5.5 kN, corresponding to 9.69 – 64.62%, 9.69 – 72.70% and 9.69 – 88.85% of the static three-point flexural strength (Table 6.1). This meant that the mean stress level on the specimens during cyclic loading increased with the increase in the upper load limit, as shown in Table 6.2. This will have ramifications for the observed fatigue life of the material (see below).

Table 6.2 Increase in the mean stress level with increasing upper limit load

Upper Stress limit (%)	Mean Stress (MPa)
64.62	8.18
72.70	9.07
88.85	10.85

Table 6.3 gives the number of cycles sustained by each test specimen. Absence of an entry points to a malfunction in the equipment. The three specimens that were cycled to 64.62% of the static three-point strength sustained one million cycles without failure (one specimen even sustained two million cycles although some minute cracks were noticed on the tension surface of this specimen). The fatigue life decreased as the applied upper load level increased.

Table 6.3 Number of cycles sustained by UHPFRC 340x100x35mm specimens

Stress amplitude range (%)	Load amplitude range (kN)	Fatigue Life (cycles)		
		N1	N2	N3
9.69 – 64.62	0.6 – 4.0	>1000000	>1000000	>2000000
9.69 – 72.70	0.6 – 4.5	99000	87600	---------
9.69 – 88.85	0.6 – 5.5	25200	5400	---------

The logarithm of the fatigue life and the logarithm of the stress range normalised by the static three-point flexural strength are plotted in Figure 4 and tabulated in Table 6.4. It can be concluded that the endurance limit of the test material is around 64% of its static three point flexural strength (Figure 6.4) at a mean stress level of 37.1% of this strength (see Table 6.5 below). This figure also shows the fatigue life at zero mean stress cyclic loading. This has not been measured experimentally but has been estimated by using the Goodman rule, as will be explained below.

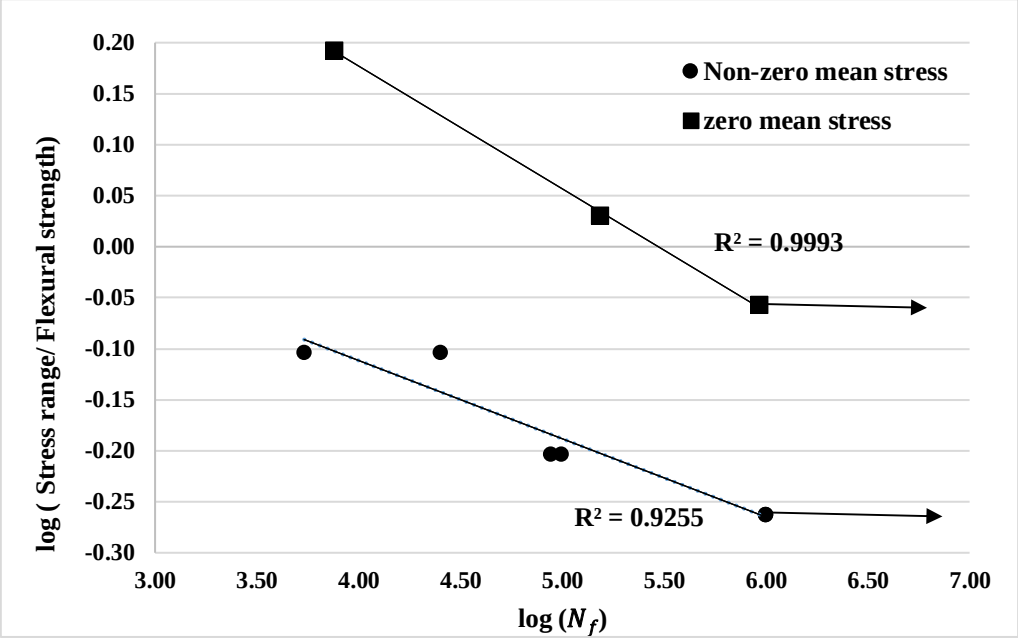

Figure 6.4 Fatigue life against stress range (logarithmic scale)

Table 6.4 Logarithm of fatigue life (N_f) and logarithm of stress range normalized by the static three-point flexural strength

Sample No.	Upper stress limit %	Log of Life Cycles(N_f)	Log of Stress range/ Flexural strength
1	64.62	6.00	-0.26
2	64.62	6.00	-0.26
3	64.62	6.00	-0.26
4	72.70	5.00	-0.20
5	72.70	4.94	-0.20
6	88.85	4.40	-0.10
8	88.85	3.73	-0.10

Several empirical models exist relating the high cycle fatigue life of un-cracked structures to the applied cyclic stress range. Of these, the Basquin Law is the most common

$$\Delta\sigma N_f^a = c_1 \qquad (6\text{-}1)$$

where $\Delta\sigma$ is the stress range (with zero mean stress), N_f is the number of cycles to failure and a and c_1 are constants to be determined from tests. From our tests, the equation that best fits the experimental data gives (Table 6.4)

$$\frac{\Delta\sigma}{\sigma_F}\left(N_f\right)^{\frac{1}{13}} = 1.57 \qquad (6\text{-}2)$$

where σ_F = 22.02 MPa (Table 6.1).

It should be stressed however that Basquin's law assumes that the stress range has a zero mean stress. In other words, the applied cyclic load is fully reversed. As pointed out above, in the tests reported here, the cyclic load had a non-zero mean value which increased as the upper limit of the cyclic load increased (Table 6.2). A non-zero mean stress reduces the fatigue life. As a result, the Basquin law (6-2) can be regarded to give a lower bound on the fatigue life of our test material. The actual fatigue life of the material at a given stress range with zero mean stress will be well in excess of that predicted by the Basquin law (6-2). To get an idea of how much the fatigue life is influenced by non-zero mean stress, we resort to the Goodman rule

$$\Delta\sigma_{\sigma m} = \Delta\sigma_0\left(1 - \frac{|\sigma_m|}{\sigma_F}\right) \qquad (6\text{-}3)$$

where $\Delta\sigma_0$ is the cyclic stress range with zero mean stress, $\Delta\sigma_{\sigma m}$ is the cyclic stress range with non-zero mean stress, $|\sigma_m|$ is the absolute value of the mean stress and σ_F is the static flexural strength.

The Goodman rule will be used in an inverse manner to calculate the stress range with zero mean stress $\Delta\sigma_0$ from equation (6-3) corresponding to the actual cyclic stress range with non-zero mean stress $\Delta\sigma_{\sigma m}$ used in the tests. The results are given in Table 6.5. A comparison of $\Delta\sigma_{\sigma m}/\sigma_F$ with $\Delta\sigma_0/\sigma_F$ shows that the fatigue life under cyclic stress range with non-zero mean stress is akin to fatigue life under a much larger cyclic stress range with zero mean stress. For example, N_f under $\Delta\sigma_{\sigma m}/\sigma_F$ = 0.55 would materialise under $\Delta\sigma_0/\sigma_F$ = 0.87. In fact, N_f under $\Delta\sigma_{\sigma m}/\sigma_F$ = 0.63 or 0.79 would materialise under $\Delta\sigma_0/\sigma_F$ = 1.07 or 1.56 which are impossible. The point of this

calculation was to demonstrate the fact that cyclic loading with non-zero mean leads to a significant reduction in the fatigue life of a material compared to fully reversed cyclic loading (Figure 6.4).

Table.6 5 Stress range with zero mean stress corresponding to stress range with non-zero mean stress according to Goodman's Rule

Upper stress limit %	Upper Stress (MPa)	Lower stress (MPa)	Stress range / Flexural strength ($\Delta\sigma_{\sigma m}/\sigma_F$)	Mean Stress σ_m (MPa)	(σ_m/σ_F)	$(\Delta\sigma_0/\sigma_F)$	log $(\Delta\sigma_0/\sigma_F)$
64.62	14.23	2.13	0.55	8.18	0.371	0.87	-0.06
72.70	16.01	2.13	0.63	9.07	0.412	1.07	0.03
88.85	19.56	2.13	0.79	10.85	0.493	1.56	0.19

6.6 Variation of Compliance of Fatigue Specimens

The compliance of a three-point bend test specimen is defined as the ratio of central displacement in mid-span load to the cyclic applied load and is expressed in mm/kN. Under cyclic loading, the compliance can increase with time, if the material sustains internal or surface damage, e.g. micro-cracking. If there is no damage then the compliance should remain constant.

The recorded load-deflection plots under cyclic loading for the specimens are shown in Appendix B.

The compliance of fatigue specimens was calculated from the corrected recorded load-central displacement traces. These recordings were made every minute, i.e. every 300 cycles. Figures 6.5-6.7 illustrate the variation of the compliance of specimens with the number of cycles.

It is clear from Figure 6.5 that the compliance of UHPFRC specimen with the number of cycles in the load range 9.69 – 64.62% of the three-point flexural strength is

practically unchanged up to one million cycles. The slight increase in compliance may be an indication of minor internal micro-cracking.

At higher cyclic load ranges (Figures 6.6 and 6.7), the specimens suffer progressive damage, initially almost linearly but then exponentially before failure. The variability in the number of cycles to failure at the same cyclic load range is no doubt due to the presence of an initial defect in the material, for example a zone with few or no fibres.

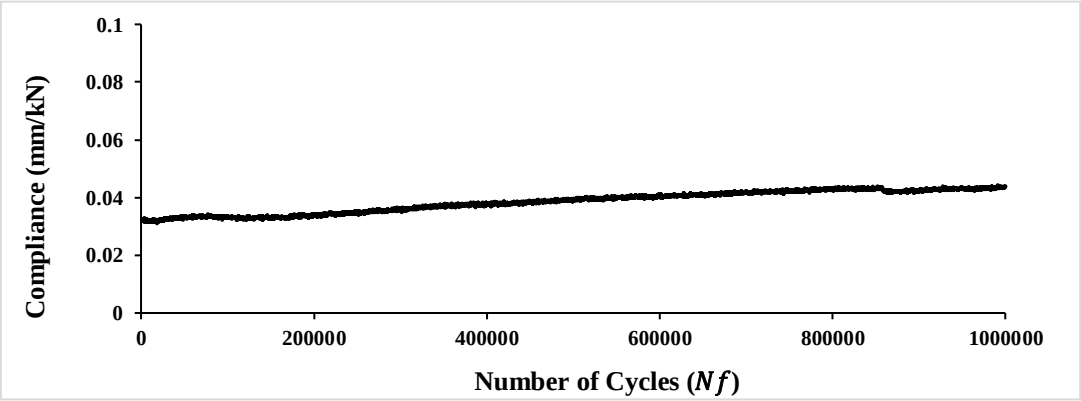

Figure 6.5 Variation of the compliance of the 340x100x35 mm UHPFRC specimen with the number of cycles in the load range 9.69 – 64.62% of the three-point flexural strength

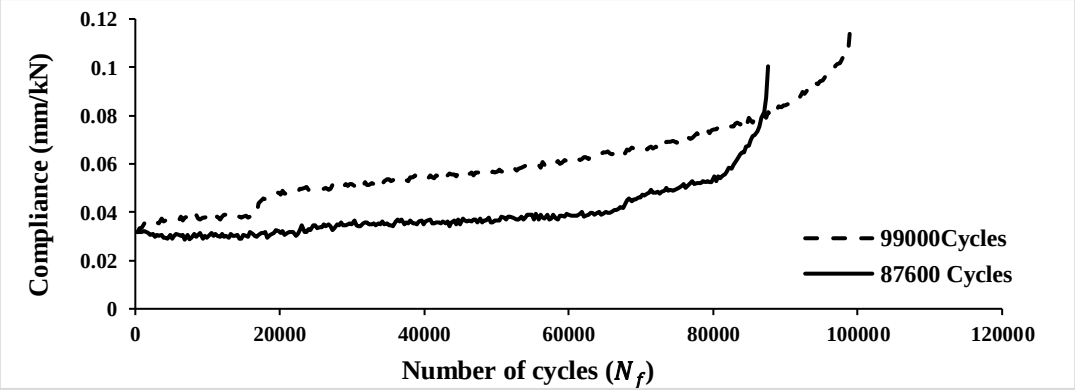

Figure 6.6 Variation of the compliance of the 340x100x35 mm UHPFRC specimens with the number of cycles in the load range 9.69 – 72.70% of the three-point flexural strength

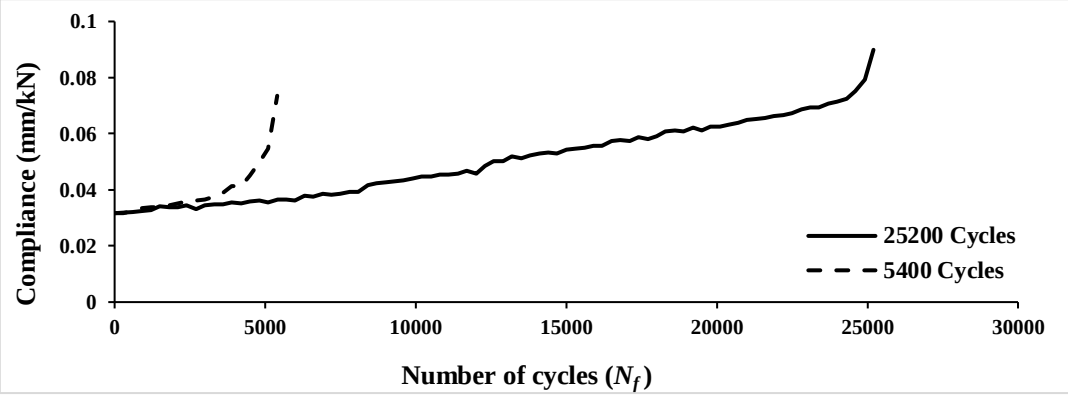

Figure 6.7 Variation of the compliance of the 340x100x35 mm UHPFRC specimens with the number of cycles in the load range 9.69 – 88.85% of the three-point flexural strength

The low fatigue life at intermediate cyclic load range 0.6 – 4.5 kN (Table 6.3) was unexpected because the upper load limit was within the elastic range of the material (see Figure 6.2). However, it was noticeable from Figure 6.2 that there was a large scatter in the post-peak response of the specimens tested in static three-point bending. This was thought to be a result of poor distribution of fibres in the specimens. Examination of the failure surfaces of the specimens confirmed this suspicion, in that the fibres were poorly distributed in the mix with regions of low or no fibres, highlighted in white in Figure 6.8. This was no doubt a result of the fact that the mix prepared in the pan mixer lacked self-compactabilty, i.e. flowing and filling ability, so that it did not flow as a homogeneous mass in the mould, as a self-compacting mix should.

It is important to note in this context that a self-compacting mix is far more sensitive to variations in temperature and humidity than a vibrated mix. For this reason, it is necessary to perform at least the slump flow test on the mix on the day of its preparation and to adjust the dosage of superplasticizer, if necessary, to ensure that it flows as a homogeneous mass without any segregation of the ingredients. It is a mistake to presume that a mix that has met the flowing, filling ability, and homogeneity self-compacting criteria on a certain day will automatically meet these criteria on a different

day because the temperature and humidity on that day may be different. This was the case with the mix used to make the slab specimens tested under static and cyclic loading, reported above. The mix was not tested for self-compatibility on the day of its preparation, but it was presumed to be so based on successful self- compactabilty tests performed on the same mix several days previously (see results of slump spread and t_{500} reported in last two rows of Table 5.1 in Chapter Five).

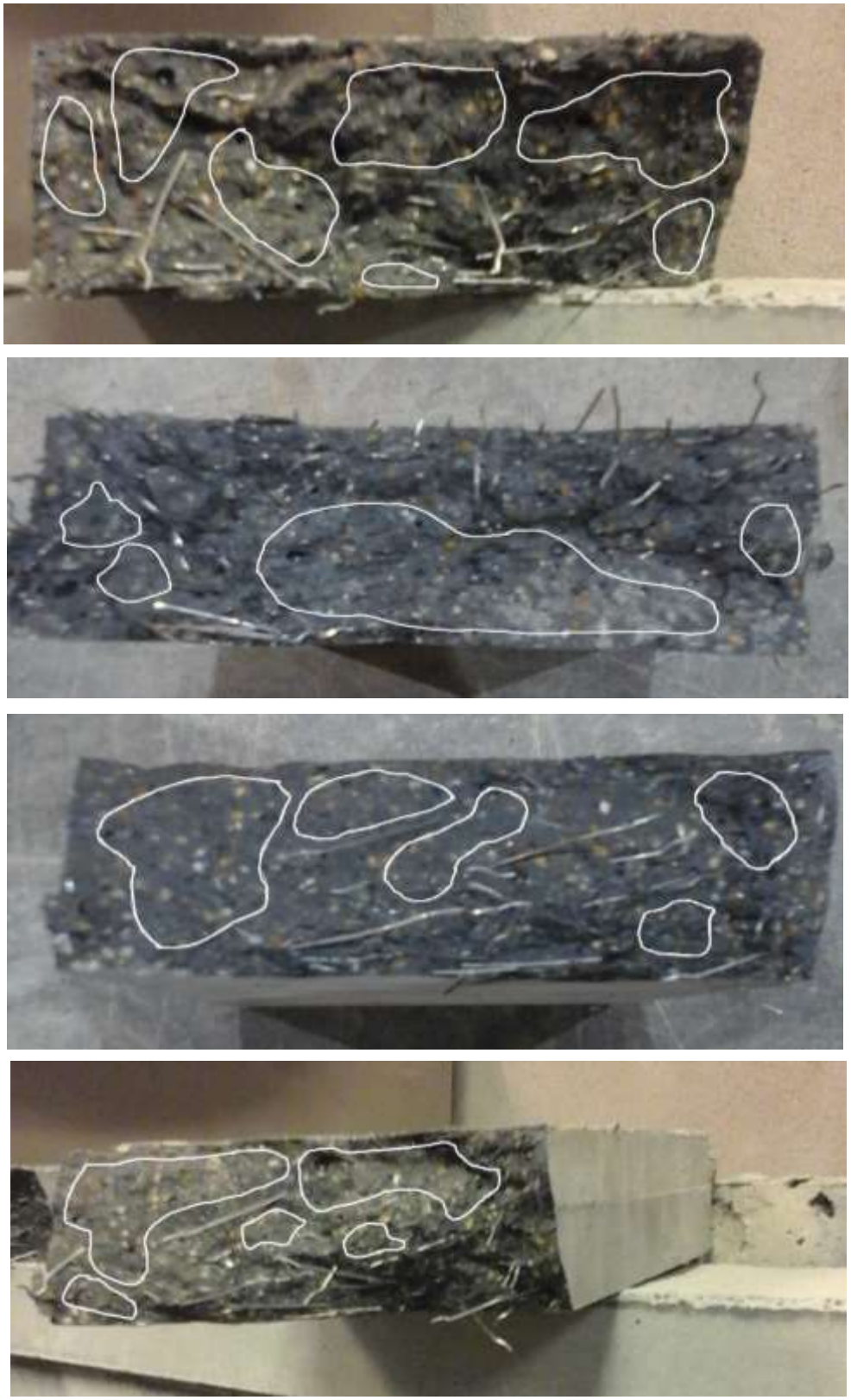

Figure 6.8 Poor distribution of steel fibres

6.7 Repeated Three-Point Flexural Fatigue and Static Tests

Accordingly, a second batch of the mix was prepared in the pan mixer and specimens were cast anew in the same way as described above (see Section 6.2 "Materials and mix preparation"). It was ensured that the mix had the required flow-ability and non-segregation property by performing a slump flow test on the mix on the day of its preparation as self-compacting concrete is sensitive to temperature and relative humidity. The specimens were cured and prepared for testing in the same manner as described above. Flexural fatigue tests were performed first in the same sinusoidal load ranges 0.6 – 4.0 kN, 0.6 – 4.5 kN and 0.6 – 5.5 kN, as before, and additionally in the load range 0.6 – 5.0 kN. Table 6.6 gives the number of cycles sustained by each test specimen. Seven specimens were tested; two for each load range, except the lowest load range for which only one specimen was tested. All specimens sustained one million cycles without failure (although some hairline cracks were noticed on the tension surface of some specimens). The cyclic load-central deflection traces of the specimens were recorded every minute, i.e. every 300 cycles, as before from which the compliance of the specimens was calculated.

The compliance vs number of cycles plots are shown in Figures 6.9 − 6.12. The recorded load-deflection plots under cyclic loading for the specimens are shown in Appendix B.

Table 6.6 Number of cycles sustained by UHPFRC 340x100x35mm specimens from the second batch

Load amplitude range (kN)	Fatigue Life (cycles)	
	N1	N2
0.6 – 4.0	>1000000	----------
0.6 – 4.5	>1000000	>1000000
0.6 – 5.0	>1000000	>1000000
0.6 – 5.5	>1000000	>1000000

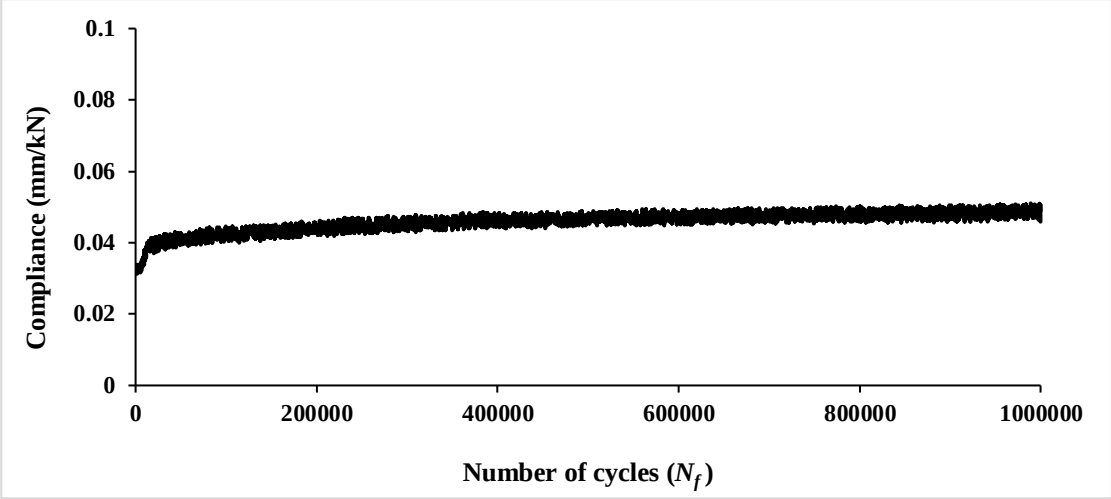

Figure 6.9 Compliance of the 340x100x35 mm UHPFRC specimen with the number of cycles from the second batch under the load range 0.6 – 4.0 kN

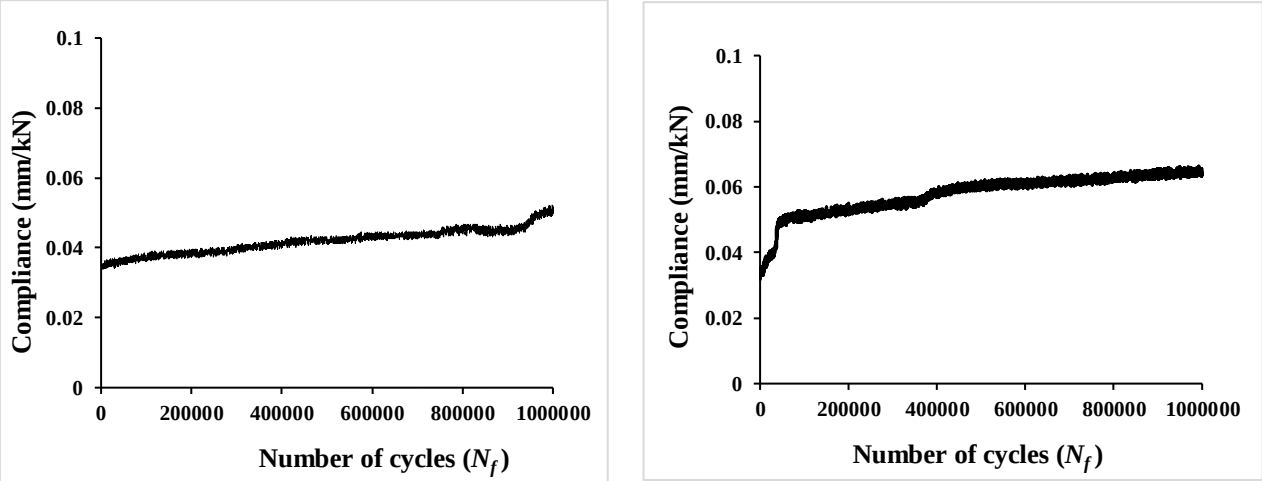

Figure 6.10 Compliance of the 340x100x35 mm UHPFRC specimen with the number of cycles from the second batch under the load range 0.6 – 4.5 kN

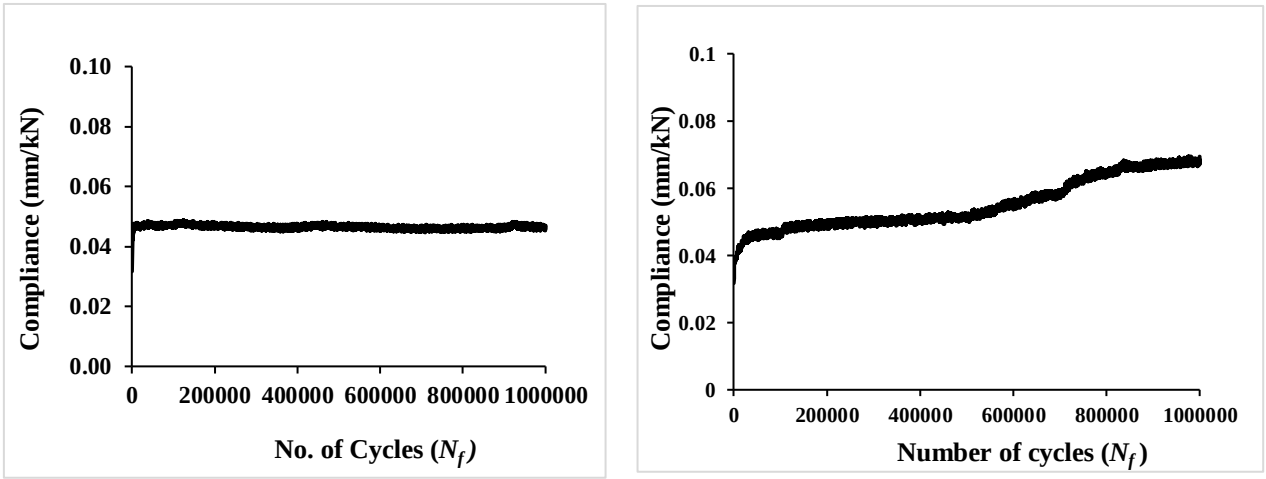

Figure 6.11 Compliance of the 340x100x35 mm UHPFRC specimen with the number of cycles from the second batch under the load range 0.6 – 5 kN

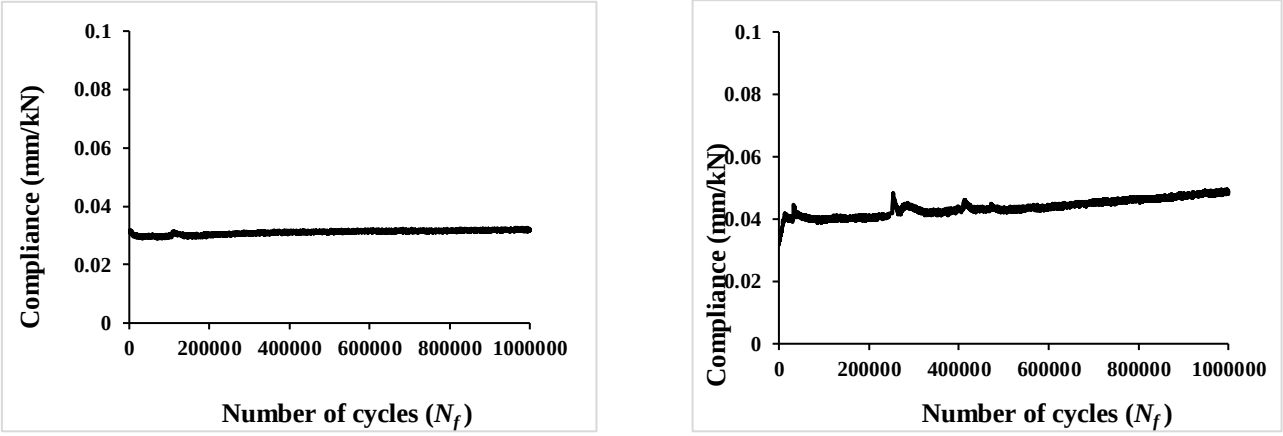

Figure 6.12 Compliance of the 340x100x35 mm UHPFRC specimen with the number of cycles from the second batch under the load range 0.6 – 5.5 kN

As all the specimens were still intact after sustaining one million load cycles, four of them were tested in static three-point bending. The results are given in Table 6.7. The recorded load-central deflection plots are shown in Figure 6.13.

A comparison of entries in Tables 6.1 and 6.7 shows that the static three-point flexural strength of the specimens from the second batch of UHPFRC is approximately 10% higher than that of the specimens from the first batch. More importantly, there is much less scatter in their post peak response (compare Figure 6.13 with Figure 6.2) suggesting a good distribution of fibres. This was indeed confirmed by an examination of the failure surfaces (Figure 6.14).

Table 6.7 Three-point flexural strength of UHPFRC specimens of the second batch

Sample No.	Failure Load (kN)	3-point flexural strength (MPa)
1	7.34	26.11
2	7.35	26.14
3	6.27	22.30
4	6.43	22.87
Mean	6.85	24.36

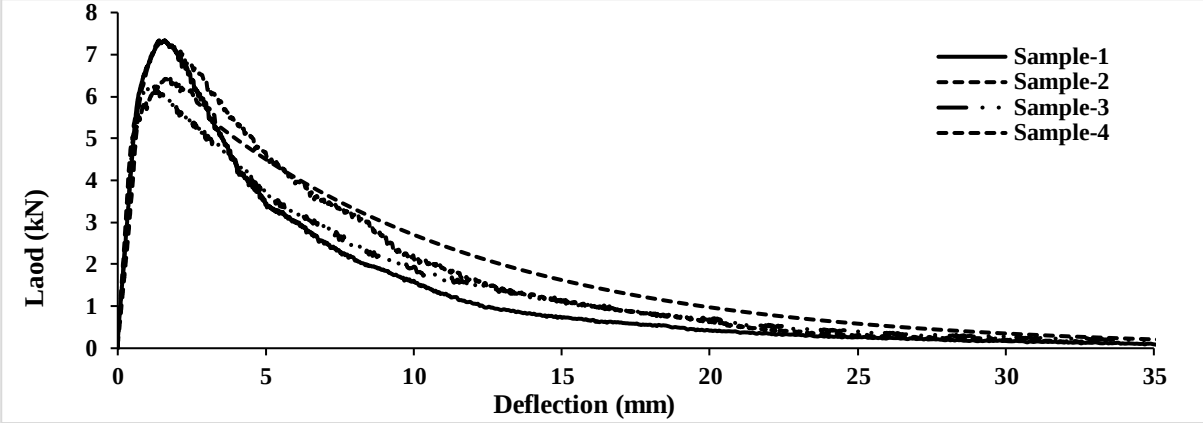

Figure 6.13 The static 3-point bend load-central deflection for four samples (340x100x35mm) from the second batch

Figure 6.14 Good distribution of fibres in the failure sections

Knowing the three-point static flexural strength of the second mix (Table 6.7), the cyclic load range (Table 6.6) can be converted into a stress range and expressed as a percentage of the static flexural strength. This is reported in Table 6.8, which also shows the increase in mean stress with increasing upper limit stress. Notwithstanding the fact that the maximum upper stress level as a fraction of the static flexural strength experienced by specimens from the second batch under fatigue loading was smaller (80.29%; Table 6.8) than by specimens from the first batch (88.85%, Table 6.3), the marked improvement in the fatigue response of the former is primarily because of the good distribution of fibres in the mix. That all the specimens withstood at least a million cycles of loading without failure is not surprising because even at the maximum upper load level of 5.5 kN (maximum upper stress level of 80.29%) the material response is still mostly linear (Figure 6.13) so that there is very little accumulation of damage. This is borne out by the evolution of the compliance of the specimens (Figures 6.9 − 6.12) that shows a very marginal increase in the compliance up to one million cycles.

Thus, if the flexural fatigue life of the UHPFRC is chosen to be one million cycles, then it can be concluded that its flexural fatigue endurance limit is at least 80% of its static flexural strength (24.36 MPa) at a mean stress of 10.85 MPa (44.5%). This can be regarded as the lower bound of the flexural fatigue life, because as shown above the flexural fatigue life under zero mean stress will be substantially longer.

Table 6.8. Increase in the mean stress level with increasing upper limit load

Load amplitude range (kN)	Stress amplitude range (%)	Mean Stress (MPa)
0.6 – 4.0	8.76 – 58.39	8.18
0.6 – 4.5	8.76 – 65.69	9.07
0.6 – 5.0	8.76 – 72.99	9.96
0.6 – 5.5	8.76 – 80.29	10.85

6.8 Estimation of the Number of Cycles Until Failure

The choice of the frequency was made taking in consideration the time required for the test specimen to reach one million cycles. The test was stopped if the specimen sustained one million cycles without failure. This does not mean that the fatigue life of the material is just one million cycles.

In order to have some idea of what is the fatigue life under a given cyclic load range, it may be for instance be assumed that the material is deemed to have failed when its compliance has doubled, i.e., its stiffness has reduced to half its pre-loading level.

For this, we can use the variation in the compliance of the specimens to predict the fatigue life for each specimen. Therefore, the predicted number of cycles was acquired using the initial compliance for each specimen and the rate of change of the compliance with the number of cycles (Figures 6.5 − 6.7 and 6.9 − 6.12):

$$\int_{c_i}^{2c_i} dc = \mathrm{R} \int_0^{N_{pf}} dN \qquad (6\text{-}4)$$

Then the predicted number of cycles:

$$N_{pf} = \frac{C_i}{R} \qquad (6\text{-}5)$$

where C_i is the initial compliance, R is the rate of change of compliance to the number of cycles and N_{pf} is the predicted number of cycles until failure.

The predicted number of cycles for each specimen with the stress range is tabulated in Table 6.9 and 6.10 for the mixes with poor and good fibre distribution.

Tables 6.9 shows that the predicted number of cycles for the first batch (poor fibre distribution) is more than what was recorded during the test for specimens sustained

one million cycles up to the maximum load amplitude of 4.0 kN, i.e. approximately 64.62% of the ultimate static three-point flexural load of 6.19 kN.

Similarly, Table 6.10 shows that the predicted number of cycles to failure for the second batch (good fibre distribution) is also well above that recorded during the test up to the maximum load amplitude of 5.0 kN, i.e. approximately 73% of the ultimate static flexural load of 6.85 kN.

Therefore, it can be concluded that these specimens (when fibres are uniformly distributed) can sustain more than one million cycles under maximum load amplitude 5.0kN (about 73% from its ultimate static flexural load 6.85 kN), and even three million cycles under maximum load amplitude 4.0kN (about 58% from its ultimate static flexural load 6.85 kN).

Table 6.9 Predicted number of cycles with load amplitude range for mix with poor fibre distribution

Load amplitude range (kN)	No of Cycles N_{pf}
0.6 – 4.0	2614962
0.6 – 4.5	93300
0.6 – 5.5	15300

Table 6.10 Predicted number of cycles with load amplitude range for mix with good fibre distribution

Load amplitude range (kN)	No of Cycles N_{pf}
0.6 – 4.0	2976485
0.6 – 4.5	1410771
0.6 – 5.0	1389938
0.6 – 5.5	1000000*

* For some unknown reasons, the actual number of cycles in this load range according to this method of calculation worked out to be even larger than that in the load range 0.6 – 4.0 kN, which cannot be correct. Therefore, the number of cycles shown is the lower bound of 10^6.

6.9 Concluding Remarks

- The fatigue life of the self-compacting ultra-high performance fibre-reinforced concrete based on an earlier vibrated mix is well in excess of one million cycles and its endurance limit is around 80% of its static three-point flexural strength (24.36 MPa), i.e. approximately 19 MPa, at a mean stress level of the cyclic loading of 44.5% of this strength (10.85 MPa) .
- A vital role in the fatigue performance is played by the distribution of fibres; uniform distribution of fibres ensures that the material has the above high fatigue endurance limit but this limit reduces crucially to approximately 64% of the corresponding lower static three-point flexural strength (22.02 MPa), i.e. approximately to 14 MPa at a mean stress level of approximately 8 MPa, if the distribution is non-uniform with regions of few or no fibres.
- To ensure that the fibres are uniformly distributed it is important that the UHPFRC meets all three self-compactibilty criteria of flow-ability, passing ability and non-segregation on the day it is manufactured because self-compacting mixes are far more sensitive to changes in temperature and relative humidity than their vibrated counterparts.
- An indication of the expected fatigue life under a given cyclic load range was obtained from the recorded variation in the compliance, since the tests were terminated at one million cycles.

Chapter Seven

Application of a Self-Compacting Ultra-High Performance Fibre-Reinforced Concrete to Retrofit RC Beams Subjected to Repeated Loading

7.1 Introduction

RILEM (1984) states that fatigue occurs in concrete due to the deterioration of the bond between the coarse aggregate and cement paste with the reduction of the section of the specimen. Alternatively, it happens simultaneously with the aforementioned one, due to the formation and diffusion of micro-cracks in the cement paste until macro-cracks weaken the section and cannot withstand the applied load.

The strengthening of reinforced concrete structures is, and will continue to be, a relevant problem to accommodate for a load carrying capacity higher than the original design value. In the last decades, rapid progress has been made in the development of strengthening materials and technologies (Derkowski and Zych, 2004).

The earliest method used to strengthen concrete structure is by bonding steel plates to its surface. This method is simple to execute and results in only small changes in the size of the strengthened structure, but it has several drawbacks (Jones et al., 1988). Among these are, for example the corrosion of steel, deterioration of the bond at the glued steel–concrete interface, difficulty in the installation of heavy steel plates, and limitations in supplying steel plates of required length.

In a later method, fibre reinforced plastic (FRP) plates have been used. Extensive investigations have been performed using this technique (Nanni, 1995; Sen et al., 2000; Heffernan and Erki, 2004; Saikaly et al., 2014). In contrast to the steel plates, the FRP has high strength to weight ratio, good chemical resistance, is easy to handle thus reducing the labour costs (Buyukozturk and Hearing, 1998; Bakis et al., 2002). However, long exposure to temperature variations and sunlight can weaken the bond between the FRP composite and concrete (Karbhari, 1998; Mei and Chung, 2000).

Furthermore, it has been shown that the concept of hybridization with two different fibres in normal cement matrix instead of single fibre offers more attractive engineering properties that may promote the traits acquired as a result of the use of a mono-fibre (Sharmila and Thirugnanam, 2013, Khan et al., 2017).

Another promising material that can be used to enhance the fatigue strength of reinforced concrete is the ultra-high performance fibre-reinforced concrete materials (UHPFRC). They possess eminent properties: relatively high compressive strength, high tensile strength, strain-hardening behaviour under tensile stress (given a certain volume of fibres) and very low permeability since an optimised dense matrix is used. Therefore, these properties make UHPFRC suitable for strengthening structural members that are subjected to severe mechanical and environmental actions (Makita and Brühwiler, 2014b, Li et al., 2017).

Several studies have previously been undertaken at Cardiff into the feasibility of using an UHPFRC material for the rehabilitation and strengthening of damaged RC flexural members [Karihaloo et al., 2000; Karihaloo et al., 2002; Alaee and Karihaloo, 2003a; Alaee and Karihaloo, 2003b; Farhat et al., 2007; Farhat et al., 2010]. This material is however not cost-competitive because of the use of expensive brass-coated thin steel fibres.

The aim of this chapter is to describe the performance of RC beams retrofitted with and without the self-compacting UHPFRC material under three-point bend static and cyclic loading. The mechanical and fracture properties (i.e. size-independent fracture energy and the corresponding bi-linear stress-crack opening relationship) of this UHPFRC material were reported in Chapter Five and its flexural fatigue performance in Chapter Six.

7.2 Control Beams

7.2.1 Mixing and Casting

A standard concrete mix (cement: fine aggregate: coarse aggregate: water in the ratio 1:1.8:2.8:0.5) was used. The proportions of materials used are summarised in Table 7.1.

The Portland cement used was Type II Class 42.5 N. The fine aggregate used was dried sand sieved to remove any large pieces of shell or gravel. The coarse aggregate (crushed limestone) had a maximum size of 10 mm.

Due to the extensive use of this mix in the Concrete laboratory, Cardiff University, no fresh tests were performed on this mix, but the previously reported values (Alaee, 2002) of the compressive strength and the split tensile strength (53.5 MPa and 4.4MPa, respectively) were adopted.

The mould was suitably prepared, the spacer block was inserted and the reinforcing bar (φ12 mm) for each of the two beams was placed (with a cover of 26mm from the bar centre to the tension face) on wooden support plates. To prevent leakage, the mould

Table 7.1 Material proportions

Constituents	Mass (kg/m^3)
Cement	394
Fine aggregate	709.3
Coarse aggregate	1103.4
Water	196.61
w/c	0.5

sides were tightened and any gaps were filled with a sealant. The fresh concrete was then poured in layers using scoops, and to ensure adequate compaction and removal of entrapped air a poker vibrator was used. The top face was then finished with a plasterer's float. The beams were removed from the mould after one day and water cured at ambient temperature (20°C) for 28 days.

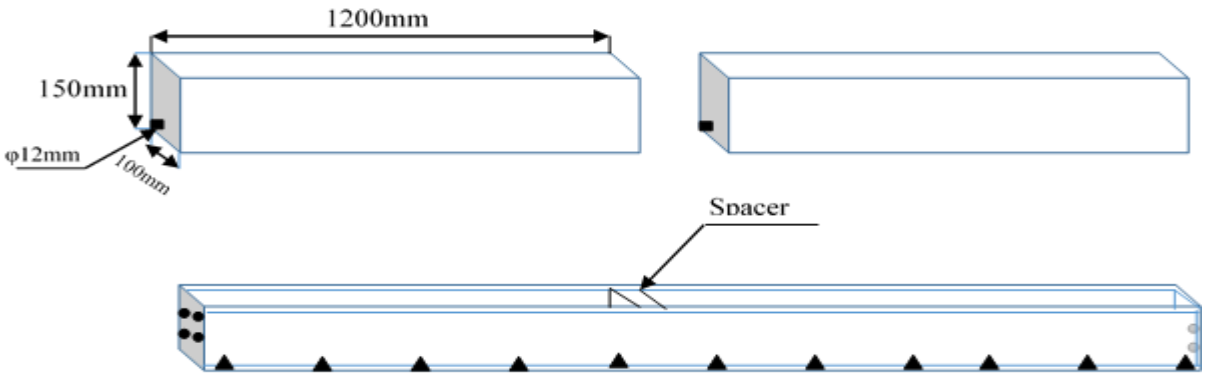

Figure 7.1 Steel mould for casting two beams

7.2.2 Three-point Static Flexural Test of Control RC beam

A control RC beam was tested under three-point loading over a span of 1000mm, taking care that the test beam is aligned as symmetrically as possible in the testing machine relative to the central load and supports. The rate of loading was 0.01mm/sec at the beginning of the test, but it was increased to 0.02mm/sec after passing the maximum load. The central deflection was measured by a single LVDT placed at its mid-span. Figure 7.2 shows the load- central deflection response of the control beam. When the load exceeded 5.5kN, the stiffness of the beam decreased but there were no cracks or damage observed with a naked eye at this stage. As the load was increased, hairline cracks appeared on the tension face of the beam near the mid-span and at a

quarter span from the support. Under further loading, these cracks diffused to the sides of the beam and began to grow towards the compressive zone. The crack that first appeared in the quarter span from the support started opening and propagated diagonally towards the loading point. Then a sudden failure occurred at 30.4kN. The failure of this beam occurred in mixed shear and flexural mode (Figure 7.3).

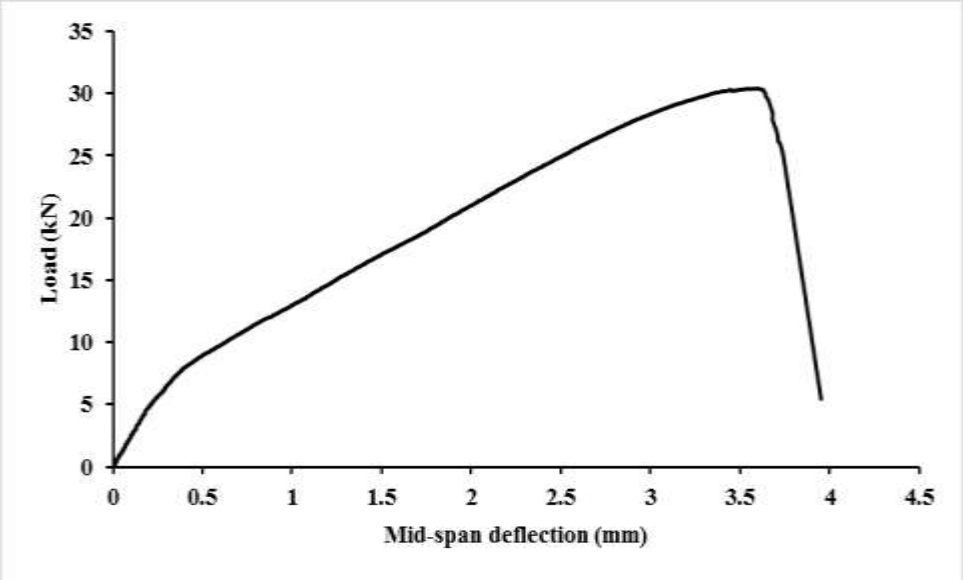

Figure 7.2 Load- central deflection response of the control reinforced concrete beam

Figure 7.3 Failure mode of the control RC beam

7.2.3 Three-Point Flexural Fatigue Test of Control RC beams

Four beams were cast following the procedure for the control beam (Section Mixing and Casting). The beams were cured at ambient temperature (20°C) for 28 days.

The cyclic fatigue test was carried out in three-point bending in a stiff testing frame. The central deflection was measured by a single LVDT placed underneath the beam at its mid-span. The beam was simply supported over a span of 1000 mm. It was clamped at the supports to prevent lateral movement during the cyclic load application.

Four measurements were recorded on each beam: (1) the cyclic load range; (2) the central deflection; (3) the time; and (4) the number of cycles. Tests were performed in the sinusoidal load ranges between 1.5 – 5.5 kN, 1.5 – 12.5 kN, 1.5 – 19.5 kN and 1.5 – 24.5kN corresponding to 4.93 – 18.1%, 4.93 – 41.12%, 4.93 – 64.14% and 4.93– 80.59% of the static three-point failure load (30.4 kN).

Before the cyclic load was applied, the beam was loaded and unloaded three times between 0.6 kN and 3 kN in order to eliminate any slack in the machine-specimen testing system. The frequency of cyclic loading used was different for each beam according the applied load level. The test was stopped after the specimen failure or after one million cycles, whichever occurred first.

7.2.3.1 Flexural Fatigue Test Results

Table 7.2 gives the number of cycles sustained by each test beam. The first beam that was cycled at 5 Hz to 18.1% of the static three-point failure load sustained one million cycles without failure (not even minute cracks were noticed on the tension surface of this specimen). The second beam that was cycled at 4 Hz to 41.93% of the static three-

point failure load also sustained one million cycles without failure but with some minor hairline cracks on the surface. The third beam was cycled at 3.5 Hz to 64.14% and fourth beam at 2.5 Hz to 80.59%. The reason for decreasing the frequency as the upper cyclic load level increased was to avoid any play in the machine-specimen testing system and to minimise inertial effects. The cyclic load-central deflection curves for tested samples can be seen in Appendix C. The failure mode crack patterns of the specimens are shown in Figures 7.4 – 7.7.

The beam with the upper cyclic load level 64.14% of the static flexural strength, sustained 596136 cycles and failed by the splitting of the steel rebar (Figure 7.6). Calculations showed that at this load level the stress in the steel rebar was 379.63MPa. The stress ratio used in this test was 4.93/64.14 =

Table 7.2. Number of cycles sustained by RC Beam (1200*150*100mm)

Load Amplitude Range (%)	Stress Ratio	Load Amplitude Range (kN)	Fatigue Life (cycles)
4.93% – 18.10%	0.272	1.5 - 5.5	>1000000
4.93 % – 41.12%	0.120	1.5 - 12.5	>1000000
4.93% – 64.14%	0.077	1.5 - 19.5	596136
4.93% – 80.59%	0.061	1.5 - 24.5	11458

0.077 and the stress range applied to the steel bar was 350MPa. The supplier's data sheet for this steel gave its fatigue life to be in excess of five million cycles at the cyclic stress range of 200 MPa and a stress ratio of 0.2. As the actual cyclic stress range was 350 MPa, fatigue failure of the steel rebar led to the failure of the RC beam.

The maximum service level stress range for straight deformed reinforcing bars according to ACI 215-74 (1992) is:

$$S_r = 161 - 0.33S_{min} \quad (7.1)$$

where S_r is the stress range in MPa and S_{min} is the magnitude of the minimum stress in MPa. In the above beam, this gives the maximum service level stress range to be just 151.4 MPa. In addition, Helgason and Hanson (1974) performed a statistical analysis of test data from deformed bars tested under axial cyclic loading in air. They concluded that the lowest average stress range on reinforcing steel that causes fatigue failure is 165 MPa and it is related to the fatigue life as follows

$$\log(N) = 6.969 - 0.0055\sigma_r \quad (7.2)$$

where N = number of cycles to failure; and σ_r = stress range applied to the steel in MPa.

By using equation (7.2), the number of cycles to failure for the beam loaded to 64.14% in which the reinforcement failed by fatigue works out to be 110662 cycles, which is lower than the number of cycles sustained by the beam (596136, Table 7.2). This may be explained as follows. At the locations of the flexural cracks in the RC beam the steel rebar experiences local stress concentrations. However, as the defect in the steel rebar from which the fatigue crack in it initiates is unlikely to coincide with one of these locations, the fatigue life of the steel rebar embedded in concrete will exceed that measured in air at the same stress range.

For the beam loaded at 80.59% the stress in the steel rebar was 477MPa and the stress ratio used in this test was 4.93/80.59 = 0.061 with a stress range 447.8MPa. The number of cycles until fatigue failure of rebar will be 32397 cycles according to equation (7.2). However, the failure of this beam occurred in the shear-flexural mode after just 11458

cycles (Table 7.2 and Figure 7.7), i.e. well before the fatigue failure of rebar. Even so, it is important to ensure that the reinforcing steel is not stressed beyond its fatigue endurance limit, calculated as per equation (7.1) or (7.2).

Figure 7.4 Beam sustained 1000000 cycles without any noticeable cracks

Figure 7.5 Beam sustained 1000000 cycles with some minor cracks

Figure 7.6 Beam sustained 596136 cycles and failed due to rebar fatigue

Figure 7.7 Flexural shear crack, beam sustained 11458 cycles

7.2.3.2 Compliance of Fatigue Test Beams

The compliance of fatigue test beams was calculated from their recorded load-displacement curves. Under cyclic loading the compliance can increase with time, if the material sustains internal or surface damage, e.g. micro-cracking. If there is no damage then the compliance should remain constant.

Figures 7.8 – 7.11 show the variation of the compliance with the number of cycles. It is clear from Figures 7.8 and 7.9 that the compliance of the test beams remained essentially constant up to 1,000,000 cycles attesting to a lack of damage growth under cycling, and hence to no fatigue failure.

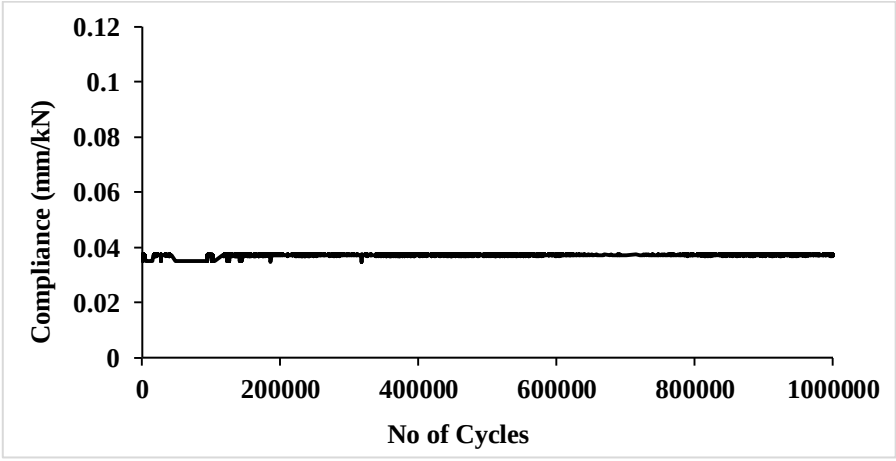

Figure 7.8 Compliance of RC beam during the ascending part of the cyclic load from 1.5 to 5.5 kN

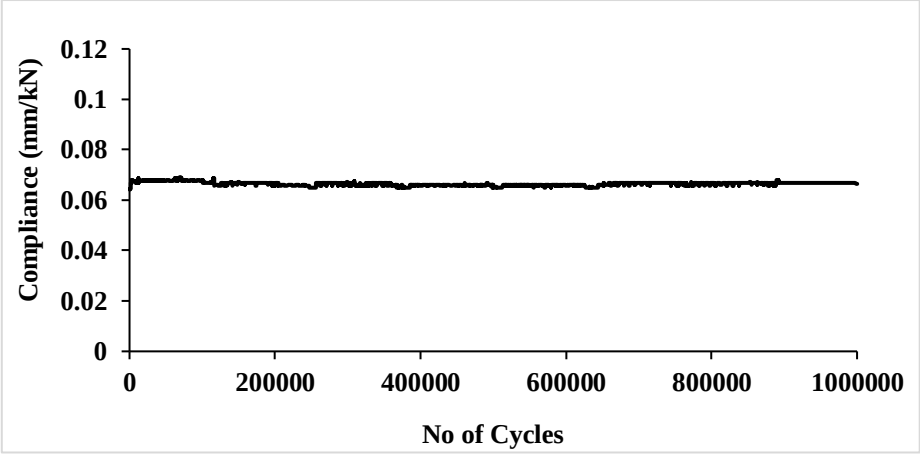

Figure 7.9 Compliance of RC beam during the ascending part of the cyclic load from 1.5 to 12.5 kN

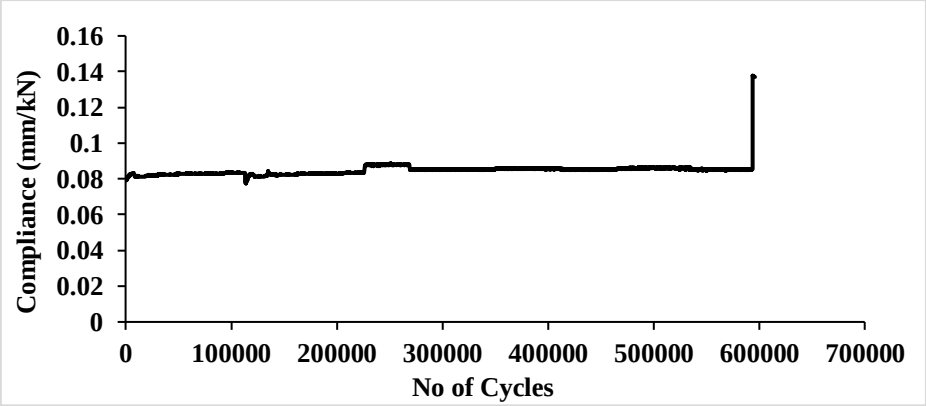

Figure 7.10 Compliance of RC beam during the ascending part of the cyclic load from 1.5 to 19.5 kN

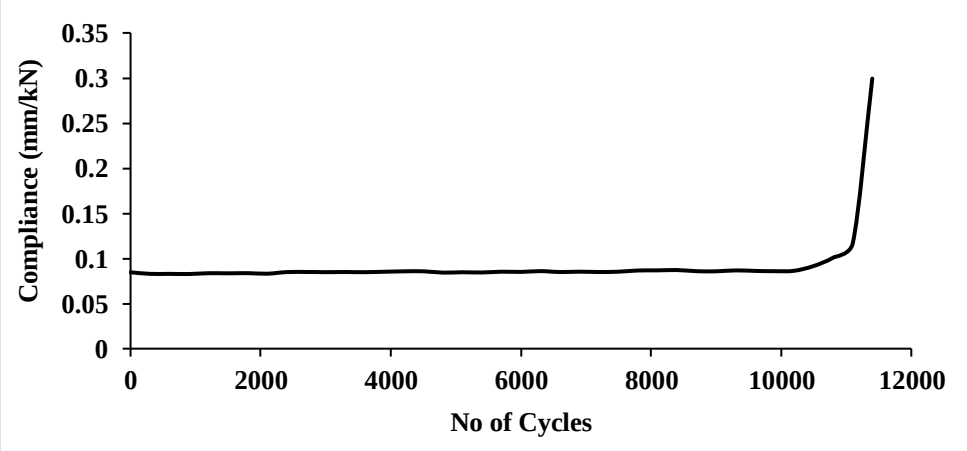

Figure 7.11 Compliance of RC beam during the ascending part of the cyclic load from 1.5 to 24.5 kN

The compliance of the other two specimens (Figure 7.10 and 7.11) increases slowly in the beginning as the number of cycles increases before suddenly reaching infinity at failure, attesting to a brittle kind of fatigue failure.

7.3 Retrofitting Reinforced Concrete Beams

Four reinforced concrete beams were cast (1200x150x100 mm) using the same mix quantities and procedure as described above for control beams. They were retrofitted with the UHPFRC strips. One of these beams was tested under static three-point bending and used as a control beam for the other three beams which were tested under different three-point bend cyclic load ranges.

7.3.1 UHPFRC Strips: Materials and Mix Preparation

The mix was prepared in a pan mixer using the mix proportions given in Chapter Five (Table 5.1). The quantity of mix prepared was calculated based on the volume of required specimens. The mixing followed the procedure recommended in (Benson and Karihaloo 2005a) by adding the finest constituent to the coarsest one (details can be found in Chapter Five, Section 5.3.1). The UHPFRC strips with dimensions 1030x100x35mm were cast in a larger steel mould partitioned for two strips. Then after 24 hours, they were demoulded and cured in a heated water tank for 9 days (for details, see Chapter Five, Section 5.3.3).

7.3.1.1 Preparation of Concrete Surfaces

To ensure good bond between the beam and the strip, the contacting surfaces were cleaned of any debris and roughened using an angle grinder to create a grid of diagonal grooves (2mm deep at a spacing of 50mm) (Figure 7.12).

Figure 7.12 A grid of diagonal grooves to roughen the surface for bonding

7.3.1.2 Adhesive Bonding of Strips

The strips were bonded to the prepared tension surface of the beams with a commercial thixotropic epoxy (Sikadur 31). The two parts of the adhesive were thoroughly mixed and applied to the tension side of the beam with a serrated trowel to a uniform thickness of 3mm. The strip was then placed on the adhesive and evenly pressed. To ensure good adhesion, pressure was applied by placing weights along the strip during the hardening of the adhesive for 24 hours (G-clamps can be used instead of weights).

7.3.2 Testing Retrofitted Beam

One of the retrofitted reinforced concrete beams was tested under three-point static bend over a clear span of 1000 mm following the same procedure as for the control bean

without retrofitting. Figure 7.13 shows the load-central deflection response of this retrofitted beam.

The failure mode of this beam, shown in Figure 7.14, can be regarded a flexural mode. The maximum load carried by this beam was 42.63 kN. This means that retrofitting by a single 35 mm thick strip of UHPFRC on the tension face has increased the load carrying capacity by approximately 40% (from 30.4 to 42.63 kN) and led to a failure mode transition from nearly brittle to ductile (cf. Figures 7.3 and 7.14).

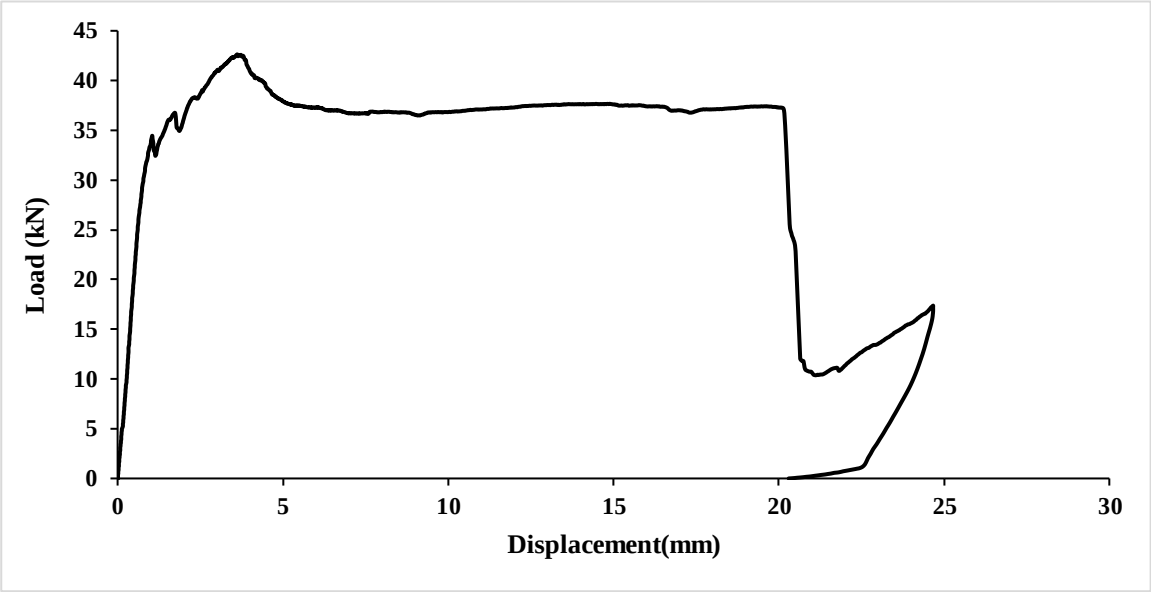

Figure 7.13 Static load-central deflection response of the retrofitted reinforced concrete beam

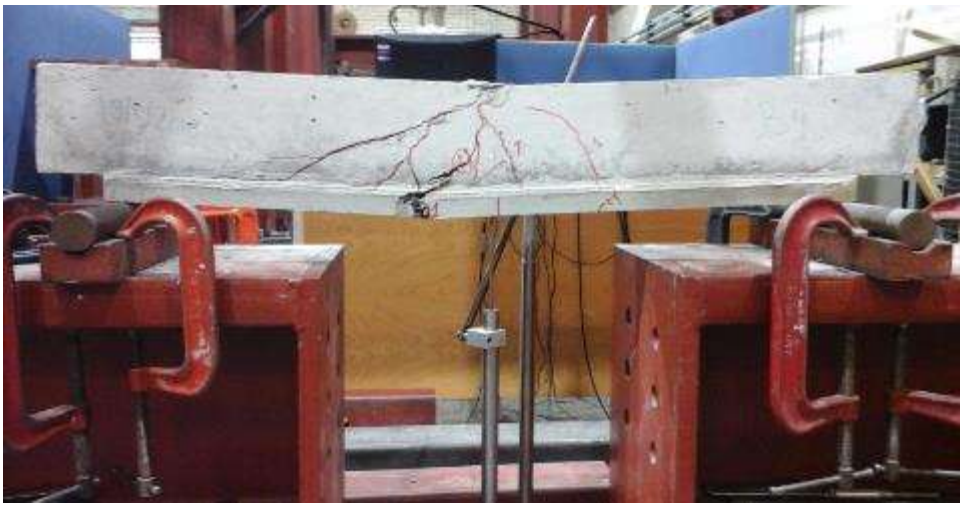

Figure 7.14 Flexural cracking in the beam retrofitted with 35mm thick strip

7.3.3 Fatigue of Retrofitted Concrete Beams

7.3.3.1 Flexural Fatigue Results

The remaining three retrofitted beams were subjected to cyclic three-point bending in a DARTEC 250 kN dynamic-static actuator. The central deflection was measured by a single LVDT placed underneath the beam at its mid-span. The beam was simply supported over a span of 1000 mm. To prevent the beam from moving laterally during the cyclic load application, the base plates of the roller simple supports were clamped (Figure 7.14).

The actuator was connected to a DARTEC 9600 Digital Feedback Controller. Four measurements were recorded on each beam: (1) the cyclic load; (2) the central deflection; (3) the time and (4) the number of cycles.

The sinusoidal load ranges were between 1.5 – 20 kN, 1.5 – 26 kN, and 1.5 – 35 kN, corresponding to 3.52 – 46.91%, 3.52 – 60.99% and 3.52 – 82.1% of the static three-

point strength. Table 7.3 gives the number of cycles sustained by each test specimen. The failure mode crack patterns of the specimens are shown in Figures 7.15 – 7.17.

The beam that was cycled to 46.91% of the static three-point failure load sustained one million cycles without failure (not even minute cracks were noticed on the tension surface of this specimen, Figure 7.15). The frequency of cyclic loading used was 5 Hz. The second beam that was cycled to 60.99% of the static three-point strength also sustained one million cycles without failure but a few hairline cracks were noticed in the middle third area, Figure 7.16 . This time the frequency of cyclic loading used was 3.5 Hz. The third beam was cycled to 82.1% at a frequency of 2.5Hz (Figure 7.17).

The cyclic load-central deflection curves for tested samples can be seen in Appendix C.

It is important to mention that the beam that was loaded to 82.1% of the static three-point strength failed by fatigue of the reinforcing steel bar. An explanation will be provided below after considering the compliance of the retrofitted beam.

Table 7. 3 Number of cycles sustained by retrofitted RC Beam (1200*150*100mm)

Load Amplitude Range (%)	Stress Ratio	Load Amplitude Range (kN)	Fatigue Life (cycles)
3.52 % – 46.91%	0.075	1.5 - 20	>1000000
3.52 % – 60.99%	0.058	1.5 - 26	>1000000
3.52 % – 82.10%	0.043	1.5 - 35	32100

Figure 7.15 Beam sustained 1000000 cycles without any noticeable cracks (maximum cyclic load level 46.91%)

Figure 7.16 Beam sustained 1000000 cycles with some cracks (maximum cyclic load level 60.99%)

Figure 7.17 Beam sustained 32100 cycles and failed by rebar fatigue (maximum cyclic load level 82.1%)

7.3.3.2 Compliance of Fatigue Test Beams

Figures 7.18 – 7.20 show the variation in the compliance of test beams with the number of cycles. The compliance of the beam subjected to the load range 1.5 to 20 kN remained practically unchanged with increasing number of cycles (Figure 7.18) confirming that there was no damage evolution or accumulation in this beam right up to 10^6 cycles (Figure 7.15). The compliance of the beam subjected to the load range 1.5 to 26 kN did change slightly (Figure 7.19) when cracks formed on the surface (Figure 7.16) that led to the well-known tension stiffening. However, overall this beam sustained 10^6 load cycles, despite the minor damage in the form of hairline flexural cracks.

The compliance of the beam subjected to the load range 1.5 to 35 kN increased noticeably after just 5000 cycles (Figure 7.20) due to the formation of a major flexural crack in the UHPFRC strip. As a result, the contribution of the strip to the tensile load carrying capacity is reduced and that of the reinforcing steel bar is increased. The reinforcing bar is therefore subjected to an elevated cyclic stress range of approximately 268.46 MPa (see Appendix D). This stress range is much higher than the allowable limit recommended by the supplier's data sheet (cyclic stress range 200 MPa for a fatigue life in excess of five million cycles), thus leading to the fatigue of the reinforcing bar (Figure 7.17).

As the minimum stress used was the same for all tested beams, the maximum service level stress range should be just 151.4MPa according to the ACI 215-74 (1992) (Equation 7.1), which is well below the actual stress range (268.46 MPa) in the test beam subjected to maximum load amplitude of 35 kN. Additional guidance is provided by Papakonstantinou et al. (2001) who have given a regression equation to estimate the fatigue life of beams retrofitted with GFRP sheets

$$\log(N) = 6.677 - 0.00613\sigma_r \quad (7.3)$$

From Equation (7.3) the number of cycles to failure for the beam cycled up to 82.1% will be 107475 cycles, whereas the beam sustained only 32100 cycles. This is no doubt due to the fact that GPRP makes a much larger contribution to the tensile load carrying capacity than the UHPFRC material used in this work for retrofitting.

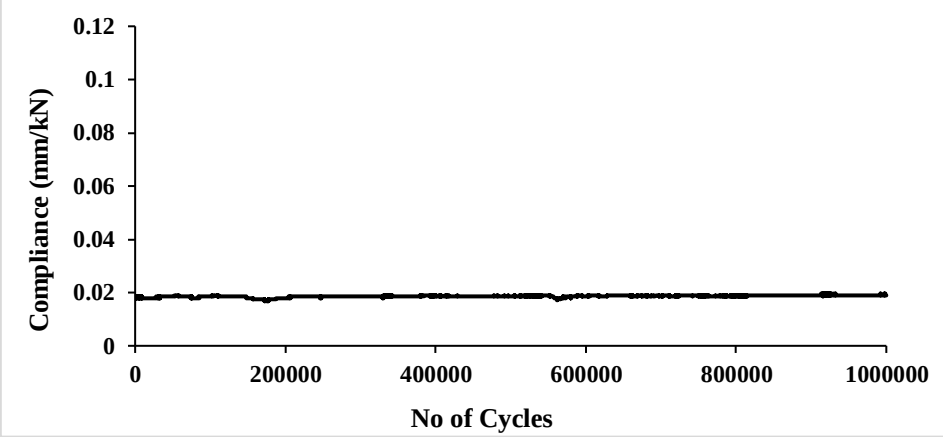

Figure 7.18 Compliance of RC beam during the ascending part of the cyclic load from 1.5 to 20 kN

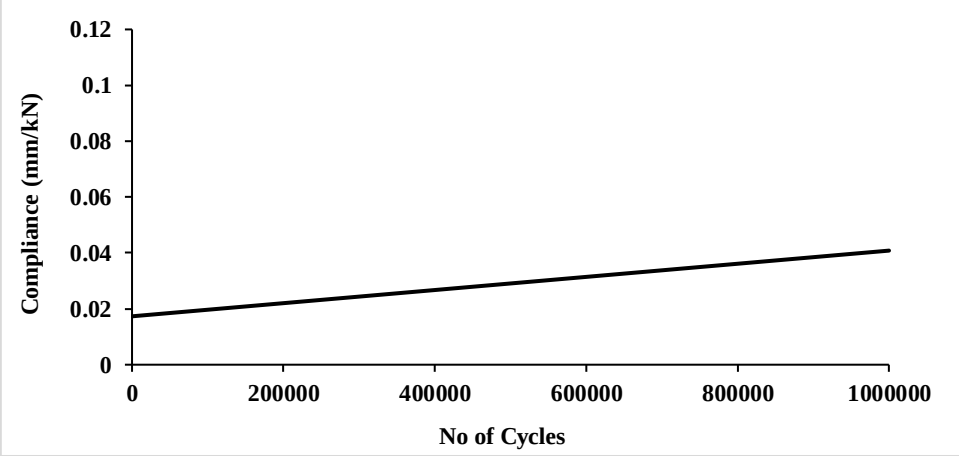

Figure 7.19 Compliance of RC beam during the ascending part of the cyclic load from 1.5 to 26 kN

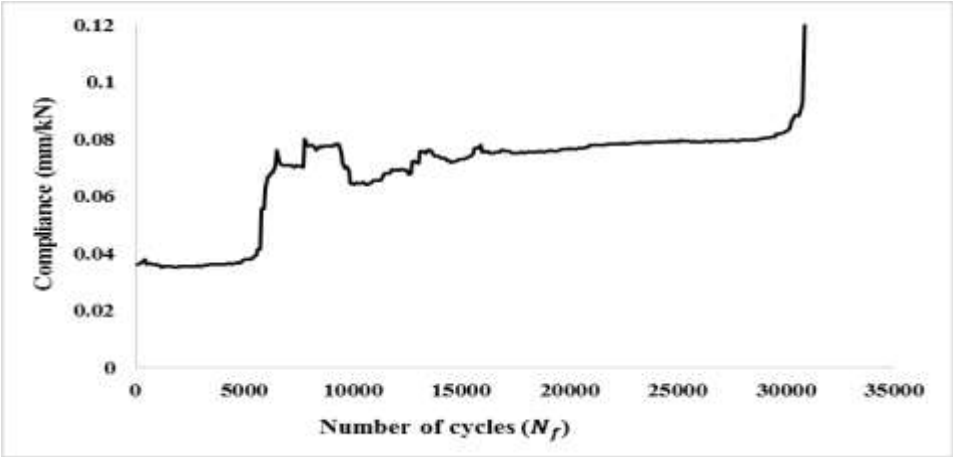

Figure 7.20 Compliance of RC beam during the ascending part of the cyclic load from 1.5 to 35 kN

It can be concluded from this limited number of fatigue tests that the endurance limit of RC beams retrofitted with a UHPFRC strip is approximately 60 % of static flexural strength, while the endurance limit of the RC beams without retrofitting, as shown above, is just 40 % of static flexural strength. It should be noted that all test beams (i.e. beams with or without retrofitting) were subjected to cyclic loading with a non-zero mean stress. What is more, the mean stress increased (the stress ratio decreased) with increasing maximum load amplitude, as the minimum load amplitude was held constant. Thus, the fatigue endurance limit under zero mean stress cyclic loading would be higher than that stated above.

7.4 Estimation of the Number of Cycles Until Failure

To have some idea of what is the fatigue life of RC beams with and without the UHPFRC strips under a given cyclic load range, the procedure that has been reported in Chapter Six (Section 6.8) will be followed in this section.

The variation in the compliance of the specimens will be used to predict the fatigue life for each specimen using the initial compliance c_i and the rate of change of the compliance with the number of cycles (Figures 7.8 − 7.11 and 7.18 − 7.20), and using Equations (6.4 and 6.5) from Chapter 6 (Section 6.8).

The predicted number of cycles for each specimen with the stress range is tabulated in Tables 7.4 and 7.5 for RC beams without and with retrofitting, respectively.

Table 7.4 shows that the predicted number of cycles to failure for RC beams without retrofitting is well above that recorded during the test which was terminated at one million cycles up to the maximum load amplitude of 12.5 kN, i.e. approximately 40% of the ultimate static three-point flexural load of 30 kN.

Likewise, Table 7.5 shows that the predicted number of cycles to failure for retrofitted RC beams is also well above that recorded during the test up to the maximum load amplitude of 20 kN, i.e. approximately 47% of the ultimate static flexural load of 42 kN. Even at the maximum load of 26kN, i.e. 60.99% of ultimate static flexural load the number of cycles to failure is one million, i.e. the same number of cycles as this retrofitted beam sustained during testing.

Table 7.4 Predicted number of cycles with load amplitude range for RC beams without retrofitting

Stress range	Load Amplitude Range (kN)	No of Cycles
4.93% – 18.10%	1.5 - 5.5	131×10^6
4.93% – 41.12%	1.5 - 12.5	25.735×10^6
4.93% – 64.14%	1.5 - 19.5	593700
4.93% – 80.59%	1.5 - 24.5	11400

Table 7.5 Predicted number of cycles with load amplitude range for retrofitted RC beams

Stress range	Load Amplitude Range (kN)	No of Cycles
3.52 % – 46.91%	1.5 - 20	10.637×10^6
3.52 % – 60.99%	1.5 - 26	10^6
3.52 % – 82.10%	1.5 - 35	32100

7.5 Concluding remarks

- Retrofitting with a 35mm thick UHPFRC strip increased the static three-point flexural strength from approximately 30 kN to approximately 42 kN, i.e. by about 40%.
- Retrofitting with a 35mm thick UHPFRC strip improves the endurance limit from approximately 40% to approximately 60% of the static three-point flexural strength. In terms of loads, this corresponds to an increase from approximately 12kN to approximately 26 kN in the upper cyclic load amplitude (the lower limit is 1.5 kN in both cases), i.e. an increase of more than 116%.

- Retrofitting with a UHPFRC strip is therefore far more effective under cyclic than static loading!
- The above increase in the endurance limit is for cyclic loading with a non-zero mean stress. What is more, the mean stress increased (the stress ratio decreased) with increasing maximum load amplitude, as the minimum load amplitude was held constant. Thus, the fatigue endurance limit under zero mean stress cyclic loading would be higher than that stated above.
- In choosing the upper cyclic load amplitude it is important to bear in mind the fatigue endurance limit of the reinforcing steel. For example, for the reinforcing steel used in the current research the supplier's data sheet stated that the cyclic stress range is only 200 MPa at a stress ratio of 0.2 for bars less than 16 mm in diameter. However, as the smallest stress ratio in our test on RC beam without retrofitting that sustained 10^6 cycles was 4.93/41.12 = 0.12 and on retrofitted beam was 3.52/60.99 = 0.058, the allowable cyclic stress range on the reinforcing steel would be above 200 MPa.
- An indication of the expected fatigue life under a given cyclic load range was obtained from the recorded variation in the compliance, since the tests were terminated at one million cycles.

Chapter Eight

Summary of Results, Conclusions and Recommendations for Future Work

8.1 Summary of Results and Conclusions

- A self-compacting UHPFRC based on CARDIFRC vibrated Mix II was developed and fully characterised from both the mechanical and fracture points of view. As expected, the resulting UHPFRC has inferior compressive, tensile and flexural strengths than the original CARDIFRC Mix II. This is due to the absence of thin small brass-coated steel fibres (4.5% by volume; 6 mm long) in the UHPFRC. The UHPFRC is however much tougher thanks to the use of a larger volume fraction (2.5% against 1.5%) of longer steel fibres (30 mm against 13 mm). This UHPFRC has a compressive strength of 148 MPa against 200 MPa of the original vibrated Mix II and a splitting strength 18.5 MPa against 24 MPa, but it has a much higher energy absorption capacity, i.e., toughness in excess of 36,000 N/m against 18,000 N/m of the original vibrated Mix II.
- The parameters of the bi-linear stress-crack opening relation of this UHPFRC were obtained by using an inverse approach for crack growth from a pre-existing notch. The predicted load-deflection and load-CMOD curves of notched beams have been shown to be in very good agreement with the recorded experimental results, except in the pre-peak non-linear region.
- The flexural fatigue behaviour of the self-compacted UHPFRC has been investigated on thin strip specimens of 35 mm thickness and displayed as S-N curves. The fatigue life of the self-compacting UHPFRC is well in excess of one million cycles and its endurance limit is around 80% of its static three-point flexural strength (24.36 MPa), i.e. approximately 19 MPa, at a mean stress level of the cyclic loading of 44.5% of this strength (10.85 MPa) . However, this endurance limit reduces crucially to approximately 64% of the corresponding

lower static three-point flexural strength (22.02 MPa), i.e. approximately to 14 MPa at a mean stress level of approximately 8 MPa when the fibre distribution is non-uniform. This was confirmed by the examination of the failure surfaces of the specimens (chapter Six) where fibres were poorly distributed in the failure surface of the specimens with regions of low or no fibres. Thus, the role of fibre distribution is vital in the fatigue performance; uniform distribution of fibres ensures that the material has the above high fatigue endurance limit.

- The variation in compliance of a specimen is an indicator of the internal damage development due to fatigue loading. Therefore, the variation in compliance has been used as an indication of the expected fatigue life under a given cyclic load range, since the tests were terminated at one million cycles. The results show that the predicted number of cycles to failure are well above the one million cycles at which the tests were terminated.
- The Goodman rule has been employed in an inverse manner to calculate the stress range with zero mean stress $\Delta\sigma_0$ from equation (6-3) corresponding to the actual cyclic stress range with non-zero mean stress $\Delta\sigma_{\sigma m}$ used in the tests. The results illustrate that the fatigue life under cyclic stress range with non-zero mean stress is akin to fatigue life under a much larger cyclic stress range with zero mean stress (Figure 6.4).
- The performance of RC beams retrofitted with self-compacting UHPFRC strips under three-point bend cyclic loading has been studied. It has been found that retrofitting the RC beams with a thin UHPFRC strip on the tension face increases their endurance limit under a non-zero mean stress cyclic loading from approximately 40% to approximately 60% of their static three-point flexural strength. In terms of loads, this corresponds to an increase from approximately

12 kN to approximately 26 kN in the upper cyclic load amplitude (the lower limit is 1.5 kN in both cases), i.e. an increase of more than 116%. Moreover, the retrofitted beams behave as a composite structure with no delamination of the retrofit strip being observed in any of the fatigue tests. The variation in compliance has been also used as an indication of the expected fatigue life for RC beams retrofitted with the UHPFRC strips under a given cyclic load range. The results show that the predicted number of cycles to failure are well above the one million cycles at which the tests were terminated.

- It is important to bear in mind the fatigue endurance limit of the reinforcing steel when the upper cyclic load amplitude is chosen. For this, the steel supplier's data sheet for the reinforcing steel should be used.

8.2 Recommendations for Future Work

- The pre-peak non-linearity is known to be a result of diffuse micro-cracking whose density increases as the load is increased from the linear elastic proportional limit to the peak load. Since the non-linear hinge assumes that the response is linear elastic up to the peak load the pre-peak non-linear strain-hardening cannot be captured by the hinge model. Therefore, it is recommended to consider this pre-peak non-linearity by taking into account the effect of micro-cracks on the reduction in the stiffness using for example the micromechanical formulation described in Budiansky and Connell, (1976).
- It is recommended that the flexural fatigue behaviour of RC beams retrofitted with the new UHPFRC version of CARDIFRC Mix II specimens be modelled

to verify the experimental work. For this, the post-peak bilinear stress-crack opening relationship developed in this thesis will be found helpful.

- It will be valuable to retrofit the RC beams with strips on the sides and monitor its influence on the flexural behaviour of the retrofitted RC beams under static and cyclic loading.
- As the self-compacting UHPFRC has inferior compressive, tensile and flexural strengths than the original vibrated CARDIFRC Mix II due to the absence of thin small brass-coated steel fibres it would be interesting to add inexpensive short fibres to the mix to increase the mechanical properties of the UHPFRC bearing in mind the workability of the mix.
- It is recommended to conducted many more tests in order to be sure that the results of the limited number of tests reported in this thesis are indeed representative of the developed self-compacting UHPFRC.
- It is recommended that the RC beams be retrofitted with casting strips on tension faces using fresh UHPFRC. As this material is self-compacting, the casting should be easy, but it would require temporary formwork.

List of References

List of References

- Abdalla, H.M. and Karihaloo, B.L., 2003. Determination of size-independent specific fracture energy of concrete from three point-bend and wedge splitting tests. *Magazine of Concrete Research*, 55(2), pp.133-141.
- Abdalla, H.M. and Karihaloo, B.L., 2004. A method for constructing the bilinear tension softening diagram of concrete corresponding to its true fracture energy. *Magazine of Concrete Research*, 56(10), pp.597-604.
- Adhikary, B.B. and Mutsuyoshi, H., 2006. Shear strengthening of RC beams with web-bonded continuous steel plates. *Construction and Building Materials*, *20*(5), pp.296-307.
- Aïtcin, P.C., 20004. *High Performance Concrete*. E & FN SPON, London and New York.
- Alaee, F.J. and Karihaloo, B.L., 2003a. Retrofitting of reinforced concrete beams with CARDIFRC. *ASCE Journal of Composites for Construction*, 7(3), pp.174-186.
- Alaee, F.J. and Karihaloo, B.L., 2003b. Fracture model for flexural failure of beams retrofitted with CARDIFRC. *ASCE Journal of Engineering Mechanics*, 129(9), pp.1028-1038.
- Alaee, F.J., 2002. *Retrofitting of concrete structures using high performance fibre reinforced cementitious composite (HPFRCC)*. PhD Thesis, Cardiff University, UK.
- Al-Azzawi, B.S. and Karihaloo, B.L., 2017a. Mechanical and fracture properties of a self-compacting version of CARDIFRC Mix II. *Sādhanā*, doi: 10.1007/s12046-017-0641-9, 42(5), pp.795-803.

- Al-Azzawi, B.S. and Karihaloo, B.L., 2017b. Flexural fatigue behavior of a self-compacting ultrahigh performance fiber-reinforced concrete. *ASCE Journal of Materials in Civil Engineering*, doi: 10.1061/ (ASCE) MT. 1943-5533.0002051, 29(11*)*, p.04017210.

- Al-Sulaimani, G.J., Sharif, A., Basunbul, I.A., Baluch, M.H. and Ghaleb, B.N., 1994. Shear repair for reinforced concrete by fiberglass plate bonding. *ACI Structural Journal*, 91(4), pp.458-464.

- Altin, S., Anil, Ö. and Kara, M.E., 2005. Improving shear capacity of existing RC beams using external bonding of steel plates. *Engineering Structures*, 27(5), pp.781-791.

- American Concrete Institute-ACI Committee, 1991. ACI 446.1R-91: *Fracture mechanics of concrete: Concepts, models and determination of material properties*. Detroit, USA.

- American Concrete Institute-ACI Committee, 1992. ACI 215R-74: *Considerations for Design of Concrete Structures Subjected to Fatigue Loading*. Detroit, USA.

- American Concrete Institute-ACI Committee, 1996. ACI 544.1 R-96: *State-of-the-Art Report on Fiber Reinforced Concrete*. Detroit, USA.

- An, W., Saadatmanesh, H. and Ehsani, M.R., 1991. RC beams strengthened with FRP plates. II: Analysis and parametric study. *ASCE Journal of Structural Engineering*, 117(11), pp.3434-3455.

- Arslan, G., Sevuk, F. and Ekiz, I., 2008. Steel plate contribution to load-carrying capacity of retrofitted RC beams. *Construction and Building Materials*, 22(3), pp.143-153.

- Ashby, M.F. and Jones, D.R., 1996. *Engineering Materials 1: An Introduction to Their Properties and Applications*. 2nd Ed., Butterworth-Heinemann, USA.

- Aykac, S., Kalkan, I., Aykac, B., Karahan, S. and Kayar, S., 2012. Strengthening and repair of reinforced concrete beams using external steel plates. *ASCE Journal of Structural Engineering*, 139(6), pp.929-939.

- Bache, H.H., 1981. Densified cement ultra-fine particle-based materials. *CBL Report No. 40*, Aalborg Portland, Denmark, pp.35.

- Bache, H.H., 1987. Introduction to compact reinforced composite. *Nordic Concrete Research*, (6), pp.19-33.

- Bakis, C.E., Bank, L.C., Brown, V., Cosenza, E., Davalos, J.F., Lesko, J.J., Machida, A., Rizkalla, S.H. and Triantafillou, T.C., 2002. Fiber-reinforced polymer composites for construction—State-of-the-art review. *ASCE Journal of Composites for Construction*, 6(2), pp.73-87.

- Balaguru, P.N. and Shah, S.P., 1992. *Fiber-Reinforced Cement Composites*. McGraw - Hill, New York, USA.

- Ballatore, E. and Bocca, P., 1997. Variations in the mechanical properties of concrete subjected to low cyclic loads. *Cement and Concrete Research*, 27(3), pp.453-462.

- Baluch, M.H., Qureshy, A.B. and Azad, A.K., 1989. Fatigue crack propagation in plain concrete. In: *International Conference on Fracture of Concrete and Rock, SEM/RLEM, Shah, S.P., Swartz, S.E. (eds.)*, Springer, New York, pp. 80-87.

- Banthia, N. and Gupta, R., 2004. Hybrid fiber reinforced concrete (HyFRC): fiber synergy in high strength matrices. *Materials and Structures*, 37(10), pp.707-716.

- Barenblatt, G.I., 1959. The formation of equilibrium cracks during brittle fracture. General ideas and hypotheses. Axially-symmetric cracks. *Journal of Applied Mathematics and Mechanics*, 23(3), pp.622-636.

- Barluenga, G., 2010. Fiber–matrix interaction at early ages of concrete with short fibers. *Cement and Concrete Research*, 40(5), pp.802-809.

- Barnes, R.A. and Mays, G.C., 1999. Fatigue performance of concrete beams strengthened with CFRP plates. *ASCE Journal of Composites for Construction*, 3(2), pp.63-72.

- Barnes, R.A. and Mays, G.C., 2006. Strengthening of reinforced concrete beams in shear by the use of externally bonded steel plates: Part 1–Experimental programme. *Construction and Building Materials*, 20(6), pp.396-402.

- Barnes, R.A., Baglin, P.S., Mays, G.C. and Subedi, N.K., 2001. External steel plate systems for the shear strengthening of reinforced concrete beams. *Engineering Structures*, 23(9), pp.1162-1176.

- Bazant, Z.P. and Oh, B.H., 1983. Crack band theory for fracture of concrete. *Materials and Structures*, 16(3), pp.155-177.

- Bazant, Z.P. and Planas, J., 1997. *Fracture and Size Effect in Concrete and Other Quasibrittle Materials* (Vol. 16). CRC Press, USA.

- Bazant, Z.P. and Schell, W.F., 1993. Fatigue fracture of high-strength concrete and size effect. *ACI Materials Journal*, 90, pp.472-472.

- Benson, S.D.P., 1999. *Retrofitting damaged reinforced concrete flexural members with HPFRCC.* MEng Thesis, Cardiff University, UK**.**

- Benson, S.D.P., 2003. *CARDIFRC-Development and constitutive behaviour*. PhD. Thesis, Cardiff University, UK.

- Benson, S.D.P., and Karihaloo, B.L., 2005a. CARDIFRC®-Development and mechanical properties. Part 1: development and workability. *Magazine of Concrete Research*, 57(6), pp.347-352.

- Benson, S.D.P., and Karihaloo, B.L., 2005b. CARDIFRC®-Development and mechanical properties. Part III: Uniaxial tensile response and other mechanical properties. *Magazine of Concrete Research*, 57(8), pp.433-443.

- Benson, S.D.P., Nicolaides, D. and Karihaloo, B.L., 2005. CARDIFRC®–Development and mechanical properties. Part II: Fibre distribution. *Magazine of Concrete Research*, 57(7), pp.421-432.

- Bentur, A. and Mindess, S., 1986. The effect of concrete strength on crack patterns. *Cement and Concrete Research*, 16(1), pp.59-66.

- Bentur, A. and Mindess, S., 2007. *Fiber Reinforced Cementitious Composites*, 2nd Ed., Taylor and Francis, London.

- Bilby, B.A., Cottrell, A.H. and Swinden, K.H., 1963. The spread of plastic yield from a notch. *Proceedings of the Royal Society of London A: Mathematical, Physical and Engineering Sciences*, The Royal Society, 272(1350*)*, pp. 304-314.

- Biswal, K.C. and Sadangi, S.C., 2011. Effect of superplasticizer and silica fume on properties of concrete. In: *The Conference Trivandrum, Kerela*, National Institute of Technology- Rourkela, India.

- Bonen, D. and Shah, S.P., 2005. Fresh and hardened properties of self-consolidating concrete. *Progress in Structural Engineering and Materials*, DOI:10.1002/pse.186, 7(1), pp.14-26.

- Bonneau, O., Lachemi, M., Dallaire, E., Dugat, J. and Aïtcin, P.C., 1997. Mechanical properties and durability of two industrial reactive powder concretes. *ACI Materials Journal*, 94(4), pp.286-290.

- Bonneau, O., Poulin, C., Dugat, M. and Tcin, P.C.A., 1996. Reactive powder concretes: from theory to practice. *ACI Concrete International*, 18(4), pp.47-49.
- Bragov, A.M., Petrov, Y.V., Karihaloo, B.L., Konstantinov, A.Y., Lamzin, D.A., Lomunov, A.K. and Smirnov, I.V., 2013. Dynamic strengths and toughness of an ultra-high performance fibre reinforced concrete. *Engineering Fracture Mechanics*, 110, pp.477-488.
- Brandt, A.M., 2008. Fibre reinforced cement-based (FRC) composites after over 40 years of development in building and civil engineering. *Composite Structures*, 86(1), pp.3-9.
- Brown, W. and Srawley, J., 1966. Plane strain crack toughness testing of high strength metallic materials. *ASTM Special Technical Publication STP410*, Philadelphia.
- BS 1881-118 1983. Testing concrete: method for determination of flexural strength. British Standards publication.
- BS 1881-121 1983. Testing concrete: Method for determination of static modulus of elasticity in compression. British Standards publication.
- BS EN 12350-8, 2010. Testing fresh concrete, Part 8: Self-compacting concrete-slump-flow test. British Standards publication.
- BS EN 12390-3. 2009. Testing hardened concrete, Part 3: Compressive strength of test specimens. British Standards publication.
- BS EN 12390-6 2009. Testing hardened concrete, Part 6: Tensile splitting strength of test specimens. British Standards publication.
- BS EN 206-9, 2010. Concrete, Part 9: Additional rules for self-compacting concrete (SCC). British Standards publication.

- Budiansky, B. and O'connell, R.J., 1976. Elastic moduli of a cracked solid. *International Journal of Solids and Structures*, 12(2), pp.81-97.
- Buyukozturk, O. and Hearing, B., 1998. Failure behavior of precracked concrete beams retrofitted with FRP. *ASCE Journal of Composites for Construction*, 2(3), pp.138-144.
- Buyukozturk, O., Gunes, O. and Karaca, E., 2004. Progress on understanding debonding problems in reinforced concrete and steel members strengthened using FRP composites. *Construction and Building Materials*, 18(1), pp.9-19.
- Cachim, P.B., 1999. *Experimental and numerical analysis of the behaviour of structural concrete under fatigue loading with applications to concrete pavements*. PhD Thesis. University of Porto, Portugal.
- Cachim, P.B., Figueiras, J.A. and Pereira, P.A., 2002. Fatigue behavior of fiber-reinforced concrete in compression. *Cement and Concrete Composites*, 24(2), pp.211-217.
- Caldarone, M.A., 2008. *High-Strength Concrete: A Practical Guide*. Taylor and Francis, London .
- Campbell, F.C., 2008. *Elements of Metallurgy and Engineering Alloys.* ASM International, USA.
- Cangiano, S., Plizzari, G.A. and Slowik, V., 1998. Experimental investigations into the fatigue crack growth in concrete. In: *Proceedings Fracture Mechanics of Concrete Structures (FRAMCOS-3)*, AEDIFICATIO, D-79104 Freiburg, Germany, pp.645-654.
- Caverzan, A., Cadoni, E. and Di Prisco, M., 2012. Tensile behaviour of high performance fibre-reinforced cementitious composites at high strain rates. *International Journal of Impact Engineering*, 45, pp.28-38.

- Chen, X., Bu, J., Fan, X., Lu, J. and Xu, L., 2017. Effect of loading frequency and stress level on low cycle fatigue behavior of plain concrete in direct tension. *Construction and Building Materials*, 133, pp.367-375.

- Choi, S.J., Mun, J.S., Yang, K.H. and Kim, S.J., 2016. Compressive fatigue performance of fiber-reinforced lightweight concrete with high-volume supplementary cementitious materials. *Cement and Concrete Composites*, 73, pp.89-97.

- Deeb, R., Karihaloo, B.L. and Kulasegaram, S., 2014. Reorientation of short steel fibres during the flow of self-compacting concrete mix and determination of the fibre orientation factor. *Cement and Concrete Research*, 56, pp.112-120.

- Derkowski, W. and Zych, T., 2004. Modern composite materials for reinforcing building structures. *Technical Journal Construction*, 101, pp.15-25.

- Dong, J., Wang, Q. and Guan, Z., 2013. Structural behaviour of RC beams with external flexural and flexural–shear strengthening by FRP sheets. *Composites Part B: Engineering*, 44(1), pp.604-612.

- Dowling, N.E., 2012. *Mechanical Behavior of Materials: Engineering Methods for Deformation, Fracture, and Fatigue*. 4th Ed. Pearson, USA

- Duan, K., Hu, X. and Wittmann, F.H., 2003. Boundary effect on concrete fracture and non-constant fracture energy distribution. *Engineering Fracture Mechanics*, 70(16), pp.2257-2268.

- Duan, K., Hu, X. and Wittmann, F.H., 2007. Size effect on specific fracture energy of concrete. *Engineering Fracture Mechanics*, 74(1), pp.87-96.

- Dugat, J., Roux, N. and Bernier, G., 1996. Mechanical properties of reactive powder concretes. *Materials and Structures*, 29(4), pp.233-240.

- Dugdale, D.S., 1960. Yielding of steel sheets containing slits. *Journal of the Mechanics and Physics of Solids*, 8(2), pp.100-104.

- Ekenel, M., Rizzo, A., Myers, J.J. and Nanni, A., 2006. Flexural fatigue behavior of reinforced concrete beams strengthened with FRP fabric and precured laminate systems. *ASCE Journal of Composites for Construction*, 10(5), pp.433-442.

- El-Dieb, A.S. and Taha, M.R., 2012. Flow characteristics and acceptance criteria of fiber-reinforced self-compacted concrete (FR-SCC). *Construction and Building Materials*, 27(1), pp.585-596.

- Elices, M., Guinea, G.V. and Planas, J., 1992. Measurement of the fracture energy using three-point bend tests: Part 3-Influence of cutting the P-δ tail. *Materials and Structures*, 25(6), pp.327-334.

- Esfahani, M.R., Kianoush, M.R. and Tajari, A.R., 2007. Flexural behaviour of reinforced concrete beams strengthened by CFRP sheets. *Engineering Structures*, 29(10), pp.2428-2444.

- Farhat, F.A., 2004. *Performance of concrete structures retrofited with CARDIFRC after thermal cycling*. PhD Thesis, Cardiff University, UK.

- Farhat, F.A., Nicolaides, D., Kanellopoulos, A. and Karihaloo, B.L., 2007. High performance fibre-reinforced cementitious composite (CARDIFRC)–Performance and application to retrofitting. *Engineering Fracture Mechanics*, 74(1), pp.151-167.

- Farhat, F.A., Nicolaides, D., Kanellopoulos, A. and Karihaloo, B.L., 2010. Behavior of RC beams retrofitted with CARDIFRC after thermal cycling. *ASCE Journal of Materials in Civil Engineering*, 22(1), pp.21-28.

- Ferrara, L., Ozyurt, N. and Di Prisco, M., 2011. High mechanical performance of fibre reinforced cementitious composites: the role of "casting-flow induced" fibre orientation. *Materials and Structures*, 44(1), pp.109-128.

- FIB Model Code, 2010. Fibre reinforced concrete. First complete draft. *International Federation for Structural Concrete*, Bulletin, 55, Switzerland.

- Gaimster, R. and Dixon, N., 2003. *Self-Compacting Concrete. Advance Concrete Technology: Processes*. Butterworth- Heinemann, London, UK.

- Gao, B., Leung, C.K. and Kim, J.K., 2007. Failure diagrams of FRP strengthened RC beams. *Composite Structures*, 77(4), pp.493-508.

- Gao, L. and Hsu, C.T.T., 1998. Fatigue of concrete under uniaxial compression cyclic loading. *ACI Materials Journal*, 95(5), pp.575-581.

- Gettu, R., Gardner, D.R., Saldivar, H. and Barragán, B.E., 2005. Study of the distribution and orientation of fibers in SFRC specimens. *Materials and Structures*, 38(1), pp.31-37.

- Goel, S. and Singh, S.P., 2014. Fatigue performance of plain and steel fibre reinforced self compacting concrete using S–N relationship. *Engineering Structures*, 74, pp.65-73.

- Gopalaratnam, V.S. and Shah, S.P., 1986. Properties of steel fiber reinforced concrete subjected to impact loading. *ACI Journal Proceedings*, 83 (1), pp. 117-126.

- Grace, N.F., Sayed, G.A., Soliman, A.K. and Saleh, K.R., 1999. Strengthening reinforced concrete beams using fiber reinforced polymer (FRP) laminates. *ACI Structural Journal*, 96(5), pp.865-874.

- Griffith, A.A., 1921. The phenomena of rupture and flow in solids. *Philosophical Transactions of the Royal Society of London. Series A*, 221, pp.163-198.

- Grünewald, S., 2004. *Performance-based design of self-compacting fibre reinforced concrete*. PhD Thesis, Delft University, Netherlands.
- Grunewald, S., Shionaga, R. and Walraven, J.C., 2013. Self-compacting fibre reinforced concrete applied in thin plates. In: *7th RILEM International Conference on Self-Compacting Concrete and 1st RILEM International Conference on Rheology and Processing of Construction Materials, Roussel N., and Bessaies-Bey H. (eds.),* RILEM Publications, Paris, France, pp. 341-348.
- Grzybowski, M. and Meyer, C., 1993. Damage accumulation in concrete with and without fiber reinforcement. *ACI Materials Journal*, 90(6), pp.594-604.
- Habel, K., Denarié, E. and Brühwiler, E., 2006. Structural response of elements combining ultrahigh-performance fiber-reinforced concretes and reinforced concrete. *ASCE Journal of Structural Engineering*, 132(11), pp.1793-1800.
- Heffernan, P.J. and Erki, M.A., 2004. Fatigue behavior of reinforced concrete beams strengthened with carbon fiber reinforced plastic laminates. *ASCE Journal of Composites for Construction*, 8(2), pp.132-140.
- Helagson, T. and Hanson, J.M., 1974. Investigation of design factors affecting fatigue strength of reinforcing bars-statistical analysis. *ACI Special Publication*, 41, pp.107-138.
- Hertzberg R. W., 1995. *Deformation and Fracture Mechanics of Engineering Materials*, 4th Ed., John Wiley & Sons Inc, USA.
- Hillerborg, A., 1980. Analysis of fracture by means of the fictitious crack model, particularly for fibre reinforced concrete. *International Journal of Cement Composites*, 2(4), pp.177-184.
- Hillerborg, A., 1985. The theoretical basis of a method to determine the fracture energy G_F of concrete. *Materials and Structures*, 18(4), pp.291-296.

- Hillerborg, A., Modéer, M. and Petersson, P.E., 1976. Analysis of crack formation and crack growth in concrete by means of fracture mechanics and finite elements. *Cement and Concrete Research*, 6(6), pp.773-781.
- Holmen, J.O., 1982. Fatigue of concrete by constant and variable amplitude loading. *ACI Special Publication*, 75, pp.71-110.
- Hoy, C.W. and Bartos, P.J.M., 1999. Interaction and packing of fibres: effects on the mixing process. In: *Proceedings 6: 3rd International RILEM Workshop on High Performance Fiber Reinforced Cement Composites (HPFRCC 3)*, *Reinhardt, H.W. and Naaman, A.E. (eds)*, RILEM Publications, Mainz, Germany, 3, p. 181-191.
- Hsu, T.T.C., 1981. Fatigue of plain concrete. *ACI Journal Proceedings*.78 (4), pp. 292-305.
- Hu, X. and Duan, K., 2004. Influence of fracture process zone height on fracture energy of concrete. *Cement and Concrete Research*, 34(8), pp.1321-1330.
- Hu, X. and Wittmann, F., 2000. Size effect on toughness induced by crack close to free surface. *Engineering Fracture Mechanics*, 65(2), pp.209-221.
- Hu, X., 1995. *Fracture Process Zone and Strain Softening in Cementitious Materials*. ETH Building Materials Report No.1, ETH Switzerland, AEDIFICATIO, Freiburg.
- Hu, X.Z. and Wittmann, F.H., 1992. Fracture energy and fracture process zone. *Materials and Structures*, 25(6), pp.319-326.
- Inglis, C.E., 1913. Stresses in a plate due to the presence of cracks and sharp corners. *Transactions of the Institute of Naval Architects*, 55, pp. 219-241
- Irwin, G.R., 1957. Analysis of stresses and strains near the end of a crack traversing a plate. *Journal of Applied Mechanics*, 24(3), pp.361-364.

- Islam, M.R., Mansur, M.A. and Maalej, M., 2005. Shear strengthening of RC deep beams using externally bonded FRP systems. *Cement and Concrete Composites*, 27(3), pp.413-420.
- Jain, N. and Sikka, V.K., 2015. Strengthening of RC Beams with Externally Bonded CFRPs. *IOSR Journal of Mechanical and Civil Engineering*, 12(2), pp.139-142.
- Johansson, U., 2004. Fatigue tests and analysis of reinforced concrete bridge deck models. *Trita-BKN. Bulletin*, Royal Institute of Technology, Stockholm, Sweden, 76, pp.1-197.
- Jones, R., Swamy, R.N. and Charif, A., 1988. Plate separation and anchorage of reinforced concrete beams strengthened by epoxy-bonded steel plates. *The Structural Engineer*, 66(5), pp: 85-94.
- Jumaat, M.Z., Rahman, M.A., Alam, M.A. and Rahman, M.M., 2011. Premature failures in plate bonded strengthened RC beams with an emphasis on premature shear: A review. *International Journal of Physical Sciences*, 6(2), pp.156-168.
- Jun, Z. and Stang, H., 1998. Fatigue performance in flexure of fiber reinforced concrete. *ACI Materials Journal*, 95(1), pp.58-67.
- Karatas, M., Turk, K. and Ulucan, Z.C., 2010. Investigation of bond between lap-spliced steel bar and self-compacting concrete: the role of silica fume. *Canadian Journal of Civil Engineering*, 37(3), pp.420-428.
- Karbhari, V.M., 1998. Materials and design considerations in FRP rehabilitation of concrete structures. In: *Proceedings Fracture Mechanics of Concrete Structures-3* (*FRAMCOS-3),* AEDIFICATIO, D-79104 Freiburg, Germany, pp: 1805-1816.

- Karihaloo, B.L. 1995. *Fracture Mechanics and Structural Concrete*. Addison Wesley Longman, UK.
- Karihaloo, B.L. and De Vriese, K.M.B., 1999. Short-fibre reinforced reactive powder concrete. In: *Proceedings 3rd International RILEM Workshop on High Performance Fiber Reinforced Cement Composites (HPFRCC 3)*, *Reinhardt, H.W. and Naaman, A.E. (eds)*, RILEM Publications, Mainz, Germany, 3, pp. 53-63.
- Karihaloo, B.L. and Jefferson, A.D., 2001. Looking into concrete. *Magazine of Concrete Research*, 53(2), pp.135-147.
- Karihaloo, B.L. and Wang, J., 2000. Mechanics of fibre-reinforced cementitious composites. *Computers & Structures*, 76(1), pp.19-34.
- Karihaloo, B.L., 2012a. CARDIFRC–From concept to industrial application. In: *Proceedings 6th RILEM Workshop on High Performance Fiber Reinforced Cement Composites (HPFRCC6), Parra Montesinos GJ, Reinhardt HW, and Naaman AE (eds.)*, RILEM Publications SARL, France, pp 397–404.
- Karihaloo, B.L., 2012b. Influence of micro-structural parameters and thermal cycling on the properties of CARDIFRC. *Sadhana*, 37(1), pp.125-132.
- Karihaloo, B.L., Abdalla, H.M. and Imjai, T., 2003a. A simple method for determining the true specific fracture energy of concrete. *Magazine of Concrete Research*, 55(5), pp.471-481.
- Karihaloo, B.L., Alaee, F.J. and Benson, S.D.P., 2002. A new technique for retrofitting damaged concrete structures. In: *Proceedings of the Institution of Civil Engineers, Buildings and Structures*, 152(4), pp.309-318.
- Karihaloo, B.L., Benson, S.D.P. and Alaee, F.J., 2003b. Retrofitting of RC beams with CARDIFRC. . In: *Proceedings of 10th International Conference on*

Structural Faults and Repair, Forde, M C (ed.), Engineering Tecnics Press, London, UK.

- Karihaloo, B.L., Benson, S.D.P., Didiuk, P.M., Fraser, S.A., Hamill, N. and Jenkins, T.A., 2000. Retrofitting damaged RC beams with high-performance fibre-reinforced concrete. In: *Proceedings of the Tenth Annual BCA, British Cement Association*. Birmingham University, pp.153-164.
- Karihaloo, B.L., Murthy, A.R. and Iyer, N.R., 2013. Determination of size-independent specific fracture energy of concrete mixes by the tri-linear model. *Cement and Concrete Research*, 49, pp.82-88.
- Karihaloo, B.L., Wang, J. and Grzybowski, M., 1996. Doubly periodic arrays of bridged cracks and short fibre-reinforced cementitious composites. *Journal of the Mechanics and Physics of Solids*, 44(10), pp.1565-1586.
- Khan, M.I., Abbas, Y.M. and Fares, G., 2017. Review of high and ultrahigh performance cementitious composites incorporating various combinations of fibers and ultrafines. *Journal of King Saud University-Engineering Sciences*, doi:10.1016/j.jksues.2017.03.006.
- Khayat, K. and De Schutter, G. eds., 2014. *Mechanical Properties of Self-Compacting Concrete: State-of-the-Art Report of the RILEM Technical Committee 228-MPS on Mechanical Properties of Self-Compacting Concrete*. (Vol. 14). Springer Science & Business Media, USA.
- Kim, J.K. and Kim, Y.Y., 1996. Experimental study of the fatigue behavior of high strength concrete. *Cement and Concrete Research*, 26(10), pp.1513-1523.
- King, D., Fict, H., Dip, M. and Chartered, M.C.I.M., 2012. The effect of silica fume on the properties of concrete as defined in concrete society report 74,

cementitious materials. In: *37th Conference on Our World in Concrete and Structures*, CI-PREMIER PTE LTD, *Singapore*, pp. 29-31.

- Kitsutaka, Y., 1997. Fracture parameters by polylinear tension-softening analysis. *ASCE Journal of Engineering Mechanics*, 123(5), pp.444-450.
- Korte, S., Boel, V., De Corte, W. and De Schutter, G., 2014. Behaviour of fatigue loaded self-compacting concrete compared to vibrated concrete. *Journal of the FIB Structural Concrete*, 15(4), pp.575-589.
- Lange-Kornbak, D. and Karihaloo, B.L., 1996. Design of concrete mixes for minimum brittleness. *Advanced Cement Based Materials*, 3(3), pp.124-132.
- Lange-Kornbak, D. and Karihaloo, B.L., 1997. Tension softening of fibre-reinforced cementitious composites. *Cement and Concrete Composites*, 19(4), pp.315-328.
- Lee, M.K. and Barr, B.I.G., 2004. An overview of the fatigue behaviour of plain and fibre reinforced concrete. *Cement and Concrete Composites*, 26(4), pp.299-305.
- Li, Q., Huang, B., Xu, S., Zhou, B. and Rena, C.Y., 2016. Compressive fatigue damage and failure mechanism of fiber reinforced cementitious material with high ductility. *Cement and Concrete Research*, 90, pp.174-183.
- Li, V. and Fischer, G., 2006. *International RILEM Workshop on High Performance Fiber Reinforced Cementitious Composites (HPFRCC) in Structural Applications*, RILEM Publications SARL: Bagneux, France.
- Li, V.C., Wang, Y. and Backer, S., 1991. A micromechanical model of tension-softening and bridging toughening of short random fiber reinforced brittle matrix composites. *Journal of the Mechanics and Physics of Solids*, 39(5), pp.607-625.

- Li, X., Wang, J., Bao, Y. and Chen, G., 2017. Cyclic behavior of damaged reinforced concrete columns repaired with high-performance fiber-reinforced cementitious composite. *Engineering Structures*, 136, pp.26-35.
- Lim, Y.M. and Li, V.C., 1997. Durable repair of aged infrastructures using trapping mechanism of engineered cementitious composites. *Cement and Concrete Composites*, 19(4), pp.373-385.
- Loo, K.Y.M., Foster, S.J. and Smith, S.T., 2012. Fatigue behavior of carbon fiber-reinforced polymer-repaired corroded reinforced concrete beams. *ACI Structural Journal*, 109(6), p.795.
- Maddox, S.J., 1975. The effect of mean stress on fatigue crack propagation a literature review. *International Journal of Fracture*, 11(3), pp.389-408.
- Makita, T. and Brühwiler, E., 2014a. Tensile fatigue behaviour of ultra-high performance fibre reinforced concrete (UHPFRC). *Materials and Structures*, 47(3), pp.475-491.
- Makita, T. and Brühwiler, E., 2014b. Tensile fatigue behaviour of Ultra-High Performance Fibre Reinforced Concrete combined with steel rebars (R-UHPFRC). *International Journal of Fatigue*, 59, pp.145-152.
- Malek, A.M., Saadatmanesh, H. and Ehsani, M.R., 1998. Prediction of failure load of R/C beams strengthened with FRP plate due to stress concentration at the plate end. *ACI Structural Journal*, 95, pp.142-152.
- Martín-Sanz, H., Chatzi, E. and Brühwiler, E., 2016. The use of ultra high performance fibre reinforced cement-based composites in rehabilitation projects: A Review. In *9th International conference on fracture mechanics of concrete and concrete structures (FRAMCOS-9), Saouma, V., Bolander, J. and. Landis, E (eds),* USA, doi:10.21012/FC9.219.

- Matsumoto, T. and Li, V.C., 1999. Fatigue life analysis of fiber reinforced concrete with a fracture mechanics based model. *Cement and Concrete Composites*, 21(4), pp.249-261.
- Medeiros, A., Zhang, X., Ruiz, G., Rena, C.Y. and Velasco, M.D.S.L., 2015. Effect of the loading frequency on the compressive fatigue behavior of plain and fiber reinforced concrete. *International Journal of Fatigue*, 70, pp.342-350.
- Mei, Z. and Chung, D.D.L., 2000. Effects of temperature and stress on the interface between concrete and its carbon fiber epoxy-matrix composite retrofit, studied by electrical resistance measurement. *Cement and Concrete Research*, 30(5), pp.799-802.
- Meier, U., 1997. Post strengthening by continuous fiber laminates in Europe. *Non-metallic (FRP) reinforcement for concrete structures*, Japan Concrete Institute, 1, pp.41-56.
- Memon, F.A., Nuruddin, M.F. and Shafiq, N., 2013. Effect of silica fume on the fresh and hardened properties of fly ash-based self-compacting geopolymer concrete. *International Journal of Minerals, Metallurgy and Materials*, 20(2), pp.205-213.
- Meng, W., Valipour, M. and Khayat, K.H., 2017. Optimization and performance of cost-effective ultra-high performance concrete. *Materials and Structures*, 50(1), p.29.
- Mindess, S., 2014. *Developments in the Formulation and Reinforcement of Concrete*. Woodhead Publishing Limited, England.
- Mobasher, B., Stang, H. and Shah, S.P., 1990. Microcracking in fiber reinforced concrete. *Cement and Concrete Research*, 20(5), pp.665-676.

- Morin, V., Tenoudji, F.C., Feylessoufi, A. and Richard, P., 2001. Superplasticizer effects on setting and structuration mechanisms of ultrahigh-performance concrete. *Cement and Concrete Research*, 31(1), pp.63-71.
- Morris, A.D. and Garrett, G.G., 1981. A comparative study of the static and fatigue behaviour of plain and steel fibre reinforced mortar in compression and direct tension. *International Journal of Cement Composites and Lightweight Concrete*, 3(2), pp.73-91.
- Müller, S. and Mechtcherine, V., 2017. Fatigue behaviour of strain-hardening cement-based composites (SHCC). *Cement and Concrete Research*, 92, pp.75-83.
- Muralidhara, S., Prasad, B.R., Eskandari, H. and Karihaloo, B.L., 2010. Fracture process zone size and true fracture energy of concrete using acoustic emission. *Construction and Building Materials*, 24(4), pp.479-486.
- Muralidhara, S., Prasad, B.R., Karihaloo, B.L. and Singh, R.K., 2011. Size-independent fracture energy in plain concrete beams using tri-linear model. *Construction and Building Materials*, 25(7), pp.3051-3058.
- Murthy, A.R., Karihaloo, B.L., Iyer, N.R. and Prasad, B.R., 2013. Determination of size-independent specific fracture energy of concrete mixes by two methods. *Cement and Concrete Research*, 50, pp.19-25.
- Naaman, A.E. and Hammoud, H., 1998. Fatigue characteristics of high performance fiber-reinforced concrete. *Cement and Concrete Composites*, 20(5), pp.353-363.
- Naaman, A.E. and Shah, S.R., 1976. Pull-out mechanism in steel fibre-reinforced concrete. *ASCE Journal of the Structural Division*, 102 (ST8), pp. 1537-1548.

- Naaman, A.E., 2007. High performance fiber reinforced cement composites: classification and applications. *CBM-CI international workshop, Karachi, Pakistan*, pp. 389-401.
- Nanni, A., 1995. Concrete repair with externally bonded FRP reinforcement. *Concrete International*, 17(6), pp.22-26.
- Neville, A. M., 1995. *Properties of Concrete*. 4th Ed., Longman Scientific Group Limited, UK.
- Neville, A.M. and Brooks, J.J., 2010. *Concrete Technology*. 2nd Ed., Prentice Hall, England.
- Newman, K., 1965. The structure and properties of concrete-an introductory review. In: *Proceedings of an International Conference on the Structure of Concrete and its Behaviour under Load, Brooks, A.E. and Newman, K.* (eds.), Cement and Concrete Association, London, UK, pp: xiii-
- Nicolaides, D., 2004. *Fracture and fatigue of CARDIFRC*. PhD Thesis, Cardiff University, UK.
- Nicolaides, D., Kanellopoulos, A.D. and Karihaloo, B.L., 2010. Fatigue life and self-induced volumetric changes of CARDIFRC. *Magazine of Concrete Research*, 62(9), pp.679-683.
- Obaidat, Y.T., Heyden, S., Dahlblom, O., Abu-Farsakh, G. and Abdel-Jawad, Y., 2011. Retrofitting of reinforced concrete beams using composite laminates. *Construction and Building Materials*, 25(2), pp.591-597.
- Oh, B.H., 1986. Fatigue analysis of plain concrete in flexure. *ASCE Journal of Structural Engineering*, 112(2), pp.273-288.

- Okamura, H. and Ouchi, M., 2003. Self-compacting concrete. *JCI Journal of Advanced Concrete Technology*, 1(1), pp.5-15.
- Olesen, J.F., 2001. Fictitious crack propagation in fiber-reinforced concrete beams. *ASCE Journal of Engineering Mechanics*, 127(3), pp.272-280.
- Önal, M.M., 2014. Strengthening reinforced concrete beams with CFRP and GFRP. *Advances in Materials Science and Engineering*, doi.org/10.1155/2014/967964
- Orbe, A., Cuadrado, J., Losada, R. and Rojí, E., 2012. Framework for the design and analysis of steel fiber reinforced self-compacting concrete structures. *Construction and Building Materials*, 35, pp.676-686.
- Ostergaard, L., 2003. *Early age fracture mechanics and cracking of concrete: Experiments and Modelling*. PhD Thesis, Technical University of Denmark.
- Ozawa, K., Maekawa, K., Kunishima, M. and Okamura, H., 1989. Development of high performance concrete based on the durability design of concrete structures. In: *proceedings 2nd East Asia-Pacific Conference on Structural Engineering & Construction, (EASEC-2), Kanok -Nukulchai, W (ed.).,* Asian Institute of Technology, Chiang-Mai, Thailand,1, pp. 445-450.
- Pakravan, H.R., Latifi, M. and Jamshidi, M., 2017. Hybrid short fiber reinforcement system in concrete: A review. *Construction and Building Materials*, 142, pp.280-294.
- Papakonstantinou, C.G., Petrou, M.F. and Harries, K.A., 2001. Fatigue behavior of RC beams strengthened with GFRP sheets. *ASCE Journal of Composites for Construction*, 5(4), pp.246-253.
- Parvez, A. and Foster, S.J., 2014. Fatigue behavior of steel-fiber-reinforced concrete beams. *ASCE Journal of Structural Engineering*, 141(4), p.04014117.

- Petrov, Y.V., Karihaloo, B.L., Bratov, V.V. and Bragov, A.M., 2012. Multi-scale dynamic fracture model for quasi-brittle materials. *International Journal of Engineering Science*, 61, pp.3-9.
- Qian, C.X. and Stroeven, P., 2000. Development of hybrid polypropylene-steel fibre-reinforced concrete. *Cement and Concrete Research*, 30(1), pp.63-69.
- Ramakrishnan, V., 1995. Concrete Fiber Composites for the Twenty-First Century. *Real World Concrete*, pp.111-144.
- Ramesh, K., Seshu, D.R. and Prabhakar, M., 2003. Constitutive behaviour of confined fibre reinforced concrete under axial compression. *Cement and Concrete Composites*, 25(3), pp.343-350.
- Reinhardt, H.W., Parra-Montesinos, G.J., Garrecht, H., 2015. The 7th *International RILEM Workshop on High-Performance Fiber Reinforced Cement Composites (HPFRCC7),* RILEM Publications PRO 94, Fraunhofer IRB Verlag, Stuttgart Germany.
- Richard, P. and Cheyrezy, M.H, 1995. Composition of reactive powder concretes. *Cement and Concrete Research*, 25(7), pp.1501-1511.
- Richard, P. and Cheyrezy, M.H., 1994. Reactive powder concretes with high ductility and 200-800 MPa compressive strength. *ACI Special Publication*, 144, pp.507-518.
- RILEM Committee, RILEM-36-RDL, 1984. Long-term random dynamic loading of concrete structures. *Materials and Structures*, 17(97), pp.1-28.
- RILEM Committee, RILEM-50FMC, 1985. Determination of the Fracture Energy of Mortar and Concrete by Means of Three-Point Bend Tests on Notched Beams. *Materials and Structures*, 18(106), pp.285-290.

- Roelfstra, P.E.and Wittmann, F.H., 1986. Numerical method to link strain softening with failure of concrete. In: *Fracture Toughness and Fracture Energy of Concrete, Wittmann, F.H. (ed.),* Elsevier Science Publishers Amsterdam, pp.163-175.
- Ruiz, G., Medeiros, A. and Zhang, X., 2012. Infulence of loading frequency on the compressive fatigue behavior of plain and fiber-reinforced concretes. *15th International Conference on Experimental Mechanics, Porto Ed. INEGI*, Portugal.
- Saikaly, G., Chaallal, O. and Godat, A., 2014. Fatigue behavior of RC beams strengthened in shear with externally bonded CFRP sheets. In: *7th International Conference on Fiber Reinforced Polymer (FRP) Composites in Civil Engineering*, CICE, *Raafat El-Hacha (ed.),* the International Institute for FRP in Construction, Vancouver, Canada.
- Sen, R., Mullins, G., Shahawy, M. and Spain, J., 2000. Durability of CFRP/epoxy/concrete bond, Composite in the transportation industry, In: *Proceedings of the International Composite Conference, ACUN-2,* University of South Wales, Australia.
- Shah, S.P., Peled, A., Aldea, C.M. and Akkaya, Y., 1999. Scope of high performance fiber reinforced cement composites. In: *Proceedings 6: 3rd International RILEM Workshop on High Performance Fiber Reinforced Cement Composites (HPFRCC 3), Reinhardt H.W. and Naaman A.E. (eds),* RILEM Publications, Mains, Germany, 3, pp. 113-129.
- Shah, S.P., Swartz, S.E. and Ouyang, C., 1995. *Fracture Mechanics of Concrete: Applications of Fracture Mechanics to Concrete, Rock and other Quasi-Brittle Materials*. John Wiley & Sons INC., USA.

- Sharmila, S. and Thirugnanam, G.S., 2013. Behavior of Reinforced Concrete Flexural Member with Hybrid Fibre under Cyclic Loading. *International Journal of Science, Environment and Technology*, 2(4), pp.725-734.
- Shetty, M.S., 2005. *Concrete Technology Theory & Practice*. Published by S. CHAND & Company, Ram Nagar, New Delhi.
- Siddique, R. and Khan, M.I., 2011. Silica Fume. In: *Supplementary Cementing Materials, Engineering Materials.* Springer Berlin Heidelberg, Germany, 37, pp. 67-119.
- Singh, H., 2016. *Steel Fiber Reinforced Concrete: Behavior, Modelling and Design*. Springer, Singapore.
- Singh, S.P., Ambedkar, B.R., Mohammadi, Y. and Kaushik, S.K., 2008. Flexural fatigue strength prediction of steel fibre reinforced concrete beams. *Electronic Journal of Structural Engineering*, 8, pp.46-54.
- Sivakumar, A. and Santhanam, M., 2007. Mechanical properties of high strength concrete reinforced with metallic and non-metallic fibres. *Cement and Concrete Composites*, 29(8), pp.603-608.
- Skarendahl, A., 2000. Definitions. Self-Compacting Concrete. *State-of-the-Art Report (23) of RILEM Technical Committee 174-SCC*, Skarendahl, A. and Peterson, O. (eds.), RILEM Publications SARL, Francs, pp.3-5.
- Smith, S.T., Hu, S., Kim, S.J. and Seracino, R., 2011. FRP-strengthened RC slabs anchored with FRP anchors. *Engineering Structures*, 33(4), pp.1075-1087.
- Sousa, J.L.A. and Gettu, R., 2006. Determining the tensile stress-crack opening curve of concrete by inverse analysis. *ASCE Journal of Engineering Mechanics*, 132(2), pp.141-148.

- Stang, H. and Olesen, J.F., 1998. On the interpretation of bending tests on FRC-materials. In: *Proceedings Fracture Mechanics of Concrete Structures-3* (*FRAMCOS-3),* AEDIFICATIO, Freiburg, Germany, pp. 511– 520.
- Stroeven, P. and Babut, R., 1986. Fracture mechanics and structural aspects of concrete. *Heron*, 31(2), pp.15-44.
- Struble, L., Skalny, J. and Mindess, S., 1980. A review of the cement-aggregate bond. *Cement and Concrete Research*, 10(2), pp.277-286.
- Sullivan, A.P., 1999. *The effect of hydro-thermal curing at 90°C and the use of 12 mm steel fibres on reactive powder concrete*. MSc Thesis, Cardiff University, UK.
- Takada K. and Tangtermsirikul S. 2000. Part IV: Self-compacting concrete: Testing of fresh concrete. *State-of-the-Art Report (23) of RILEM Technical Committee 174-SCC*, Skarendahl, A. and Peterson, O. (eds.), RILEM Publications SARL, France, pp. 25–39.
- Teng, J. G., Smith, S. T. & Chen, J. F. 2008. Flexural strengthening of reinforced concrete (RC) beams with fiber reinforced polymer (FRP) composites. *Strengthening and Rehabilitation of Civil Infrastructures using Fibre-Reinforced Polymer (FRP) Composites,* Chapter 4, Hollaway, L. C. & Teng, J. G. (eds.), Woodhead Publishing Limited, England, UK, pp. 112-140.
- Tilly, G.P., 1979. Fatigue of steel reinforcement bars in concrete: a review. *Fatigue & Fracture of Engineering Materials & Structures*, 2(3), pp.251-268.
- Tjiptobroto, P. and Hansen, W., 1993. Tensile strain hardening and multiple cracking in high-performance cement-based composites containing discontinuous fibers. *ACI Materials Journal*, 90(1), pp.16-25.

- Uchida, Y., Kurihara, N., Rokugo, K. and Koyanagi, W., 1995. Determination of tension softening diagrams of various kinds of concrete by means of numerical analysis. In: *Proceedings Fracture Mechanics of Concrete Structures (FRAMCOS-2)*, AEDIFICATIO, D-79104, Freiburg, Germany, pp.17-30.
- Ulfkjær, J.P., Krenk, S. and Brincker, R., 1995. Analytical model for fictitious crack propagation in concrete beams. *ASCE Journal of Engineering Mechanics*, 121(1), pp.7-15.
- Vodicka, J., Spura, D. and Kratky, J., 2004. Homogeneity of steel fiber reinforced concrete (SFRC). In: *6th International RILEM Symposium on Fibre Reinforced Concretes, Di Prisco, M., Felicetti, R. and Plizzari, G.A. (eds.)* RILEM Publications SARL, Bagneaux France pp. 537-544.
- Wang, Y., Wu, H.C. and Li, V.C., 2000. Concrete reinforcement with recycled fibers. *ASCE Journal of Materials in Civil Engineering*, 12(4), pp.314-319.
- Wille, K., Naaman, A.E. and Parra-Montesinos, G.J., 2011. Ultra-High Performance Concrete with Compressive Strength Exceeding 150 MPa (22 ksi): A Simpler Way. *ACI Materials Journal*, 108(1), pp: 45–54.
- Wongkeo, W., Thongsanitgarn, P., Ngamjarurojana, A. and Chaipanich, A., 2014. Compressive strength and chloride resistance of self-compacting concrete containing high-level fly ash and silica fume. *Materials & Design*, 64, pp.261-269.
- Xiao, J., Li, H. and Yang, Z., 2013. Fatigue behavior of recycled aggregate concrete under compression and bending cyclic loadings. *Construction and Building Materials*, 38, pp.681-688.

- Yan, H., Sun, W. and Chen, H., 1999. The effect of silica fume and steel fiber on the dynamic mechanical performance of high-strength concrete. *Cement and Concrete Research*, 29(3), pp.423-426.
- Zanuy, C., Albajar, L. and De la Fuente, P., 2009. Sectional analysis of concrete structures under fatigue loading. *ACI Structural Journal*, 106(5), p.667.
- Zanuy, C., de la Fuente, P. and Albajar, L., 2007. Effect of fatigue degradation of the compression zone of concrete in reinforced concrete.

Appendix A

Full Analytical Expressions Relating the Hinge Rotation to the Bending Moment for Phases I, II And III and the Applied Central Load on the Beam

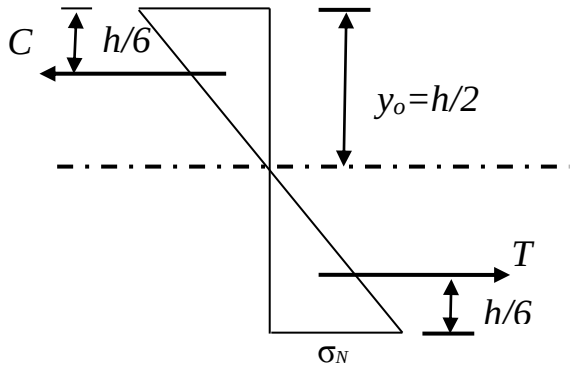

Phase 0 $\boldsymbol{\alpha = 0}$

$$\frac{M}{I} = \frac{E}{R} \Rightarrow \frac{\mu f_t h^2 t}{6\frac{th^3}{12}} = \frac{2E\varphi}{s} = \frac{2Esf_t}{hEs}\theta$$

$$\Rightarrow \frac{2\mu f_t}{h} = \frac{2f_t}{h}\theta \Rightarrow \mu = \theta$$

Note that $h = h_g$ and $\alpha = \alpha_h$ appears in chapters 5.
The balance of longitudinal forces requires that $\sigma_N < f_t$

$$\frac{N}{ht} < f_t \Rightarrow \frac{N}{f_t ht} < 1 \Rightarrow \rho < 1$$

Note: $N = \sigma_{N.\frac{1}{2}}.\frac{th}{2}$, $M = \frac{2}{3}hN = \frac{\sigma_N th^2}{6}$

$$\theta = \frac{hE}{2f_t}k^*, \qquad k^* = \frac{1}{R} = \frac{M}{EI} = \frac{\sigma_N th^2}{6E.\frac{th^3}{12}} = \frac{2\sigma_N}{Eh}$$

$$\theta = \frac{\sigma_N}{f_t} < 1$$

Transition from phase 0 to phase I at $\theta = 1$

Phase I $\boldsymbol{\alpha \neq 0 \ < 1}$

In phase I, the stress is decreasing along the first branch of the bilinear $\sigma(w)$ diagram.

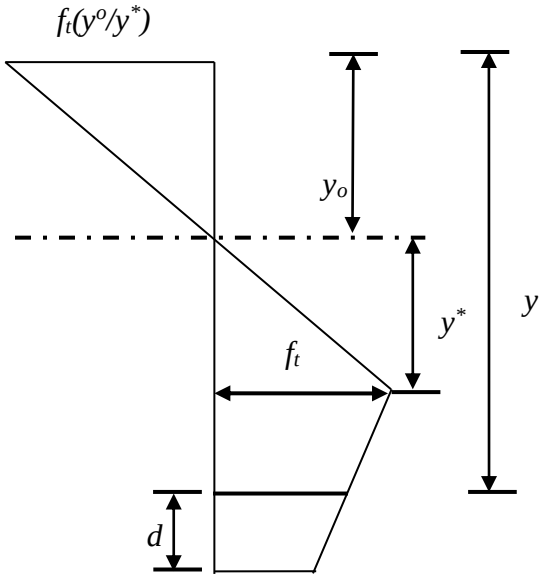

$$s\frac{\sigma_w(w(y))}{E} + w(y) = 2s(y - y_0)\frac{\varphi}{s} = 2(y - y_0)\varphi$$

$$\sigma_w\big(w(y)\big) = \frac{1}{s}\{2E((y - y_0)\varphi - Ew(y)\} = \frac{E}{s}\{2(y - y_0)\varphi - w(y)\}$$

Also $\sigma_w\big(w(y)\big) = f_t\{b_i - a_i w(y)\}$

By Subtracting the above two equations from each other, we get

$$-f_t\{b_i - a_i w(y)\} + \frac{E}{s}\{2(y-y_0)\varphi - w(y)\} = 0$$

$$\Rightarrow \frac{f_t s}{E}\{(b_i - a_i w(y)\} - \{2(y-y_0)\varphi - w(y)\} = 0$$

$$\Rightarrow -\frac{f_t s}{E} b_i + 2(y-y_0)\varphi = w(y) - \frac{f_t s}{E} a_i w(y) = w(y)\left\{1 - \frac{f_t s a_i}{E}\right\}$$

$$\Rightarrow w(y) = \frac{2(y-y_0)\varphi - \varsigma_i}{1-\beta_i}$$

$$\sigma_w(\, w(y) = \, f_t b_i - \, f_t a_i\{\frac{2(y-y_0)\varphi-\varsigma_i}{1-\beta_i}\}$$

$$= \varsigma_i \frac{E}{S} - \beta_i \frac{E}{S}\{\frac{2(y-y_0)\varphi-\varsigma_i}{1-\beta_i}\}$$

$$\varsigma_i \frac{E}{S}\left\{\frac{1-\beta_i+\beta_i}{1-\beta_i}\right\} - \frac{2(y-y_0)\varphi\beta_i}{1-\beta_i}\frac{E}{S}$$

$$\frac{\varsigma_i - 2(y-y_0)\varphi\beta_i}{1-\beta_i}\frac{E}{S}$$

$$\beta_i = \frac{f_t s a_i}{E} \quad , \quad \varsigma_i = \frac{f_t s b_i}{E}$$

Tensile force $= {}^1\!/_2\, f_t y^* t +$ contribution from tension softening zone of length *d*.
The latter contribution is obtained from the stress at distance *y* from top, given by equation (5.9)

$$\sigma_w(\, w(y) = \frac{\varsigma_1 - \, 2(y-y_0)\varphi\beta_i}{1-\beta_i}\frac{E}{S}$$

$$\sigma_w(\, w(h) = \frac{\varsigma_1 - \, 2(h-y_0)\varphi\beta_1}{1-\beta_1}\frac{E}{S}$$

$$\sigma_w(\, w(h-d) = \frac{\varsigma_1 - \, 2(h-d-y_0)\varphi\beta_1}{1-\beta_1}\frac{E}{S}$$

Area of trapezium $= \frac{dt}{2}\{\sigma\big(w(h)\big) + \big(w(h - \, d)\big)\}$

$$= \frac{dtE}{2s}\left\{\frac{2\varsigma_1 - 2(2h-d-2y_0)\varphi\beta_1}{1-\beta_1}\right\}, \varsigma_1 = \frac{f_t b_1 s}{E} = \frac{f_t s}{E}$$

$$= \frac{dt}{(1-\beta_1)}\left\{f_t - \left(2 - \alpha - 2\frac{y_0}{h}\right)\frac{h\varphi E}{E}\beta_1\right\}$$

$$= \frac{dtf_t}{(1-\beta_1)}\left\{1 - \left(2 - \alpha - 2\frac{y_0}{h}\right)\theta\beta_1\right\}$$

$$= \frac{\alpha dtf_t}{(1-\beta_1)}\left\{1 - 2\theta\beta_1 + \alpha\theta\beta_1 + 2\frac{y_0}{h}\theta\beta_1\right\}$$

Total tensile force $= \frac{\alpha(thf_t)}{(1-\beta_1)}\left\{1 - \left(2 - \alpha - 2\frac{y_0}{h}\right)\theta\beta_1\right\} + \frac{1}{2}f_t y^* t$

$$y^* = \frac{sf_t}{2\varphi E} = \frac{sf_t.hE}{2.sf_t\theta E} = \frac{h}{2\theta}, \quad \text{Note also } h - y_0 = d + y^*$$

So, that $1 - \frac{y_0}{h} = \alpha + \frac{y^*}{h}\alpha + \frac{1}{2\theta} = \frac{(1+2\alpha\theta)}{2\theta}$

Total tensile force $=$

$$\begin{aligned} T &= \frac{\alpha(thf_t)}{(1-\beta_1)}\left\{1 - \left(2\alpha - \frac{1}{\theta} - \alpha\right)\theta\beta_1\right\} + \frac{f_t th}{4\theta} \\ &= \frac{f_t th}{(1-\beta_1)}\left\{\alpha - \left(2\alpha^2 + \frac{\alpha}{\theta}\right)\theta\beta_1\right\} + \frac{f_t th}{4\theta} \\ &= \frac{f_t th}{(1-\beta_1)}\{(1-\beta_1)\alpha - \alpha^2\theta\beta_1\} + \frac{f_t th}{4\theta} \\ &= f_t th\left\{\alpha - \frac{\alpha^2\theta\beta_1}{(1-\beta_1)} + \frac{1}{4\theta}\right\} \end{aligned}$$

Total compressive force $= \frac{1}{2}f_t\frac{y_0}{y^*}.y_0 t = \frac{1}{2}(f_t ht).\frac{y_0}{y^*}.\frac{y_0}{h}$

Now $\frac{y_0}{h} = 1 - \alpha - \frac{1}{2\theta}$

Also $\frac{y^*}{h} = 1 - \alpha - \frac{y_0}{h} = 1 - \alpha - 1 + \alpha + \frac{1}{2\theta} = \frac{1}{2\theta}$

$$\frac{y^*}{h}\left(\frac{y_0}{y^*} + 1\right) = 1 - \alpha \qquad (\text{from } y_0 + y^* = h - d)$$

$$\Rightarrow \frac{1}{2\theta}\left(\frac{y_0}{y^*} + 1\right) = 1 - \alpha \quad \Rightarrow \frac{y_0}{y^*} + 1 = (1-\alpha)2\theta$$

$$\Rightarrow \frac{y_0}{y^*} = (1-\alpha)2\theta - 1$$

C=Total compressive force

$$= \frac{1}{2}(f_t ht)\{(1-\alpha)2\theta - 1\}\left\{1 - \alpha - \frac{1}{2\theta}\right\}$$

$$= \frac{f_t ht}{\theta}\left\{(1-\alpha)\theta - \frac{1}{2}\right\}\left\{(1-\alpha)\theta - \frac{1}{2}\right\}$$

$$= \frac{f_t h t}{\theta}\left\{(1-\alpha)\theta - \frac{1}{2}\right\}^2$$

C=T ⇒

$$\alpha - \frac{\alpha^2\theta\beta_1}{(1-\beta_1)} + \frac{1}{4\theta} = (1-\alpha)^2\theta - (1-\alpha) + \frac{1}{4\theta}$$

$$(1-2\alpha-\alpha^2)\theta - 1 = -\frac{\alpha^2\theta\beta_1}{(1-\beta_1)}$$

$$\Rightarrow \quad \alpha^2\theta\left\{1 + \frac{\beta_1}{(1-\beta_1)}\right\} - 2\alpha\theta - (1-\theta) = 0$$

$$\Rightarrow \quad \frac{\alpha^2\theta}{(1-\beta_1)} - 2\alpha\theta - -(1-\theta) = 0$$

$$\Rightarrow \quad \alpha^2 - 2(1-\beta_1)\alpha - (1-\beta_1)\left(\frac{1-\theta}{\theta}\right) = 0$$

$$\alpha = \frac{2(1-\beta_1) \pm \sqrt{(1-\beta_1)^2 + 4(1-\beta_1)\left(\frac{1}{\theta}-1\right)}}{2}$$

$$\alpha = (1-\beta_1) \pm \sqrt{(1-\beta_1)^2 + (1-\beta_1)\left(\frac{1}{\theta}-1\right)}$$

$$\alpha = (1-\beta_1) - \sqrt{(1-\beta_1) + \left(1-\beta_1+\frac{1}{\theta}-1\right)} \qquad \alpha \ll 1$$

$$\alpha = (1-\beta_1) - \sqrt{(1-\beta_1)\left(\frac{1}{\theta}-\beta_1\right)}$$

Phase I (moment)

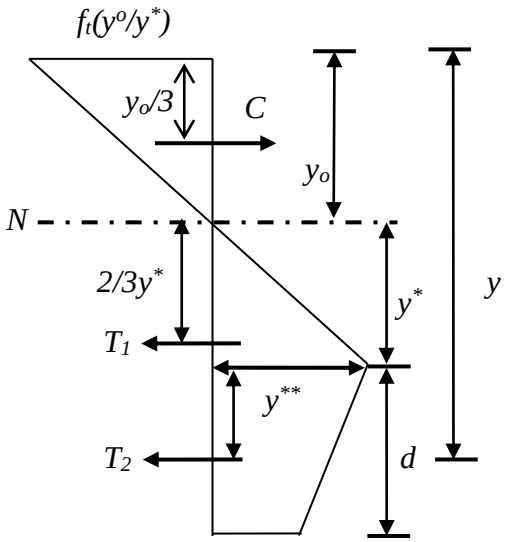

Now take moments about neutral axis

$$M = C\left(\frac{2y_0}{3}\right) + T_1\left(\frac{2y^*}{3}\right) + T_2(y^* + y^{**})$$

The distance y^{**} can be calculated by dividing the trapezium into a rectangle and a triangle

$$\sigma\big(w(h)\big) = \frac{\frac{f_t s}{\mathrm{E}} - 2(\mathrm{h} - y_0)\varphi\beta_1}{(1-\beta_1)}\frac{\mathrm{E}}{\mathrm{S}}$$

$$= \frac{f_t - 2(\mathrm{h} - y_0)\frac{\varphi f_t}{h}\beta_1}{(1-\beta_1)}$$

$$= \frac{f_t}{(1-\beta_1)}\left\{1 - 2(\mathrm{d} + y^*)\frac{\theta}{h}\beta_1\right\}$$

$$= \frac{f_t}{(1-\beta_1)}\left\{1 - 2\left(\alpha + \frac{1}{2\theta}\right)\theta\beta_1\right\}$$

$$= \frac{f_t}{(1-\beta_1)}\{1 - 2\alpha\theta\beta_1 - \beta_1\}$$

$$= \frac{f_t}{(1-\beta_1)}\{(1-\beta_1) - 2\alpha\theta\beta_1\}$$

$$= f_t\left\{1 - \frac{2\alpha\theta\beta_1}{(1-\beta_1)}\right\}$$

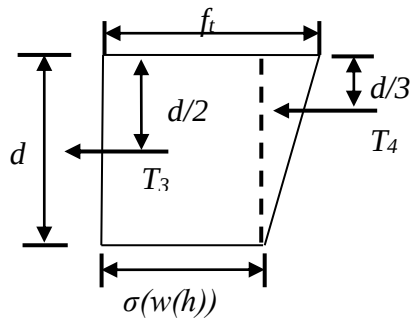

$$T_2 = f_t th\left\{\alpha - \frac{2\alpha^2\theta\beta_1}{1-\beta}\right\}$$

$$T_3 = f_t dt\left\{1 - \frac{2\alpha\theta\beta_1}{1-\beta}\right\}$$

$$T_4 = \frac{1}{2}f_t dt\frac{2\alpha\theta\beta_1}{(1-\beta_1)}$$

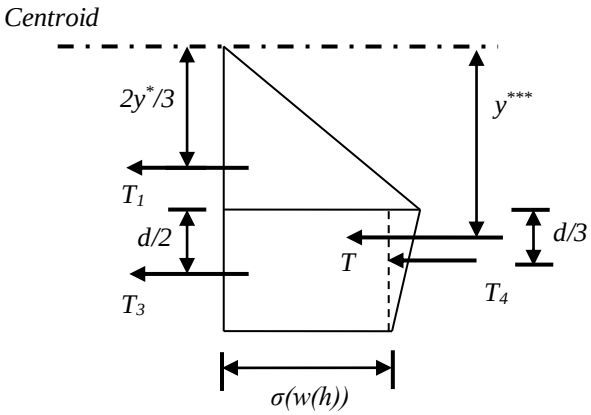

$$T_2 y^{**} = T_3 \frac{d}{2} + T_4 \frac{d}{3} \qquad \Rightarrow y^{**} = \frac{T_3 \frac{d}{2} + T_4 \frac{d}{3}}{T_2}$$

We need $T_2 y^{**}$, so no need to calculate y^{**}

$$y^{***} = \frac{T_1 \left(\frac{2y^*}{3}\right) + T_3 (y^* + \frac{d}{2}) + T_4 (y^* + \frac{d}{3})}{T_1 + T_3 + T_4}$$

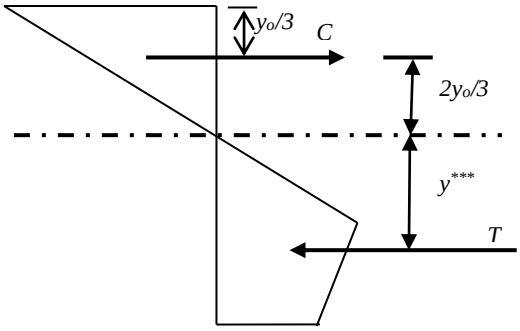

Note: $T_1 + T_3 + T_4 = C = T$

$$M = C\left(\frac{2y^*}{3} + y^{***}\right)$$

$$= C\left(\frac{2y^*}{3}\right) + Cy^{***}$$

$$= C\left(\frac{2y_0}{3}\right) + T_1\left(\frac{2y^*}{3}\right) + T_3(y^*) + T_3(\frac{d}{2}) + T_4(y^*) + T_4(\frac{d}{3})$$

$$= C\left(\frac{2y_0}{3}\right) + (T_1 + T_3 + T_4)y^* - T_1\left(\frac{y^*}{3}\right) + T_3\left(\frac{d}{2}\right) + T_4\left(\frac{d}{3}\right)$$

$$= C\left(y^* + \frac{2y_0}{3}\right) - T_1\left(\frac{y^*}{3}\right) + T_3\left(\frac{d}{2}\right) + T_4\left(\frac{d}{3}\right)$$

$$= C\left(h - y_0 - d + \frac{2y_0}{3}\right) - T_1\left(\frac{y^*}{3}\right) + T_3\left(\frac{d}{2}\right) + T_4\left(\frac{d}{3}\right)$$

$$= C\left(h - d - \frac{y_0}{3}\right) - T_1\left(\frac{y^*}{3}\right) + T_3\left(\frac{d}{2}\right) + T_4\left(\frac{d}{3}\right)$$

$$= \frac{f_t h^2 t}{\theta}\left\{(1-\alpha)\theta - \frac{1}{2}\right\}^2 \left(1 - \alpha - \frac{y_0}{3h}\right) - \frac{1}{2} f_t y^* t . \frac{y^*}{3}$$

$$+ \frac{f_t d^2 t}{2}\left(1 - \frac{2\alpha\theta\beta_1}{1-\beta_1}\right) + \frac{f_t d^2 t}{3} . \frac{\alpha\theta\beta_1}{1-\beta_1}$$

$$\frac{6M}{f_t h^2 t} = \frac{6}{\theta}\left(1 - \alpha - \frac{1}{3} + \frac{\alpha}{3} + \frac{y^*}{3h}\right)\left\{(1-\alpha)\theta - \frac{1}{2}\right\}^2 - \frac{y^{*2}}{h^2} + \frac{3d^2}{h^2}\left(1 - \frac{2\alpha\theta\beta_1}{1-\beta_1}\right)$$

$$+ \frac{2d^2}{h^2} . \frac{\alpha\theta\beta_1}{1-\beta_1}$$

$$\mu = \frac{6}{\theta}\left(\frac{2}{3} - \frac{2\alpha}{3} - \frac{1}{3} + \frac{\alpha}{3} + \frac{1}{6\theta}\right)\left\{(1-\alpha)\theta - \frac{1}{2}\right\}^2 - \frac{1}{4\theta^2} + 3\alpha^2\left(1 - \frac{2\alpha\theta\beta_1}{1-\beta_1}\right) + \frac{2\alpha^3\theta\beta_1}{1-\beta_1}$$

$$\mu = \frac{4}{\theta}\left(1 - \alpha + \frac{1}{4\theta}\right)\left\{(1-\alpha)\theta - \frac{1}{2}\right\}^2 - \frac{1}{4\theta^2} + \alpha^2\left(3 - \frac{6\alpha\theta\beta_1}{1-\beta_1} + \frac{2\alpha\theta\beta_1}{1-\beta_1}\right)$$

$$\mu = \frac{4}{\theta}\left(1-\alpha+\frac{1}{4\theta}\right)\left\{(1-\alpha)\theta-\frac{1}{2}\right\}^2-\frac{1}{4\theta^2}+\alpha^2\left(3-\frac{4\alpha\theta\beta_1}{1-\beta_1}\right)$$

$$\mu = \frac{4\theta^2}{\theta}\left((1-\alpha)+\frac{1}{4\theta}\right)\left\{(1-\alpha)-\frac{1}{2\theta}\right\}^2-\frac{1}{4\theta^2}+\alpha^2\left(3-\frac{4\alpha\theta\beta_1}{1-\beta_1}\right)$$

$$= 4\theta\left(1-\alpha+\frac{1}{4\theta}\right)\left(1-2\alpha-\alpha^2-\frac{1-\alpha}{\theta}+\frac{1}{4\theta^2}\right)-\frac{1}{4\theta^2}+\alpha^2\left(3-\frac{4\alpha\theta\beta_1}{1-\beta_1}\right)$$

$$= \{4(1-\varepsilon)\theta+1)\left\{(1-\alpha)^2-\frac{(1-\alpha)}{\theta}+\frac{1}{4\theta^2}\right\}-\frac{1}{4\theta^2}+3\alpha^2-\frac{4\alpha^3\theta\beta_1}{1-\beta_1}$$

$$= (1-\alpha)^2-\frac{1-\alpha}{\theta}+\frac{1}{4\theta^2}+4(1-\alpha)^3\theta-4(1-\alpha)^2+\frac{1-\alpha}{\theta}-\frac{1}{4\theta^2}+3\alpha^3 - \frac{4\alpha^3\theta\beta_1}{1-\beta_1}$$

$$= 4(1-\alpha)^3\theta-3(1-2\alpha-\alpha^2)+3\alpha^3-\frac{4\alpha^3\theta\beta_1}{1-\beta_1}$$

$$= 4\theta\left\{1-3\alpha-3\alpha^2-\alpha^3-\frac{\alpha^3\beta_1}{1-\beta_1}\right\}-3+6\alpha$$

$$\mu = 4\theta(1-3\alpha+3\alpha^2-\tfrac{\alpha^3}{1-\beta_1})-3+6\alpha$$

Phase II (crack length, a)

$$\frac{y^*}{h} = \frac{1}{2\theta} \quad ; \quad \frac{y_0}{h} = 1 - \alpha - \frac{1}{2\theta}$$

$$h - d = y^* + d \quad ; \quad y^* = \frac{sf_t}{2\varphi E}$$

$$y_1 = y_0 + \frac{1}{2\varphi}\ [\zeta_1 - w_1(\beta_1 - 1)]\varphi = \frac{\theta s f_t}{hE}, \quad \zeta_1 = \frac{f_t s b_1}{E} = \frac{f_t s}{E} \quad (b_1 = 1)$$

$$y_1 = y_0 + \frac{hE}{2\varphi s f_t}\ \left[\frac{f_t s}{E} - w_1(\beta_1 - 1)\right]$$

$$\sigma_w\big(w(h)\big) = \frac{\zeta_2 - 2(y - y_0)\varphi\beta_2}{1 - \beta_2}\,\frac{E}{\mathrm{s}} \quad ; \ \zeta_2 = \frac{f_t b_2 s}{E},$$

$$\sigma_w\big(w(y_1)\big) = \frac{\zeta_1 - 2(y_1 - y_0)\varphi\beta_1}{1 - \beta_i}\,\frac{E}{\mathrm{s}}$$

$$(h - y_0) = \mathrm{y}^* + d = \frac{h}{2\theta} + d$$

$$(y_1 - y_0) = \frac{hE}{2\varphi s f_t}\ \left[\frac{f_t s}{E} - w_1(\beta_1 - 1)\right]$$

Total compressive force, *C*

$$C = \frac{1}{2}\, f_t \frac{y_0}{y^*}.y_0 t = \frac{f_t h t}{\theta}\ \left\{(1 - \alpha)\theta - \frac{1}{2}\right\}^2, \qquad \text{as before}$$

Note

$$y_1 - y_0 = \frac{h}{2\theta}\ \left[1 + \frac{f_t s}{E} - w_1(1 - \beta_1)\right]$$

$$y_1 - y_0 - y^* = \frac{f_t s}{E}\frac{h}{2\theta}w_1(1 - \beta_1) = \ \frac{\alpha_1}{\beta_1}\frac{h}{2\theta}w_1(1 - \beta_1)$$

Total tensile force, T

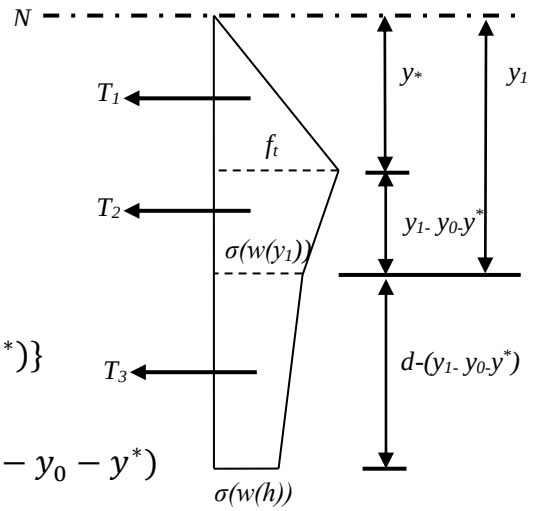

$$T_1 = \frac{1}{2} f_t y^* t = \frac{f_t t h}{4\theta}$$

$$T_2 = \frac{t}{2}\{f_t + \sigma(w(y_1))\}(y_1 - y_0 - y^*)$$

$$T_3 = \frac{t}{2}\{\sigma(w(y_1)) + \sigma(w(h))\}\{d - (y_1 - y_0 - y^*)\}$$

$$T_2 + T_3 = \frac{t}{2}\{f_t(y_1 - y_0 - y^*)\} + \frac{t}{2}\sigma(w(y_1))(y_1 - y_0 - y^*)$$
$$+ \frac{t}{2}\sigma(w(y_1))d + \frac{t}{2}\sigma(w(h))d - \frac{t}{2}\sigma(w(y_1))(y_1 - y_0 - y^*)$$
$$- \frac{t}{2}\sigma(w(h))(y_1 - y_0 - y^*)$$

$$= \frac{1}{2}\{f_t + \sigma(w(h))\}(y_1 - y_0 - y^*) + \frac{1}{2} d\{\sigma(w(y_1)) + \sigma(w(h))\}$$

$$w_1 = \frac{1 - b_2}{a_1 - a_2}, \quad w_2 = \frac{b_2}{a_2} \qquad Eq.(5.9a, b)$$

$$Note: 1 - a_1 w_1 = 1 - \frac{(1 - b_2)a_1}{a_1 - a_2} = \frac{b_2\beta_1 - \beta_2}{(\beta_1 - \beta_2)}$$

$$y_1 - y_0 - y^* = \frac{w_1}{2\varphi}(1 - \beta_1) = \frac{h}{2\theta} \cdot \frac{(1 - b_2)(1 - \beta)}{(\beta_1 - \beta_2)}$$

$$T_2 + T_3 = \frac{f_t t h}{4\theta}\left\{1 - \frac{[b_2 - (1 + 2\alpha\theta)]\beta_2}{1 - \beta_2}\right\}\frac{(1 - b_2)(1 - \beta_1)}{(\beta_1 - \beta_2)}$$
$$+ \frac{f_t t d}{2}\left\{\frac{b_2\beta_1 - \beta_2}{\beta_1 - \beta_2} + \frac{b_2 - (1 + 2\alpha\theta)\beta_2}{(1 - \beta_2)}\right\}$$

$$= \frac{f_t t h}{4\theta}\left\{\frac{(1 - b_2) + 2\alpha\theta\beta_2}{(1 - \beta_2)}\right\}\frac{(1 - b_2)(1 - \beta_1)}{(\beta_1 - \beta_2)}$$
$$+ \frac{f_t t d}{2}\left\{\frac{b_2\beta_1 - \beta_2}{\beta_1 - \beta_2} + \frac{b_2 - (1 + 2\alpha\theta)\beta_2}{(1 - \beta_2)}\right\}$$

$$T_1 + T_2 = \frac{f_t t h}{4\theta}\left\{1 + \frac{(1 - b_2) + 2\alpha\theta\beta_2}{(1 - \beta_2)}\right\}\frac{(1 - b_2)(1 - \beta_1)}{(\beta_1 - \beta_2)}$$

$$T_1 + T_2 + T_3 = \frac{f_t th}{4\theta}\left\{1 + \left[\frac{(1-b_2)+2\alpha\theta\beta_2}{(1-\beta_2)}\right]\frac{(1-b_2)(1-\beta_1)}{(\beta_1-\beta_2)}\right\}$$

$$+ \frac{f_t th}{4\theta}\left\{2\alpha\theta\left[\frac{b_2\beta_1-\beta_2}{\beta_1-\beta_2} + \frac{b_2-(1+2\alpha\theta)\beta_2}{1-\beta_2}\right]\right\} = C$$

$$4\left\{(1-\alpha)\theta - \frac{1}{2}\right\}^2 = RHS$$

$$4\theta^2\left\{\alpha^2 - 2\left(1-\frac{1}{2\theta}\right)\alpha + \left(1+\frac{1}{2\theta}\right)^2\right\} = RHS$$

$$RHS = 1 + \frac{(1-b_2)^2(1-\beta_1)}{(1-\beta_2)(\beta_1-\beta_2)} + \frac{2\alpha\theta\beta_2(1-b_2)(1-\beta_1)}{(1-\beta_2)(\beta_1-\beta_2)} + \frac{2\alpha\theta(b_2\beta_1-\beta_2)}{(\beta_1-\beta_2)}$$
$$+ \frac{2\alpha\theta b_2}{1-\beta_2} - \frac{2\alpha\theta\beta_2}{1-\beta_2} - \frac{(2\alpha\theta)^2\beta_2}{1-\beta_2}$$

$$= 1 + \frac{(1-b_2)^2(1-\beta_1)}{(1-\beta_2)(\beta_1-\beta_2)} - \frac{(2\alpha\theta)^2\beta_2}{1-\beta_2} + \frac{2\alpha\theta}{(1-\beta_2)(\beta_1-\beta_2)}$$

$$+\{\beta_2(1-b_2)(1-\beta_1) + (1-\beta_2)(b_2\beta_1-\beta_2) + (b_2-\beta_2)(\beta_1-\beta_2)\}$$

$$= 1 + \frac{(1-b_2)^2(1-\beta_1)}{(1-\beta_2)(\beta_1-\beta_2)} - \frac{4\alpha^2\theta^2\beta_2}{1-\beta_2} + \frac{4\alpha\theta(b_2-\beta_2)}{1-\beta_2}$$

$C = T \Rightarrow$

$$4\alpha^2\theta^2 + \frac{4\alpha^2\theta^2\beta_2}{1-\beta_2} - 8\alpha\theta^2 + 4\alpha\theta - \frac{4\alpha\theta(b_2-\beta_2)}{1-\beta_2} + 4\theta^2\left(1-\frac{1}{2\theta}\right)^2$$
$$- \frac{(1-b_2)^2(1-\beta_1)}{(1-\beta_2)(\beta_1-\beta_2)} - 1 = 0$$

$$\Rightarrow \frac{4\alpha^2\theta^2}{1-\beta_2} - 8\alpha\theta^2 + \frac{4\alpha\theta - 4\alpha\theta(b_2-\beta_2)}{1-\beta_2} + 4\theta^2\left(1-\frac{1}{2\theta}\right)^2 - \frac{(1-b_2)^2(1-\beta_1)}{(1-\beta_2)(\beta_1-\beta_2)}$$
$$- 1 = 0$$

$$\Rightarrow \alpha^2 - 2(1-\beta_2)\alpha + \frac{1}{\theta}(1-b_2)\alpha + (1-\beta_2)\left(1-\frac{1}{2\theta}\right)^2 - \frac{(1-b_2)^2(1-\beta_1)}{(1-\beta_2)(\beta_1-\beta_2)}$$
$$- \frac{(1-\beta_1)}{4\theta^2} = 0$$

$$\Rightarrow \alpha^2 - 2\alpha\left\{(1-\beta_2) - \frac{(1-b_2)}{2\theta}\right\} + (1-\beta_2)\left(1-\frac{1}{\theta}\right) - \frac{(1-b_2)^2(1-\beta_1)}{(1-\beta_2)(\beta_1-\beta_2)4\theta^2} = 0$$

$$\alpha = (1-\beta_2) - \frac{(1-b_2)}{2\theta} - \frac{1}{2}\sqrt{4\left\{(1-\beta_2) - \frac{(1-b_2)}{2\theta}\right\}^2 - 4(1-\beta_2)\left(1-\frac{1}{\theta}\right) + \frac{4(1-b_2)^2(1-\beta_1)}{(\beta_1-\beta_2)4\theta^2}}$$

$$= \left(1-\beta_2-\frac{1-b_2}{2\theta}\right) - \sqrt{(1-\beta_2)^2 - \frac{(1-b_2)(1-\beta_1)}{\theta} + \frac{(1-b_2)^2}{4\theta^2} - (1-\beta_2)\left(1-\frac{1}{\theta}\right) + \frac{(1-b_2)^2(1-\beta_1)}{(\beta_1-\beta_2)4\theta^2}}$$

$$= \left(1-\beta_2-\frac{1-b_2}{2\theta}\right) - \sqrt{(1-\beta_2)^2 - (1-\beta_2) + \left(1-\frac{b_2}{\theta}\right) + \frac{(1-b_2)^2(1-\beta_2)}{4\theta^2(\beta_1-\beta_2)}}$$

$$= \left(1-\beta_2-\frac{1-b_2}{2\theta}\right) - \sqrt{(1-\beta_2)\left\{1-\beta_2-1+\frac{b_2}{\theta} + \frac{(1-b_2)^2}{4\theta^2(\beta_1-\beta_2)}\right\}}$$

$$\boxed{\alpha = 1-\beta_2-\frac{1-b_2}{2\theta} - \sqrt{(1-\beta_2)\left\{\frac{(1-b_2)^2}{4\theta^2(\beta_1-\beta_2)} - \beta_2 + \frac{b_2}{\theta}\right\}}}$$

Phase III (Crack length, a_h)

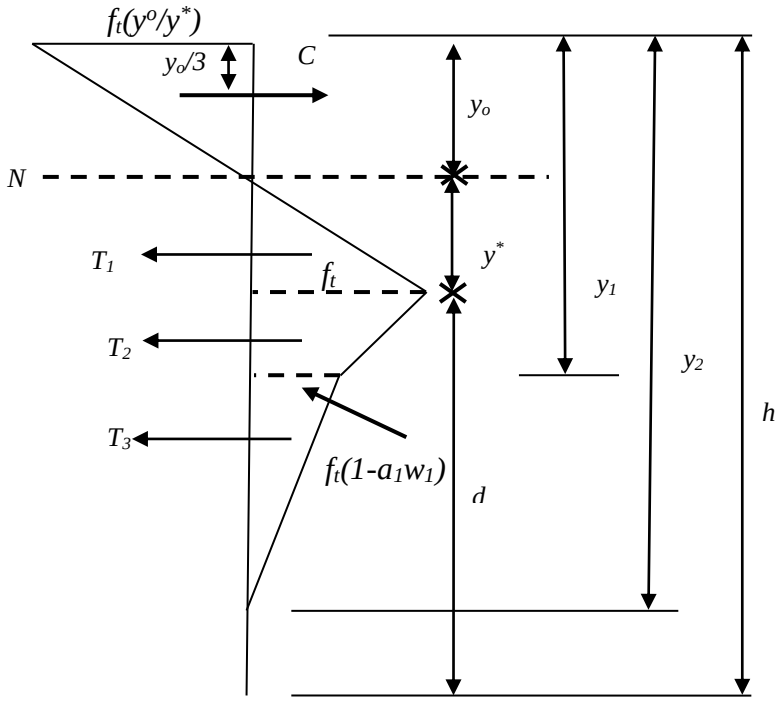

$$C = \frac{1}{2} f_t \frac{y_0}{y^*} \ . \ y_0 t = \frac{f_t th}{\theta} \left\{(1-\alpha)\theta - \frac{1}{2}\right\}^2, \quad as\ before$$

$$T_1 = \frac{1}{2}\ f_t\, y^* t = \frac{f_t th}{4\theta} \qquad , \quad as\ before$$

$$T_2 = \frac{t}{2}\{\, f_t + \, f_t(1-\alpha_1 w_1)\}(\, y_1 - \, y_0 - \, y^*\,)$$

$$T_3 = \frac{t}{2}\{\, f_t(1-\alpha_1 w_1)\}(\, y_2 - \, y_1\,)$$

$$y_1 = \, y_0 + \frac{1}{2\varphi}[\zeta_1 + \, w_1(1-\beta_1)] \quad \zeta_1 = \frac{f_t s b_1}{E} = \frac{f_t s}{E}$$

$$y_2 = \, y_0 + \frac{1}{2\varphi}[\zeta_2 + \, w_2(1-\beta_2)] \quad \zeta_2 = \frac{f_t b_2 s}{E}$$

$$y_1 - y_0 - y^* = \frac{1}{2\varphi}\left[\frac{f_t s}{E} + \, w_1(1-\beta_1)\right] - \frac{h}{2\theta}$$

$$= y^* + \frac{w_1}{2\varphi}(1-\beta_1) - y^* = \frac{w_1}{2\varphi}(1-\beta_1); \qquad y^* = \frac{s f_t}{2\varphi E}$$

$$y_2 - y_1 \ = \frac{1}{2\varphi}[\zeta_2 - \zeta_1 + w_2(1-\beta_2) - w_1(1-\beta_1)]$$

$$= \, y^*(b_2 - 1) + \frac{1}{2\varphi}[w_2(1-\beta_2) - w_1(1-\beta_1)]$$

$$= -\frac{h}{2\theta}(b_2 - 1) + \frac{1}{2\varphi}[w_2(1-\beta_2) - w_1(1-\beta_1)]$$

Note: $w_1 = \frac{1-b_2}{a_1-a_2}, \qquad w_2 = \frac{b_2}{a_2}$

$$y_1 - y_0 - y^* = \frac{w_1}{2\varphi}(1-\beta_1) = \frac{(1-b_2)(1-\beta_1)}{2\varphi(a_1-a_2)} = \frac{(1-b_2)(1-\beta_1)}{\frac{2\varphi E}{f_t s}(\beta_1-\beta_2)}$$

$$= \frac{y^*(1-b_2)(1-\beta_1)}{(\beta_1-\beta_2)} = \frac{h}{2\theta}\frac{(1-b_2)(1-\beta_1)}{(\beta_1-\beta_2)}$$

$$y_2 - y_1 = \frac{h}{2\theta}(1-b_2) + \frac{1}{2\varphi}\left[\frac{b_2}{a_2}(1-\beta_2) - \frac{(1-b_2)}{a_1-a_2}(1-\beta_1)\right]$$

$$= \frac{h}{2\theta}(1-b_2) + \frac{1}{2\varphi}\left[\frac{b_2(1-\beta_2)}{\beta_2} - \frac{(1-b_2)(1-\beta_1)}{\beta_1-\beta_2}\right]$$

$$= \frac{h}{2\theta}\left[\frac{-(1-b_2)\beta_2(\beta_1-\beta_2) + b_2(1-\beta_2)(\beta_1-\beta_2) - (1-b_2)(1-\beta_2)\,\beta_2}{\beta_2(\beta_1-\beta_2)}\right]$$

$$= \frac{h}{2\theta}\left[\frac{(1-\beta_2)(\beta_1 b_2 - \beta_2)}{\beta_2(\beta_1-\beta_2)}\right]$$

$$T_2 + T_3 = \frac{f_t th}{4\theta}(2-\alpha_1 w_1)\frac{(1-b_2)(1-\beta_1)}{(\beta_1-\beta_2)} + \frac{f_t th}{4\theta}(1 - \alpha_1 w_1)\frac{(1-\beta_2)(\beta_1 b_2-\beta_2)}{\beta_2(\beta_1-\beta_2)}$$

Note: $\alpha_1 w_1 \frac{(1-b_2)a_2}{(a_1-a_2)} = \frac{(1-b_2)\beta_1}{\beta_1-\beta_2}$

$$1 - \alpha_1 w_1 = 1 - \frac{(1-b_2)\beta_1}{\beta_1-\beta_2} = \frac{b_2\beta_1-\beta_2}{(\beta_1-\beta_2)}$$

$$2 - \alpha_1 w_1 = 2 - \frac{(1-b_2)\beta_1}{\beta_1-\beta_2} = \frac{\beta_1 - 2\beta_2 + b_2\beta_1}{(\beta_1-\beta_2)} = 1 + \frac{b_2\beta_1-\beta_2}{\beta_1-\beta_2}$$

$$T_2 + T_3 = \frac{f_t th}{4\theta}\left\{\left[1 + \frac{b_2\beta_1-\beta_2}{\beta_1-\beta_2}\right]\frac{(1-b_2)(1-\beta_1)}{(\beta_1-\beta_2)} + \frac{(b_2\beta_1-\beta_2)^2(1-\beta_2)}{(\beta_1-\beta_2)^2\,\beta_2}\right\}$$

$$= \frac{f_t th}{4\theta}\left\{\frac{(1-b_2)(1-\beta_1)}{(\beta_1-\beta_2)} + \frac{(b_2\beta_1-\beta_2)(1-b_2)(1-\beta_2)}{(\beta_1-\beta_2)^2} + \frac{(b_2\beta_1-\beta_2)^2(1-\beta_2)}{(\beta_1-\beta_2)^2\,\beta_2}\right\}$$

$$= \frac{f_t th}{4\theta}\left\{\frac{(1-b_2)(1-\beta_1)}{(\beta_1-\beta_2)} + \frac{(b_2\beta_1-\beta_2)}{(\beta_1-\beta_2)^2\beta_2} + [(1-b_2)(1-\beta_1)\beta_2 + (b_2\beta_1-\beta_2)\beta_2]\right\}$$

$$= \frac{f_t th}{4\theta}\left\{\frac{(1-b_2)(1-\beta_1)}{(\beta_1-\beta_2)} + \frac{(b_2\beta_1-\beta_2)(b_2-\beta_2)}{(\beta_1-\beta_2)\beta_2}\right\}$$

$$= \frac{f_t th}{4\theta}\left\{\frac{\beta_2 - b_2\beta_2 - \beta_1\beta_2 + b_2\beta_1\beta_2 + {b_2}^2\beta_1 - \beta_2 b_2 - b_2\beta_1\beta_2 + {\beta_2}^2}{\beta_2(\beta_1-\beta_2)}\right\}$$

$$T_1 + T_2 + T_3 = \frac{f_t th}{4\theta}\left\{1 + \frac{\beta_2 - b_2\beta_2 - \beta_1\beta_2 + {b_2}^2\beta_1 - \beta_2 b_2 + {\beta_2}^2}{\beta_2(\beta_1-\beta_2)}\right\}$$

$$= \frac{f_t th}{4\theta}\left\{\frac{\beta_1\beta_2 - {\beta_2}^2 + \beta_2 - b_2\beta_2 - \beta_1\beta_2 + {b_2}^2\beta_1 - \beta_2 b_2 + {\beta_2}^2}{\beta_2(\beta_1-\beta_2)}\right\}$$

$$= \frac{f_t th}{4\theta}\left\{\frac{\beta_2(1-b_2) + b_2(b_2\beta_1-\beta_2)}{\beta_2(\beta_1-\beta_2)}\right\}$$

$C = T \Rightarrow$

$$4\left\{(1-\alpha)\theta - \frac{1}{2}\right\}^2 = \frac{\beta_2(1-b_2) + b_2(b_2\beta_1-\beta_2)}{\beta_2(\beta_1-\beta_2)}$$

$$\alpha^2 - 2\left(1-\frac{1}{2\theta}\right)\varepsilon + \left(1-\frac{1}{2\theta}\right)^2 - \frac{\beta_2(1-b_2) + b_2(b_2\beta_1-\beta_2)}{4\theta^2\beta_2(\beta_1-\beta_2)} = 0$$

$$\alpha = \left(1-\frac{1}{2\theta}\right) - \frac{1}{2}\sqrt{4\left(1-\frac{1}{\theta}\right)^2 - 4\left(1-\frac{1}{\theta}\right)^2 + \frac{4\beta_2(1-b_2) + 4b_2(b_2\beta_1-\beta_2)}{4\theta^2\beta_2(\beta_1-\beta_2)}}$$

$$\alpha = 1 - \frac{1}{2\theta} - \frac{1}{2\theta}\sqrt{\frac{\beta_2(1-b_2) + 4b_2(b_2\beta_1-\beta_2)}{\beta_2(\beta_1-\beta_2)}}$$

$$\alpha = 1 - \frac{1}{2\theta}\left(1 + \sqrt{\frac{(1-b_2)^2}{\beta_1-\beta_2} + \frac{{b_2}^2}{\beta_2}}\right)$$

Phase III (Moment, μ)

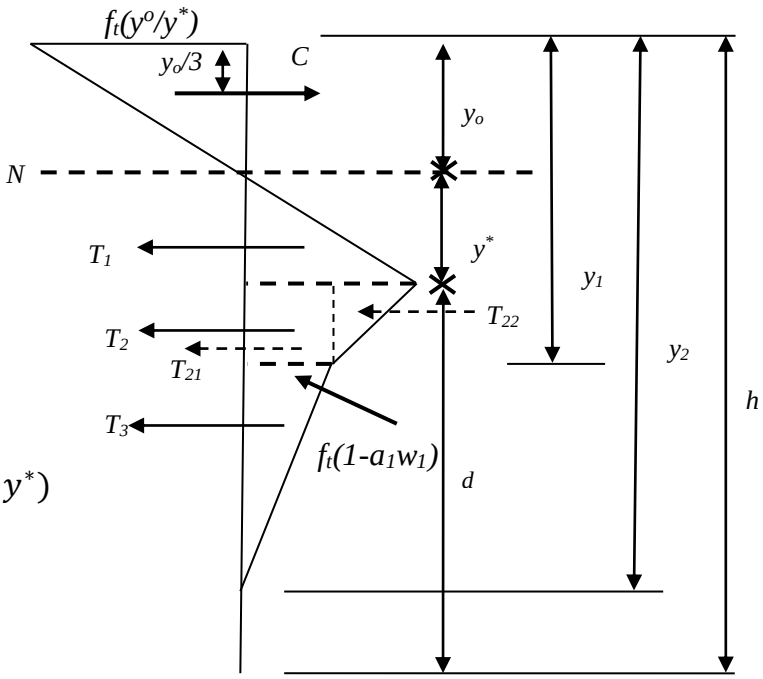

$$C = \frac{f_t th}{\theta}\left\{(1-\alpha)\theta - \frac{1}{2}\right\}^2 , \quad \text{as before}$$

$$T_1 = \frac{1}{2} f_t\, y^* t = \frac{f_t th}{4\theta} , \qquad \text{as before}$$

$$T_2 = T_{21} + T_{22}$$

$$T_{21} = t f_t (1 - a_1 w_1)(y_1 - y_0 - y^*)$$

$$T_{22} = \frac{t}{2}\{ f_t - f_t(1 - a_1 w_1)\}(y_1 - y_0 - y^*)$$

$$T_3 = \frac{t}{2}\{ f_t(1 - a_1 w_1)\}(y_2 - y_1)$$

$$y_1 - y_0 - y^* = \frac{h}{2\theta} . \frac{(1-b_2)\,(1-\beta)}{(\beta_1 - \beta_2)} , \qquad \text{as before}$$

$$y_2 - y_1 = \frac{h}{2\theta}\left[\frac{(1-b_2)\,(\beta_1 b_2 - \beta_2)}{\beta_2(\beta_1 - \beta_2)}\right] , \quad \text{as before}$$

$$y^{***} = \frac{T_1\left(\frac{2y^*}{3}\right) + T_{21}\left(\frac{y_1 - y_0 - y^*}{2} + y^*\right) + T_{22}\left(\frac{y_1 - y_0 - y^*}{3} + y^*\right) + T_3\left(\frac{y_2 - y_1}{3} + (y_1 - y_0)\right)}{T_1 + T_{21} + T_{22} + T_3}$$

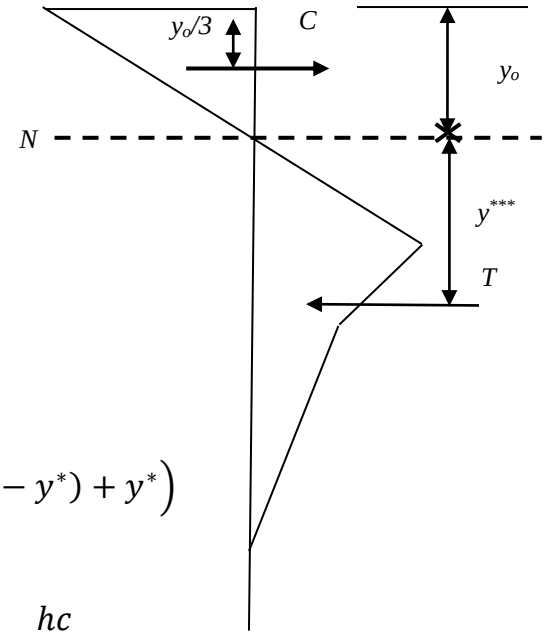

$$Note: \; T_1 + T_2 + T_3 = C = T$$

$$M = C\left(\frac{2y_0}{3} + y^{***}\right)$$

$$= C\left(\frac{2y_0}{3}\right) + Cy^{***}$$

$$M = C\left(\frac{2y_0}{3}\right) + T_1\left(\frac{2y^*}{3}\right) + T_{21}\left(\frac{y_1 - y_0 - y^*}{2} + y^*\right)$$

$$+T_{22}\left(\frac{y_1 - y_0 - y^*}{3} + y^*\right) + T_3\left(\frac{y_2 - y_1}{3} + (y_1 - y_0 - y^*) + y^*\right)$$

$$let\ c = \frac{(1-b_2)\,(1-\beta)}{(\beta_1 - \beta_2)} \quad then , \qquad y_1 - y_0 - y^* = \frac{hc}{2\theta}$$

$$M = C\left(\frac{2y_0}{3}\right) + T_1\left(\frac{2y^*}{3}\right) + T_{21}\left(\frac{hc}{4\theta} + y^*\right) + T_{22}\left(\frac{hc}{6\theta} + y^*\right) + T_3\left(\frac{h}{6\theta}\left[\frac{(1-\beta_2)\,(\beta_1 b_2 - \beta_2)}{\beta_2(\beta_1 - \beta_2)}\right] + \frac{hc}{2\theta} + y^*\right)$$

$$M = C\left(\frac{2y_0}{3}\right) + (T_1 + T_{21} + T_{22} + T_3)y^* - T_1\left(\frac{y^*}{3}\right) + T_{21}\left(\frac{hc}{4\theta}\right) + T_{22}\left(\frac{hc}{6\theta}\right) + T_3\left(\frac{h}{6\theta}\left[\frac{(1-\beta_2)\,(\beta_1 b_2 - \beta_2)}{\beta_2(\beta_1 - \beta_2)}\right] + \frac{hc}{2\theta}\right)$$

$\frac{2y_0}{3} + y^* = 1 - \alpha - \frac{y_0}{3h}, \quad y^* = \frac{h}{2\theta}$ as before

$$M = C\left(\frac{2y_0}{3} + y^*\right) - T_1\left(\frac{y^*}{3}\right) + T_{21}\left(\frac{hc}{4\theta}\right) + T_{22}\left(\frac{hc}{6\theta}\right) + T_3\left(\frac{h}{6\theta}\left[\frac{(1-\beta_2)\,(\beta_1 b_2 - \beta_2)}{\beta_2(\beta_1 - \beta_2)}\right] + \frac{hc}{2\theta}\right)$$

$$M = \frac{f_t th}{\theta}\left\{(1-\alpha)\theta - \frac{1}{2}\right\}^2\left(1 - \alpha - \frac{y_0}{3h}\right) - \frac{f_t th}{4\theta}\left(\frac{h}{6\theta}\right)$$

$$+ f_t(1 - a_1 w_1)\frac{hc}{2\theta}\left(\frac{hc}{4\theta}\right) + \frac{t}{2}\{f_t - f_t(1 - a_1 w_1)\}\frac{hc}{2\theta}\left(\frac{hc}{6\theta}\right)$$

$$+ \left\{\frac{t}{2}\{f_t - f_t(1 - a_1 w_1)\}\,\frac{h}{2\theta}\left[\frac{(1-\beta_2)\,(\beta_1 b_2 - \beta_2)}{\beta_2(\beta_1 - \beta_2)}\right]\right\}\left(\frac{h}{6\theta}\left[\frac{(1-\beta_2)\,(\beta_1 b_2 - \beta_2)}{\beta_2(\beta_1 - \beta_2)}\right] + \frac{hc}{2\theta}\right)$$

$1 - a_1 w_1 = \frac{b_2\beta_1 - \beta_2}{(\beta_1 - \beta_{2)}}$ as before

$$M = \frac{f_t th}{\theta}\left\{(1-\alpha)\theta - \frac{1}{2}\right\}^2\left(1 - \alpha - \frac{y_0}{3h}\right) - \frac{f_t th}{4\theta}\left(\frac{h}{6\theta}\right)$$

$$+ tf_t\frac{b_2\beta_1 - \beta_2}{\beta_1 - \beta_2}\frac{hc}{2\theta}\left(\frac{hc}{4\theta}\right) + \frac{f_t t}{2}\left\{1 - \frac{b_2\beta_1 - \beta_2}{\beta_1 - \beta_2}\right\}\frac{hc}{2\theta}\left(\frac{hc}{6\theta}\right)$$

$$+ \left\{\frac{tf_t}{2}\left\{\frac{b_2\beta_1 - \beta_2}{\beta_1 - \beta_2}\right\}\,\frac{h}{2\theta}\left[\frac{(1-\beta_2)\,(\beta_1 b_2 - \beta_2)}{\beta_2(\beta_1 - \beta_2)}\right]\right\}\left(\frac{h}{6\theta}\left[\frac{(1-\beta_2)\,(\beta_1 b_2 - \beta_2)}{\beta_2(\beta_1 - \beta_2)}\right] + \frac{hc}{2\theta}\right)$$

$$M = \frac{f_t th}{\theta}\left\{(1-\alpha)\theta - \frac{1}{2}\right\}^2\left(1 - \alpha - \frac{1}{3}\left(1 - \alpha - \frac{1}{2\theta}\right)\right) - \frac{f_t th^2}{24\theta^2}$$

$$+ \frac{f_t h^2 c^2}{8\theta^2}\frac{b_2\beta_1 - \beta_2}{(\beta_1 - \beta_2)} + \frac{f_t th^2 c^2}{24\theta^2}\left\{1 - \frac{b_2\beta_1 - \beta_2}{(\beta_1 - \beta_2)}\right\}$$

$$+\frac{fth^2}{24\theta^2}\left\{\frac{b_2\beta_1-\beta_2}{\beta_1-\beta_2}\right\}\left[\frac{(1-\beta_2)\,(\beta_1 b_2-\beta_2)}{\beta_2(\beta_1-\beta_2)}\right]^2+\frac{fth^2\mathrm{c}}{8\theta^2}\left\{\frac{b_2\beta_1-\beta_2}{(\beta_1-\beta_2)}\right\}\frac{(1-\beta_2)\,(\beta_1 b_2-\beta_2)}{\beta_2(\beta_1-\beta_2)}$$

$$\frac{6M}{f_t h^2 t}=\frac{6}{h\theta}\left\{(1-\alpha)\theta-\frac{1}{2}\right\}^2\left(\frac{2}{3}+\frac{1}{2\theta}\right)-\frac{1}{4\theta^2}+\frac{3c^2}{4\theta^2}\frac{b_2\beta_1-\beta_2}{(\beta_1-\beta_2)}+\frac{c^2}{4\theta^2}\left\{1-\frac{b_2\beta_1-\beta_2}{(\beta_1-\beta_2)}\right\}$$

$$+\frac{1}{4\theta^2}\left\{\frac{b_2\beta_1-\beta_2}{(\beta_1-\beta_2)}\right\}\left[\frac{(1-\beta_2)\,(\beta_1 b_2-\beta_2)}{\beta_2(\beta_1-\beta_2)}\right]^2+\frac{3c}{4\theta^2}\left\{\frac{b_2\beta_1-\beta_2}{(\beta_1-\beta_2)}\right\}\frac{(1-\beta_2)\,(\beta_1 b_2-\beta_2)}{\beta_2(\beta_1-\beta_2)}$$

$$\mu=4(1-3\alpha+3\alpha^2-\alpha^3)\theta-3+6\alpha-3\alpha^2+\frac{1}{4\theta^2}\left(1-\frac{b_2}{\beta_2}\right)\left(1-\frac{b_2}{\beta_2}+c\right)\left(1+\frac{\beta_1 c}{1-\beta_1}\right)+\left(\frac{c}{2\theta}\right)^2$$

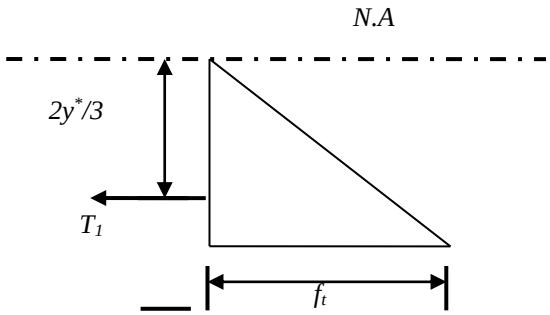

Phase II (Moment, μ)

$$T_1 = \frac{1}{2} f_t\, y^* t = \frac{f_t th}{4\theta}$$

$$T_2 = T_{21} + T_{22}$$

$$T_{21} = \sigma(w(y_1))td^*$$

$$T_{22} = \frac{1}{2}\{f_t - \sigma(w(y_1))\}td^*$$

$$T_3 = T_{31} + T_{32}$$

$$T_{31} = \{\sigma(w(h))\}t(d - d^*)$$

$$T_{32} = \frac{1}{2}\{\sigma(w(y_1)) - \sigma(w(h))\}t(d - d^*)$$

$$d^* = y_1 - y_0 - y^*$$

$$d - d^* = h - y_1$$

$$\sigma(w(y_1)) = \frac{f_t\, b_2\, \beta_1 - \beta_2}{(\beta_1 - \beta_2)}$$

$$\sigma\big(w(h)\big) = \frac{f_t\, (b_2 - (1 + 2\alpha\theta)\, \beta_2)}{(1_1 - \beta_2)}$$

$$T_{21} = \frac{f_t\, td^*\, (b_2\, \beta_1 - \beta_2)}{(\beta_1 - \beta_2)}$$

$$T_{22} = \frac{td^* f_t}{2}\left\{1 - \frac{(b_2\, \beta_1 - \beta_2)}{(\beta_1 - \beta_2)}\right\}$$

$$T_{31} = \left\{\frac{f_t\, t(d - d^*)(b_2 - (1 + 2\alpha\theta)\, \beta_2)}{(1_1 - \beta_2)}\right\}$$

$$T_{32} = \frac{f_t\, t(d - d^*)}{2}\left\{\frac{(b_2\, \beta_1 - \beta_2)}{(\beta_1 - \beta_2)} - \frac{(b_2 - (1 + 2\alpha\theta)\, \beta_2)}{(1_1 - \beta_2)}\right\}$$

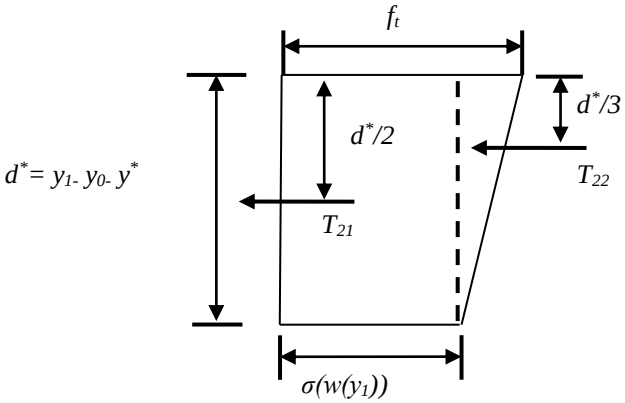

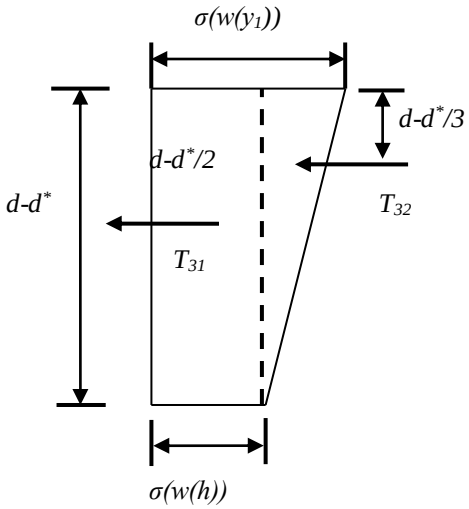

$$Note:\ T_1 + T_2 + T_3 = C = T$$

$$y^{***} = \frac{T_1\left(\frac{2y^*}{3}\right) + T_{21}\left(y^* + \frac{d^*}{2}\right) + T_{22}\left(y^* + \frac{d^*}{3}\right) + T_{31}\left(y^* + d^* + \frac{d-d^*}{2}\right) + T_{32}\left(y^* + d^* + \frac{d-d^*}{3}\right)}{T_1 + T_{21} + T_{22} + T_{31} + T_{32}}$$

$$M = C\left(\frac{2y_0}{3} + y^{***}\right)$$

$$= C\left(\frac{2y_0}{3}\right) + Cy^{***}$$

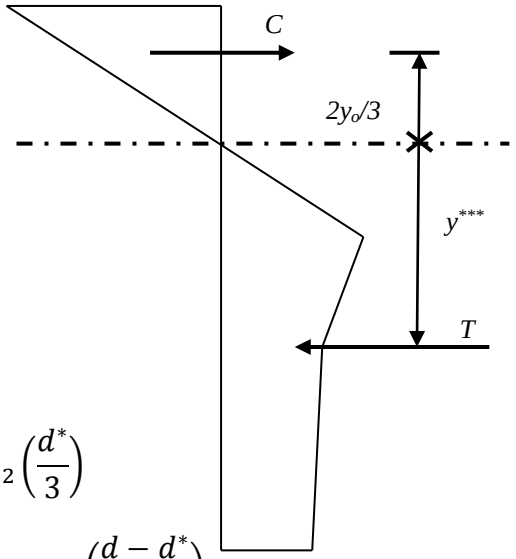

$$M = C\left(\frac{2y_0}{3}\right) + T_1\left(\frac{2y^*}{3}\right) + T_{21}\left(y^* + \frac{d^*}{2}\right) + T_{22}\left(y^* + \frac{d^*}{3}\right) + T_{31}\left(y^* + d^* + \frac{d-d^*}{2}\right) + T_{32}\left(y^* + d^* + \frac{d-d^*}{3}\right)$$

$$M = C\left(\frac{2y_0}{3}\right) + T_1\left(\frac{2y^*}{3}\right) + T_{21}(y^*) + T_{21}\left(\frac{d^*}{2}\right) + T_{22}(y^*) + T_{22}\left(\frac{d^*}{3}\right) + T_{31}(y^*) + T_{31}(d^*) + T_{31}\left(\frac{d-d^*}{2}\right) + T_{32}(y^*) + T_{32}(d^*) + T_{32}\left(\frac{d-d^*}{3}\right)$$

$$M = C\left(\frac{2y_0}{3}\right) + (T_1 + T_{21} + T_{22} + T_{31} + T_{32})\,y^* - T_1\left(\frac{y^*}{3}\right) + (T_1 + T_{21} + T_{22} + T_{31} + T_{32})d^* - T_1 d^* - \frac{1}{2}T_{21}d^* - \frac{2}{3}T_{22}d^* - \frac{1}{2}T_{31}d^* - \frac{1}{2}T_{32}d^* - \frac{1}{2}T_{31}d + \frac{1}{2}T_{32}d$$

$$M = C\left(\frac{2y_0}{3}\right) + Cy^* - T_1\left(\frac{y^*}{3}\right) + Cd^* - d^*(T_1 + T_{21} + T_{22} + T_{31} + T_{32}) + \frac{1}{2}T_{21}d^* + \frac{1}{3}T_{22}d^* + \frac{1}{2}T_{31}d^* + \frac{1}{2}T_{32}d^* + \frac{1}{2}T_{31}d + \frac{1}{2}T_{32}d$$

$$M = C\left(\frac{2y_0}{3}\right) + Cy^* - T_1\left(\frac{y^*}{3}\right) + Cd^* - Cd^* + \frac{1}{2}T_{21}d^* + \frac{1}{3}T_{22}d^* + \frac{1}{2}T_{31}d^* + \frac{1}{2}T_{32}d^* + \frac{1}{2}T_{31}d + \frac{1}{2}T_{32}d$$

$$M = \frac{f_t ht}{\theta}\left\{(1-\alpha)\theta - \frac{1}{2}\right\}^2\left(\frac{2y_0}{3}\right) + \frac{f_t ht}{\theta}\left\{(1-\alpha)\theta - \frac{1}{2}\right\}^2 y^* - T_1\left(\frac{y^*}{3}\right) + \frac{1}{2}T_{21}d^* + \frac{1}{3}T_{22}d^* + \frac{1}{2}T_{31}d^* + \frac{1}{2}T_{32}d^* + \frac{1}{2}T_{31}d + \frac{1}{2}T_{32}d$$

$$M = \frac{f_t ht}{\theta}\left\{(1-\alpha)\theta - \frac{1}{2}\right\}^2\left(y^* + \frac{2y_0}{3}\right) - \frac{f_t ht}{4\theta}\left(\frac{y^*}{3}\right) + \frac{d^*}{2}\frac{f_t\, td^*\,(b_2\,\beta_1 - \beta_2)}{(\beta_1 - \beta_2)}$$
$$+ \frac{1}{3}\frac{td^{*2}f_t}{2}\left\{1 - \frac{(b_2\,\beta_1 - \beta_2)}{(\beta_1 - \beta_2)}\right\} + \frac{d^*}{2}\left\{\frac{f_t\, t(d-d^*)(b_2 - (1+2\alpha\theta)\,\beta_2)}{(1-\beta_2)}\right\}$$
$$+ \frac{d^*}{2}\frac{f_t\, t(d-d^*)}{2}\left\{1 - \frac{(b_2\,\beta_1 - \beta_2)}{(\beta_1 - \beta_2)} - \frac{(b_2 - (1+2\alpha\theta)\,\beta_2)}{(1-\beta_2)}\right\}$$
$$+ \frac{d}{2}\left\{\frac{f_t\, t(d-d^*)(b_2 - (1+2\alpha\theta)\,\beta_2)}{(1-\beta_2)}\right\}$$
$$+ \frac{d}{2}\frac{f_t\, t(d-d^*)}{2}\left\{\frac{(b_2\,\beta_1 - \beta_2)}{(\beta_1 - \beta_2)} - \frac{(b_2 - (1+2\alpha\theta)\,\beta_2)}{(1-\beta_2)}\right\}$$

$$d^* = y_1 - y_0 - y^* == \frac{h}{2\theta}.\frac{(1-b_2)\,(1-\beta)}{(\beta_1 - \beta_2)} \quad , \; d - d^* = h - y_1$$

$$M = \frac{f_t ht}{\theta}\left\{(1-\alpha)\theta - \frac{1}{2}\right\}^2\left(h - d - \frac{y_0}{3}\right) - \frac{f_t ht}{4\theta}\left(\frac{y^*}{3}\right) + \left\{\frac{h}{4\theta}.\frac{(1-b_2)\,(1-\beta)}{(\beta_1 - \beta_2)}\right\}^2\frac{f_t t\,(b_2\,\beta_1 - \beta_2)}{2(\beta_1 - \beta_2)}$$
$$+ \frac{tf_t}{6}\left\{\frac{h}{4\theta}.\frac{(1-b_2)\,(1-\beta)}{(\beta_1 - \beta_2)}\right\}^2\left\{1 - \frac{(b_2\,\beta_1 - \beta_2)}{(\beta_1 - \beta_2)}\right\}$$

$$\mu = 4\theta\left(1 - 3\alpha + 3\alpha^2 - \frac{\alpha^3}{1-\beta_2}\right) - 3 + 6\alpha - \frac{(1-b_2)(3\alpha^2 - (c/2\theta)^2}{1-\beta_2}$$

These expressions were coded in MATLAB Program that is appended below:

```
%*****************************************************************
%                          CARDIFF UNIVERSITY
%                         SCHOOL OF ENGINEERING
% A MATLAB code for Determination of the static response of self-
% compacting UHPFRC beams under three-point bending, using a
% bilinear tension-softening (stress-crack opening) relationship
% based on the fictitious crack model (Non-Linear Cracked Hinge
Model)
%*****************************************************************
%     References
% 1. Hillerborg A. (1980). Analysis of fracture by means of the
%    fictitious crack model, particularly for fibre-reinforced
%    concrete, Int J Cement Composites, 2, 177-184.
% 2. Hillerborg A., Modeer M. and Petersson P. (1976). Analysis of
%    crack formation and crack growth in concrete by means of
%    fracture mechanics and finite elements, Cement Concrete
%    Research, 6, 773-782.
% 3. Olesen J.F. (2001). Fictitious crack propagation in fibre-
%    reinforced concrete beams, J Engineering Mechanics, 127, 272-80
%*****************************************************************
%                       Part One Load Deflection Response
%*****************************************************************
%     List of variables
%     Name              Description
%     -----             ------------
%     alp0              Initial notch depth to beam depth ratio
%     db                beam depth, mm
%     h                 Height of the hinge, mm
%     L                 Span length of the TPB, mm
%     t                 Thickness of the hinge, mm
%     S                 Width of the hinge, mm
%     a1, a2, b1 & b2    Parameters for the bilinear relation
%     a1 & a2           1/mm
%     b1 & b2           Dimensionless
%     E                 Young modulus, GPa
%     ft                Splitting tensile strength, GPa
 %*****************************************************************
clc
clear all
close all
%*****************************************************************
%     Enter the beam dimensions details
%*****************************************************************
L=400;                              %  the span length;
t=100;                              %  the normal thickness;
db=100;                             %  the beam depth;
a0=60;
themin=0;
themax=2000;
%*****************************************************************
%      Enter a1, a2, b2, ft, E limits values
%*****************************************************************
a1=0.256;
a2=0.11;
b2=0.63;
ft=0.01044;
E1=45.25;
alp0=a0/db;
h=(1-alp0)*db;
s=0.5*h;
%*****************************************************************
```

```
%*********************************************************************
rho=0;
k=0;
increment=themax/999;

for the=themin :increment:themax
the01=1-rho ;
bet1=ft*a1*s/E1;
bet2=ft*a2*s/E1;
c =(1-b2)*(1-bet1)/(bet2-bet1);
the12=.5*(1-rho-c+((1-rho-c)^2+c^2/(bet1-1))^0.5);
the23=.5*(rho*(bet2-1)+b2/bet2+(rho^2*(bet2-1)^2+2*rho*(bet2-1)*b2/bet2+(1-
b2)^2/(bet1 -bet2)+b2^2/bet2)^.5);
mu=the;
%*********************************************************************
% Alpha & Mu Calculation
%*********************************************************************
% For phase 0
if (0<=the & the<=the01)
alp = 0;
mu = the;
def = 0;

%---------------------------------------------------------------------
% For phase I
%---------------------------------------------------------------------
elseif(the01<the && the<the12)
bi=1 ;
beti = bet1;
alp = 1-bet1-((1-bet1)*((1-rho)/the-bet1))^.5;
mu = 4*(1-3*alp+3*alp^2-alp^3/(1-bet1))*the+(6*alp-3)*(1-rho);

%---------------------------------------------------------------------
 % For phase II
%---------------------------------------------------------------------
elseif(the12<the && the<the23)
bi = b2;
beti = bet2;
alp =1-bet2-(1-b2)/(2*the)-(( 1-bet2)*(( 1-b2)^2/(4*the^2)/(bet1 -bet2)-
bet2+(b2-rho)/the))^.5;
mu = 4*(1-3*alp+3*alp^2-alp^3/(1-bet2))*the+(6*alp-3)*(1-rho)-(((1-
b2)*(3*alp^2-(c/(2*the))^2))/(1-bet2));

%---------------------------------------------------------------------
 % For phase III
%---------------------------------------------------------------------
elseif(the23<the)
bi =0;
beti = 0;
alp = 1 -1 /(2*the)*(1+((1-b2)^2/(bet1-bet2)+b2^2/bet2-4*rho*the)^.5);
mu = 4*(1-3*alp+3*alp^2-alp^3)*the+(6*alp-3)*(1-rho)-
3*alp^2+1/(4*the^2)*(1-b2/bet2)*(1-b2/bet2+c)*(1+bet1*c/(1-
bet1))+(c/(2*the))^2;
end
k=k+1;
def = the+((L/(3*s))-1)*mu;
pp(k) = (2/3*ft*h^2*t/L)*mu;
DEF(k)= def *L*s*ft/(2*h*E1);
end
Sami = [DEF;pp];
x = Sami(:,1);                              % the x value
y = Sami(:,2);                              % the y value
```

```
sortedValuesload = unique(pp(:));          % Unique sorted values
maxValuesload = sortedValuesload(end) ;    % Get the  largest values

sortedValuesdeflection = unique(DEF(:));
maxValuesdeflection = sortedValuesdeflection(end);

%%%%%%%%%%%%%%%%%%%%%%%%%%%%%%%%%%%%%%%%%%%%%%%%%%%%%%%%%%%%%%%%%%%%%%%%%%%%
%%%%%%%%%%%%%%%%%%%%%%%%%%%%%%%%%%%%%%%%%%%%%%%%%%%%%%%%%%%%%%%%%%%%%%%%%%%%
%%%%%%%%%%%%%%%%%%%%%%%%%%%%%%%%%%%%%%%%%%%%%%%%%%%%%%%%%%%%%%%%%%%%%%%%%%%%


%                      Part Two Load CMOD Response
%%%%%%%%%%%%%%%%%%%%%%%%%%%%%%%%%%%%%%%%%%%%%%%%%%%%%%%%%%%%%%%%%%%%%%%%%%%%
%     List of variables
%     Name               Description
%     -----              ------------
%     alp0               Initial notch depth to beam depth ratio
%     db                 beam depth, mm
%     h                  Height of the hinge, mm
%     L                  Span length of the TPB, mm
%     t                  Thickness of the hinge, mm
%     S                  Width of the hinge, mm
%     a1, a2, b1 & b2     Parameters for the bilinear relation
%     a1 & a2            1/mm
%     b1 & b2            Dimensionless
%     E                  Young modulus, GPa
%     ft                 Splitting tensile strength, GPa
%%%%%%%%%%%%%%%%%%%%%%%%%%%%%%%%%%%%%%%%%%%%%%%%%%%%%%%%%%%%%%%%%%%%%%%%%%%%
%%%%%%%%%%%%%%%%%%%%%%%%%%%%%%%%%%%%%%%%%%%%%%%%%%%%%%%%%%%%%%%%%%%%%%%%%%%%
clc
clear all
close all
%%%%%%%%%%%%%%%%%%%%%%%%%%%%%%%%%%%%%%%%%%%%%%%%%%%%%%%%%%%%%%%%%%%%%%%%%%%%
%     Enter the beam dimensions details
%%%%%%%%%%%%%%%%%%%%%%%%%%%%%%%%%%%%%%%%%%%%%%%%%%%%%%%%%%%%%%%%%%%%%%%%%%%%
**********
E=45.25;
ft=0.00954;
L=400;                        % enter the span length;
t=100;                        % enter the normal thickness;
db=100;                       % enter the beam depth;
a0=10;
themin=0;
themax=200;
a1=0.16;
a2=0.07;
b2=0.59;
alp0=a0/db;
h=(1-alp0)*db;
s=0.5*h;

%%%%%%%%%%%%%%%%%%%%%%%%%%%%%%%%%%%%%%%%%%%%%%%%%%%%%%%%%%%%%%%%%%%%%%%%%%%%
%%%%%%%%%%%%%%%%%%%%%%%%%%%%%%%%%%%%%%%%%%%%%%%%%%%%%%%%%%%%%%%%%%%%%%%%%%%%
rho=0;
k=0;
increment=themax/999;
for the=themin :increment:themax
the01=1-rho ;
bet1=ft*a1*s/E;
bet2=ft*a2*s/E;
c =(1-b2)*(1-bet1)/(bet2-bet1);
the12=.5*(1-rho-c+((1-rho-c)^2+c^2/(bet1-1))^0.5);
```

```
the23=.5*(rho*(bet2-1)+b2/bet2+(rho^2*(bet2-1)^2+2*rho*(bet2-1)*b2/bet2+(1-
b2)^2/(bet1 -bet2)+b2^2/bet2)^.5);
%*****************************************************************
%  Alpha & Mu Calculation
%*****************************************************************

%-----------------------------------------------------------------
% For phase I
%-----------------------------------------------------------------
if (0<=the && the<the01)
mu=the01;
alp = 0;
cod = 0;
%-----------------------------------------------------------------
% For phase I
%-----------------------------------------------------------------
elseif(the01<=the && the<the12)
bi= 1;
beti = bet1;
alp = 1-bet1-((1-bet1)*((1-rho)/the-bet1))^.5;
mu = 4*(1-3*alp+3*alp^2-alp^3/(1-bet1))*the+(6*alp-3)*(1-rho);
cod = s*ft/E*(1-bi+2*alp*the)/(1-beti);
%-----------------------------------------------------------------
% For phase I
%-----------------------------------------------------------------
elseif(the12<=the && the<the23)
bi = b2;
beti = bet2;
alp =1-bet2-(1-b2)/(2*the)-(( 1-bet2)*(( 1-b2)^2/(4*the^2)/(bet1 -bet2)-
bet2+(b2-rho)/the))^.5;
mu = 4*(1-3*alp+3*alp^2-alp^3/(1-bet2))*the+(6*alp-3)*(1-rho)-(((1-
b2)*(3*alp^2-(c/(2*the))^2))/(1-bet2));
cod = s*ft/E*(1-bi+2*alp*the)/(1-beti);
%-----------------------------------------------------------------
% For phase I
%-----------------------------------------------------------------
elseif(the23<=the)
bi =0;
beti = 0;
alp = 1 -1 /(2*the)*(1+((1-b2)^2/(bet1-bet2)+b2^2/bet2-4*rho*the)^.5);
mu = 4*(1-3*alp+3*alp^2-alp^3)*the+(6*alp-3)*(1-rho)-
3*alp^2+1/(4*the^2)*(1-b2/bet2)*(1-b2/bet2+c)*(1+bet1*c/(1-
bet1))+(c/(2*the))^2;
 cod = s*ft/E*(1-bi+2*alp*the)/(1-beti);
%-----------------------------------------------------------------
end
k=k+1;
pp(k) = 2/3*ft*h^2*t/L*mu;
m = pp(k)*L/4;
sigm = 6*m/(t*db^2);
cod0 = 4*sigm*a0/E*(0.76-2.28*alp0+3.87*alp0^2-2.04*alp0^3+0.66/(1-
alp0)^2);
CMOD(k) = cod + cod0;
end
Sami = [CMOD;pp]';
x = Sami(:,1);                          % the x value
y = Sami(:,2);                          % the y value
sortedValuesload = unique(pp(:));       % Unique sorted values
maxValuesload = sortedValuesload(end) % Get the largest values
sortedValuesdeflection = unique(CMOD(:));
maxValuesdeflection = sortedValuesdeflection(end)
```

Appendix B

Load Deflection Curves for Self-Compacting Ultra-High Performance Fibre-Reinforced Concrete Strips

Cyclic Load- Central Deflection Plots for Self-Compacting Ultra-High Performance Fibre-Reinforced Concrete Strips.

The recorded load-deflection plots under cyclic loading for the UHPFRC strips need to be corrected in order to take into account the inevitable drift in the LVDT because of dynamic loading. This has been achieved by calculating the actual deflection at the upper load limit using elastic theory. This was possible in most cyclic load ranges because the upper limit load was still within the elastic range of the material. The corrected cyclic load- central deflection traces of the specimens are plotted for specimens with poor and good fibre distribution (Figures B.1– B.7).

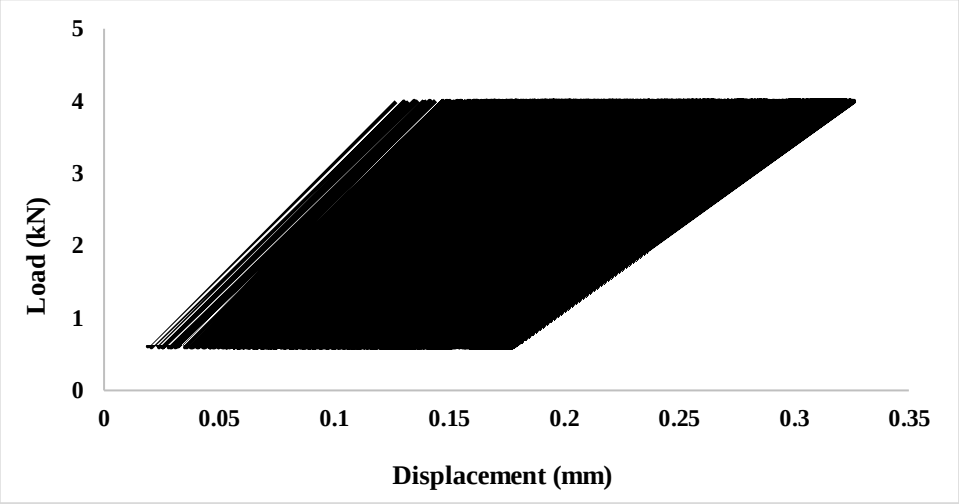

Figure B.1 Cyclic load- central deflection plot of specimen load range 0.6 – 4.0 kN. Specimen sustained 1000000 cycles (poor fibre distribution)

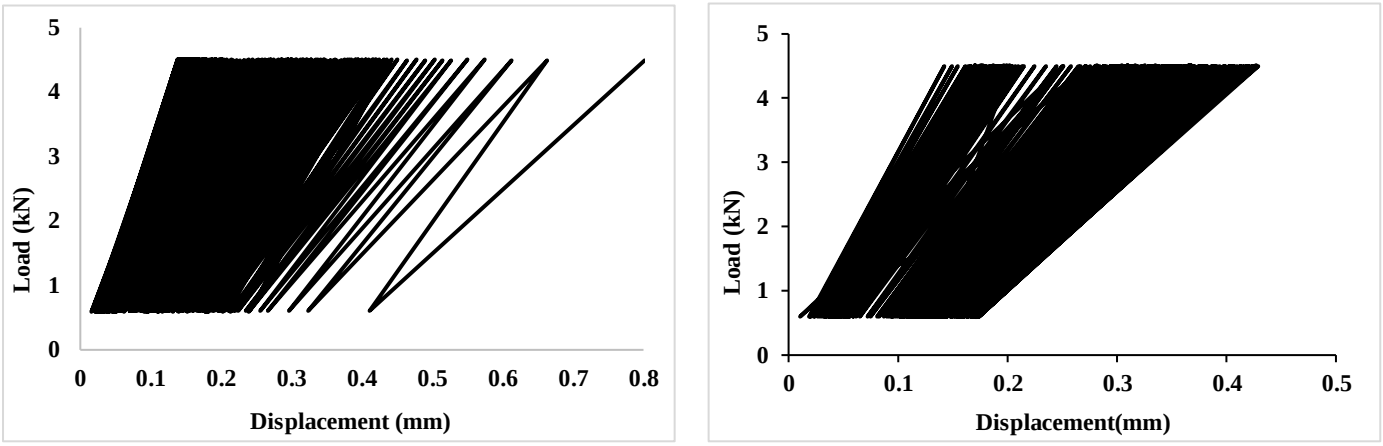

a- Specimen sustained 87600 cycles **b-** Specimen sustained 99000 cycles

Figure B.2 Cyclic load- central deflection plot of specimens load range 0.6 – 4.5 kN (poor fibre distribution)

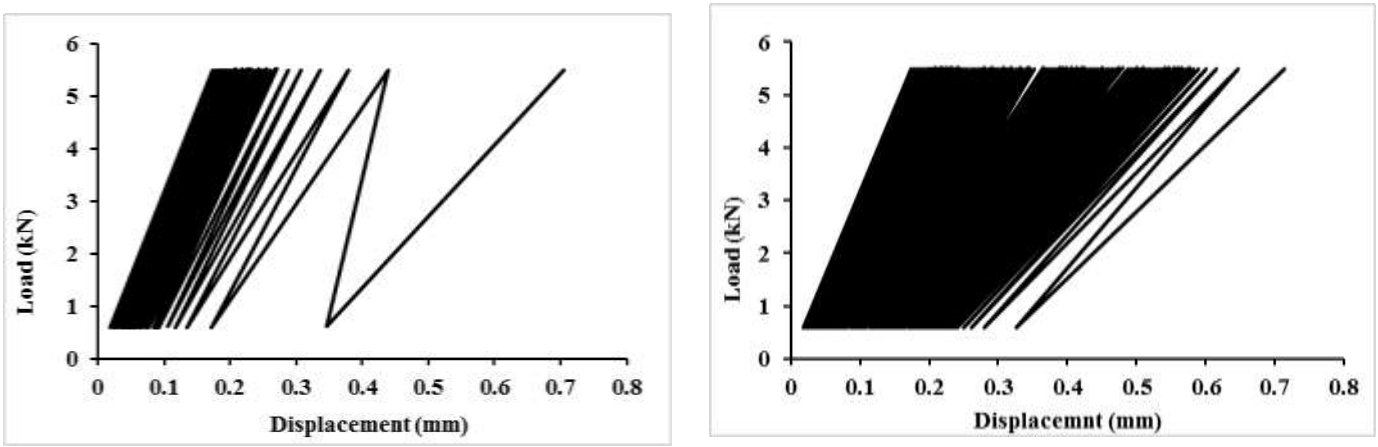

a-Specimen sustained 5400 cycles **b-** Specimen sustained 25200 cycles

Figure B.3 Cyclic load-central deflection plot of specimens under load range 0.6 – 5.5 kN (poor fibre distribution)

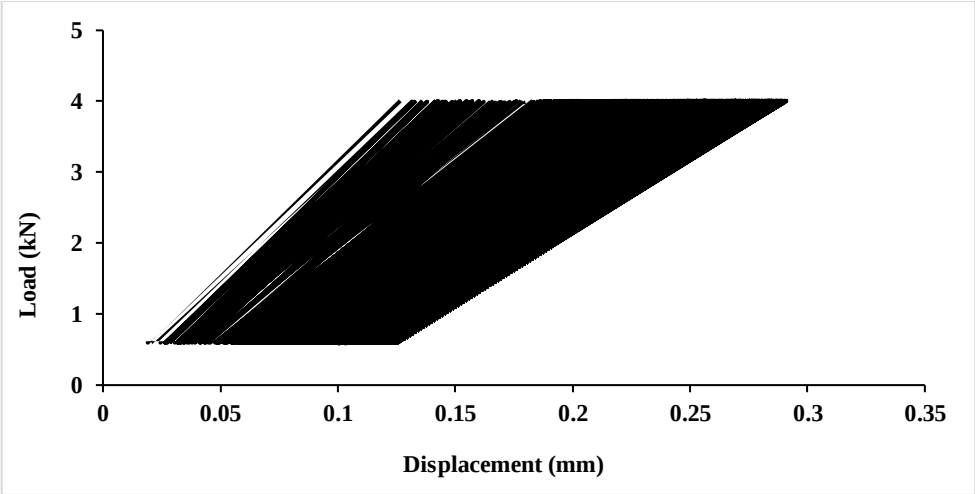

Figure B.4 Cyclic load- central deflection plot of specimen under load range 0.6 – 4 kN

Specimen sustained 1000000 cycles (good fibre distribution)

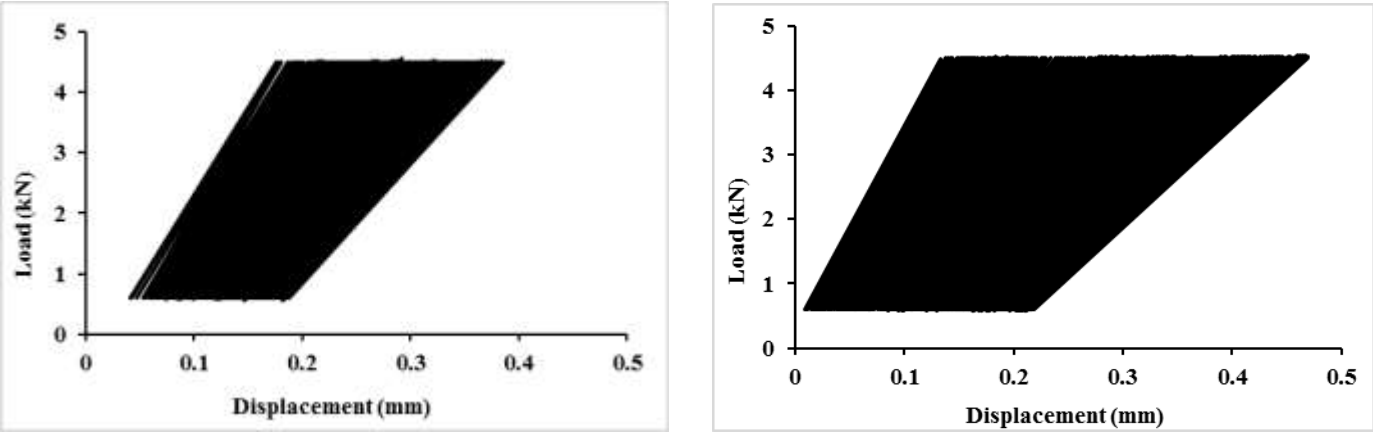

Figure B.5 Cyclic load- central deflection plot of specimen under load range 0.6 – 4.5 kN

Specimen sustained 1000000 cycles (good fibre distribution)

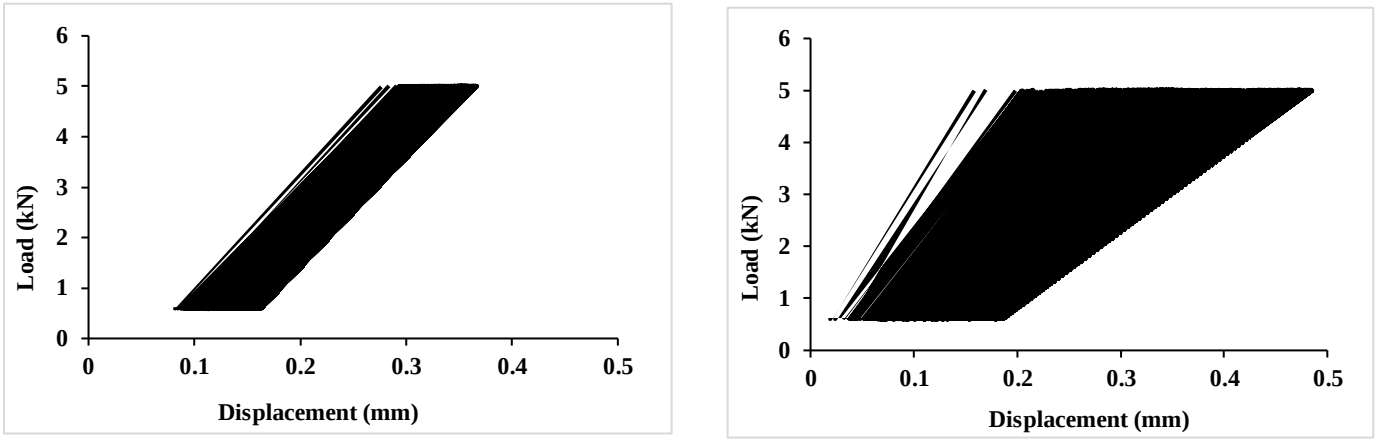

Figure B.6 Cyclic load- central deflection plot of specimen under load range 0.6 – 5.0 kN

Specimen sustained 1000000 cycles (good fibre distribution)

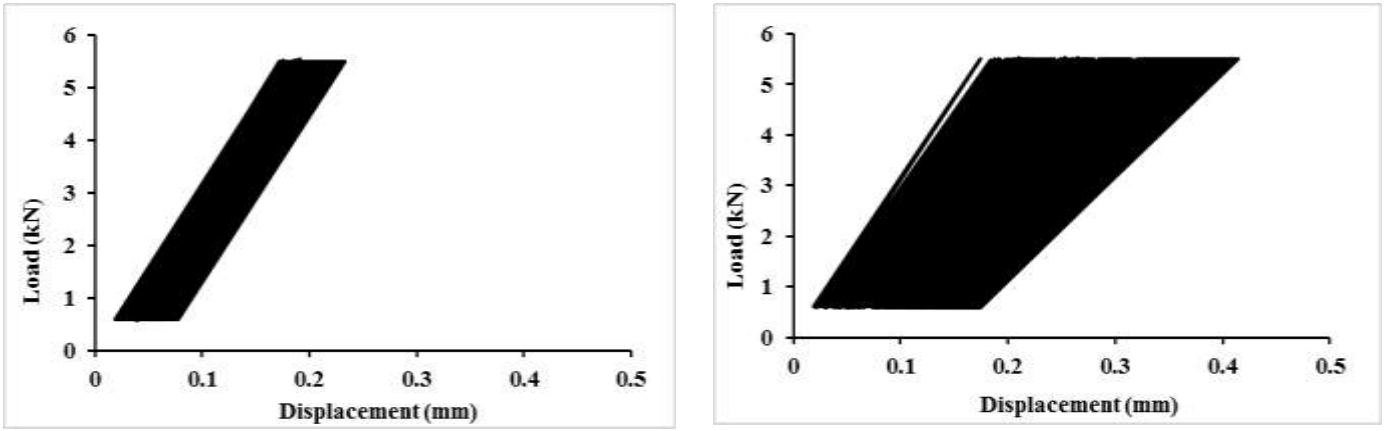

Figure B.7 Cyclic load- central deflection plot of specimen under load range 0.6 – 5.5 kN

Specimen sustained 1000000 cycles (good fibre distribution)

Appendix C

Cyclic Load- Central Deflection Plots of RC Beam with and without UHPFRC Strips

Cyclic Load- Central Deflection Plots of RC Beam with and without UHPFRC Strips

The recorded load-deflection plots under cyclic loading for the RC beams with and without the UHPFRC strips need to be corrected in order to take into account the inevitable drift in the LVDT because of dynamic loading. This has been achieved by calculating the actual deflection at the upper load limit using elastic theory. This was possible in most cyclic load ranges because the upper limit load was still within the elastic range of the material. The corrected cyclic load- central deflection traces of the RC beams are plotted for specimens with poor and good fibre distribution (Figures C.1–C.7).

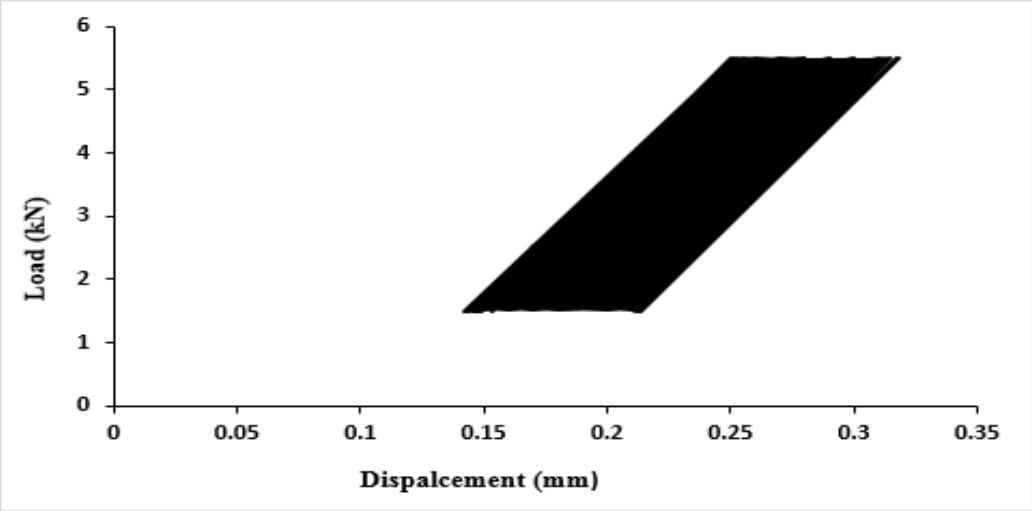

Figure C.1 Cyclic load- central deflection plot of a beam under maximum cyclic load level 18.1%

(Beam sustained 1000000 cycles without any noticeable cracks)

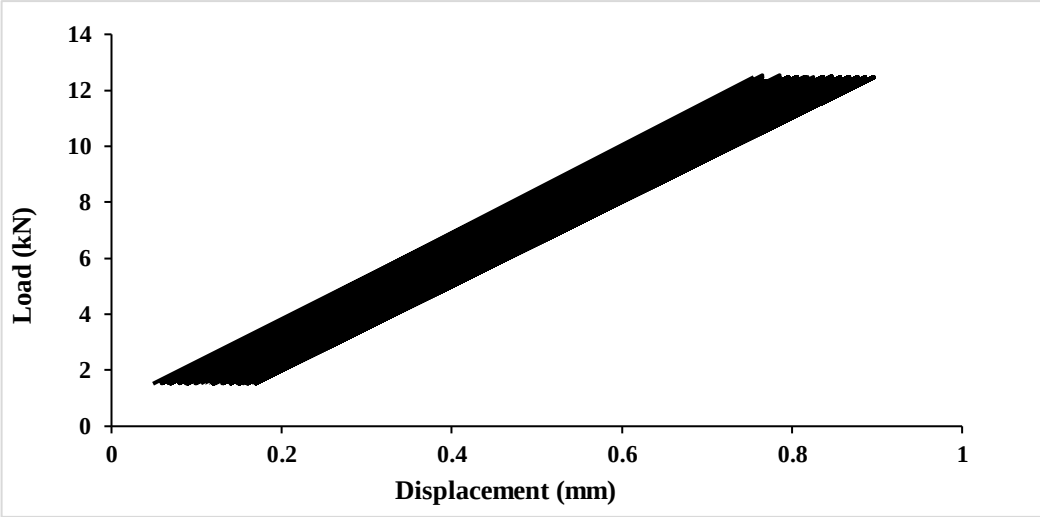

Figure C.2 Cyclic load- central deflection plot of a beam under maximum cyclic load level 41.12%

(Beam sustained 1000000 cycles with some minor cracks)

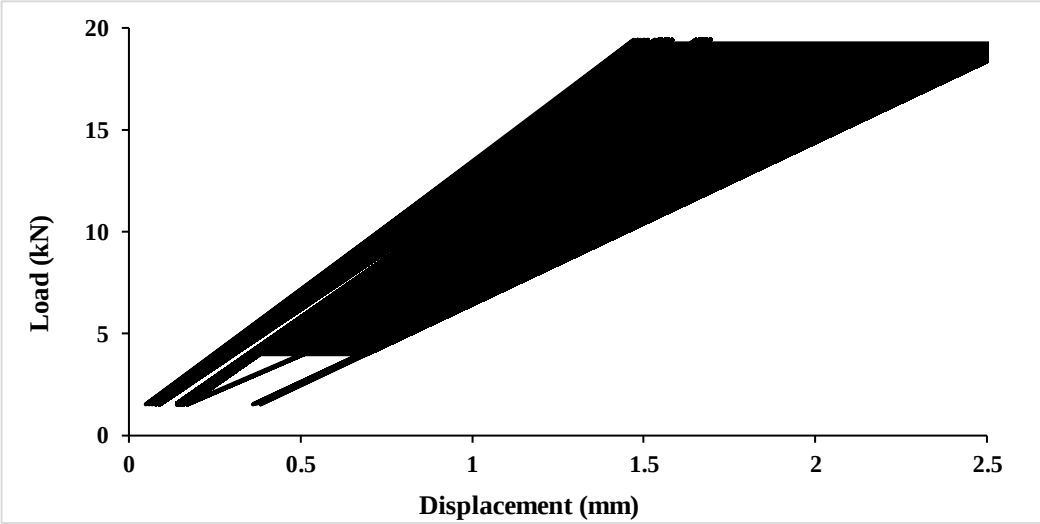

Figure C.3 Cyclic load- central deflection plot of a beam under maximum cyclic load level 64.14%

(Beam sustained 596136 cycles)

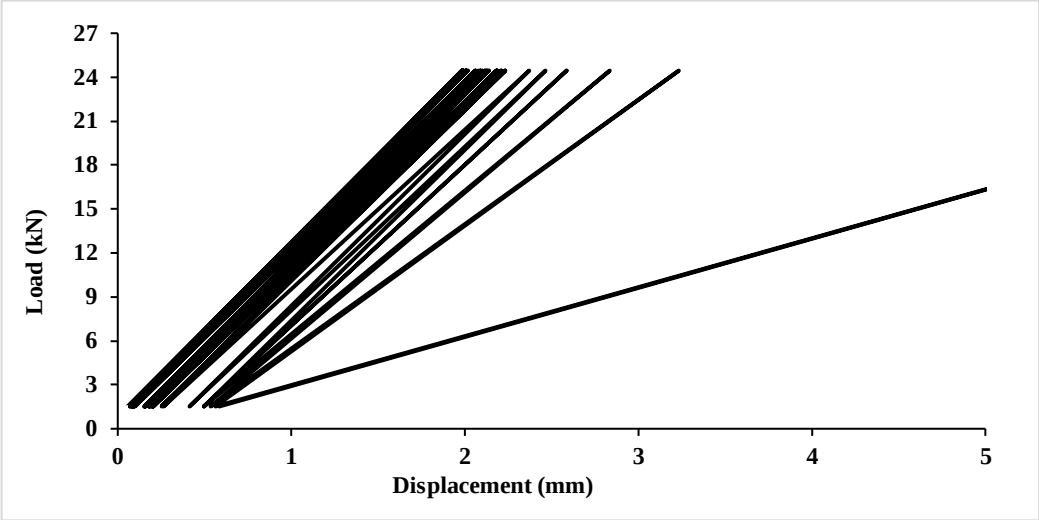

Figure C.4 Cyclic load- central deflection plot of a RC beam under maximum cyclic load level 80.59% (Beam sustained 11458 cycles)

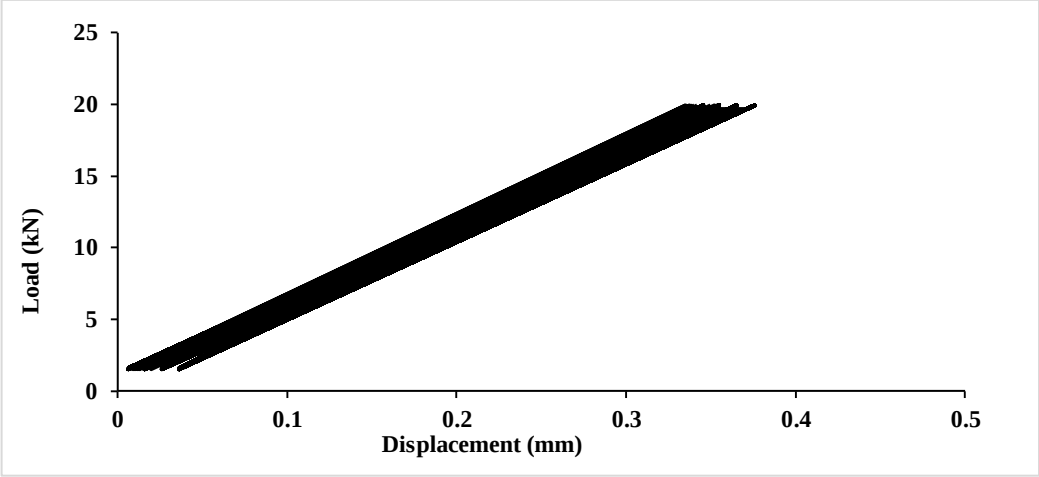

Figure C.5 Cyclic load- central deflection plot of RC beam retrofitted with UHPFRC strips under maximum cyclic load level 46.91% (Beam sustained 1000000 cycles without any noticeable cracks)

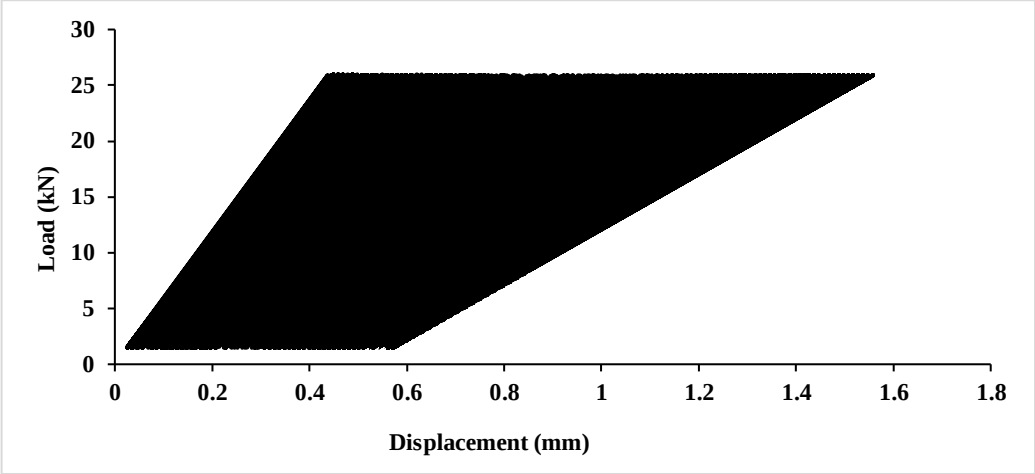

Figure C.6 Cyclic load- central deflection plot of RC beam retrofitted with UHPFRC strips under maximum cyclic load level 60.99% (Beam sustained 1000000 cycle with some cracks)

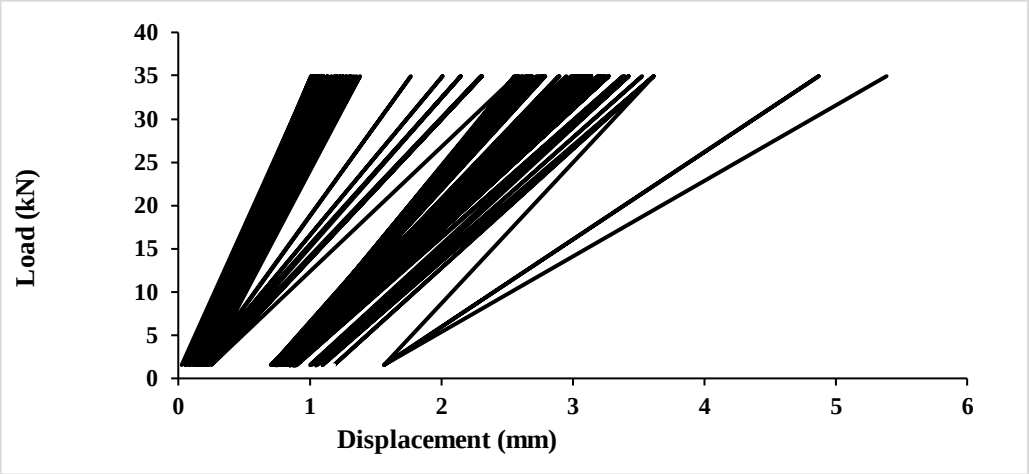

Figure C.7 Cyclic load- central deflection plot of RC beam retrofitted with UHPFRC strips under maximum cyclic load level 82.1% (Beam sustained 32100 cycles and failed by rebar fatigue)

Appendix D

Stress Analysis of Reinforcing Bar Under High Cyclic Load

Stress Analysis of Reinforcing Bar under High Cyclic Load (Beam Subjected to Upper Maximum Load 35kN)

Applying the traditional transformed area methodology to the retrofitted RC beam subjected to the three-point bend cyclic load range 1.5 to 35 kN, it is found that the neutral axis lies at 91.3 mm from the extreme compression fibre and the second moment of area of the cross section is 56.08×10^6 mm^4. Accordingly, at the lower load limit of 1.5 kN, the stresses in concrete extreme fibre, steel reinforcing bar, and the extreme fibre of the retrofitting UHPFRC strip are 0.61, 1.47, and 0.75 MPa, respectively. Assuming the UHPFRC strip had reached its tensile strength of 12.02 MPa (Chapter Five) but not cracked at the upper load limit of 35 kN, then the corresponding stresses in concrete would be 14.25 MPa and in the steel bar 203.1 MPa. The cyclic stress range in the steel bar would be 201.63 MPa at a stress ratio of 1.47/203.1 = 0.0072. This cyclic stress range is very close to the allowable limit in the supplier's data sheet (cyclic stress range 200 MPa and a stress ratio of 0.2 for a fatigue life in excess of five million cycles).

However, as noted in the text a major flexural crack formed in the UHPFRC strip under this cyclic load range after approximately 5000 cycles. The reduced tension carrying capacity of the UHPFRC strip can be estimated from its known stress-crack opening relation (Chapter Five), Fig. D.1. At a crack opening of, say 1mm, the tensile strength of UHPFRC reduces from 12.02 to 9.86 MPa, so that its contribution to the tensile capacity of the retrofitted beam reduces from 42.07 kN to 34.5 kN and that of the reinforcing steel must increase to 30.53 kN from 22.97 kN (Fig. D.2). As a result the stress in steel increases to 269.93 MPa. The cyclic stress range in the steel bar is 268.46 MPa at a stress ratio of 1.47/269.93 = 0.0054 which is well in excess of the supplier's recommended stress range of 200 MPa for this steel.

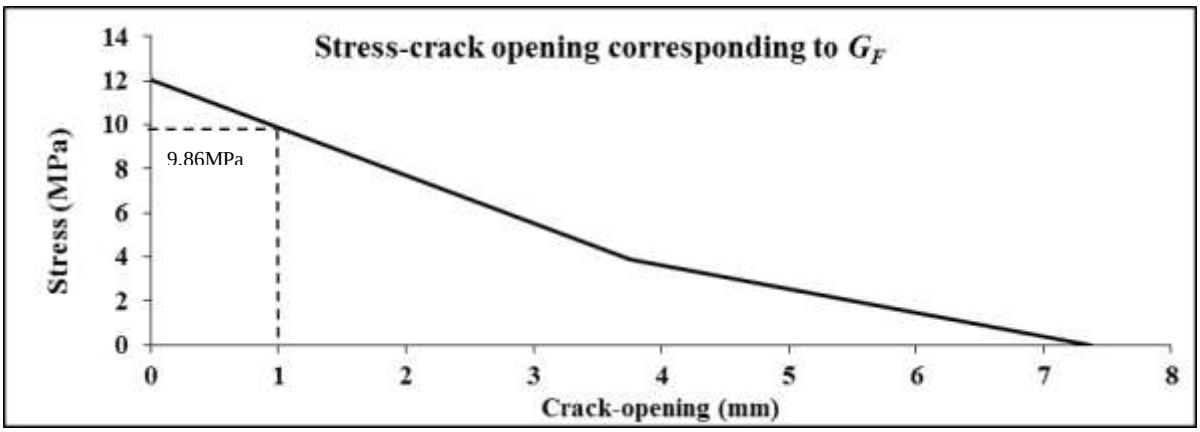

Figure D.1 Tensile stress-crack opening relation of UHPFRC corresponding to its size-independent specific fracture energy

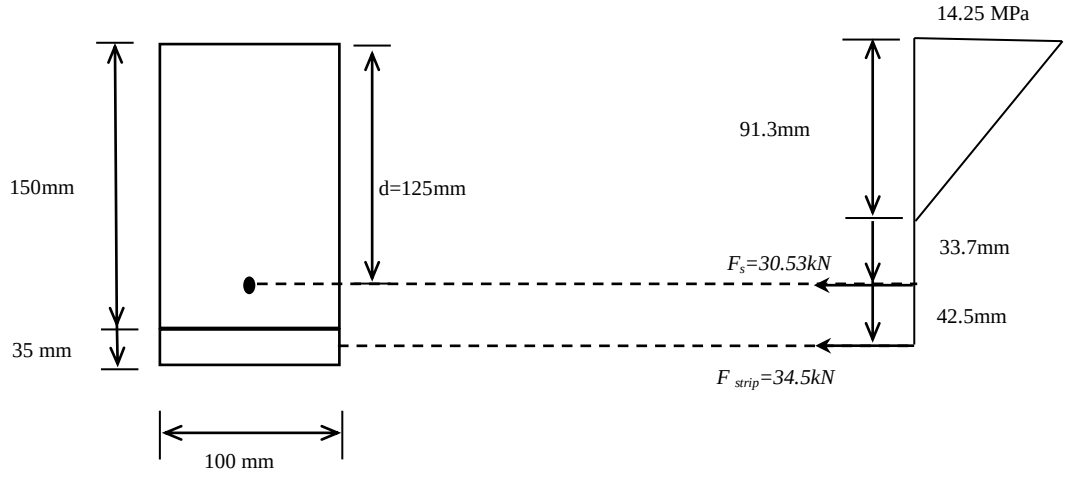

Beam with UHPFRC strip **Force distribution in the section**

Figure D.2 Contributions of retrofitting strip after it has cracked and of steel bar to tension under a mid-span load of 35 kN